Department of Biomedical Engineering
University of Strathclyde

# Towards advanced manufacturing for personalised vascular grafts

Lisa Asciak

A thesis submitted in partial fulfilment of the requirements for the Degree of Doctor of Philosophy

September 2023

## Declaration of Authenticity

This thesis is the result of the author's original research. It has been composed by the author and has not been previously submitted for examination which has led to the award of a degree.



Signed:  Date: 26/09/2023

# Abstract

Surgical repair of aortic pathologies involves synthetic tubular grafts generally made of a polyester fabric. Despite being the gold-standard, such grafts do not readily endothelialise and are unable to mimic the mechanical behaviour and intricate anatomical geometry of the native aorta, contributing to suboptimal haemocompatibility, haemodynamic disruption, and long-term cardiovascular-related complications. Moreover, to date, vascular graft research has predominantly focussed on developing small diameter conduits (<6 mm) with little attention paid to larger grafts. Therefore, the primary aims of this thesis were to develop an aortic graft substitute that addresses the main limitations of the current graft technologies: (1) mechanically matches aortic tissue, (2) closely mimics the patient's anatomy, and (3) promotes endothelialisation. To achieve this, hydrogels in combination with stereolithography (SLA) 3D-printing were investigated.

Alginate, a natural monomer derived from seaweed, was first investigated due to its ease of gelling ability in the presence of divalent cations. However, single-networked, calcium-crosslinked alginate hydrogels exhibited poor elastic properties (strength: 0.02 ± 0.006 MPa, stiffness: 0.05±0.004 MPa, elongation at break: 51.60 ±11.66%) when compared to aortic tissue data reported in the literature. Therefore, to enhance the mechanical properties, a synthetic polyethylene glycol diacrylate (PEGDA) monomer was incorporated to create an interpenetrating polymer network (IPN). Moreover, PEGDA in the presence of a photoinitiator enables photopolymerisation, rendering the IPN suitable for SLA 3D-printing. The alginate:PEGDA IPN hydrogels both moulded and 3D-printed demonstrated strength (moulded: 0.39 ±0.05 MPa; 3D-printed: 0.34 ±0.05 MPa) and stiffness (moulded: 1.61 ±0.19 MPa; 3D-printed: 1.79 ±0.19 MPa) within range of the human aorta. Tubular conduits of similar dimensions to the human aorta were also fabricated via moulding and SLA 3D-printing, with the latter facilitating the fabrication of more complex, patient-specific structures.

Finally, given the poor cell adhesion of both alginate and PEGDA monomers, an arginine-glycine-aspartic acid (RGD)-based peptide was synthesised and incorporated within each individual monomer, to biofunctionalise the IPN for endothelialisation. Alginate:RGD showed successful endothelial cell adhesion and coverage on the hydrogel's surface. However, this was not the case with the PEGDA:RGD hydrogel. Furthermore, incorporating the RGD peptide to the alginate:PEGDA IPN proved to be challenging due to significant phase separation during hydrogel synthesis, and further work is required to optimise this. Nonetheless, this work shows great promise towards the development of more compliant, patient-specific aortic grafts.

# Acknowledgements

First, I would like to express my sincere gratitude to my supervisor Dr Christopher McCormick for giving me the opportunity to work on this project, and for his continuous support and guidance over the last four years. Special thanks also go to my second supervisor, Professor Will Shu, and my industry supervisors at Terumo Aortic, Dr Robbie Brodie and Dr Niall Paterson, for their keen interest in the project and invaluable advice provided in our catch-up meetings.

I would also like to acknowledge the financial support provided by the University of Strathclyde, the Scottish Research Partnership in Engineering, the National Manufacturing Institute Scotland - Industrial Doctorate Programme (SRPe NMIS-IDP-006), Terumo Aortic Limited, and the Fund for the Replacement of Animals in Medical Experiments (FRAME, FIGStrat21), without whom this project would not have been possible.

It has been an amazing experience working in the BME department, and I am thankful to all past and present members of our research group, and to the rest of the PGR cohort in the level 3 office of the Wolfson. A special thanks goes to several BME members of staff who have helped me in this project in one way or another, especially Mrs Catherine Henderson for her technical expertise, but mostly for our lovely chats, and for always being there for me and offering to help with a lovely smile, no matter how busy she gets!

To everyone else that I have worked closely with throughout the last four years, especially Dr Roger Domingo-Roca for showing me the ropes on everything related with 3D-printing, for giving me the opportunity to be a part of the FRAME project, for collaborating with me on the John Gaylor project, and for all the helpful discussions that we had over the past two years from which I have learnt a lot – thank you, it's been great fun working with you!

Thanks also goes to Dr K. H. Aaron Lau whose expertise in bioinspired molecular interfaces was essential in the biofunctionalisation process of the hydrogel formulation. I truly appreciate his never-ending patience in explaining everything behind solid phase peptide synthesis, for allowing me to work in his lab, and for including me in his research group. Thanks also to Hamish Swanson, Dr Lau's PhD student, for his help in the lab and with NMR measurements.

I am also deeply grateful for the friends that I have made along the way, most especially, Perrine and Raquel – thank you for the wonderful memories, your friendship and support mean a lot to me!

Finally, to my family back home in Malta, especially my parents and my brother, for their continuous support and for being with me every step of the way – *'Grazzi!*'.

# List of publications and presentations

***Journal publications***

**Asciak, L.**, Domingo-Roca, R., Dow, J. R., Brodie, R., Paterson, N., Riches, P. E., Shu, W., & McCormick, C. (2024). Exploiting light-based 3D-printing for the fabrication of mechanically enhanced, patient-specific aortic grafts. Journal of the Mechanical Behavior of Biomedical Materials, 106531. https://doi.org/10.1016/j.jmbbm.2024.106531

**Asciak L**, Gilmour L, Williams J. A., Foster E., Díaz-García L., McCormick C., Windmill J. F. C., Mulvana H. E., Jackson-Camargo J. C., and Domingo-Roca R. 2023. Investigating multi-material hydrogel three-dimensional printing for in vitro representation of the neo-vasculature of solid tumours: a comprehensive mechanical analysis and assessment of nitric oxide release from human umbilical vein endothelial cells*. R. Soc. open sci*.10230929230929

**Asciak, L**., Dow, J.R., Brodie, R., Maclean, C., Shu, W. and McCormick, C., 2020. P3 Towards advanced manufacturing for personalised vascular grafts. *Heart*, *106* (Suppl 1), p.A6. (Abstract-reviewed)

***Poster presentations***

**Asciak, L**., Domingo-Roca, R., Brodie, R., Paterson, N., Shu, W., McCormick, C., (2022). Advanced Manufacturing for personalised vascular grafts. In: Scottish Research Partnership in Engineering (SRPe) Annual Conference, John McIntyre Conference Centre, Edinburgh, 21st November 2022.

**Asciak, L**., Brodie, R., Paterson, N., Shu, W., McCormick, C., (2022). Enhancing the mechanical properties of alginate hydrogels: towards the development of personalised and more compliant aortic grafts. In: 44th Annual International Conference of the IEEE Engineering in Medicine and Biology Society, Scottish Event Campus, Glasgow, 11-15th July 2022.

**Asciak, L**., Brodie, R., Paterson, N., Shu, W., McCormick, C., (2020). Investigating the mechanical properties of alginate-based hydrogels: towards advanced manufacturing for personalised vascular grafts. In: World Biomaterials Congress 2020 [online] 11-15th December 2020.

**Asciak, L**., Brodie, R., Maclean, C., Shu, W., McCormick, C., (2019). Advanced Manufacturing for personalised vascular grafts. In: Scottish Research Partnership in Engineering (SRPe) Annual Conference, Technology and Innovation Centre, University of Strathclyde, Glasgow, 13th November 2019.

***Oral presentations***

**Asciak, L**. (2023). Materials optimisation for advanced manufacturing of vascular grafts for improved biomechanics and biointegration. In: Terumo Aortic Academic Collaborations Conference, Technology and Innovation Centre, University of Strathclyde, Glasgow 6th June 2023.

**Asciak, L**. (2021). Investigating the mechanical properties of alginate-based hydrogels for vascular graft applications. In: BioMedEng21, The University of Sheffield 6-7th September 2021.

# Table of Contents

# List of Figures

# List of Tables

# List of Abbreviations

| | |
|---|---|
| $^{1}$H NMR | Proton nuclear magnetic resonance |
| 3DP | 3D-printing |
| AAA | Abdominal aortic aneurysms |
| $BaCl_2$ | Barium chloride |
| $CaCl_2$ | Calcium chloride |
| $CaCO_3$ | Calcium carbonate |
| CAD | Computer-aided design |
| Circ | Circumferential direction |
| CVD | Cardiovascular Disease |
| DI water | Deionised water |
| DPBS | Dulbecco's Phosphate Buffered Saline |
| ECM | Extracellular matrix |
| ECs | Endothelial Cells |
| ePTFE | expanded polytetrafluoroethylene |
| ET | Exposure time |
| FEP | fluoroethylene propylene |
| FLET | First layer exposure time |
| Fmoc | fluorenyl methoxycarbonyl |
| GDL | Glucono delta-lactone |
| HPLC | High performance liquid chromatography |
| HUVECs | Human Umbilical Vein Endothelial Cells |
| I2959 | Irgacure 2959 (2-Hydroxy-4′-(2-hydroxyethoxy)-2 methylpropiophenone) |
| IPN | Interpenetrating polymer network |
| LAP | Lithium phenyl-2,4,6-trimethylbenzoylphosphinate |
| LCMS | Liquid chromatography – mass spectrometry |
| Long | Longitudinal direction |
| LVER | Linear viscoelastic region |
| MEM | Maximum elastic modulus |
| MW or Mn | Molecular weight |
| PB | photoblocker |
| PBS | Phosphate buffered saline |
| PEGDA | Polyethylene glycol diacrylate |
| PET | Polyethylene terephthalate |
| PM | Physiological elastic modulus |
| RGD | Arginine-glycine-aspartic acid |
| SEM | Scanning electron microscope |
| SLA | stereolithography |
| SMCs | Smooth Muscle Cells |
| SPPS | Solid phase peptide synthesis |
| TAA | Thoracic abdominal aneurysms |
| TCP | Tissue Culture Plastic |
| TEVGs | Tissue engineering vascular grafts |
| UTS | Ultimate tensile strength |
| UV | Ultraviolet |

# Chapter 1 Introduction and Thesis Outline

Cardiovascular disease (CVD), an umbrella term that covers a wide range of conditions affecting the heart and the vasculature, remains the leading cause of mortality and morbidity worldwide (Townsend *et al.*, 2022). A major contributor to CVD deaths includes aortic pathologies, primarily aneurysm formation, where the greatest artery in the human body exhibits significant bulging, which if left untreated could result in rupture causing fatal blood loss (Bossone and Eagle, 2021; Hynes, Acharya and Sultan, 2022).

Typically, such conditions, require surgical interventions involving a synthetic tubular graft or a stent-graft made of standard polymeric materials, either polyester (polyethylene terephthalate; PET or Dacron®) or expanded polytetrafluoroethylene (ePTFE or GORE-TEX®) in fabric form. These grafts have been widely implemented in vascular surgery for over 50 years, and research has shown that they perform better in the long-term in larger vessels (>8 mm), such as the aorta or iliac arteries, rather than in smaller vessels (<6 mm), such as the coronary artery (Pashneh-Tala, Macneil and Claeyssens, 2016; Spadaccio *et al.*, 2016). For the latter, surgeons prefer the use of autologous grafts (i.e., arteries or veins from the patient's own body, such as the saphenous vein or radial artery), however their limited availability and high-risk associated with extraction, often requires the use of synthetic grafts. In small-diameter blood vessels, synthetic grafts have been associated with several post-operative complications, namely thrombus formation, intimal hyperplasia, and occlusion, owing to their poor patency and lack of endothelial cell lining along the graft lumen (Pashneh-Tala, Macneil and Claeyssens, 2016). Consequently, over the years, it has been the primary purpose of researchers in the field of vascular engineering to develop improved biomaterials for the fabrication of vascular tissue-mimicking small-diameter grafts that would ensure optimal *in vivo* behaviour. Numerous attempts have been reported, with special attention given to

tissue-engineered vascular grafts composed of biological materials, yet to date successful clinical translation remains to be achieved.

Additionally, despite synthetic vascular conduits being the gold standard in the surgical repair of large-diameter vessels such as the aorta, these grafts still present significant limitations that have been predominantly overlooked. A major limitation is the inability to mimic the biomechanical behaviour of the human aorta, owing to both Dacron® and ePTFE being highly rigid materials in comparison with native aortic tissue (Tremblay *et al.*, 2009; Bustos, García-Herrera and Celentano, 2016). Annually, the human aorta undergoes approximately 35 million cardiac cycles (Lejay *et al.*, 2018). To accommodate this pulsatile flow, durability and flexibility of graft materials is key (Vahabli *et al.*, 2022). Rigid implants that are unable to distend in a similar manner to the host tissue contribute to compliance mismatch leading to haemodynamic disruptions, culminating in cardiovascular complications such as high blood pressure and heart strain (Obrien, Morris and McGloughlin, 2008; Vardoulis *et al.*, 2011; Spadaccio *et al.*, 2016; Lejay *et al.*, 2019; Hynes, Acharya and Sultan, 2022).

Since the advent of synthetic aortic grafts, several attempts have been made to improve their functionality, but these have mostly focussed on alterations to graft design such as axial crimping, branching, and fenestrations to enhance surgical procedures and to slightly mimic aortic geometry (Vahabli *et al.*, 2022). Nevertheless, graft failures still occur, and there remains a paucity of investigations aimed at addressing the discrepancies in mechanical behaviour between synthetic grafts and the aorta and how this could be exploited to develop more compliant implants (Lejay *et al.*, 2018). Moreover, despite the vast catalogue of commercially-available aortic grafts, the fabrication method lacks patient-specificity. Given that pathological conditions, such as the way an aneurysm develops and how vascular anatomy varies from one patient to another, a personalised fabrication method that takes into account the patient's own anatomical

geometry would potentially minimise events associated with poor implant fit. Overall, considering that most vascular tissue engineering research has been predominantly focussed on the development of small-diameter vascular grafts, this thesis attempts to address the issues concerning large-diameter synthetic vascular conduits used in aortic surgical repair.

Aortic graft limitations have also sparked industrial interest. Thus, this project was developed in collaboration with one of the leading global vascular graft manufacturers, Terumo Aortic. Through in-depth discussions with the company, it was emphasised how they aspire to develop alternative vascular grafts with improved biomechanical and biological performance, whilst also expressing their interest in moving towards a more personalised and advanced manufacturing approach. By partnering with Terumo Aortic, this project benefitted both from a financial aspect but also from a technical perspective, with input provided from the Research and Development department in the form of quarterly meetings. This helped identify the project's aims and objectives, formulate experimental plans, and the overall trajectory of the project.

Thus, the aim of this research was to investigate alternative biomaterials and manufacturing methods to the existing aortic graft technologies to potentially minimise mechanical and geometrical mismatches between the graft and host tissue whilst also providing a degree of bioactivity to promote endothelialisation. To achieve this, inspiration from techniques that have already been explored in the production of smaller vessels, primarily the use of hydrogels – a class of materials comprising a highly hydrated 3D-polymeric network – in combination with state-of-the-art 3D-printing technologies, were investigated to ultimately fabricate personalised and more compliant conduits. The results that have been generated in pursuit of the above aims contributes to new knowledge, both through the innovations in materials and methods developed and their exploitation for the first time to the development of new vascular grafts.

## 1.1. Thesis outline

The overall structure of this thesis takes the form of nine chapters. The following chapter is a review of the literature outlining the anatomy of the aorta, aneurysm formation and its surgical treatment, the existing vascular graft technologies used in aortic repair surgeries and how such grafts inadequately mimic the mechanical and geometrical behaviour of the host tissue, together with different strategies currently being investigated for the fabrication of tissue-engineered and synthetic vascular grafts, with special attention paid to hydrogels and 3D-printing.

Chapter 3 covers the material and methods generally used throughout the thesis. Any additional experimental methods information specific to a particular chapter is provided within that chapter.

Chapter 4 investigates the mechanical properties of state-of-the-art Dacron® graft material using a series of mechanical characterisation techniques, namely uniaxial tensile testing under static and dynamic conditions, to demonstrate the existing mismatch in mechanical properties between this material and human aortic tissue.

Chapter 5 introduces alginate hydrogels as an alternative to Dacron® graft materials, that are characterised mechanically via confined compression and uniaxial tensile tests to determine their mechanical properties in comparison with aortic tissue data reported in the literature.

Chapter 6 focuses on the optimisation of the mechanical properties of the alginate hydrogels to closely mimic the human aorta by incorporating a secondary monomer to the alginate matrix, creating an interpenetrating polymer network (IPN) hydrogel. Mechanical characterisation of different IPN hydrogel formulations through confined compression, tensile uniaxial stretch to failure tests, and rheological measurements helped identify a suitable hydrogel formulation that demonstrates similar mechanical

behaviour to aortic tissue data reported in the literature. Moreover, the alginate-based hydrogels were physically characterised (swelling, degradation, visualised via scanning electron microscopy) and the hydrogel formulation was used to fabricate tubular conduits via a moulding technique.

Chapter 7 explores the use of light-based 3D-printing as the manufacturing method for the production of aortic-like tubular vessels using the hydrogel formulation obtained in the previous chapters.

Chapter 8 investigates the possibility of biofunctionalising the hydrogel formulation via the incorporation of an arginine-glycine-aspartic acid (RGD)-based peptide to create cell binding sites and promote endothelialisation of the material.

Finally, Chapter 9 provides a summary of the whole thesis together with general study limitations and recommendations for future work. The key contributions to knowledge of this research are also discussed followed by a brief conclusions section.

# Chapter 2 Literature Review, Research Aims and Objectives

## 2.1. Introduction

The aorta is the major artery in the human body from which the rest of the vasculature originates (Figure 2.1(A)) therefore, any type of aortic disease or trauma is life-threatening. Aortic disease may manifest itself in several forms, primarily as: (1) aneurysms, which involve local dilations of the aorta (Figure 2.1(B)), (2) dissections, which involve tears in the layers that make up the aortic wall often leading to aneurysm formation and even rupture (Figure 2.1(C)), (3) stiffening of the aortic wall due to age, and (4) inflammatory conditions, such as aortitis and atherosclerosis (Figure 2.1(D)) (Tsamis, Krawiec and Vorp, 2013; Ladich *et al.*, 2016; Sherifova and Holzapfel, 2019).

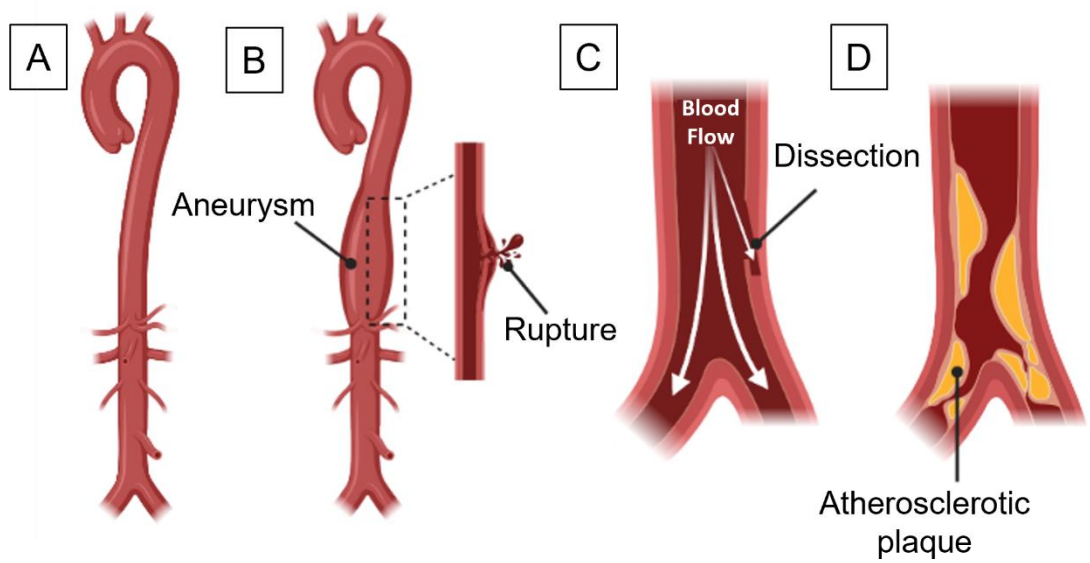


*Figure 2.1: Schematic illustration of (A) the healthy aorta in comparison with aortic diseases, including (B) aneurysm formation represented as a bulge which may rupture if left untreated, (C) dissection where blood flows through the tear in the aortic wall, and (D) atherosclerosis which involves the build-up of plaque that might lead to vessel occlusion (Created in Biorender.com).*

Of these conditions, aortic aneurysm formation is a very common event accompanied with high mortality risk. According to the Global Burden Disease report in 2019, 172,000 deaths were recorded globally in relation to aortic aneurysms (Virani *et al.*, 2020). This

may be attributed its asymptomatic nature rendering it difficult to detect at early stages. Hence, when left untreated, the aneurysm undergoes further expansion until it ruptures causing fatal bleeding. Surgical interventions are often required to replace the diseased section with a synthetic graft or stent. However, current grafts are associated with several limitations, and thus the need for alternative aortic graft technologies persists.

Therefore, this literature review provides an overview of: (1) the structure and mechanical behaviour of the healthy aorta, (2) aneurysm formation at the abdominal region, (3) current aortic graft technologies and associated limitations, (4) the mechanical properties and characterisation methods of healthy aortic tissue to be used as target properties for the development of novel aortic grafts, (5) current alternative technologies used in vascular tissue engineering, and (6) the emergence of 3D-printed vascular grafts as a promising approach.

## 2.2. The healthy aorta

### 2.2.1. Structure and physiology

Originating from the heart's left ventricle, the aorta ascends into an arch, then descends into the thorax and abdomen, where it bifurcates into the common iliac arteries (Figure 2.2(A)). Generally, the aorta is sectioned into major segments: the ascending, the aortic arch, the descending thoracic, and the abdominal aorta (Figure 2.2(B)). Physiologically, the aorta has two primary functions: (1) that of a conduit where it distributes oxygenated blood throughout the body, and (2) that of a buffer where it converts the pulsatile flow originating from the heart to an almost steady distal flow. The latter is known as the Windkessel effect whereby during systole the aorta distends to accommodate the high pulsatile pressure, as a consequence of blood being ejected from the left ventricle, and returns to its original configuration without permanent damage during diastole (Kassab, 2006).

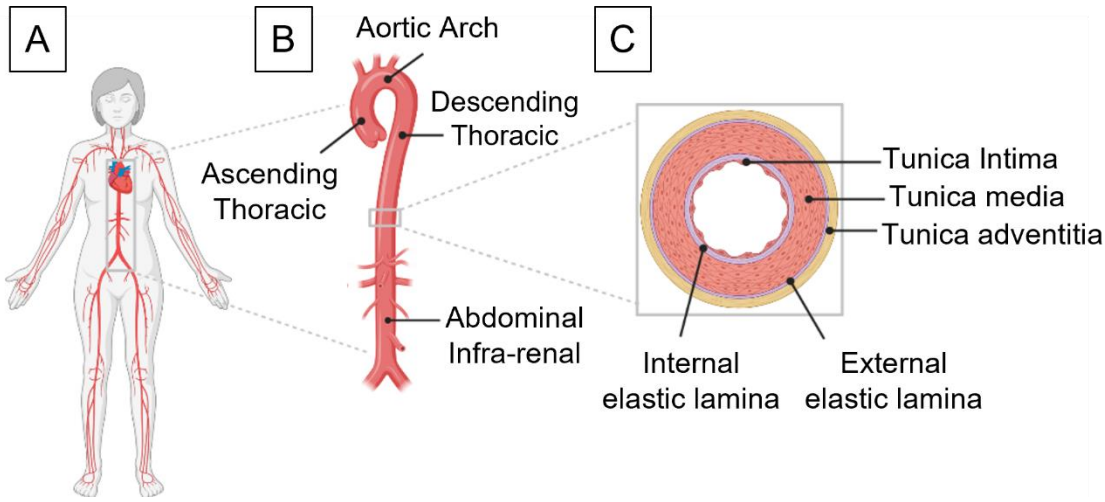


*Figure 2.2: Schematic illustration showing (A) location and (B) anatomy of the aorta in the human body, and (C) the structure of the aortic wall. (Created in Biorender.com).*

Microstructurally, similar to the other arteries in the human body, the aortic wall comprises three layers: the *tunica adventitia*, *tunica media*, and *tunica intima* (Figure 2.2 (C)). The *intima* is the inner layer and consists of a single layer of endothelial cells (ECs), also known as the endothelium. The *media*, or middle layer, consists of circumferentially arranged lamellar units filled with smooth muscle cells (SMCs), which are grouped together by elastin and collagen fibres (Sherifova and Holzapfel, 2019). Both elastin and collagen contribute to the elasticity and strength required for the aorta to withstand pulsatile flow from the heart (Tsamis, Krawiec and Vorp, 2013). The *adventitia* is the outermost layer constituting primarily of fibroblasts, vasa vasorum, collagen fibres, and connective tissue that aid in anchoring the aorta to surrounding tissue (Gasser, 2017). Layers of elastic lamina separate the intima and media (internal elastic lamina), and media and adventitia (external elastic lamina) (Kassab, 2006).

### 2.2.2. Mechanical Behaviour

Arterial tissue mechanics is primarily dominated by compliance, non-linear stress-strain behaviour, anisotropy, and viscoelastic characteristics (Camasão and Mantovani, 2021), originating from the heterogeneous structure of the arterial wall, where elastin, collagen and SMCs play a significant role (Singh, Wong and Wang, 2015; Pena *et al.*, 2018).

Elastin is a fibrous protein, that is responsible for aortic wall elasticity which is essential for the Windkessel effect to function properly (Cocciolone *et al.*, 2018). Moreover, in order to accommodate the variations in pressure along the aortic tree, the elastin content decreases with distance away from the heart (Dobrin, 1978). Collagen, also a fibrous protein, is present all over the human body in up to 29 different types, with the aortic wall being predominantly (more than 80%) composed of Type I and Type III (Emmott *et al.*, 2016). Conversely to elastin, collagen concentration increases with distance away from the heart. In fact, canine studies have shown that segments of the aorta proximal to the heart, such as the thoracic, comprise 60% elastin and 40% collagen, whereas segments distal to the heart, such as the abdominal, comprise 30% elastin and 70% collagen (Harkness *et al.*, 1957). Moreover, collagen has a higher elastic modulus (approximately a thousand times greater) than elastin, thereby contributing to the increase in stiffness as the distance away from the heart increases (Sokolis, 2007; Emmott *et al.*, 2016; Pena *et al.*, 2018).

The arterial compliance is defined as the absolute change in volume ($\Delta$V, or strain) with pressure variations ($\Delta$P, or stress): $C = \Delta V/\Delta P$ (London and Pannier, 2010). Consistent with the Windkessel effect, compliance indicates the artery's ability to withstand blood pressure, therefore a high compliance is required for the aorta to maintain pulsatile pressure. In fact, aortic compliance was found to decrease with distance away from the heart (Kassab, 2006). The reciprocal of compliance is elastance: $E = \Delta P/\Delta V$, which describes the stiffness of the aorta as a conduit (London and Pannier, 2010). The pressure-volume or stress-strain relationship of arterial tissue is non-linear with a characteristic "J-shape" curve, as illustrated in Figure 2.3. This may be sectioned into three distinct regions: (1) the initial slope, indicates a low stress response at low levels of pressure and is dominated by the stretching of elastin fibres, (2) the upturning region, corresponds to physiological pressures (80 - 120 mm Hg) and indicates a shift in fibre

recruitment from elastin to collagen, hence the onset of tissue stiffening, and (3) the final steep slope, indicates a sudden increase in stiffness dominated primarily by the stretching of collagen fibres (Roach and Burton, 1957; Singh, Wong and Wang, 2015).

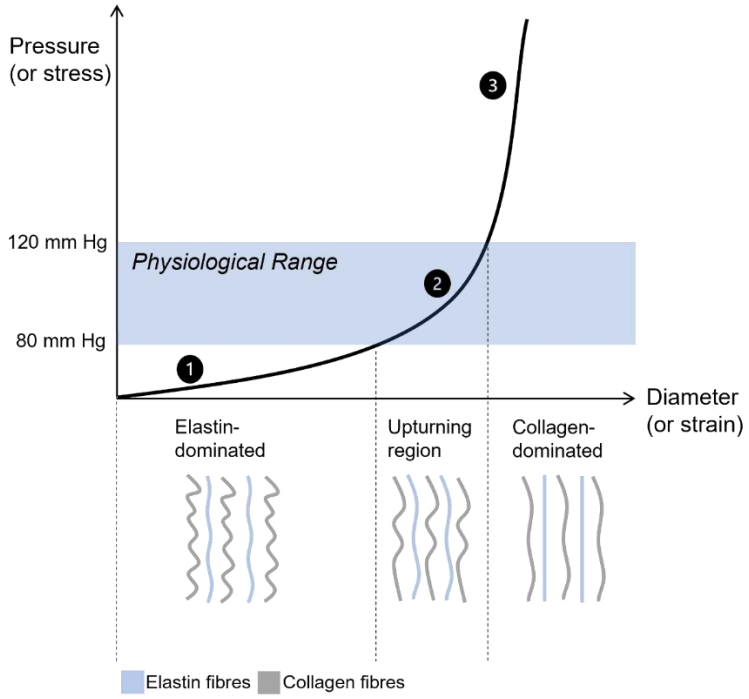


*Figure 2.3: Pressure-diameter (or stress-strain) 'J-shape' curve of arterial tissue and the role of elastin and collagen fibres; (1) indicates the initial slope dominated by the stretching of elastin fibres, (2) the upturning region at physiological pressure where elastin fibres exhibit further straightening and collagen fibres start to stretch, and (3) the final slope dominated by the straightening of collagen fibres.*

Arterial tissue is also known for its anisotropy, where the mechanical properties are dependent on the loading and/or deformation direction; therefore, properties vary in the longitudinal, circumferential, and radial directions. This arises from the distribution of collagen fibres, which are mostly abundant in the circumferential direction, hence the stiffness in the circumferential direction is higher than the longitudinal (Emmott *et al.*, 2016; Gasser, 2017; Pena *et al.*, 2018). Similarly, to stiffness and compliance, Peña *et al.,* (2018), demonstrated that anisotropy also increases with distance away from the heart.

Under physiological conditions, arteries are subjected to continuous cycles of deformation consistent with the systolic and diastolic phases of the cardiac cycle. After each deformation cycle, arterial tissue dissipates energy, characteristic of its viscous nature. This energy dissipation is evident in pressure-diameter or stress-strain curves as hysteresis, the area between the loading and unloading curves, and accounts to a small percentage (15-20%) of the strain energy (Dobrin, 1978; Cocciolone *et al.*, 2018) suggesting that the majority of strain energy is elastically recovered (Shadwick, 1998). This small energy loss results from the continuous loading-unloading cycles which limit the arterial tissue from exhibiting long stress relaxation times (Dobrin, 1978). In terms of the Windkessel effect, this energy dissipation is essential as it helps dampen the pulsatile pressure in the arterial system (Shadwick, 1998). While it is clearly understood that elastin and collagen promote non-linearity, compliance, and anisotropy, the determinant of viscoelasticity is still a subject of investigation. Most studies suggest that the viscous nature of arterial tissue is dependent on the dissipative mechanism of SMCs (Cocciolone *et al.*, 2018). This is consistent with the pronounced viscoelasticity in small-diameter (muscular) arteries where SMCs are most abundant (Gasser, Ogden and Holzapfel, 2006; Faturechi *et al.*, 2019).

## 2.3. Abdominal Aortic Aneurysms (AAA)

Aortic aneurysms may occur at any region along the aortic tree, with the abdominal or infrarenal area being the most susceptible to aneurysm formation. In fact, it is estimated that approximately 80% of aortic aneurysm cases occur at the abdominal region (Ladich *et al.*, 2016). There are several factors that contribute to this occurrence, all related to the heterogeneity of the aortic tree, including: (1) the variation in elastin content – the abdominal region comprises fewer elastin lamellar units than the thoracic region rendering the abdominal aorta more susceptible to elastin degeneration, (2) the variation in vasa-vasorum concentration – the abdominal aorta has lower vasa vasorum

concentration, therefore it is more susceptible to stiffening, and (3) the variation in blood flow patterns – the abdominal region experiences higher levels of oscillating flow and reflected pressure waves thereby increasing aortic wall tension (Humphrey and Holzapfel, 2012; Pande and Beckman, 2013).

The lack of symptoms together with the increase in incidence of AAA has given rise to population screening programmes in order to detect aneurysms at an early stage. Aneurysm rupture is said to occur when the intramural mechanical stress exceeds strength, however rupture prediction is still based on the aneurysm's geometrical variations (Humphrey and Holzapfel, 2012). In fact, screening via ultrasonography is used to detect whether the abdominal aortic diameter exceeds 30 mm in order for the bulge to be considered as an aneurysm. These programmes particularly target males over the age of 50 who are considered as high risk, since AAA manifestations are more common in males than females for this age group (Golledge, 2019). The latter is mostly the result of age-induced vasculature remodelling being less pronounced in women than men, potentially due to protective sex hormones (the following review articles provide a more detailed understanding of sex differences on aortic aneurysm formation (Norman and Powell, 2007; Villard and Hultgren, 2018).

Current treatment strategies involve diameter monitoring for aneurysms that are considered small (30 to 55 mm) and elective surgical intervention when the diameter exceeds 55 mm since the risk of rupture is high (1% to 6% in patients per year) (Farotto *et al.*, 2018; Golledge, 2019). The latter may involve either an open or a minimally invasive surgery as shown in Figure 2.4. In open surgery, the diseased aortic section is completely excised and replaced with a synthetic tubular graft. In a minimally invasive intervention (also known as an endovascular aneurysm repair, EVAR), typically used in the events of AAA, a stented graft is inserted percutaneously through the arteries present in the groin area with the use of a catheter. Being less invasive, this procedure eliminates

the risks associated with open heart surgery; however, it also has its complications such as endoleaks and stent-graft migration, thereby requiring continuous monitoring (Farotto *et al.*, 2018).

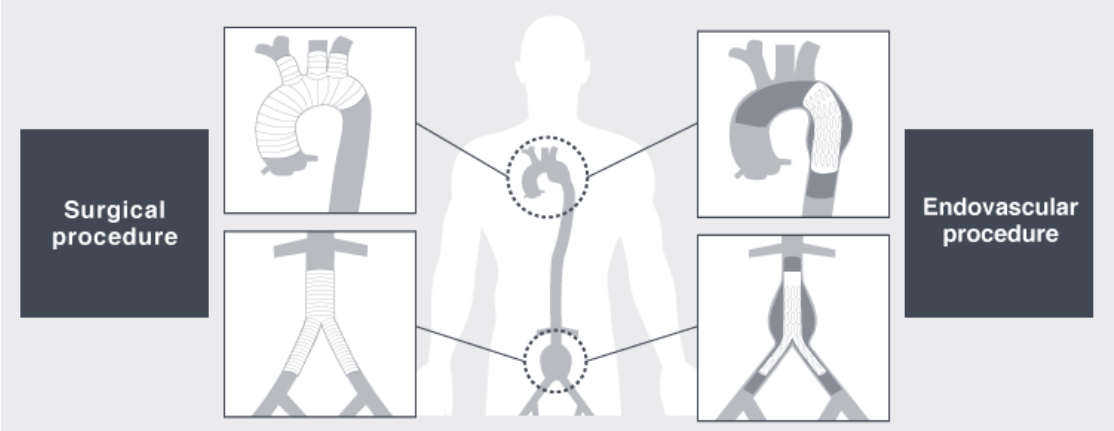


*Figure 2.4: Aortic grafts used in open surgical repair (left) versus minimally invasive surgery or endovascular procedure (right). Figure obtained from Terumo Aortic (2023).*

According to the UK's National Vascular Registry (NVR) (Birmpili *et al*., 2022), from 2020 to 2022, for the abdominal aorta alone, 10,678 AAA repair procedures were performed using either an implantable graft or stent-graft. Considering the overall population of the UK, this might be interpreted as a small percentage of aortic surgeries, and therefore limited use of aortic grafts per year. However, the problem with such major surgeries is the need for reinterventions. For the same 2020-2022 period, 373 interventions were registered as re-interventions for EVAR, and 40 revisions for open repair, with re-intervention causes including abdominal aortic sac expansion, graft migration, the onset of new arterial disease, pseudo-aneurysm, graft stenosis or occlusion, and infection. Revision rates for open repair and EVAR of abdominal aortic aneurysms for a longer period, between January 2014 and December 2020, revealed a total of 8,407 and 11,687 revisions for each surgical procedure respectively. Moreover, given that aneurysm formation may occur anywhere along the aortic tree, the surgical burden of such interventions together with the use of aortic grafts, is much greater. For instance, an

additional 800 thoracic endovascular aortic repair (TEVAR) surgeries were performed between 2020 and 2022, not considering open repair surgeries of the thoracic aorta (Waton *et al*., 2023), as well as other surgeries such as complex procedures involving aneurysms of the aorta close to the renal arteries, where typically a fenestrated EVAR is performed (1,056 reported between 2020 and 2022), and aneurysms close to the branched sections of the aorta, where a branched EVAR is performed (161 procedures between 2020 and 2022) (Waton *et al*., 2023).

### 2.4. Current synthetic aortic graft materials and associated limitations

The aforementioned surgical intervention methods utilise a synthetic vascular graft with the material being either of two standard polymers: polyethylene terephthalate (PET or polyester), commercially known as Dacron®, or expanded polytetrafluoroethylene (ePTFE). On a molecular scale, both polymers are highly crystalline and hydrophobic, and therefore less susceptible to *in vivo* degradation via hydrolysis (Xue and Greisler, 2003). These materials have been used for all types of arterial repair with the most success in large-diameter vessels such as the aorta, iliac and femoral arteries.

Dacron® as a vascular graft material was first introduced in the late 1950s and has dominated the field of large-diameter vascular grafts ever since. Figure 2.5 shows the different types of Dacron®-based vascular grafts used in open and endovascular aortic repair surgeries. Manufacturing techniques of Dacron® vascular grafts involve typical textile fabrication methods: weaving or knitting, which impact greatly the physical and mechanical behaviour of the graft. In fact, woven grafts, fabricated by interlacing two sets of Dacron® fibres in an over-and-under pattern, result in a tight weave structure with limited porosity, whereas knitted vascular grafts, fabricated by looping Dacron® fibres in an interlocking chain, result in a soft, stretchable graft with improved compliance and higher porosity than woven grafts (Xue and Greisler, 2003; Singh, Wong and Wang, 2015). Another advantage over woven Dacron® grafts is that knitted grafts exhibit a

degree of anisotropy with longitudinal elasticity exceeding the circumferential (Singh, Wong and Wang, 2015). The highly porous structure of knitted vascular grafts necessitates preclotting with the patient's blood prior to implantation, however this step has since been eliminated with the introduction of gel impregnated grafts using collagen, gelatine, or albumin (Chlupác, Filová and Bacáková, 2009; Takami *et al.*, 2012). Another improvement implemented to both types of Dacron® grafts was the introduction of longitudinal crimping (as shown in Figure 2.5 top row) to address issues of kink resistance, compliance, and flexibility (Xue and Greisler, 2003).

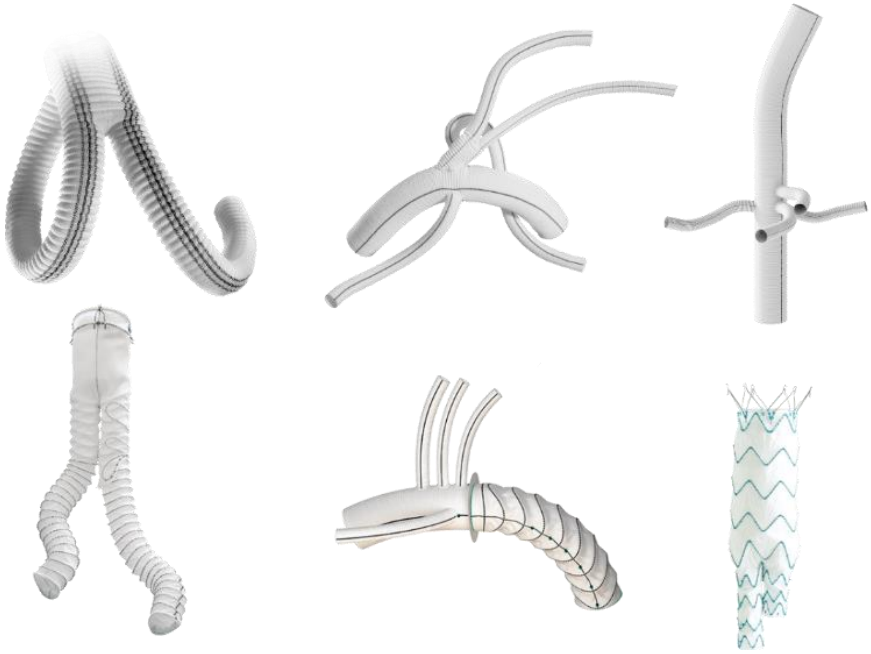

*Figure 2.5: Different types of Dacron®-based aortic grafts used in open surgery repair (top row) and stent-grafts for endovascular repair (bottom row). Images obtained from Terumo Aortic (2023).*

ePTFE as a non-textile alternative to Dacron® was introduced a few years later. It is an expanded version of PTFE, an inert fluorocarbon polymer, manufactured by a process of heating, stretching and extrusion, ultimately resulting in a microporous polymer characterised by a node-fibril structure. Thus, the porosity of ePTFE may be described

by the distance between nodes, otherwise known as the inter-nodal distance, which typically is in the range between 30 and 90 μm (Chlupác, Filová and Bacáková, 2009).

The implementation of either Dacron® or ePTFE as aortic substitutes is primarily attributed to their large availability, ease of use, and high long-term patency rates ranging from 91% to 95% after 5 years of implantation (Prager *et al.*, 2001). Despite the widespread use of such grafts and their generally good performance, limitations associated with the graft material remain a major concern (Spadaccio *et al.*, 2016; Lejay *et al.*, 2019). Both types of synthetic grafts have a propensity to dilate *in vivo*. Investigations suggest that this is more pronounced in knitted Dacron® grafts (Nunn *et al.*, 1990; Berman *et al.*, 1995; Schroeder *et al.*, 2009). The impact of dilation on the onset of other complications, such as aneurysm formation, is still unclear, however it is hypothesised that dilation decreases the graft's burst strength and could potentially result in graft weakening (e.g., holes and tears) and consequent rupture (Nunn *et al.*, 1990; Schroeder *et al.*, 2009).

Other major long-term complications are attributed to the graft's inability to mimic the biomechanical behaviour of arterial tissue. This is primarily evident when comparing the stress-strain (or pressure-diameter) relationship of synthetic grafts and arterial tissue, as shown in Figure 2.6. Synthetic grafts, characterised by a homogenous wall structure, exhibit a relatively linear stress-strain response with high stresses at low strains indicating limited elasticity (or high stiffness), whereas the heterogeneous structure of arterial tissue (as discussed in Section 2.2.1) contributes to a non-linear, elastic response (Singh, Wong and Wang, 2015; Faturechi *et al.*, 2019). This difference in stress-strain response is evident in the study by Faturechi *et al.*, (2019) where commercial synthetic grafts and different healthy human arteries, including the abdominal aorta, were stretched until failure, revealing steep slopes for ePTFE and Dacron® grafts, and 'J-shaped' curves for natural arteries, indicating elasticity. Additionally, the investigation by

Tremblay *et al.,* (2009) showed that at physiological strains the stiffness of Dacron® grafts is approximately 25 times and 18 times greater than the healthy and dilated ascending aorta, respectively.

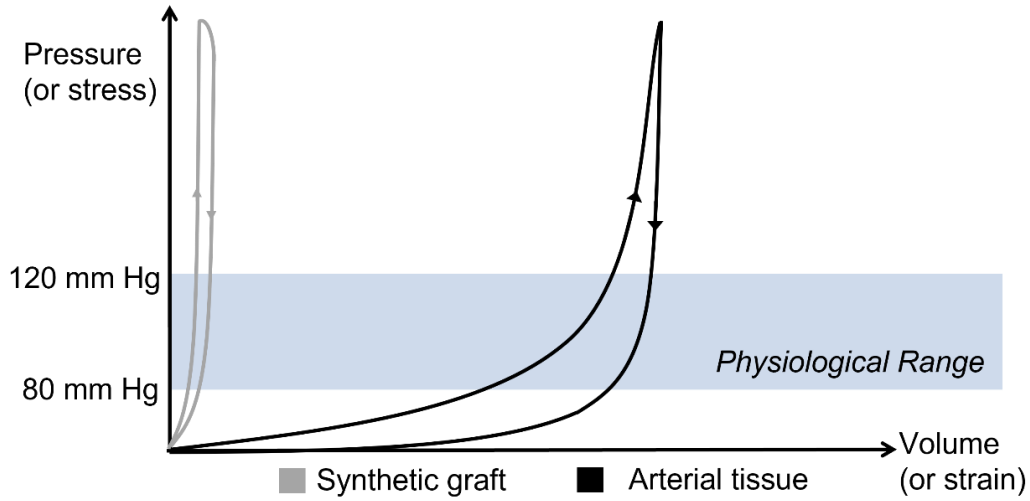


*Figure 2.6: Pressure-diameter (or stress-strain) response comparison between arterial tissue and synthetic grafts. The area between the loading and unloading curves indicates hysteresis which is more pronounced in arterial tissue. (Adapted from (Singh, Wong and Wang, 2015)).*

The lack of elasticity is associated with inadequate compliance, in fact, studies on external iliac arteries have shown that synthetic grafts (Dacron® and ePTFE) are four times less compliant than native arteries (Tai *et al.*, 2000). Therefore, the introduction of a stiff, non-compliant aortic graft has been found to not only contribute to graft-related complications (e.g., dilation), but also to the disruption of cardiovascular homeostasis (Spadaccio *et al.*, 2016). The latter is triggered by the inability of the aorta to fulfil its buffering function (Windkessel effect), particularly if aortic repair is performed in the highly compliant regions proximal to the heart (ascending/aortic arch) (Vardoulis *et al.*, 2011) culminating in left ventricular overload and hypertrophy (Mitsui *et al.*, 1986; Ioannou *et al.*, 2009). A limited Windkessel function generates changes in pressure wave propagation, higher systolic blood pressure (Obrien, Morris and McGloughlin, 2008) and an overall increase in aortic stiffness, as demonstrated by Lantalme *et al.,* (2009) when

measuring the pulse wave velocity from the carotid to the femoral artery. In this investigation, both open and endovascular surgical procedures contributed to aortic stiffness, however stent-grafts exhibited higher wave reflections when compared to open surgery graft implants (Lantelme *et al.*, 2009). Moreover, the loss in the Windkessel function limits the transmission of oxygenated blood to distal areas in the body during diastole (Obrien, Morris and McGloughlin, 2008), thereby preventing appropriate organ perfusion which might lead to deleterious events such as myocardial ischaemia, if this disrupts coronary blood flow (Lejay *et al.*, 2019). Compliance mismatch also contributes to an increase in stress concentration at the graft-artery suture line (Ferrari *et al.*, 2019) resulting in aneurysm formation, otherwise known as a para-anastomotic aneurysm (Bianchi *et al.*, 2009). This is a major complication; owing to its asymptomatic nature and late development it could lead to life-threatening events (rupture), if left undiagnosed. In addition to this, synthetic grafts lack the ability of growth and remodelling, therefore when implanted in young subjects, for instance in patients with congenital defects, the need for revision surgeries in the long-term is inevitable. Also, aortic stiffness increases with age, therefore in young people the aorta is more compliant and the mismatch in mechanical behaviour is more pronounced (Amabili *et al.*, 2020).

The use of Dacron® or ePTFE synthetic grafts remains the primary option for aortic aneurysm repair, with the associated limitations and complications being constantly overlooked. Moreover, considering the issue of surgical reinterventions, and how this can be a burden on both the healthcare system and the patient themselves, the development of alternative vascular conduits that mimic the biomechanical behaviour and intricate geometries of native arterial tissue is highly desirable, since this could potentially extend the performance of such grafts *in vivo*, which could drastically reduce reintervention rates.

## 2.5. Design considerations for improved aortic grafts

### 2.5.1. Mechanical considerations

In the attempt to develop novel aortic grafts, where the mismatches and complications discussed in Section 2.4 are to be minimised, it is crucial to understand the mechanical behaviour of native aortic tissue (Section 2.2.2) and to have good knowledge on the engineering data and characterisation methods used to determine the mechanical properties of such vessels.

Identifying the mechanical properties of healthy and/or diseased aortic tissue has been the subject of investigation for many years, primarily since this data is helpful in predicting disease progression (Macrae, Miller and Doyle, 2016; Sherifova and Holzapfel, 2019) and the effect of aging (Vande Geest, Sacks and Vorp, 2004; Haskett *et al.*, 2010). Mechanical characterisation of aortic tissue may be achieved either through *in vivo* or *ex vivo* methods. The former is non-invasive and comprises a series of clinical imaging technologies, such as echocardiography, ultrasonography, computer tomographic (CT) and magnetic resonance (MR) angiography. These techniques provide an insight on aortic stiffness, some through pulse wave velocity measurements and others through strain imaging (Lantelme *et al.*, 2009; Emmott *et al.*, 2016; Khan *et al.*, 2018).

Conversely, *ex vivo* methods are invasive whereby mechanical characterisation tests are performed on excised human donor or animal tissue. The latter typically involves porcine subjects due to anatomical similarities between pigs and humans, including similar structure, thickness, and composition, whilst also demonstrating good agreement in stiffness values (0.46 ±0.03 MPa porcine (4-10 months) versus 1.04 ±0.70 MPa human (<60 years) for the circumferential aorta (de Beaufort *et al.*, 2018)). *Ex-vivo* tests are considered as the “gold standard” for the measurement of elastic and/or viscoelastic properties of native aortic tissue (Emmott *et al.*, 2016). Therefore, this section presents an overview of the different *ex vivo* mechanical tests (illustrated in Figure 2.7) and the

associated mechanical properties, to be ultimately used as target properties when designing novel aortic grafts.

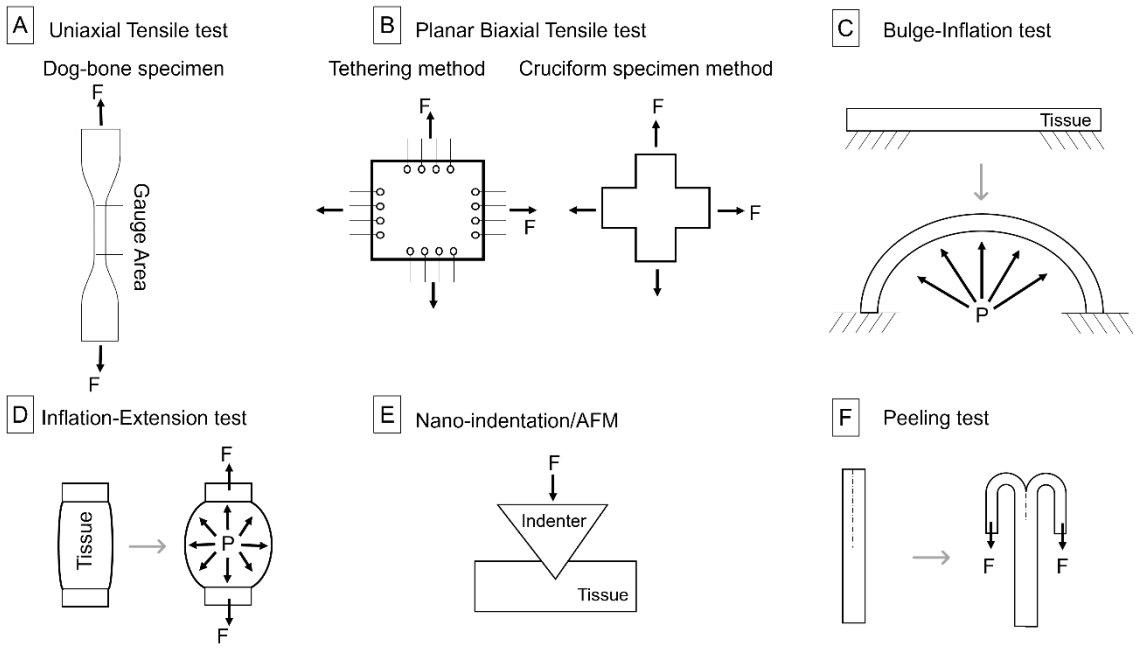


*Figure 2.7: Schematic representation of the different mechanical tests, including (A) uniaxial tensile tests, (B) planar biaxial tensile tests, (C) bulge-inflation tests, (D) inflation-extension tests, (E) nano-indentation or atomic force microscopy (AFM), and (F) peeling tests, used to obtain the mechanical properties of ex vivo aortic tissue specimens.*

The most common *ex vivo* mechanical characterisation method is the uniaxial tensile test**,** where the specimen, in this case aortic tissue, is cut into a rectangular or dog-bone shape and stretched to a specific strain or until specimen failure (Figure 2.7(A)). The dog-bone structure is suitable for gripping the specimen at the end-tabs and for rupture to take place at the narrow section (gauge area) rather than at the specimen-grip junction. Due to the anisotropic nature of arterial tissue, these tests are usually performed on specimens cut in the longitudinal and circumferential direction. The force required for stretching, and the extension exhibited by the specimen are recorded, and used to generate a stress-strain relationship.

Prior to uniaxial testing, tissue specimens are subjected to preconditioning, which typically involves a series of loading and unloading cycles. This is a crucial step when investigating the elastic response of soft biological tissue since the cyclic loading stabilises the tissue by minimising the viscoelastic (hysteresis) effect which in turn produces a stable and reliable stress-strain response (Sokolis, Boudoulas and Karayannacos, 2002; Miller *et al.*, 2012).

When stretched until failure, a stress-strain curve is obtained, with stress and strain at specimen failure corresponding to properties known as the ultimate tensile stress (UTS) and elongation at break ($\varepsilon_B$), both useful in indicating tissue strength. Additionally, since arterial tissue exhibits a non-linear stress-strain behaviour, tissue stiffness which typically corresponds to the slope of a linear stress-strain curve, is determined by considering different points along the curve, for example at maximum slope or at loads comparable to physiological stresses, yielding a tangential modulus. There exist many variants of stress and strain (e.g., engineering stress, engineering strain, true or Cauchy stress, first and second Piola Kirchhoff stress, and Green-Langrage strain) and their respective definitions depend on the properties considered during calculations from load-extension data (i.e., the sample thickness, gauge area, and range of strain considered). Currently, there is no clear consensus on which stress-strain definitions should be used when testing soft biological tissue, contributing to the difficulty in comparing measurements reported by various investigations (Khanafer, Schlicht and Berguer, 2013).

Table 2.1 shows uniaxial tensile tests performed on abdominal aortic specimens indicating ultimate tensile strength and strain, and elastic moduli where available. This table does not represent every uniaxial test performed in the literature, but it gives an overview of the variability in the data, even though the tests performed are similar.

*Table 2.1: Overview of uniaxial tensile tests performed on abdominal aortic tissue (Long: longitudinal, Circ: circumferential directions, UTS: ultimate tensile strength, NA: non-aneurysmatic).*

| Study | Specimen species, age | Healthy/ Diseased | Mechanical property | Direction | Engineering Data (MPa) | Additional comments |
|---|---|---|---|---|---|---|
| **(Vorp *et al.*, 1996)** | Human,<br>Diseased long 69±2 years,<br>Diseased circ 76±2 years,<br>NA: 47±4 years. | Both | Stiffness | <br>Long<br>Circ<br><br><br>Long | AAA:<br>3.51± 0.43<br>5.81± 0.93<br><br>NA:<br>5.69±1.38 | Stiffness is defined as the maximum slope of the stress-strain curve prior to failure. |
| **(Raghavan, Webster and Vorp, 1996)** | Human,<br>Diseased long 69±2 years,<br>Diseased circ 76±2 years,<br>NA: 47±4 years. | Both | UTS | <br>Long<br>Circ<br><br><br>Long | AAA:<br>0.86± 0.10<br>1.01± 0.16<br><br>NA:<br>2.01± 0.39 | Study shows a 50% reduction in tensile strength from non-aneurysmal to aneurysmal aorta. |
| **(Vorp *et al.*, 2001)** | Human,<br>73.4 ± 2.4 years | Diseased, aneurysm | UTS | Circ | Group I:<br>1.38 ± 0.19<br>Group II:<br>2.16 ±0.34 | Groups indicate the difference in intraluminal thrombus (ILT) thickness: ILT>4mm – Group I, ILT<4mm – Group II.<br>Study shows that thick ILT regions may lead to adjacent wall weakening. |
| **(Silver, Snowhill and Foran, 2003)** | Porcine,<br>juvenile | Healthy | Initial stress (or total stress) measured after a strain increment of 10%. | <br>Long<br>Circ<br><br>Long<br>Circ | At low strain:<br>0.491<br>0.0754<br><br>At high strain:<br>5 .22<br>3.59 | The abdominal aorta was compared to the carotid artery and vena cava. Low strain behaviour suggests that it was dominated by the elastic fibres whereas high strain behaviour was dominated by the collagen fibres and SMCs (as discussed in Section 2.2). |
| **(Vallabhaneni *et al.*, 2004)** | Human | Both | UTS<br><br><br><br><br><br><br>Stiffness | <br>Long<br><br><br><br>Circ<br><br>Long<br><br><br>Circ | AAA:<br>0.53±0.02<br>NA:<br>1.3±0.11<br>NA:<br>0.61±0.07<br>AAA:<br>1.8±0.10<br>NA:<br>1.38±0.12<br>NA:<br>1.82±0.10 | Stiffness was measured at loads comparable to physiological stresses.<br>Only longitudinal specimens were tested for aneurysmal tissue.<br>Tissue strength is greater in the longitudinal direction than in the circumferential, and vice versa for stiffness. |
| **(Walraevens *et al.*, 2008)** | Porcine,<br>6 to 8 months | Both | UTS<br><br><br>Strain at failure (no units) | Long | 1.34±0.18 (Calcified)<br>1.55±0.31 (Healthy)<br><br>~0.55 for both healthy and calcified specimens | This study compares healthy versus artificially calcified porcine aortic tissue.<br>For the ultimate tensile strain, no significant difference between the two was evident, but the strain of calcified specimens was slightly greater than the healthy specimens. |

From these investigations, it is evident that disease has a great impact on the mechanical properties of aortic tissue, with a reduction in tensile strength observed in most studies (Raghavan, Webster and Vorp, 1996; Vallabhaneni *et al.*, 2004; Walraevens *et al.*, 2008). Moreover, Silver, Snowhill and Foran (2003) demonstrated how the stress response of arterial tissue is strain dependent and is dominated by the elastin, collagen and SMCs present in the arterial wall (as discussed in Section 2.2.1). The anisotropic behaviour of aortic tissue is also prominent, with tensile strength and stiffness variations observed in the longitudinal and circumferential directions (Vallabhaneni *et al.*, 2004).

The uniaxial tensile experimental procedure may be modified to elicit viscoelastic behaviour responses through dynamic testing and stress relaxation (or creep) tests (Berglund, Nerem and Sambanis, 2005; Faturechi *et al.*, 2019). However, these tests have been seldomly applied on human aortas, and thus aortic viscoelastic data is limited. Recently, this gap in the literature has been noted by Amabili's group in the light of developing improved aortic grafts (Amabili *et al.*, 2019; Amabili, Balasubramanian and Breslavsky, 2019; Amabili *et al.*, 2020). The aortic region of interest in Amabili's work is mostly the descending thoracic aorta and the viscoelastic behaviour is assessed through dynamic tests. Typically, dynamic testing involves an initial stretch followed by sinusoidal strain oscillations, covering a range of frequencies (e.g., 1 Hz – 40 Hz (Amabili *et al.,* 2019)). Due to the specimen's viscoelastic nature, a phase lag (δ) develops between the strain input and the stress response as a function of time. The stress-strain ratio at each frequency yields the complex modulus which is derived from Euler's formula, and thus comprises both real and imaginary parts ($E(i\omega) = E' + iE''$). The real part is the in-phase modulus, otherwise known as the storage modulus (E′) which represents the elastic phase of the material. The imaginary part is the out-of-phase modulus, otherwise known as the loss modulus (E′′), which represents the viscous phase of the material. The storage to loss modulus ratio is equivalent to $tan\delta$, also known as the loss tangent (η),

which is a measure of the viscous nature of the material. In fact, for a purely elastic material $tan\delta = 0$, whereas for a viscoelastic material, $tan\delta$ exhibits an increase ($0 < \delta < \frac{\pi}{2}$) indicating that the stress is out of phase with strain. In a recent aortic wall layer-specific study, Amabili *et al.,* (2019) demonstrated that the intact aortic wall and the corresponding medial layer (*tunica media*) exhibit similar loss tangent values thereby suggesting that the media is mostly responsible to the viscoelasticity of the descending thoracic aorta. Moreover, Faturechi *et al.,*(2019) investigated the viscoelasticity of aortic tissue via stress relaxation tests. Typically, these tests include a ramp phase where the specimen is deformed to a specific strain followed by a hold phase where the specimen is held at that strain over time. During the hold phase, a viscoelastic material exhibits a decaying stress response (relaxation). Faturechi *et al.,* 2019 concluded that the abdominal aorta is less viscoelastic than the iliac arteries when comparing the stress relaxation level after 5 minutes, since the relaxation percentage of iliac arteries was twice that of the abdominal aorta. A complement to stress relaxation testing is creep testing, where stress (or load) is applied as the ramp-hold input, thereby yielding a decaying strain response over time.

Although uniaxial tensile testing is a common *ex vivo* characterisation test for both elastic and viscoelastic investigations, it also has its limitations. Tissue specimens are sometimes limited in size and therefore uniaxial testing can only be performed in one direction, as in the case of the aneurysmal specimens in Vallabhaneni *et al.*, (2004) (Table 2.1). Additionally, uniaxial testing does not accurately reflect the multiaxial loading conditions present *in vivo*. Therefore, another common *ex vivo* test is the planar biaxial test**,** where the specimen is stretched longitudinally and circumferentially at one at the same time. Another advantage over uniaxial tests, is that testing is performed on a single specimen rather than on two adjacent strips cut into both directions which might elicit different responses. In fact, a typical biaxial specimen is prepared by cutting a thin, flat

square of arterial tissue which is then mounted onto the biaxial instrument using a clamping or tethering method (Figure 2.7(B)). The former tends to create high stress concentrations at the clamp-specimen junction, and therefore the latter makes a much more suitable choice since its multiple thin threads (or surgical sutures) hooked along the edges allows the specimen to expand freely in the lateral direction (Sacks, 2000; Macrae, Miller and Doyle, 2016). However, in stretching until failure tests, the tethering method has been found to facilitate failure at the thread-sample junction, and therefore tissue strength investigations via planar biaxial tests are limited. To overcome this, the use of a cruciform shape specimen (Figure 2.7(B)) has been reported (Arroyave *et al.*, 2015). This way, the stress is concentrated at the centre of the specimen, therefore minimising failure at the gripping area (Macrae, Miller and Doyle, 2016), in a manner similar to the dog-bone specimens in uniaxial tensile tests.

Experimentally, strain (or stretch) is typically measured optically by tracking markers affixed on the central region of the sample surface, with Digital Image Correlation (DIC) being a common technique (Pena *et al.*, 2018). The engineering stress (or First Piola Kirchhoff stress) is typically calculated to represent the stresses in biaxial tensile tests, using the forces measured by the load cells in both direction and the initial specimen dimensions (undeformed) while assuming incompressibility and negligible shear. Some investigations, as in Arroyave *et al.*, (2015), the stress is expressed as the second Piola Kirchhoff with the difference being that this type of stress considers the deformed specimen dimensions. To identify the degree of anisotropy, Kamenskiy *et al.*, (2014) introduced the anisotropy index (A) by calculating the difference in longitudinal and circumferential strains divided by their average value (Kamenskiy *et al.*, 2014; Pena *et al.*, 2018). Table 2.2 summarises some of the investigations on biaxial testing of abdominal aortic tissue, with most of the engineering data being stretches in the longitudinal and circumferential direction at physiological stresses, and tangential

moduli. Additionally, since Arroyave *et al.*, (2015) uses a cruciform-shaped specimen, peak stresses and strains at rupture are also reported.

Even with the introduction of cruciform-shaped specimens, planar biaxial tensile testing is seldomly used in tissue strength quantification studies. Instead, a variant of biaxial testing known as **bulge-inflation,** has been reported in aortic tissue investigations (Mohan and Melvin, 1983; Marra *et al.*, 2006). This method requires a flat, rectangular specimen which is positioned onto the inflation device between two clamping plates and hermetically sealed (Figure 2.7(C)). This type of specimen fixation prevents the formation of excessive stress concentrations at the specimen-clamp regions, thereby overcoming the clamping limitation associated with biaxial tensile testing. Following fixation, pressurisation (loading) is applied from underneath the specimen via air or fluid flow, and the pressure can be increased until specimen failure. Similar to biaxial tensile testing, images captured via cameras are used to calculate strain and in this case the radius of curvature of the pressurised tissue. To the author's knowledge, bulge-inflation tests on abdominal aortic tissue are limited in the literature, with several work performed on other segments along the aortic tree, especially the thoracic region (Mohan and Melvin, 1983; Marra *et al.*, 2006).

*Table 2.2: Overview of the planar biaxial tensile, and inflation-extension tests (marked with an *) performed on abdominal aortic tissue (Long: longitudinal, Circ: circumferential directions, NA: non-aneurysmatic)*

| Study | Specimen species, age | Healthy/ Diseased | Mechanical property | Direction | Engineering Data | Additional comments |
|---|---|---|---|---|---|---|
| **(Vande Geest, Sacks and Vorp, 2006)** | Human, NA mean age: 70.6 ± 1.9, AAA mean age: 72.3 ± 1.8 | Both | Peak Strain (or Green's deformation) | Circ<br>Long | NA:<br>1.12 ±0.02<br>1.11±0.02 | The peak strain corresponds to an equibiaxial tension of 120 N/m, value for the abdominal aorta (20 mm diameter and 2 mm thickness) at physiological pressure of ~113 mmHg. |
| | | | | Circ<br>Long | AAA:<br>0.07 ±0.01<br>0.091±0.01 | The maximum tangential modulus is the maximum slope of the stress-strain curve in both directions. |
| | | | Maximum Tangential Modulus | Circ<br>Long | NA:<br>3.9 ±1.1 MPa<br>3.3 ±0.6 MPa | Aneurysmal tissue is stiffer and less extensible than non-aneurysmatic aortic tissue, especially in the circumferential direction. |
| | | | | Circ<br>Long | AAA:<br>11.7 ±1.9 MPa<br>8.3 ±01.2 MPa | |
| **(Haskett *et al.*, 2010)** | Human, 0-30 years (Group I), 31-60 years (Group II), 61+ years (Group III) | Healthy | Peak Strain | Circ<br>Long | ~ 0.10 for all ages<br>~0.10 (Group I),<br>~0.07(Group II),<br>~0.05(Group III) | Approximate engineering data values are given for this investigation since the results are presented graphically. |
| | | | Tangential Modulus | Circ | ~1.0 MPa (Group I),<br>~2.0 MPa (Group II),<br>~3.0 MPa (Group III) | The Tangential Modulus is calculated from the slope of the stress-strain curve at physiological stress (89.77 kPa) and the peak strain is the corresponding strain at the physiological stress. |
| | | | | Long | ~1.0 MPa (Group I),<br>~4.0 MPa (Group II),<br>~5.0MPa (Group III) | Group III exhibited the greatest stiffness and anisotropy followed by Group II and Group I which suggests that these properties increase with age. |
| **(Kamenskiy *et al.*, 2014)** | Human, 54 ±21 years | Both | In-plane stretches | Circ<br>Long | At diastole (80 mmHg):<br>1.17 ± 0.10<br>1.11 ±0.08 | The anisotropy index A was calculated for both diastole and systole. The difference between these pressures ($\Delta A$ = 0.007 ±0.003) indicates that anisotropy increases from diastole to systole in abdominal aortic tissue. |
| | | | | Circ<br>Long | At systole (120 mmHg):<br>1.19 ±0.13<br>1.13 ±0.11 | The average in-plane stretches include both healthy and diseased (atherosclerotic) aortic tissue. |

*Table 2.2: (continued).*

| Study | Specimen species, age | Healthy/ Diseased | Mechanical property | Direction | Engineering Data | Additional comments |
|---|---|---|---|---|---|---|
| **(Arroyave *et al.*, 2015)** | Porcine | Healthy | Peak Stress (or second Piola Kirchhoff stress) | Circ<br>Long | 0.387 ±0.14 MPa<br>0.644 ±0.25 MPa | Peak stress and strain correspond to the stress and strain at rupture in both directions. |
| | | | Peak Strain (or Green's deformation) | Circ<br>Long | 2.15 ±0.41<br>2.00 ±0.24 | The abdominal aorta was compared to the thoracic aorta and left subclavian artery. Results show higher tensile strength in the longitudinal direction for all three arteries. |
| **(Pena *et al.*, 2018)** | Porcine, 3.5 ± 0.6 months | Healthy | In-plane stretches | Circ<br>Long | At 30 kPa:<br>1.03 ±0.04<br>1.13 ±0.05 | This investigation compared abdominal aortic tissue with ascending thoracic and descending thoracic tissue. |
| | | | Anisotropic Index, A | | 0.10 ±0.04 | Abdominal tissues were found to be stiffer, highly anisotropic, and non-linear. |
| | | | | Circ<br>Long | At 60 kPa:<br>1.05 ±0.04<br>1.15 ±0.05 | An increase in the distance from the heart, resulted in less compliant and stiffer tissue. |
| | | | Anisotropic Index, A | | 0.11 ±0.04 | |
| ***(Labrosse *et al.*, 2013)** | Human,<br>Group I: Females 44 – 77 years<br>Group II: Males 38-66 years<br>Group III: Males 67-77 years | Healthy | Inflation-Extension<br><br>Longitudinal and circumferential stretch ratio at 13.3 kPa (100 mmHg). | Long<br><br><br>Circ | Group I: 1.11 ±0.03<br>Group II: 1.10±0.09<br>Group III: 1.05±0.04<br><br>Group I: 1.27 ±0.09<br>Group II: 1.35 ±0.16<br>Group III: 1.15±0.03 | This investigation compares the abdominal aorta with the ascending and thoracic aorta.<br>It demonstrates that the aorta becomes less distensible with age in all three segments.<br>Unpressurised aortic radii indicated a decrease with distance away from the heart. |

One limitation of the aforementioned methods is the need for planar specimens to be cut into specific shapes (e.g., dog-bone, square, or cruciform), which differs from *in vivo* conditions. Alternatively, inflation-extension tests (Kim and Baek, 2011; Labrosse *et al.*, 2013) have been introduced to investigate the mechanical behaviour of whole arteries, without the need for geometrical variations. Similar to biaxial tensile tests, the specimen is stretched axially (longitudinal load) while fluid is applied through the lumen, thereby pressurising the vessel transmurally (circumferential load) (Figure 2.7(D)). Both load types are measured via transducers while deformation is measured by tracking affixed markers on the outer diameter of the vessel using camera sensors, or by measuring optically the outer diameter before and after inflation, however the latter works only on the assumption that the vessel is a perfect cylinder (Macrae, Miller and Doyle, 2016). Apart from biaxial loading, inflation tests may also be modified either for uniaxial loading, by sealing one end of the vessel and allowing it to expand radially (Labrosse *et al.*, 2013) or for multiaxial loading, by allowing the vessel to twist thereby eliciting shear properties (Deng *et al.*, 1994; Blase *et al.*, 2012). Although inflation-extension tests yield a realistic *in vivo* stress measurement by closely mimicking the aortic wall behaviour during a typical cardiac cycle (Kim and Baek, 2011), it is not widely implemented for aortic characterisation, especially for tissue strength quantification (Marra *et al.*, 2006). This is potentially due to limited availability of large aortic sections, the complex boundary conditions, and the set-up required to pressurise and stretch a whole vessel (Mohan and Melvin, 1983).

Although tensile and inflation tests are both useful in identifying the mechanical properties of arterial tissue on the macroscale, there has been a growing interest on the micro/nano mechanical behaviour. Consequently, nanoindentation and Atomic Force Microscopy (AFM)-indentation have emerged as useful techniques for localised aortic tissue stiffness measurements on the micron/nano scale (Figure 2.7(E)). This opens up

the possibility of testing multiple sites on a single specimen, which in aortic tissue is valuable for analysing variations along the aortic wall and hence the microstructural contributions to the mechanical properties (Hemmasizadeh, Autieri and Darvish, 2012; Rezvani-Sharif, Tafazzoli-Shadpour and Avolio, 2019; Meekel *et al.*, 2019). While this proves advantageous over other characterization methods, a major limitation of indentation tests is the lack of realistic representation of physiological conditions since the sample tissue is tested in an unloaded state and the stiffness measurement is in compression rather than tension (Rezvani-Sharif, Tafazzoli-Shadpour and Avolio, 2019; Spronck and Humphrey, 2019). Therefore, the stiffness values obtained from these tests may differ from the elastic response of tensile and inflation tests. Both nanoindentation and AFM-indentation methods generate force-indentation curves which are typically analysed through constitutive models to yield specimen stiffness values.

A nanoindentation setup primarily consists of a loading unit where the load may be actuated piezoelectrically, magnetically, or electrostatically, and a detecting unit to monitor indentation depth through capacitive or inductive sensors. Experimentally, the nanoindentation test involves a load- or depth- controlled procedure where an indenter tip locally deforms the specimen surface, thus generating load-depth curves (Qian and Zhao, 2018). As for AFM-indentation, a typical setup constitutes of a force sensor in the form of a flexible cantilever with a probe at the tip to interact with the sample surface. For probe-sample contact, the cantilever is moved towards the sample via piezoelectric translators. The deformation of the cantilever during probe-sample contact is detected via an optical system. This involves a laser beam that is directed onto the cantilever which upon deflection is reflected and detected by a photodiode. Similarly, to nanoindentation, using the deflection and piezoelectric depth measurements, force-depth indentation curves are generated (Spronck and Humphrey, 2019).

Hemmasizadeh and co-workers have contributed greatly to the characterisation of aortic tissue via nanoindentation, with the region of interest in these investigations being the descending thoracic aorta (Hemmasizadeh, Autieri and Darvish, 2012; Hemmasizadeh *et al.*, 2015; Kermani *et al.*, 2017). To the author's knowledge limited nanoindentation (including AFM) investigations have been performed on abdominal aortic tissue and the few that have been published are layer-specific studies. For example, Meekel *et al.,*(2019) investigated both aneurysmal and non-aneurysmal abdominal aortic tissue by performing nanoindentation tests from the inner to outer layers, and vice versa. Aneurysmal tissue exhibited lower stiffness values than non-aneurysmal, with the reduction being more pronounced from the media to the intima. Additionally, Rezvani-Sharif, Tafazzoli-Shadpour and Avolio (2019) investigated the difference between atherosclerotic and non-atherosclerotic abdominal aortic tissue via AFM. Again, this is a layer-specific study with indentation measurements performed at the medial layer including the elastin and interlamellar zones, and the different regions within the atherosclerotic plaque. This study revealed that diseased aortic tissue exhibits a decrease in stiffness at the elastin lamellar zones and an increase at the interlamellar zones when compared to non-atherosclerotic tissue. Material properties and further details on these studies can be found in Table 2.3.

*Table 2.3: Overview of layer-specific mechanical characterization tests (nanoindentation (NI), atomic force microscopy (AFM), and peel tests) performed on abdominal aortic tissue (Long: longitudinal, Circ: circumferential directions, NA: non-aneurysmatic).*

| Study | Test | Specimen species/ age/layer | Healthy/ Diseased | Mechanical property | Direction/ Position | Engineering Data | Additional comments |
|---|---|---|---|---|---|---|---|
| **(Rezvani-Sharif, Tafazzoli-Shadpour and Avolio, 2019)** | AFM | Human,<br>medial layer | Both<br><br>Group A: healthy<br>Group B: mildly atherosclerotic<br>Group C: advanced atherosclerotic | Elastic Modulus, MPa<br><br>(conical indenter, Hertz Model) | Elastin lamellae<br><br>Interlamellar zones | Group A: 0.039±0.004<br>Group B: 0.036±0.004<br>Group C: 0.032±0.004<br><br>Group A: 0.011±0.003<br>Group B: 0.013±0.004<br>Group C: 0.015±0.004 | The stiffness of the elastin lamellae and interlamellar zones of diseased aortic wall was comparable to healthy aortic tissue. However, with atherosclerosis progression, elastin stiffness decreased whereas interlamellar stiffness increased. |
| **(Meekel *et al.*, 2019)** | NI | Human,<br>NA: 29 – 64 years<br>AAA: 69 – 76 years | Both | Elastic Modulus, MPa<br><br>(spherical indenter, Hertz Model) | Intact aortic wall | NA (median): 0.0024 [0.0002 – 0.156]<br>AAA (median): 0.0005 [0 – 0.014] | |
| **(Sommer *et al.*, 2008)** | Peel | Human,<br>36-75 years,<br>medial layer | Healthy | Force/width ratios (mN/mm)<br><br>Dissection energy/area ($mJ/cm^2$) | Circ<br>Long<br><br>Circ<br>Long | 22.9 ±2.9<br>34.8 ±15.5<br><br>5.1 ±0.6<br>7.6 ±2.7 | The higher force/width ratio in the longitudinal direction may be attributed to the anisotropic properties of aortic media. |
| **(Tong *et al.*, 2014)** | Peel | Human,<br>70 ±10 years,<br>intima-media | Diseased, Aneurysmal grouped according to thrombus age (Age I – Age IV). | Dissection energy/area ($mJ/cm^2$) | <br>Circ<br>Long<br><br>Circ<br>Long<br><br>Circ<br>Long | Age II<br>6.7 ±1.2<br>8.4 ±1.9<br>Age III<br>5.5±1.1<br>6.8±1.7<br>Age IV<br>4.2±1.1<br>5.1±1.4 | The dissection energy of the adventitia was also investigated, and it showed a higher mean force/width in both directions than the intima-media region.<br><br>For the intima-media region, thrombus progression resulted in a decrease dissection energy in both directions. |

In addition to micromechanical-based characterisation tests, layer-specific properties of the aortic wall, specifically tissue strength, have also been evaluated using peel tests (Figure 2.7(F)). These tests are designed to assess the susceptibility of aortic tissue to dissection by measuring the fracture energy of each layer (Sommer *et al.*, 2008; Tong *et al.*, 2014). The peel test performed on human abdominal aorta by Sommer *et al.*, (2008) suggested that the dissection properties of the medial layer are direction dependent (anisotropic). This is evident from the higher force/width ratio and dissection energy (Table 2.3) in the longitudinal direction when compared with the circumferential direction, however this difference is not significant. Similarly, Tong *et al.,* (2014) investigated the dissection properties of AAA tissue and the effect of thrombus age. Results showed a decrease in dissection energy with thrombus progression and anisotropic behaviour since the dissection energy in the longitudinal direction exceeded the circumferential (Table 2.3).

### 2.5.2. Other design considerations

Another important aortic graft consideration is *in vivo* remodelling and its effect on the mechanical behaviour in the long-term. As mentioned in Section 2.4 current synthetic vascular grafts lack the ability to remodel and grow like living tissue. Therefore, it would be valuable to consider materials that allow for tissue regeneration, potentially by the incorporation of degradable materials or biological cues. In investigations regarding the development of tissue-engineered small-diameter vascular grafts, it has been reported that the remodelling process alters the mechanical properties of the graft in two possible scenarios, either by (1) further mimicking the mechanical behaviour of the native artery, which is ideal in terms of preventing complications related to mechanical behaviour mismatch, or (2) by becoming weaker or stiffer than the adjacent tissue and thus resulting in graft failure (Pashneh-Tala, Macneil and Claeyssens, 2016). Therefore, it is useful to question how close to the target mechanical properties the finalised graft should be and

how it will possibly change *in vivo* (Pashneh-Tala, Macneil and Claeyssens, 2016; Schoen *et al.*, 2019).

Although a close resemblance to the mechanical behaviour of native aortic tissue is crucial in the design process of novel aortic grafts, one must not disregard other essential considerations including biocompatibility, biodegradability, and hemocompatibility (Goins, Webb and Allen, 2019). Biocompatibility is key in the design process of any implantable device. By definition, a biocompatible implant must fulfil its designated function without triggering toxic events, both locally and systemically (Williams, 2008). A lack of biocompatibility activates the immune response ultimately resulting in implant failure. Additionally, in the case of vascular grafts where the design may be in the form of a tissue engineered scaffold, where tissue regeneration takes place while the scaffold material degrades, the material of choice must be cytocompatible to support cellular activity (SMCs, ECs, and fibroblasts). The by-products released during degradation must also be biocompatible and non-cytotoxic otherwise this would trigger the immune response, consequently hindering tissue regeneration. In the case of degradable scaffolds, it is important to consider the time it takes for the selected material to degrade in the body to ensure that both degradation and tissue regeneration take place in a synergistic manner, otherwise this would also result in graft failure. Issues concerning hemocompatibility are prominent in small-diameter vascular grafts where blood flow is slower and protein accumulation is high, and thus the onset of thrombosis is greater (Ren *et al.*, 2015). However, in aortic grafts, it is still important to select a non-fouling, anti-thrombogenic and non-haemolytic material, especially for the inner surface (the lumen), to prevent platelet and protein adhesion, and thus minimise the potential of graft occlusion (Ren *et al.*, 2015). In native aortic tissue, this is achieved via the endothelium (tunica intima).

Finally, it is also important to consider the translational aspect of the graft, including its regulatory process, off-the-shelf availability, and profitability. The regulatory process depends a lot on the type of graft; tissue-engineered grafts that require cell seeding prior to implantation would face a longer and more daunting translation to commercialisation and clinical settings than a completely synthetic acellular graft. The graft should accommodate the patient's own anatomical geometry to prevent complications such as restricted organ perfusion due to geometrical mismatches between the synthetic graft and the native aorta. Additionally, the design should be suitable for mass production, conforms to quality control standards, and stored and distributed at an economic cost. Therefore, apart from performing successfully *in vivo*, an ideal aortic graft must also be readily available at a low cost. Fulfilling all the requirements to produce a clinically acceptable vascular graft is not an easy task. In fact, for the last 50 years it has been the mission of biomedical engineers to develop alternative small-diameter vascular grafts, and to date none have achieved commercial success (Stowell and Wang, 2018).

## 2.6. Current approaches to alternative synthetic vascular grafts

### 2.6.1. Tissue Engineered Vascular Grafts (TEVGs)

The limitations associated with current synthetic vascular grafts has sparked a great interest among the scientific community to develop alternative technologies. However, this research has been predominantly targeted at small-diameter (< 6 mm) conduits. This is because in smaller vessels both Dacron® and ePTFE exhibit poor patency rates (Johnson and Lee, 2000) as a result of the inhomogeneity in compliance between the graft and the native artery (Walden *et al.*, 1980), and the slow flow of blood which increases the occurrence of early thrombosis. In light of these limitations, tissue engineering has emerged as a promising approach for the fabrication of small-diameter vascular grafts. This field of engineering utilises a combination of cells and biomaterials to produce grafts that closely resemble the arterial wall and are capable of growth and

remodelling *in vivo*. This idea was first introduced by Weinberg and Bell (1986) who developed an *in vitro* multi-layer model of an artery by co-culturing bovine aortic ECs, SMCs, and adventitial fibroblasts into a Dacron®-reinforced collagen matrix tubular conduit. Many other TEVG investigations followed suit and may be grouped into three different approaches (Figure 2.8): (1) cell sheet assembly, where cells of vascular origin are cultured as monolayers and then rolled into a tubular construct, (2) decellularization, where the cells that trigger immunogenicity are removed from donor vascular tissue creating a decellularized natural matrix, and (3) scaffold-based, where biomaterial scaffolds are fabricated in tubular shapes which may then be seeded with cells or not (acellular) (Goins, Webb and Allen, 2019).

The latter approach (scaffold-base) has been widely investigated since it is highly tailorable and shows the most promise for off-the-shelf availability. The scaffold for both cellular and acellular TEVGs may be fabricated from natural (e.g., alginate, gelatine, collagen) and/or synthetic biomaterials (e.g., polylactic glycolic acid (PLGA), polyethylene glycol (PEG), polycaprolactone (PCL)). Following the scaffold fabrication, in cellular TEVGs the surface of the scaffold is typically seeded with stem cells (e.g., progenitor, mesenchymal, and induced pluripotent) due to the difficulties associated with extracting autologous adult vascular cells (ECs, SMCs and fibroblasts). The seeded scaffold is then placed in a bioreactor for the cells to proliferate and differentiate. At this stage, the scaffold starts to degrade while tissue regenerates.

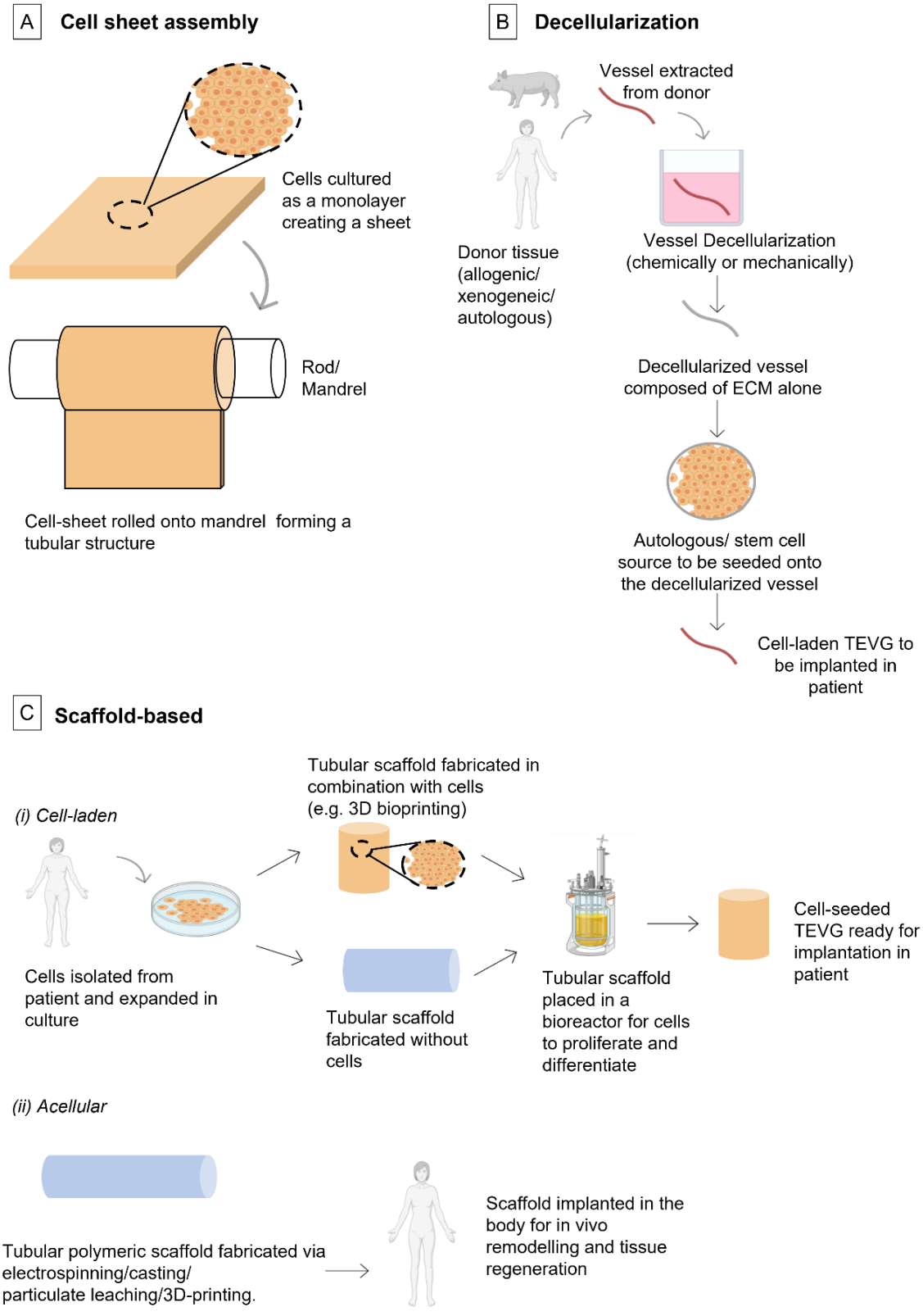


*Figure 2.8:Tissue engineering modalities for the fabrication of small-diameter vascular grafts: (A) cell sheet assembly, (B) decellularization, and (C) scaffold-based including both (i) cellular and (ii) acellular approaches. Figure created with the help of Biorender.com.*

Although the incorporation of cells further mimics the morphology of natural arteries, such grafts require a lengthy *in vitro* preparation process, with the bioreactor stage at times taking up to 8 weeks (Niklason *et al.*, 1999). Additionally, since the graft is essentially composed of living tissue this poses difficulties on storage and transportation, and more importantly it may trigger the immunogenic response once implanted in the human body. Thus, several investigations have moved on to the development of scaffold-based acellular vascular grafts. Contrarily to cell-based TEVGs, both scaffold degradation and tissue regeneration in acellular grafts take place post-implantation (*in situ*), with the host acting as the bioreactor, thereby eliminating the *in vitro* culture period. Moreover, acellular grafts, especially those comprising a synthetic scaffold, are easier to handle, sterilize, store and transport, ultimately leading to a simplified, inexpensive regulatory pathways and off-the-shelf availability.

### 2.6.2. Materials suitable for acellular vascular graft fabrication

As previously mentioned, acellular vascular grafts may be constructed using natural and/or synthetic materials. Ideally, this material should be biocompatible and possess suitable properties, preferably tuneable, to mimic the structure and mechanical behaviour of native vessels, whilst allowing for cellular adhesion or tissue regeneration. Moreover, the material must be suitable for mass production, with limited batch-to-batch variations, and off-the-shelf availability.

Material selection also depends on the type of fabrication technology used to develop the vascular graft. For instance, in 3D-printing, hydrogels, which are hydrated 3D polymer networks that swell in the presence of aqueous solutions, typically derived from synthetic and/or natural monomers, have emerged as promising materials for tissue engineering applications (Yan *et al.*, 2018; Hospodiuk *et al.*, 2017; Li, Tan and Li, 2018). This is mainly due to their biocompatibility, printability, ease of mechanical and physical properties tunability, and similarity to the ECM of natural tissue (Williams *et al.*, 2018). In

TEVGs, hydrogels have been mostly investigated for the fabrication of cell-laden scaffolds via 3D-bioprinting since their hydrophilic nature offers a hydrated and protective environment for the cells during printing.

Hydrogels may be synthesised using natural polymers such as plant-derived (alginate, agarose, cellulose) or animal-derived monomers (gelatine, collagen, elastin, chitosan, hyaluronic acid, fibrin, silk), and/or synthetic monomers (poly(ethylene) glycol (PEG), polyvinyl alcohol (PVA), poloxamers (Pluronic®)). Table 2.4 highlights the main characteristics of these polymers and their application in small-diameter TEVG fabrication. More details on the fabrication methods will be discussed in the following section.

*Table 2.4: Overview of biomaterials suitable for the fabrication of tissue-engineered vascular grafts (EB: extrusion-based, DB: droplet-based, LB: laser-based) (Merceron and Murphy, 2015; Floren, Migliaresi and Motta, 2016; Utech and Boccaccini, 2016; Hospodiuk et al., 2017; Gungor-Ozkerim et al., 2018; Li, Tan and Li, 2018).*

| **Material** | **Main Characteristics** | **TEVGs investigations** | |
|---|---|---|---|
| **Natural monomers** | | **3D-printed** | **Other fabrication methods** |
| Alginate | • Polysaccharide derived from brown algae.<br>• Various crosslinking modalities<br>• Printable at room temperature<br>• May be functionalised (methacrylated alginate).<br>• Bioinert (little/no cellular adhesion),<br>• Slow degradation kinetics (does not undergo enzyme-catalyse degradation). | EB: (Gao *et al.*, 2015), (Ghanizadeh Tabriz *et al.*, 2015), (Tan and Yeong, 2015)<br><br>DB: (Christensen *et al.*, 2015)<br><br>LB: (Yan, Huang and Chrisey, 2013) (Xiong *et al.*, 2015), | 3D Casting mould: (Guan *et al.*, 2019; Antunes *et al.*, 2021)<br><br>Micro-dip coating: (Ghanizadeh Tabriz *et al.*, 2017) |
| Agarose | • Polysaccharide derived from red seaweed.<br>• Thermo-responsive physical crosslinking (gelation occurs at low temperatures, liquifies between 20°C and 70°C)<br>• Bioinert (little/no cellular adhesion)<br>• Not biodegradable. | DB: (Blaeser *et al.*, 2013), (Duarte Campos *et al.*, 2013) | --- |
| Chitosan | • Polysaccharide derived from deacetylation of chitin.<br>• Its positive charge promotes haemostatic and antibacterial properties.<br>• Poor solubility in aqueous solutions with pH>7, soluble in diluted acids with pH<6<br>• Degrades enzymatically (lysozyme hydrolysis)<br>• Limited printability. | --- | Electrospinning: (Lee *et al.*, 2015) (chitosan/PCL)<br><br>3D casting mould: (Aussel *et al.*, 2017) |
| Collagen, type I | • Protein derived from vertebrates.<br>• Minimal immunological reactions.<br>• Gelation occurs at high temperatures forming a fibrous structure.<br>• Slow gelation rates lead to limited printability.<br>• Degrades enzymatically (MMP).<br>• Supports cell adhesion and growth due to inherent signalling molecules (RGD). | --- | Casting: (Weinberg and Bell, 1986)<br><br>Sandwich moulding process: (Kumar *et al.*, 2013) (Collagen/elastin)<br><br>Electrospinning: (Bertram *et al.*, 2017) (PCL/collagen) |
| Fibrin | • Formed by the enzymatic reaction between thrombin and fibrinogen.<br>• Rapidly dissolves in aqueous solutions.<br>• Lacks structural and mechanical stability.<br>• Supports cell adhesion and growth. | (Jan *et al.*, 2018) (fibrin/collagen) | Electrospinning: (Elliott *et al.*, 2019) (fibrin/PCL) |

*Table 2.4: (continued).*

| Material | Main Characteristics | TEVGs investigations | |
|---|---|---|---|
| **Natural monomers** | | **3D-printed** | **Other fabrication methods** |
| Gelatine | • Denatured form of collagen protein extracted from animals.<br>• Thermo-responsive physical crosslinking (gelation occurs at low temperatures, liquifies at 37°C).<br>• Maybe chemically crosslinked (e.g., via furaldehyde or glutaraldehyde) and functionalised (methacrylated Gelatine, GelMA).<br>• Degrades enzymatically (MMP).<br>• Supports cell adhesion and growth since it retains the collagen cell signalling molecules (RGD sequence).<br>• Easily dissolved in aqueous solutions at physiological temperatures. | Rod-printing EB:<br>(Liu *et al.*, 2017)<br>(Alginate-Gelatine)<br><br>Coaxial printing:<br>(Jia *et al.*, 2016b)<br>(GelMA/alginate/PEGTA)<br><br>EB:<br>(Ding and Chang, 2018)<br>(Gelatine/Alginate)<br><br>(Krishnamoorthy, Zhang and Xu, 2019)<br>(GelMA/Alginate) | Electrospinning:<br>(Johnson *et al.*, 2019)<br>(PCL/gelatine) |
| Hyaluronic Acid | • Polysaccharide (glycosaminoglycan)<br>• Degrades enzymatically (hyaluronidase).<br>• May be functionalised (HA methacrylate, MA-HA). | EB:<br>(Skardal *et al.*, 2010)<br>(HA/TetraPEG)<br>(Skardal, Zhang and Prestwich, 2010)<br>(HA/gelatine) | --- |
| Methyl-cellulose | • Polysaccharide derived from cellulose.<br>• Easily dissolved in aqueous solutions<br>• Gelation takes place at high temperatures (>60°C)<br>• Good shape fidelity. | --- | 3D casting mould:<br>(Azevedo *et al.*, 2013)<br>(cellulose/chitosan) |
| Silk fibroin | • A protein fibre derived from insect larvae (silkworm, spiders)<br>• Various gelation mechanisms (temperature, crosslinking, pH, shear forces, ultrasound, electric fields).<br>• Slow degradation kinetics but biodegradable (proteolytic).<br>• Lack specific cell binding moieties such as RGD. | --- | Braiding and electrospinning:<br>(Mi *et al.*, 2019)<br>(silk/PAM/TPU)<br><br>Moulding and electrospinning:<br>(Gupta *et al.*, 2020) |
| **Synthetic monomers** | | **3D-printed** | **Other fabrication methods** |
| Poly (ethylene glycol), PEG | • Available over a broad range of molecular weights (300 to 10,000,000 g/mol) and geometries (linear, branched).<br>• May be functionalised (methacrylate PEGMA, or diacrylate PEGDA).<br>• Not easily degradable (resistant to hydrolytic and enzymatic degradation)<br>• No cell adhesion moieties due to its synthetic nature. | EB:<br>(Gold *et al.*, 2021)<br>(PEGDA:GelMA: nanosilicates) | Electrospinning:<br>(Wu, Allen and Wang, 2012) |
| Pluronic® F-127 | • A poloxamer-based polymer.<br>• Dissolves easily and rapidly, therefore long-term stability is limited.<br>• Not biodegradable (resistant to enzymatic degradation).<br>• No cell adhesion moieties due to its synthetic nature. | EB:<br>(Suntornnond *et al.*, 2017)<br>(Pluronic-GelMa)<br>Coaxial nozzle EB:<br>(Millik *et al.*, 2019)<br>Pluronic/bisurethane methacrylate (BUM). | --- |

Natural polymers offer a high degree of biocompatibility yet suffer from limited availability, potential immunogenicity and pathogen transmission, especially in animal-derived monomers (Andersen, Auk-Emblem and Dornish, 2015), whilst lacking reliability due to the inherent diversity of material composition often leading to batch-to-batch variations. Synthetic polymers offer better reproducibility in batches, with properties that can be precisely controlled, yet they are less biocompatible as a result of the harsh chemicals used in the manufacturing process, and lack inherent cell recognition sites (Utech and Boccaccini, 2016). The monomers go through a crosslinking mechanism – either physical or chemical – in order to form the characteristic 3D polymer network of hydrogels. Thus, another way of hydrogel classification (apart from the monomer origin) is through the type of crosslinking mechanism used. Physically crosslinked hydrogels are synthesised through environmental changes (e.g., thermal, ionic, and pH sensitivity), hydrogen bonds, or protein interactions. The 3D polymeric network is prevented from dissociation in aqueous solutions by these physical yet weak interactions (Annabi *et al.*, 2014). Chemical crosslinking offers a more permanent polymeric 3D network as the chains are covalently bonded together through one of the following mechanisms: chemical reactions, radical polymerisation, energy irradiation, and enzymatic crosslinking.

Most naturally derived hydrogels utilise physical crosslinking mechanisms, for example alginate is typically ionically crosslinked using $CaCl_2$ (Christensen *et al.*, 2015; Ghanizadeh Tabriz *et al.*, 2015; Xiong *et al.*, 2015; Ghanizadeh Tabriz *et al.*, 2017), typically resulting in mechanically weak structures in comparison with blood vessel properties. Therefore, to improve the mechanical integrity and other properties such as printability and bioactivity, the hydrogel prepolymers may undergo a functionalization process, which may be in the form of chemical modification, the use of blends or composites (e.g., interpenetrating polymer networks), and physical properties

adjustments (Parak *et al.*, 2019). For example, the mechanical properties of most physically crosslinked natural polymers, such as alginate and gelatine, may be improved through chemical modification by the addition of methacrylate end groups (e.g., alginate-methacrylate, AlgMA or gelatine methacrylate, GelMA) ((Yue *et al.*, 2015; Hasany *et al.*, 2021)). This modification renders the polymer photopolymerisable suitable for UV photocrosslinking yielding an improved mechanically stable hydrogel due to the covalent bonds (Wei *et al.*, 2015).

### 2.6.3. Existing fabrication methods of acellular vascular grafts with a focus on advanced manufacturing

There exist various fabrication techniques suitable for the production of acellular vascular graft scaffolds, including conventional methods such as dip coating, casting, electrospinning, phase separation, and particulate leaching, and advanced methods primarily dominated by 3D-printing.

The dip coating and casting methods are relatively simple approaches that do not require complex, expensive equipment. In dip coating a rod is inserted (dipped) into a material solution creating a tubular structure with lumen diameter equivalent to the rod diameter. The dipping procedure may be performed multiple times to fabricate multi-layer structures as demonstrated by Ghanizadeh Tabriz *et al.*, (2017). In this investigation, vessel-like structures were fabricated with the use of stainless-steel rods of different diameters that were dipped into a sodium alginate solution with or without cells. As for casting, a sacrificial mould in a tubular shape is filled with the material solution, allowed to set (e.g., via gelation or crosslinking depending on the material used) and then demoulded to extract the tubular structure (Gargava *et al.*, 2019; Antunes *et al.*, 2021). This is the fabrication method used by Weinberg and Bell (1986) when first introducing TEVGs.

Electrospinning has been widely explored for the production of small-diameter TEVGs. This fabrication method is based on electrostatic repulsion generated from a high voltage source that separates a polymer solution into micro/nano fibres which are typically deposited onto a rotating mandrel to form a tubular conduit. The resulting fibrous alignment is very similar to the ECM of native tissue, hence its applicability in tissue engineering (Hasan *et al.*, 2014). Electrospinning is a versatile technique where a broad range of materials may be used including natural and/or synthetic polymers (e.g., gelatine, polycaprolactone (PCL), polyurethane, (PU)). Fibre formation, and therefore the resulting electrospun scaffold morphology (including porosity), depend on a variety of parameters including the material's molecular weight and viscosity, the set-up voltage and flow rate, and environmental conditions, such as temperature and humidity. For example, a polymer with high molecular weight and viscosity results in an increase in fibre diameter and pore size. Although fibre properties may be altered by varying these parameters, electrospinning is still considered as a fabrication method with poor control over the mechanical and degradation properties of scaffolds. In fact, recent studies have been focussing on improving the mechanical properties of electrospun scaffolds, some through the combination of two polymers for the same scaffold (PCL/PU (Jirofti *et al.*, 2018)), PCL/gelatine (Johnson *et al.*, 2019)) and others through the introduction of an additional fabrication method prior to electrospinning (Abdal-Hay *et al.*, 2018). Johnson *et al.*,(2019) demonstrated that the addition of a natural polymer such as gelatine improves cell adhesion and imparts viscoelasticity, compliance, swelling capability, good suturability, and kink resistance to the electrospun vascular graft. Abdal-Hay *et al.*, (2018) sought to improve the mechanical properties by first airbrushing PCL onto the mandrel followed by electrospinning PU fibres thus creating a biphasic PCL/PU scaffold. When compared to PU-alone scaffolds, the PCL/PU demonstrated superior tensile strength, elastic modulus, suturability, burst pressure, and compliance, suggesting that bilayer scaffolds fabricated via two different techniques result in a mechanically robust

structure. In terms of degradation, since most electrospun scaffolds are composed of synthetic polymers such as PCL, which take years to degrade *in vivo* (1.5 years according to Johnson *et al.*, (2019)), investigations reporting complete polymeric degradation of the scaffold are limited (Rocco *et al.*, 2014; Zhen *et al.*, 2019). To overcome this limitation, Wu, Allen and Wang (2012) introduced a fast degrading elastomer poly(glycerol sebacate) (PGS) in addition to PCL, which degrades via surface erosion within 2 months after implantation thereby allowing for *in vivo* remodelling. In fact, after 3 months implanted in rat abdominal aorta the PGS-PCL graft almost degraded completely apart from some PCL residues, as expected. Another drawback of electrospun scaffolds originates from their dense fibrous structure and limited porosity, which has been found to hinder cell infiltration and proliferation *in vivo* (Hasan *et al.*, 2014; Mi *et al.*, 2019).

Other fabrication methods such as Thermally Induced Phase Separation (TIPS) and particulate leaching have shown to improve scaffold porosity. The TIPS method involves quenching of the polymer solution below the freezing point of the solvent. This separates the solution into two liquid phases referred to as the polymer-rich and polymer-poor phases where the former solidifies, and the latter crystallises. The crystallised structure is then lyophilised forming a porous structure (Wu *et al.*, 2018; Tan, Ang and Huang, 2020). One major drawback of TIPS is the fabrication of scaffolds with poor mechanical integrity. Therefore, Mi *et al.*,(2019) have utilized this method in combination with electrospinning to fabricate triple-layered scaffolds. By combining both methods, the middle layer fabricated via TIPS provided high porosity and pore interconnectivity whereas the first and third layers fabricated via electrospinning provided the desired mechanical properties suitable for vascular graft applications. Once again to achieve a suitable degradation rate, a fast-degrading polymer poly (propylene carbonate) (PPC) was used in combination with PU.

The particulate leaching method involves the incorporation of particulates of a definite diameter, known as porogens, in the polymer solution. The polymer solution is poured into a 3D mould followed by the addition of a solvent to leach the porogens out of the solution, thereby creating pores of known diameter (Tan, Ang and Huang, 2020). In the PCL-PGS scaffold fabricated by (Wu, Allen and Wang, 2012), the PCL fibre sheath was fabricated via electrospinning, however the PGS core was fabricated via salt fusion and leaching. This resulted in a PCL-PGS-salt composite which was then immersed in water to leach out the salt particulates creating a PCL-PGS porous scaffold. Similarly to TIPS, this method yields scaffolds with poor mechanical properties and thus it is seldomly used on its own (Zhen *et al.*, 2019).

A major drawback of these conventional manufacturing methods is the inability to produce complex geometrical structures, rapidly and inexpensively, according to the patient's own anatomical geometry. Therefore, TEVGs are typically fabricated as straight tubular conduits with the same diameter throughout. Size mismatch between the graft and the native artery has similar complications to compliance mismatch (Section 2.4). Therefore, advanced manufacturing techniques, specifically 3D-printing, has gained a lot of attention due to its ease of customisation and complex structure fabrication without the need for additional moulds, thereby opening up the possibility of patient-specific vascular grafts. In 3D-printing, the material (ink/resin) is deposited or used to produce a 3D structure in a layer-by-layer manner. In tissue engineering this method has been modified to also involve cell-laden biomaterials (also referred to as bioinks) in a process known as 3D-bioprinting.

Irrespective of the type of implant or tissue to be fabricated, the 3D-printing process involves three major phases: (1) the pre-processing phase, where a model is created using a computer-aided design (CAD) software, in the case of personalised TEVGs the model may be obtained from imaging technologies, such as CT/MRI scans, (2) the

processing phase, which involves the actual layer-by-layer printing of the model after the appropriate selection of a 3D-printing platform and biomaterials (or bioinks if cells are included), and (3) the post-processing phase, where the 3D-printed part is prepared for *in vivo* implantation, this may include sterilisation, surface modifications or a bioreactor phase for cellular scaffolds (Bishop *et al.*, 2017; Wenger and Giraud, 2018).

Most 3D-printing platforms accommodate both acellular and cellular scaffold fabrication, with extrusion-, droplet-, laser-, and light- based 3D-printing being the most common modalities, illustrated in Figure 2.9.

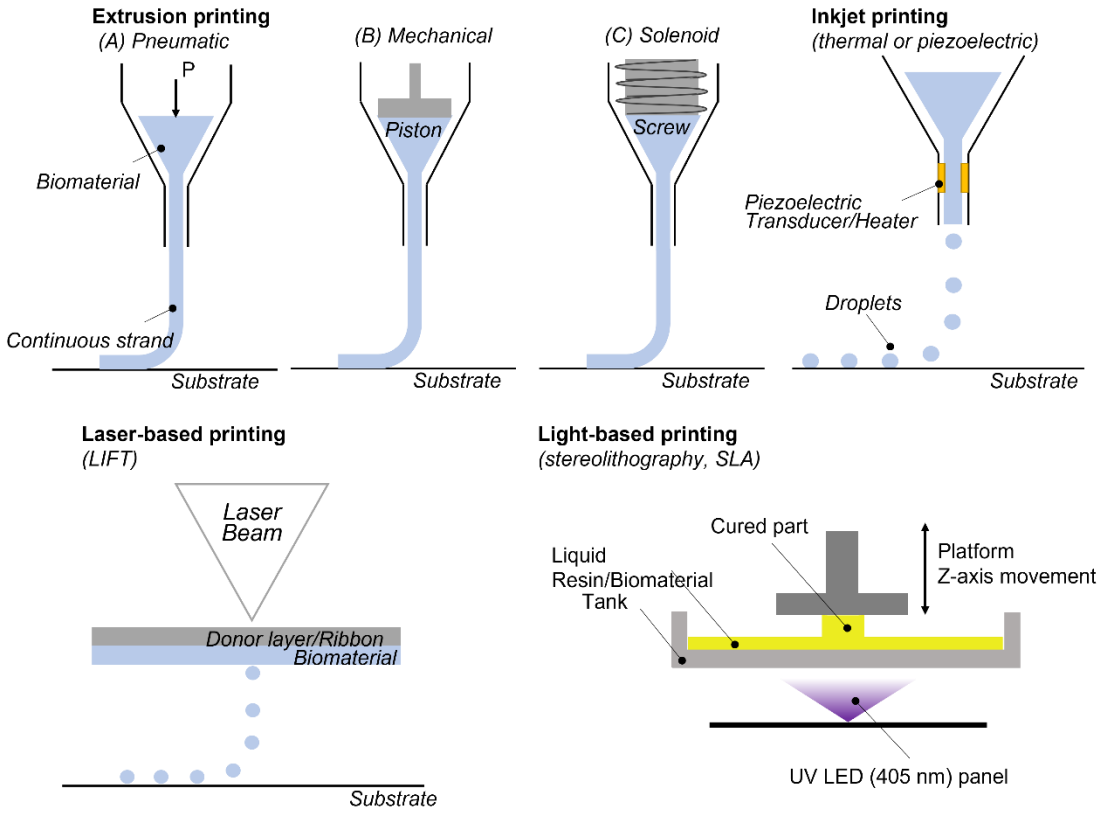


*Figure 2.9: Common 3D-printing platforms (suitable also for bioprinting): extrusion-based printing including (A) pneumatic, (B) mechanical, and (C) solenoid-driven modalities, droplet-based printing via inkjet printing including thermal- or piezoelectrical- driven modalities, laser-based printing via Laser Induced Forward Transfer (LIFT), and light-based (or vat photopolymerisation) which includes stereolithography (SLA), 3D-printing.*

Extrusion-based 3D-printing has been widely investigated for the fabrication of tissue engineered scaffolds, primarily due to its capability of printing a broad range of biomaterials with varying viscosities (30 mPa·s to $6\times10^7$ mPa·s) at high precision whilst using inexpensive equipment. The printing method involves a nozzle system which may be pneumatic-, mechanical- or solenoid- driven where the material is deposited onto a substrate in a continuous strand (Figure 2.9(A-C)). To achieve this filament type extrusion, the feeding material should ideally demonstrate a thixotropic (or shear-thinning) behaviour, meaning that with an increase in applied shear stress the viscosity decreases (Datta, Ayan and Ozbolat, 2017). Therefore, the material is in its liquid state before and during printing which then solidifies after printing. Ideally, the deposited material should solidify quickly to maintain its shape, however if this is not the case, an additional crosslinking step (chemical, pH, UV) is typically introduced. For example, Ghanizadeh Tabriz *et al.*,(2015) 3D-printed vascular-like structures using a modified extrusion-based printer and partially crosslinked alginate as the feeding material. The structures were printed onto a platform that was incrementally lowered into a bath of calcium chloride ($CaCl_2$) upon deposition of each layer, thereby providing further crosslinking and a stronger base for the following layers. Apart from these two crosslinking steps, the 3D-printed structures were also subjected to a third crosslinking step using barium chloride ($BaCl_2$), as a way to improve the structure's stability.

Unlike extrusion-based printing, in droplet-based printing, as the name implies the material is deposited in a dropwise manner to fabricate the 3D object. This method may be categorised into four possible modalities: inkjet printing, electro-hydrodynamic jetting, acoustic droplet ejection and micro-valve printing (Hospodiuk *et al.*, 2017; Holland *et al.*, 2018). The most common of the four is inkjet 3D-printing due to its availability, simple set-up, low cost, fast printing rates and high resolution. Inkjet droplets may be generated thermally or piezoelectrically (Figure 2.9). All systems consist of a nozzle from which the

droplets are ejected, therefore the material must have a low viscosity (3.5 to 12 mPa·s) and a non-fibrous structure for it to flow easily through the nozzle (Wenger and Giraud, 2018). Therefore, an ideal inkjet printing material should demonstrate a rheopectic behaviour (the opposite of thixotropic used in extrusion printing) where the viscosity increases with applied shear thereby triggering droplet formation. Following deposition, the transformation into a strong, solid-state structure is difficult to achieve due to the material's low viscosity, thus a further solidification stage is required, and this is typically achieved via crosslinking mechanisms (e.g., chemical, pH, or UV). Therefore, this method apart from restricting the material selection to low viscosity materials it also requires that the material be suitable for crosslinking (e.g., hydrogels). Other limitations of inkjet 3D-printing include frequent nozzle clogging and non-uniform droplet size. Despite these limitations, inkjet 3D-printing has been widely explored in tissue engineering. For the fabrication of TEVGs, the work by Christensen *et al.*,(2015) has successfully demonstrated the ability of inkjet printing for the fabrication of vascular-like tubular conduits (including bifurcations) using an alginate hydrogel with and without the incorporation of fibroblast cells. Similarly to Ghanizadeh Tabriz *et al.*,(2015), the vascular-like alginate structures were printed into a bath of $CaCl_2$. This approach is ideal, especially when 3D-printing tubular structures in the vertical plane, since apart from providing an additional crosslinking step, the liquid solution also prevents the structure from collapsing by providing a buoyant force.

Laser-assisted 3D-printing is less common than inkjet- and extrusion- based technologies for the fabrication of TEVGs (Datta, Ayan and Ozbolat, 2017). This 3D-printing method may be categorised into two types: cell transfer and photopolymerization. The former is based on the principle of laser-induced forward transfer (LIFT) where a laser pulse is targeted onto a donor slide (or ribbon), which constitutes of an energy-absorbing layer (composed of a titanium or gold film) and a layer

of the material to be deposited (the ink), as illustrated in Figure 2.9. The laser energy is absorbed by the metal film causing localized heating followed by vaporisation thereby generating a jet of ink microdroplets which are then deposited onto a substrate, ultimately resulting in a 3D structure (Datta, Ayan and Ozbolat, 2017). Although the 3D-printing procedure is relatively fast, preparation of the ribbon is time-consuming which slows down the whole process (Miramini *et al.*, 2020). As for photopolymerization laser-assisted 3D-printing, this includes methods such as digital light processing (DLP), stereolithography (SLA), and two-photon polymerization (2PP). The latter utilises ultra-fast laser beams directed onto a photocurable material which solidifies via polymerisation (Datta, Ayan and Ozbolat, 2017; Holland *et al.*, 2018). Alternatively, this technology may also be performed via UV light instead of laser beams which selectively cures the photopolymerisable resin (Figure 2.9), as in the case of SLA and DLP, and is a less expensive approach. In both cases (laser and UV), the material selection is limited to photosensitive materials, and for photopolymerization to take place the feeding material solution must also include a non-toxic photoinitiator (e.g., Irgacure 2959 or lithium phenyl-2,4,6-trimethylbenzoylphosphinate (LAP)). One major advantage of laser- or light- assisted 3D-printing over inkjet and extrusion printing is the nozzle-free approach, thereby eliminating the limitations associated with clogging and material viscosity (Levato *et al.*, 2023). This also facilitates bioink printing as it eliminates cell damages associated with shear stress during nozzle extrusion, however other factors come in to play including the selection of a noncytotoxic photoinitiator and a cell compatible UV wavelength range (e.g., 405 nm) (Levato *et al.*, 2023). Additionally, light-based 3D-printing, such as DLP and SLA, involves rapid fabrication times and high printing resolutions, which are highly advantageous characteristics if such technologies were to be used in clinical settings (Levato *et al.*, 2023). Xiong *et al.*,(2015) opted for laser printing of tubular constructs instead of inkjet printing to eliminate clogging-related failures. In this study, straight and bifurcated acellular (alginate-alone) and cellular

(alginate-fibroblasts) vessel-like structures were fabricated via the LIFT approach. Similar to the extrusion-based investigation by Ghanizadeh Tabriz *et al.*, (2015) and the inkjet investigation by Christensen *et al.*,(2015), the material was deposited into a bath of $CaCl_2$ solution which acts as a liquid support for vertical printing and overhang features in bifurcated structures and as a further crosslinking step.

Depositing the material in a liquid bath for additional support is one way of improving the 3D extrusion printing process of tubular structures. Other variations targeted at facilitating the fabrication of tubular conduits include concentric ring printing, coaxial printing, and rod-support printing (Figure 2.10).

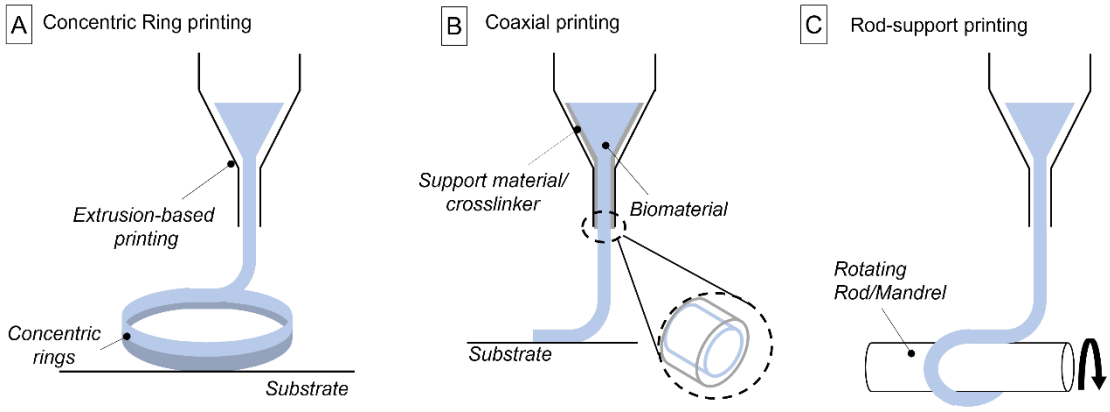


*Figure 2.10: 3D-printing variations for the fabrication of tubular conduits: (A) concentric ring printing, (B) coaxial nozzle printing, and (C) rod-support printing.*

Concentric ring printing is also suitable for the fabrication of tubular structures in the vertical plane by depositing concentric layers one on top of the other (Figure 2.10(A)). To achieve this, it is crucial that the base layer is strong enough to sustain the weight of the entire structure to be printed on top, otherwise the whole structure would collapse. This restricts material selection to high viscosity materials. However, Tan and Yeong (2015) managed to lower the viscosity of the feeding material by the incorporation of xanthan gum to alginate and successfully 3D-print tubular constructs in the vertical plane. The tubular structures were fabricated using a multi-nozzle extrusion 3D-printing set-up

which enabled hydrogel crosslinking during printing. This was achieved by depositing alginate-xanthan gum in concentric layers as the exterior and the crosslinking agent ($CaCl_2$) as the core. One of the drawbacks of this method is the possibility of shrinkage post-fabrication due to the in-process crosslinking.

Coaxial printing is a similar approach to the multi-nozzle extrusion 3D-printing process implemented in the investigation by Tan and Yeong (2015). However, instead of having two different nozzles to dispense two different materials, in coaxial printing one nozzle containing inner and outer tubes is used to deposit both materials at once (Figure 2.10(B)). This approach has been particularly investigated for the fabrication of micro-tubular structures such as microchannels used for the perfusion of 3D-printed organs. In the study by Gao *et al.*,(2015) hollowed alginate filaments were fabricated using a coaxial nozzle where alginate was dispensed via the outer tube and the crosslinking agent ($CaCl_2$) via the inner tube. Partial crosslinking was achieved within the coaxial nozzle upon contact between the alginate and $CaCl_2$, whereas complete crosslinking was achieved once the layers were deposited into a $CaCl_2$ bath. Jia *et al.*,(2016b) further extended the principle through the implementation of a multi-layered coaxial nozzle comprising three concentric channels, with the crosslinking agent located in the innermost and outermost channels and the feeding material in the middle channel. One limitation of coaxial printing is that the luminal diameter and wall thickness of tubular structures depend on nozzle dimensions. Hence, Millik *et al.*,(2019) designed and 3D-printed customised coaxial nozzles to fabricate stand-alone tubes that mimic vascular grafts with varying luminal diameters and thicknesses.

In rod-support printing, instead of depositing the material onto a flat substrate or a liquid bath, the material is deposited onto a horizontal rotating rod (or mandrel) which is then removed once the structure is deemed stable, thereby creating a tubular scaffold (Figure 2.10(C)). This method facilitates the fabrication of long tubular structures with uniform

luminal diameters throughout depending on the dimensions of the rod. Uniformity is achieved though fusion between one strand and the other, therefore it is crucial that the horizontal speed of the nozzle and the rotational speed of the rod are synchronized (Liu *et al.*, 2017). Rod-printing may also be performed using a coaxial nozzle, as demonstrated by Gao *et al.*,(2017b) where alginate and $CaCl_2$ hollowed filaments were deposited onto a rotating rod to fabricate vessel-like structures.

Evidently, 3D-printing of vascular grafts offers several benefits over conventional manufacturing techniques, including (1) the ability to 3D-print complex geometrical, potentially even patient-specific scaffolds using various biomaterials (natural and/or synthetic) and biological materials (bioprinting), (2) high versatility due to the various platform availability (inkjet, extrusion, vat) and customisation (coaxial-, rod-, concentric-printing), and (3) faster fabrication times and high reproducibility owing to its automation capability.

### 2.6.4. Existing aortic graft alternatives

Tissue engineering has been seldomly investigated for the fabrication of alternative aortic grafts, with the exception of decellularization. In fact, a recent study by Aldridge *et al.,* (2018) investigated the decellularization of human donor aortas and its effect on biocompatibility and biomechanics to potentially replace current synthetic aortic grafts. Prior to decellularization, the aortas were decalcified to remove a substantial amount of calcium (~90% reduction) which is considered as a contributing factor to vascular deterioration via calcification. Overall, the decellularization process was a success; with 94% reduction in DNA between the native and decellularized aortas, no significant changes in tensile strength and suture retention strength, and no cytotoxic results indicating no changes in biocompatibility. Although the results suggest that this method has the potential of substituting aortic grafts via decellularization, further investigations are required including *in vivo* studies in animals before even considering clinical

applications. Additionally, this approach of tissue engineering depends on donor aortas and therefore it is difficult to implement on a large scale due to the shortage of donors and the difficulty in finding a healthy, anatomically matching donor aorta.

On the same scale as the aorta, with luminal diameters ranging between 15 and 30 mm, tissue engineering has been explored for the fabrication of other large-diameter tubular structures found throughout the body, including the trachea and oesophagus. Table 2.5 highlights some of the tissue engineering investigations of tracheal and oesophageal substitutes. Most of these studies still focus on the fabrication of small-diameter tubular conduits (5 – 10 mm luminal diameter), potentially restricted by small animal models *in vivo* investigations, such as rabbit or porcine (Gao *et al.*, 2017a; Park *et al.*, 2019; Lin *et al.*, 2019; Lee *et al.*, 2020). As for large-diameter (>15 mm luminal diameter) scaffold investigations, these have been predominantly fabricated via conventional methods, rather than 3D-printing (Table 2.5). This highlights the need for investigations that focus on 3D-printing of large-diameter acellular tubular scaffolds.

*Table 2.5: Tissue engineering for the fabrication of tracheal and oesophageal substitutes (with diameters in similar to the aorta).*

| Study | Scaffold type | Fabrication Method | Biomaterial | Luminal diameter | Remarks |
|---|---|---|---|---|---|
| **(Gao *et al.*, 2017a)** | Tracheal | 3D-printing | PCL | 5 mm | *In vivo* implantation study in rabbit model following an *in vitro* cell culture period. |
| **(Best *et al.*, 2018)** | Tracheal | Electrospinning and 3D-printing | Electrospun PET/PU and 3D-printed PCL | 20 mm | The graft was designed to match juvenile ovine tracheas. The PET/PU electrospun scaffold was reinforced with 3D-printed PCL C-shaped rings to mimic tracheal architecture. |
| **(Soliman *et al.*, 2019)** | Oesophageal | Electrospinning | PU | 22 mm | The graft consisted of multiple layers with different PU pore size. |
| **(Park *et al.*, 2019)** | Tracheal | 3D-printing (rod supporting) | PCL/ Alginate | 5 mm | The alginate hydrogel was loaded with cells (bioprinting using autologous epithelial and chondrocytes). Scaffold consisted of 5 alternating layers of PCL and cell-laden alginate. |
| **(Lin *et al.*, 2019)** | Oesophageal (stent) | 3D-printing | PLA/TPU | 10 mm | Via 3D-printing, the tubular structure was reinforced with spirals along the outer diameter. Stent characterization was performed in *ex vivo* porcine oesophagus. |
| **(Cristovão *et al.*, 2019)** | Tracheal | 3D-printing (coupled with UV laser) | PEGDA/ Alginate | ~18 mm | A 3D model from a patient's CT scan was used to 3D print a tracheal section with varying wall thicknesses from 0.5 mm to 1.5 mm. As the wall thickness increased, the tracheal compliance decreased, and the structure became less fragile. |
| **(Lee *et al.*, 2020)** | Tracheal | 3D-printing | PCL/silicon/collagen | 5 mm | An acellular, off-the-shelf tracheal graft. The graft was composed primarily of PCL, silicon bands were added as reinforcement (both 3D-printed), and a collagen-covered lumen. *In vivo investigation* was performed in rabbits (complete reepithelialisation took 17 weeks). |

## 2.7. Conclusions and research opportunities

Despite the general good performance of Dacron® and ePTFE as aortic substitutes for aneurysmal repair, major limitations, primarily the mismatch in biomechanical behaviour and compliance between the graft and the native aorta, have yet to be addressed (Section 2.4). One way of minimising this mismatch is by considering the mechanical behaviour and properties of the natural aorta as target properties (Section 2.2 and Section 2.5). Several investigations have addressed the issue of compliance and mechanical properties mismatch, but these have been predominantly focussed on the realisation of tissue engineered small-diameter vessels via the incorporation of biological material (cells) throughout the fabrication process (e.g., 3D bioprinting) (Section 2.6). Although this improves the resemblance to native tissue it tends to complicate the regulatory pathway. Additionally, small-diameter TEVG investigations still do not meet all the essential requirements for the graft to be ideal, and to date none have achieved commercial success.

Based on this literature review, it is evident that there is a gap regarding alternative aortic graft technologies. This opens up several research opportunities including the fabrication of patient-specific aortic grafts via hydrogels (without cells) as the material of choice and 3D-printing as the fabrication method, in addition to several mechanical characterization tests to ensure that the graft closely resembles the mechanical behaviour and properties of natural aortic tissue.

## 2.8. Research Aims

To date, vascular graft research has been primarily focussed on developing novel small-diameter blood vessels with limited emphasis on improving the performance of their large-diameter counterparts. Consequently, this research aims to develop a synthetic large-diameter vessel to prevent the long-term complications associated with state-of-the-art, commercially-available aortic grafts. The synthetic vessel would comprise the

following characteristics: (1) similar mechanical properties to the native human, healthy (i.e., non-aneurysmatic) abdominal aorta, (2) biological cues that enable endothelialisation, and (3) the ability to be produced according to the patient's own anatomical geometry to ensure optimal blood flow.

Hydrogels were selected as the primary materials for producing the aortic-mimicking vessel. This class of materials has been widely explored for the fabrication of tissue engineered vascular grafts (Section 2.6.2), owing to its versatility in synthesisation and therefore controllability of several properties (e.g., mechanical, physical, biological), in addition to its compatibility with various manufacturing methods (e.g., casting and 3D-printing). To ensure graft to host artery mechanical compatibility, the hydrogel formulation was mechanically characterised to determine both elastic (strength, stiffness, elongation) and viscoelastic (stress relaxation behaviour, shear storage and loss moduli) properties. Additionally, this material should also be suitable for 3D-printing to be able to produce anatomically-relevant tubular conduits that also perform well in physiologically-relevant environments. Given the synthetic nature of the hydrogel formulation, cellular motifs were incorporated into the material to ensure cell compatibility and adhesion *in vivo*.

## 2.9. Research Objectives

(i) Identify suitable monomers for the fabrication of hydrogel-based aortic grafts through mechanical characterisation to obtain a material with similar mechanical properties to the native human, healthy (non-aneurysmatic) abdominal aortic tissue (stiffness: 1 – 2 MPa, strength: 0.4 – 1.0 MPa).

(ii) Select a suitable advanced manufacturing method (3D-printing) for the production of large-diameter tubular conduits with size and dimensions similar to the native human abdominal aorta (outer diameter: 12 – 15 mm, wall thickness: 1.5 – 2 mm) to demonstrate potential for patient-specific graft fabrication.

(iii) Functionalise the selected synthetic hydrogel via the introduction of biological cues (e.g., an arginine-glycine-aspartic acid (RGD) peptide) to ensure favourable cell-biomaterial interactions and promote endothelialisation.

(iv) Characterise cell adhesion and growth on the developed hydrogel under static culture conditions with the use of endothelial cells.

# Chapter 3 General Materials and Methods

## 3.1. Fabrication of alginate-based hydrogels

### 3.1.1. Materials

Alginic acid sodium salt (M/G ratio of 1.56, low viscosity: 15-25 cps), gelatine (gel strength ~ 300 g Bloom, Type A from porcine skin), elastin (soluble elastin from bovine neck ligament), calcium chloride ($CaCl_2$, 99% purity, Mw = 110.98 g/mol), calcium carbonate ($CaCO_3$), calcium sulphate ($CaSO_4$), barium chloride ($BaCl_2$, 99% purity, Mw = 244.26 g/mol), gluconic acid δ-lactone (GDL, $C_6H_{10}O_6$), poly(ethylene glycol) diacrylate (PEGDA, Mn = 575; Mn = 700; Mn = 10000), 2-Hydroxy-4′-(2-hydroxyethoxy)-2-methylpropiophenone (Irgacure 2959, 98% purity), and Lithium phenyl-2,4,6-trimethylbenzoylphosphinate (LAP), were all purchased from Sigma Aldrich, UK.

### 3.1.2. Single-network alginate, alginate-gelatine, and alginate:elastin hydrogel preparation

Stock solutions of 4 %(w/v) and 5 %(w/v) alginate were prepared by dissolving sodium alginate powder in deionised water (DI water). For the alginate-based hydrogel blends, stock solutions were prepared using a fixed gelatine concentration of 2 %(w/v) or a fixed elastin concentration of 0.5 %(w/v). Gelatine/elastin and alginate were dissolved together in DI water using a magnetic stirrer, until a homogenous mixture was obtained. Once completely dissolved, the alginate alone and alginate:elastin stock solutions were stored at 4°C, while the alginate-gelatine solution was stored in an incubator at 37°C to maintain the gelatine in its soluble form. Initially, four different types of crosslinkers were investigated: $CaCl_2$, $CaCO_3$, $CaSO_4$, and $BaCl_2$ at three different molarities: 100 mM, 200 mM and 300 mM. For instantaneous gelling ($CaCl_2$ and $BaCl_2$) and slow gelling crosslinkers ($CaSO_4$), stock solutions were prepared by mixing the powder form crosslinker in DI water. For the other slow-gelling crosslinker, $CaCO_3$ was added to a catalyst, GDL, in deionised water at a 1:2 molar ratio to maintain a neutral pH ~ 7. The

crosslinker was then added to the alginate solution and vortexed for approximately 10 s until complete dissolution was achieved. The hydrogels were prepared in tissue culture well plates for disc shaped samples or in customised dog-bone shaped moulds (Appendix 1: 3D designs used for 3D-printing.) for tensile testing.

### 3.1.3. Alginate:PEGDA interpenetrating polymer network (IPN) precursor solution preparation

8.25 %(w/v) alginate stock solution was prepared as described in Section 3.1.2. PEGDA Mn575 or Mn700 were dissolved in DI water to obtain stock solutions of 66.6 %(w/v) for both molecular weights. For the fabrication of hydrogels in moulds, Irgacure 2959 (I2959) was used as the photoinitiator. Given its limited solubility in DI water, this was dissolved in 70% (v/v) ethanol to obtain a 10 %(w/v) stock solution. The alginate:PEGDA IPN precursor solution was prepared by mixing the 8.25 %(w/v) alginate with 66.6 %(w/v) PEGDA700 or PEGDA575 at a 1:1 volume ratio, followed by the addition of the photoinitiator resulting in final concentrations of: 3.3 %(w/v) alginate, 26.6 %(w/v) PEGDA and 0.5 %(w/v) I2959. The solution was stirred on a roller mixer to ensure a homogeneous mix, followed by degassing cycles in an ultrasonic bath. Hydrogel samples were prepared by first exposing the precursor solution to UV light (Analytik Jena Short/long-wave UV lamp; 6 watts, 365 nm wavelength, 230 VAC/50 Hz, Cole-Parmer, UK) for 15 minutes (disc samples) or 30 minutes (dog-bone samples) to cure the PEGDA, followed by immersion in a $BaCl_2$ bath (66 mM) for the alginate to crosslink overnight. For the $CaCO_3$:GDL crosslinker, this was mixed with the alginate:PEGDA IPN solution prior to exposure to UV light.

## 3.2. Hydrogel characterisation methods

### 3.2.1. Confined compression tests

For mechanical characterisation of hydrogels via confined compression, samples must be confined radially and at the base. The hydrogels were therefore prepared and tested

in standard 24-well tissue culture plates. The hydrogel discs were compressed via a porous indenter (316L sintered steel mesh, $k$~$6\times10^{-7}$ $m^4$/ N s) of diameter 15.9 mm, attached to a 22 N load cell, as illustrated in Figure 3.1(A) (parameters according to (Busby *et al.*, 2013)). The load cell is controlled via the ElectroForce® 3100 Test Instrument (TA® Instruments, UK) and the WinTest® 7 software (TA® Instruments, UK) to obtain a stress response for a given strain. Prior to testing, the gels were detached from the well, washed in deionised water to stop further crosslinking and any remaining bathing fluid in the well was removed. The sample diameter and thickness were measured using digital callipers. Once loaded on the test instrument, the indenter was lowered to touch the hydrogel surface; to ensure full contact, a preload of 0.1 N was employed. The system was left to equilibrate (approximately 2 hours) prior to running the test. Once the load stabilised i.e., a negligible increase in force reading, the samples were compressed by 5% strain at a ramp rate of 0.5%/s (until reaching a peak stress) and then held at that strain for 300 s (until reaching an equilibrium stress), as illustrated in Figure 3.1(B) (Busby *et al.*, 2013).

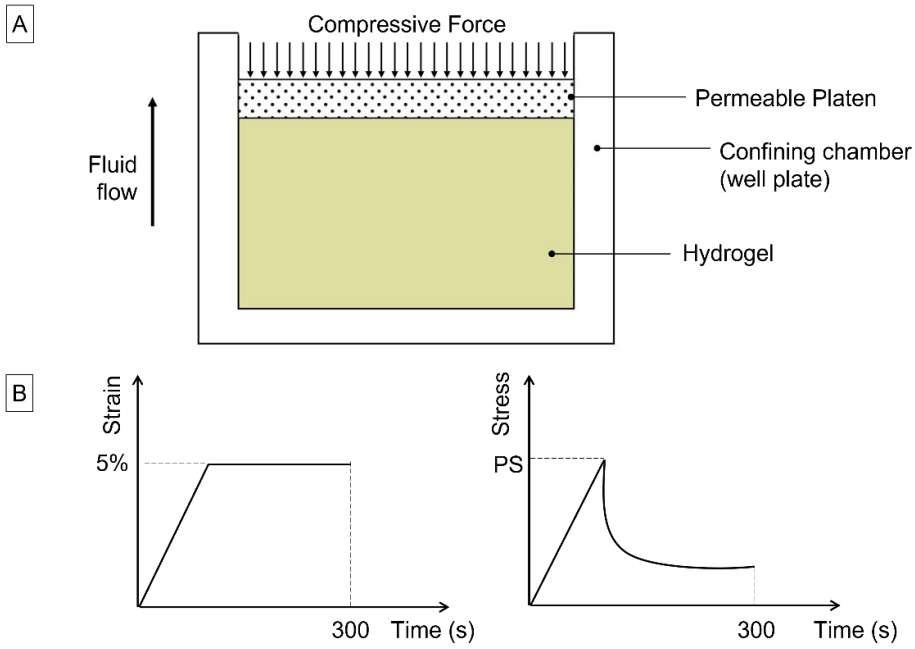


*Figure 3.1: Schematic showing (A) the confined compression of hydrogels test configuration and (B) the ramp-hold compressive strain together with the corresponding stress response.*

The raw data obtained from these tests include a load against time curve with the peak load at approximately 10 s, corresponding to 5% displacement of the original thickness of the sample (~ 0.4 mm). This is followed by a load dwelling period for an additional 300 s until reaching an equilibrium load - a total test duration of 310 s. The stress response is then calculated using Equation 3.1:

$$Stress\ (kPa) = \frac{Load(N)}{Surface\ Area\ (m^2)} \tag{3.1}$$

An open-source finite element analysis software (FEBio) was used to develop a model representing confined compression in order to calculate other parameters, including the compressive modulus and permeability ($H_A$ and *k*), that cannot be directly obtained from the experimental raw data.

**FEBio model structure**: As illustrated in Figure 3.2, a model designed to mimic the confined compression experimental setup was developed in *PreView*, which constituted of a cuboid (14.18 × 14.18 × 6 mm) representing the hydrogel sample and an indenter on top, the latter comprising of a flat plate (14.18 × 14.18 × 1 mm) and a handle (2 × 2 × 4 mm). Both plate and handle were modelled as rigid bodies, each with a density of 1 and centre of mass (COM) coordinates at (0,0,6.5) and (0,0,9), respectively. The thickness of the sample (z-direction) is critical when analysing confined compression, therefore the hydrogel sample model consisted of 100 elements in the z-direction and one element in the xy-plane ($N_x$=$N_y$=1, $N_z$=100, a total of 404 nodes). Since the indenter will not influence the analysis section, the handle and plate each consisted of 1 element in all directions ($N_x$=$N_y$=$N_z$=1, a total of 8 nodes).

**Sample material selection:** The hydrogel sample was represented by a linear biphasic poroviscoleastic (BPVE) model which describes the viscoelasticity of the material comprising fluid flow-dependent (arising from the biphasic liquid phase that is the constant isotropic permeability) and fluid flow-independent (arising from the intrinsic

viscoelasticity of the material) mechanisms. The material parameters and their respective values for this BPVE material are shown in Table 3.1, note that Poisson's ratio was considered negligible since lateral stresses in confined compression are not considered.

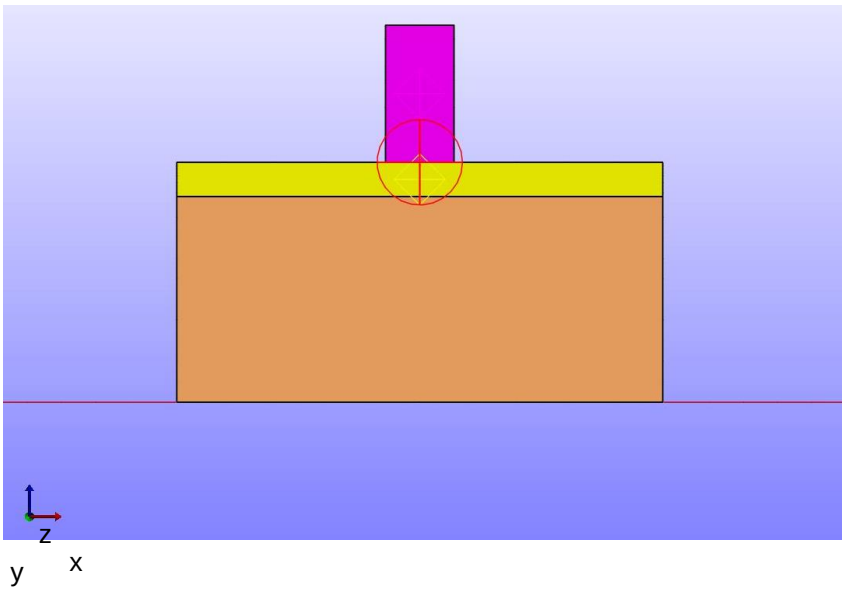


*Figure 3.2: 1D view of the confined compression model in PreView: the hydrogel sample represented in orange, and the indenter plate and handle represented in gold and purple, respectively.*

For a viscoelastic material, the stress equation (known as the second Piola Kirchhoff stress) consists of an elastic stress component ($S^e$) and a stress relaxation function (G). The elastic stress is determined from the elastic material which in this case is a compressible neo-Hookean material. The neo-Hookean constitutive equation is derived from the hyperelastic strain energy function (Equation 3.2) and is characterised by a non-linear stress-strain response which for small strains reduces to the classical linear elasticity model.

$$W = \frac{\mu}{2}(I_1 - 3) - \mu \ln J + \frac{\lambda}{2}(\ln J)^2 \qquad (3.2)$$

where $I_1$ is the 1st invariant of the right Cauchy-Green deformation tensor and J is the

Jacobian of the deformation tensor, λ and μ are Lamé parameters related to the Young's modulus and Poisson's ratio as defined by Equations (3.3) and (3.4):

$$\lambda = \frac{E}{(1+v)(1-2v)} \tag{3.3}$$

$$\mu = \frac{E}{2(1+v)} \tag{3.4}$$

The stress relaxation function (Equation 6) is defined as:

$$G(t) = 1 + \gamma \exp\left(-\frac{t}{\tau}\right) \tag{3.5}$$

where γ is the viscoelastic coefficient and τ is the relaxation time (listed in Table 3.1 as g1 and t1, respectively).

According to the biphasic theory, the stiffness in confined compression also known as the aggregate modulus, $H_A$ is related to the Young's modulus as follows:

$$H_A = \frac{E(1-v)}{(1+v)(1-2v)} \tag{3.6}$$

However, since the Poisson's ratio, $v$ is assumed to be 0, $H_A = E$.

*Table 3.1: Biphasic material parameters representing the hydrogel sample in Preview.*

| | |
|---|---|
| Solid volume fraction, φ | 0.2 |
| Fluid density (g/cm$^3$) | 1 |
| Viscoelastic coefficient g1 | 1 |
| Viscoelastic coefficient g2-g6 | 0 |
| Relaxation time, t1 (s) | 1 |
| Relaxation time, t2-t6 (s) | 0 |
| Young's Modulus, E (MPa) | 1 |
| Poisson's ratio, $v$ | 0 |
| Permeability, k (mm$^4$/Ns) | 0.001 |

**Boundary Conditions, constraints and contact interfaces:** To mimic the gel in confined compression the following boundary conditions and constraints were implemented: (1) fixed displacement at the bottom of the sample and at all nodes in the x- and y-directions thereby confining the sample laterally and at the base, (2) zero-fluid pressure at the top surface of the sample to mimic a porous and free-draining indenter, (3) a rigid constraint on the indenter to allow movement solely in the z-direction, and (4) a prescribed displacement on the indenter in the z-direction to mimic the ramp-hold compression test causing the gel to compress to 5% strain at a 0.5% ramp rate. Moreover, two types of contact interfaces were implemented: (1) a rigid joint contact between the handle and platen to ensure that the indenter acts as one body, and (2) a rigid contact between the base of the platen and the top surface of the sample to prevent the indenter from penetrating through the sample.

**Parameter optimization:** For curve-fitting analysis, the parameter optimization routine in FEBio was used to identify the unknown parameters of the model: the viscoelastic coefficient (g1), relaxation time (t1), compressive modulus ($H_A$ or E) and the hydraulic permeability (*k*), whilst obtaining the best fit between the theoretical (model) reaction force ($F_z$) experienced by the indenter during the ramp-hold compression test and the experimental load, utilising the non-linear method of least-squares (Levenberg-Marquardt algorithm).

The hydraulic permeability (*k;* units: $m^4/Ns$) describes fluid motion through a porous medium and it is best described using Darcy's Law of fluid motion:

$$q = -\frac{k}{\mu}.\frac{\Delta P}{L} \tag{3.7}$$

where, q is the flow rate (or Darcy's flux), $\mu$ is the viscosity of the perfusing fluid, $\Delta P$ is the pressure difference, and L is the length of flow direction. In soft tissue engineering, the hydraulic permeability becomes equivalent to the commonly known permeability

($\frac{k}{\mu}$; units: $m^2$) since the viscosity is usually unknown. The negative sign indicates that the fluid is moving through a pressure gradient (from high pressure to low pressure). The hydraulic permeability, *k,* is high if the fluid can flow easily through the medium and low if fluid flow is difficult.

### 3.2.2. Uniaxial tensile tests: stretch to failure

Tensile testing was performed using an Instron® ElectroPuls E10000 equipped with a 1 kN load cell and high-pressure pneumatic grips. For hydrogel testing, in order to provide firm gripping of the soft gels, a set of custom-made grip adapters comprising two mating parts (pin-hole structure) were used (see Appendix for part drawing). This adapter comprises of two mating parts (pin-hole structure) with the inner parts containing a designated space for the specimen to fit into to prevent gel damage and slippage.

The stretch to failure testing protocol involved a ramp stage at a crosshead speed of 50 mm/min in accordance with the vascular graft standard - ISO 7198 (2016) (Figure 3.3(A)). However, most aortic tissue *ex vivo* investigations implement slower strain rates, therefore a crosshead speed of 1 mm/min was also investigated. Specimen rupture beyond the gauge area was considered as a null test.

From the raw data obtained which includes load versus displacement curve, the stress response was calculated using a modified version of Equation (3.1) where instead of the surface area, the cross-sectional gauge area was considered:

$$Stress\ (kPa) = \frac{Load(N)}{Cross\text{-}sectional\ Gauge\ Area\ (m^2)} \tag{3.8}$$

where the

$$Cross\text{-}sectional\ Gauge\ Area = Specimen\ Width \times Thickness \tag{3.9}$$

The percentage strain was calculated using Equation (3.10):

$$Strain\ (\%) = \left(\frac{Displacement\ at\ time\ point - Initial\ Gauge\ Length}{Initial\ Gauge\ Length}\right) \times 100\% \quad (3.10)$$

From these calculations, a stress-strain curve was generated and from this the ultimate tensile strength and strain, considered as the stress and strain at specimen rupture were obtained. The stiffness or tensile modulus may be derived from the slope of linear section of the stress-strain curve.

### 3.2.3. Uniaxial tensile tests: stepwise stress relaxation

The relaxation tests, illustrated in Figure 3.3(B), involved an initial hold phase of 1800 s to stabilise the load followed by a four-step, incremental ramp-hold displacement protocol as outlined by Lake and Barocas (2011). During the ramp stage the specimen was stretched to 5% strain (relative to the undeformed gauge length) at a crosshead speed of 50 mm/min, whereas each interval hold phase lasted 600 s. From this, the peak and equilibrium stresses were obtained from the stress vs time curves, together with the degree of stress relaxation at each level according to Equation 3.11.

$$Degree\ of\ relaxation\ (\%) = 1 - \left(\frac{ES - ES_o}{PS - ES_o}\right) \times 100 \quad (3.11)$$

Where ES is the equilibrium stress at the end of the hold phase at each increment, $ES_o$ is the equilibrium stress of the previous hold phase, and PS is the peak stress at each increment.

### 3.2.4. Uniaxial tensile tests: dynamic oscillatory frequency sweep

The dynamic test protocol, illustrated in Figure 3.3(C), involved an initial 5 mm ramp stage at a crosshead speed of 50 mm/min followed by 20 sinusoidal displacement oscillations at an amplitude of 5% strain (relative to the specimen undeformed gauge length) at frequencies ranging from 0.25 Hz to 2.0 Hz at a frequency step of 0.25 Hz.

This lies within the typical heart rate frequency which varies from 0.66 Hz and 3.33 Hz (Amabili, Balasubramanian and Breslavsky, 2019). At each frequency step, the 18th cycle was used to calculate the dynamic stiffness with the initial cycles considered as specimen preconditioning and the latter discarded due to their proximity to the following frequency step. The strain input is described as:

$$\varepsilon = \varepsilon_o \sin(\omega t) \tag{3.12}$$

where $\varepsilon_o$ is the strain amplitude and $\omega$ the frequency, while the out-of-phase sinusoidal stress response is described as:

$$\sigma = \sigma_o \sin(\omega t + \delta) \tag{3.13}$$

where $\sigma_o$ is the stress amplitude and $\delta$ the phase lag. From this, the dynamic stiffness ($E^*$) is calculated using:

$$E^* = E' + iE'' \tag{3.14}$$

$$E' = \frac{\sigma_o}{\varepsilon_o}\cos(\delta) \tag{3.15}$$

$$E'' = \frac{\sigma_o}{\varepsilon_o}\sin(\delta) \tag{3.16}$$

Where $E'$ is the storage modulus and $E''$ is the loss modulus. The ratio of loss to storage modulus is equivalent to $\tan(\delta)$, also known as the loss factor $\eta$, which gives a measure of the material's viscous nature, with $\eta = 0$ indicating a purely elastic material and $\eta = \frac{\pi}{2}$ indicating a purely viscous material.

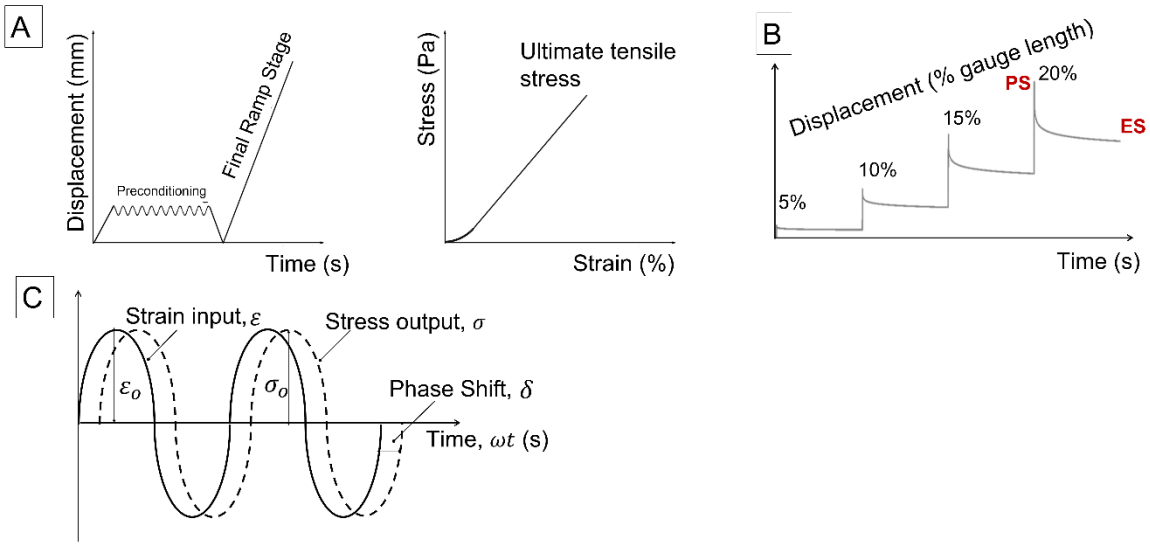


*Figure 3.3: Schematic representation of the uniaxial tensile testing protocols: (A) stretch to failure showing the input displacement (Left) and the typical stress-strain curve output (Right), (B) the stepwise stress relaxation test showing the typical stress versus time response where PS is the peak stress at each level and ES is the equilibrium stress, and (C) the dynamic oscillatory frequency test with a strain input (solid line) and a typical stress output (dotted line) showing the phase shift (δ) between the input and output response.*

### 3.2.5. Rheological measurements

Rheological measurements were performed on hydrogel disc samples (20 mm diameter, 2 mm thickness) using a rotational rheometer (NETZSCH Kinexus Pro+, Germany) fitted with parallel plate geometry (20 mm indenter diameter). To ensure contact between the indenter and the sample, a normal force of 1 N was employed. In order to determine the linear viscoelastic region (LVER) i.e., the region where stress and strain are independent of each other, amplitude sweeps were first performed at shear stresses ranging from 0.01 Pa to 500 Pa at a fixed frequency of 1 Hz. From these tests, a shear strain within the LVER (0.01%) was then selected to perform oscillatory frequency sweeps at a frequency range from 0.1 to 10 Hz. All tests were performed in replicates at room temperature.

### 3.2.6. Morphological analysis via Scanning Electron Microscopy (SEM)

Hydrogel discs prepared in 24-well tissue culture plates were freeze-dried and imaged under scanning electron microscopy (SEM, Hitachi TM 1000). For freeze-drying, the samples were first frozen at -20ºC for 24 hours followed by freeze-drying at -80ºC for another 24 hours using a benchtop freeze dryer (Labconco FreeZone ®). SEM was used to image the freeze-dried gels at the surface and at specimen cross-sections.

### 3.2.7. Swelling and degradation analysis

Water uptake was analysed in moulded hydrogel discs after freeze-drying as described in Section 3.2.6. The dried hydrogels were weighed ($m_{Dry}$), followed by immersion in calcium-supplemented PBS (1× PBS + 1.8 mM $CaCl_2$) and incubation at 37 °C. The hydrogels were weighed again at 2h, 72h, 1 week, 2 week, and 3 week timepoints to obtain the wet mass ($m_{Wet}$). The water uptake ratio was calculated using Equation 3.17.

$$Water\ uptake = (m_{Wet} - m_{Dry})/\mathrm{m}_{Dry} \tag{3.17}$$

For the degradation analysis, moulded hydrogel discs were freeze-dried, and the dry mass measured ($D_o$). The dried hydrogels were immersed in calcium-supplemented PBS (1× PBS + 1.8 mM $CaCl_2$) and incubated at 37 °C for 24 h, 72 h, 1 week, and 2 weeks. At each timepoint the gels were freeze dried again and weighed to obtain dry masses ($D_t$). The degree of degradation expressed in percentage mass loss was calculated using Equation 3.18.

$$Mass\ loss\ (\%) = [(D_o - D_t)/D_o] \times 100 \tag{3.18}$$

## 3.3. Statistical Analysis

Most of the data points for confined compression and tensile tests represent the mean and standard deviation (S.D.) for three replicates of each formulation or condition, unless otherwise stated. Two sample t-tests (unpaired and paired depending on the sample groups being investigated), and one-way *ANOVA* coupled with Tukey's post-hoc were

used to determine any statistical differences between sample groups. In all tests a statistical significance of $P < 0.05$ was accepted. All graphs were generated using OriginPro 2020 software and statistical analysis was carried out via Minitab 18 statistical software.

# Chapter 4 Mechanical characterisation of commercially available aortic graft materials

## 4.1. Introduction

As outlined in Chapter 2 (Sections 2.3 and 2.4), current surgical treatment of aortic aneurysms predominantly utilises synthetic tubular grafts composed of polyethylene terephthalate (PET) fabric, commercially known as Dacron®. Despite their off-the-shelf availability, ease of insertion during surgery, and generally good post-operative outcomes (Bustos, García-Herrera and Celentano, 2016), these grafts fall short in mimicking the compliance, mechanical properties, and anatomical geometry of the native aorta, adversely affecting cardiac cycle functionality, leading to complications such as heart strain, high blood pressure, and poor organ perfusion (Obrien, Morris and McGloughlin, 2008; Spadaccio *et al.*, 2016; Lejay *et al.*, 2019).

Despite this, the mechanical properties, especially the viscoelastic behaviour of Dacron®, have been seldom investigated. Hasegawa and Azuma (1979), Lee and Wilson (1986), and most recently Bustos *et al.,* (2016) were some of the few to perform uniaxial tensile stretch to failure tests to assess the static behaviour of Dacron® grafts. Their results confirmed significant discrepancies in the elastic properties, particularly in stiffness, between Dacron® grafts and human aortic tissue. Additionally, it was observed that the Dacron® fabric configuration (knitted versus woven), and crimping of the graft, elicit direction-dependent (anisotropic) mechanical properties. Anisotropic behaviour was also investigated by Tremblay *et al.,* (2009) via biaxial tensile testing to obtain elastic properties in both longitudinal and circumferential directions by stretching the Dacron® strips in the two perpendicular directions simultaneously. Comparison between Dacron® material and aortic tissue demonstrated that the latter exhibits a lower degree of anisotropy. Anisotropy is a key characteristic of natural blood vessels, and therefore, it

is ideal to also match the degree of anisotropy of the synthetic graft to the adjoining artery for optimal graft functionality.

In addition to static mechanical behaviour, viscoelasticity has been mostly investigated via stress relaxation tests (Hasegawa and Azuma, 1979; Michael Lee and J. Wilson, 1986; Faturechi *et al.,* 2019) where the specimen is subjected to a rapid ramp displacement and then held at that displacement allowing the material to relax over time. Moreover, given that the aorta exhibits high pulsatile pressure as blood is pumped from the heart, it is also considered to be dynamically loaded, and therefore viscoelastic behaviour analysis via dynamic testing is a better representation of physiological conditions. This gap in the literature has been recently addressed by Amabili *et al.,* who investigated the dynamic behaviour of Dacron® grafts via oscillatory frequency sweep tests on fabric strip samples and tubular conduits covering a wide range of frequencies (1 – 60 Hz) whilst measuring values for the dynamic modulus (the sum of the storage modulus, E' and loss modulus, E''), and loss factor (η) (or tan δ) (Amabili *et al.,* 2018; Ferrari *et al.,* 2019; Tubaldi *et al.,* 2019).

Therefore, prior to the design and development of an alternative viable biomaterial replacement to Dacron®, this chapter provides a comprehensive mechanical characterisation assessment of commercially available Dacron® in order to better understand the existing mechanical discrepancies between standard graft materials and native aortic tissue.

## 4.2. Aims and objectives

This aim of this chapter was to validate the existing mechanical shortcomings of Dacron® as the standard material used in state-of-the-art aortic grafts, by investigating the static, and viscoelastic (or dynamic) mechanical behaviour of Dacron® using a uniaxial tensile set-up. Samples were prepared at different orientations to the crimped configuration of the graft. Static mechanical behaviour involved stretch to failure tests to elicit properties

such as strength, stiffness, and elongation at break, and the viscoelastic behaviour was assessed via stress relaxation tests and dynamic oscillatory frequency sweeps. Given the difficulty in sourcing human aortic tissue and the associated ethical procedures, the Dacron® graft mechanical properties obtained were compared to aortic tissue data reported in the literature.

The objectives of this chapter are summarised as follows:

1. Evaluate the static mechanical behaviour via stretch to failure tests of Dacron® strips cut at different orientations to the longitudinal crimp design of the tubular graft.
2. Evaluate the stress relaxation response by stretching the Dacron® strips to a specific displacement followed by a holding phase period.
3. Evaluate the dynamic mechanical behaviour of the Dacron® strips via oscillatory frequency sweeps to elicit values such as the loss factor and dynamic modulus.

## 4.3. Materials and methods

### 4.3.1. Dacron® graft specimen preparation

Dacron® grafts were kindly provided by this project's industrial partner, Terumo Aortic (Inchinnan, UK). Two types of grafts (Terumo Aortic Gelweave™) with and without gelatine coating were investigated, hereinafter referred to as gelled and ungelled Dacron® grafts, respectively. Both grafts have a woven, axial crimp structure, and 30 mm nominal diameter (Figure 4.1(A)). Rectangular strips of dimensions approximately 10 × 45 mm were cut at different directions to the crimp, including the longitudinal (0°), circumferential (90°), and bias (45°) directions (Figure 4.1(B) and (C)). This was then followed by further cutting the strips into a dog-bone shape to facilitate rupture at the middle of the sample. It should be noted that the crimped structure was conserved as much as possible during specimen preparation to include its influence on the mechanical

response of the graft material. Prior to testing, the specimens were immersed in 1× phosphate buffered saline (PBS) for 5 minutes in accordance with the instructions for use of the Dacron® grafts (supplied by Terumo Aortic) to emulate the procedure that is typically observed before surgical implantation and for the grafts to be tested in a hydrated state. The end tabs of the dog-bone sample were glued between two cardboard strips to improve grip and prevent slipping during testing (Figure 4.1(D)). All uniaxial tensile tests were performed using the same equipment described in Chapter 3.

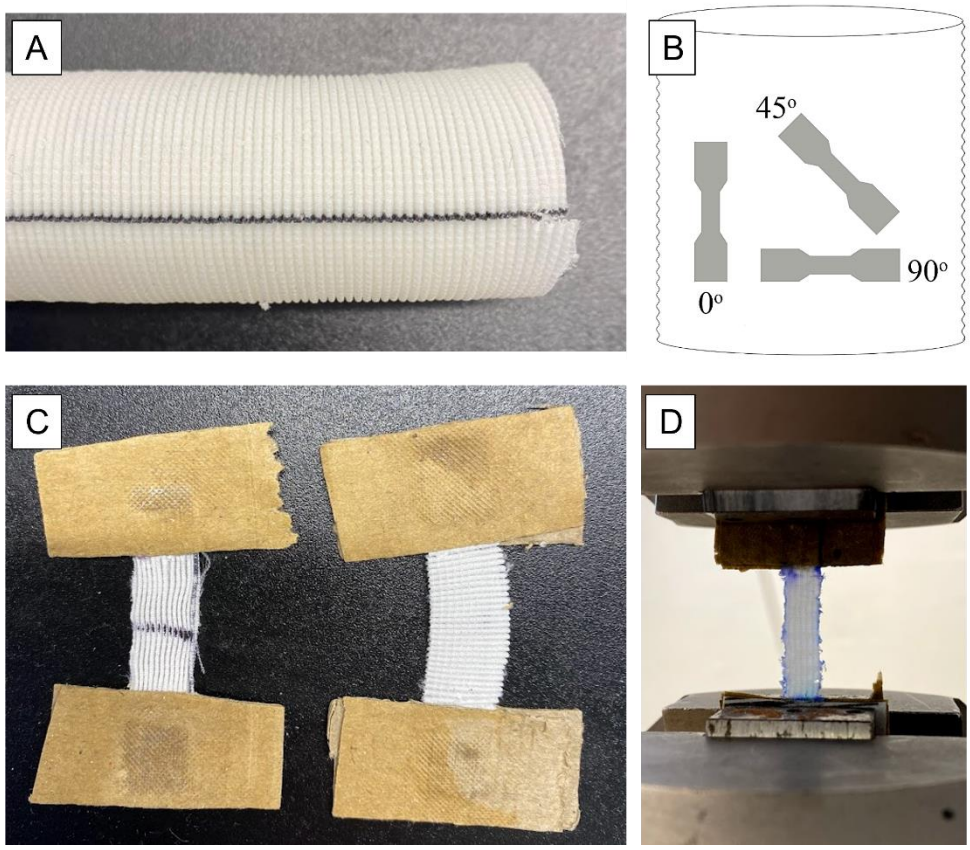


*Figure 4.1: Representative images of aortic grafts and sample preparation for uniaxial tensile testing: (A) shows a typical aortic graft and its corrugated (or crimped) structure, (B) a schematic diagram of the dog-bone samples cut at different orientations to the crimp (longitudinal, 0°; circumferential, 90°; bias, 45°), (C) strips for uniaxial tensile testing at two different orientations: circumferential to the crimp (Left) and longitudinal to the crimp (Right) with the end tabs covered in cardboard to eliminate sample slip during testing, and (D) circumferential sample during uniaxial tensile testing.*

### 4.3.2. Uniaxial tensile testing: stretch to failure, stress-relaxation, and dynamic oscillatory frequency sweep.

The stretch to failure uniaxial tensile test used to characterise Dacron® grafts was performed using the same method described in Chapter 3. A crosshead speed of 50 mm/min was employed according to the ISO standard 7198: Cardiovascular implants and extracorporeal systems — Vascular prostheses — Tubular vascular grafts and vascular patches. From the stress-strain curve, stiffness measurements such as the maximum elastic modulus (MEM) was calculated at the maximum slope prior to Dacron® graft specimen rupture and the physiological modulus (PM) at the slope corresponding to the physiological pressure range (80 mmHg -120 mmHg). The stress corresponding to the physiological pressure range was calculated using Laplace law for thin-walled cylindrical pipes:

$$\sigma_\theta = \frac{Pr}{t} \tag{4.1}$$

where $\sigma_\theta$ is the stress in the circumferential direction, *P* the physiological pressure, *r* the vessel radius, and *t* the wall thickness (Duprey *et al.,* 2010). This corresponds to a circumferential stress range of 0.13 MPa to 0.2 MPa for Dacron® grafts. Given that the stress-strain response at the physiological range is almost linear, a linear fit was implemented to obtain the slope corresponding to the elastic modulus.

The uniaxial stress relaxation and dynamic oscillatory frequency sweeps were carried out as described in Chapter 3 Sections 3.2.3 and 3.2.4.

## 4.4. Results

### 4.4.1. Uniaxial tensile tests: stretch to failure

The mechanical properties at failure for both gelled and ungelled Dacron® specimens cut at different orientations to the crimped graft structure are presented in Figure 4.2. It is clearly evident that the ultimate tensile strength (UTS) in the circumferential direction to

the crimp is significantly higher than the other two directions (Figure 4.2(A)), and vice versa for the elongation at break (Figure 4.2(B)).

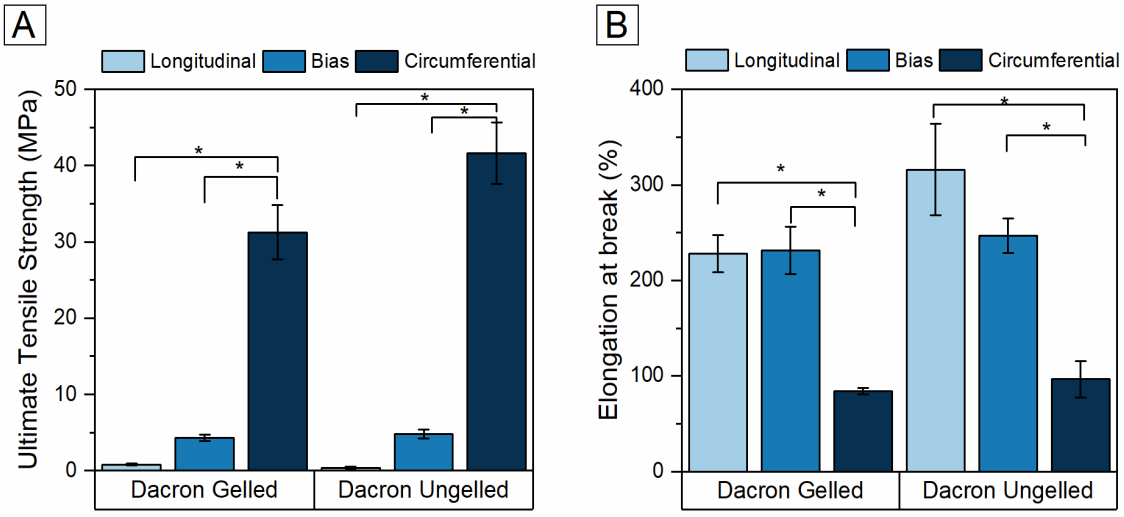


*Figure 4.2: Stretch to failure properties including (A) ultimate tensile strength (UTS) and (B) elongation at break of crimped Dacron® grafts both ungelled and gelled specimens cut at different directions to the crimp (longitudinal, bias, and circumferential) and stretched at a crosshead speed of 50 mm/min (mean ± S.D.; n=3). Asterisks (*) show a significant difference ($p < 0.05$) in the circumferential direction when compared with the other two directions for both the gelled and ungelled Dacron® grafts.*

The elastic modulus of Dacron® grafts was calculated for the specimens cut in the circumferential direction to the crimp. Figure 4.3(A) represents the typical stress-strain curve for Dacron® graft specimens and the regions used to calculate the physiological modulus (PM) and the maximum tangential elastic modulus (MEM). The PM was calculated at physiological pressures by implementing Laplace law for thin-walled cylindrical pipes (Equation 4.1 in Section 4.3.2). As shown in Figure 4.3(B), the PM for Dacron® ungelled is 9.64 ± 1.24 MPa and 9.92 ± 0.56 MPa for Dacron® gelled. The MEM was calculated from the failure region eliciting values of 43.15 ± 2.19 MPa and 36.38 ± 2.02 MPa for ungelled and gelled Dacron® grafts, respectively (Figure 4.3(B)). As expected, the MEM values are higher than the PM values as shown by the typical J-shape profile of the stress-strain curve (Figure 4.3(A)).

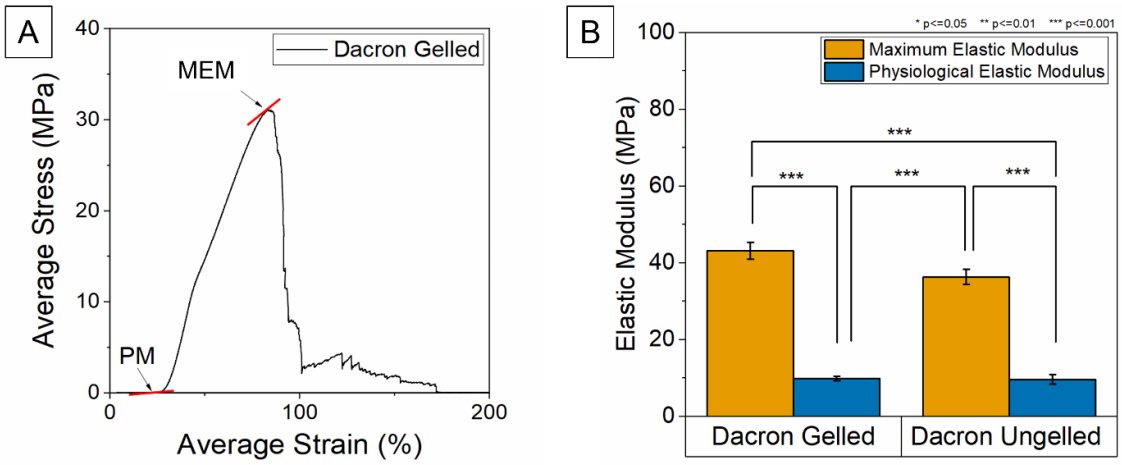


*Figure 4.3: Elastic modulus obtained from stretch to failure tests: (A) Representative stress-strain curve (mean ± S.D; n=3) of Dacron® graft specimens; arrows indicating the regions used to calculate the physiological modulus (PM) and maximum tangential elastic modulus (MEM), and (B) PM and MEM for both gelled and ungelled Dacron® samples in the circumferential direction to the crimp. Asterisks (***) show a significant difference p < 0.001.*

### 4.4.2. Uniaxial tensile tests: stress relaxation

Figure 4.4 shows the stress relaxation curves obtained at 4 levels of displacement (5%, 10%, 15%, and 20% relative to the sample's gauge length) for both Dacron® gelled and ungelled specimens at two different directions to the crimp (circumferential and longitudinal). All specimens exhibited a stress peak at the end of the ramp phase followed by a period of stress decay during the hold phase. Both the gelled and ungelled specimens in the circumferential direction exhibited similar stress relaxation response with maximum peak stresses reaching 9.63 ±1.15 MPa and 10.42 ±0.90 MPa, respectively, by the final displacement level (Figure 4.4(A) and (B)). Lower loads between the range of 6 kPa and 10 kPa were observed for the longitudinal samples which is to be expected due to the crimped structure (Figure 4.4(C) and (D)).

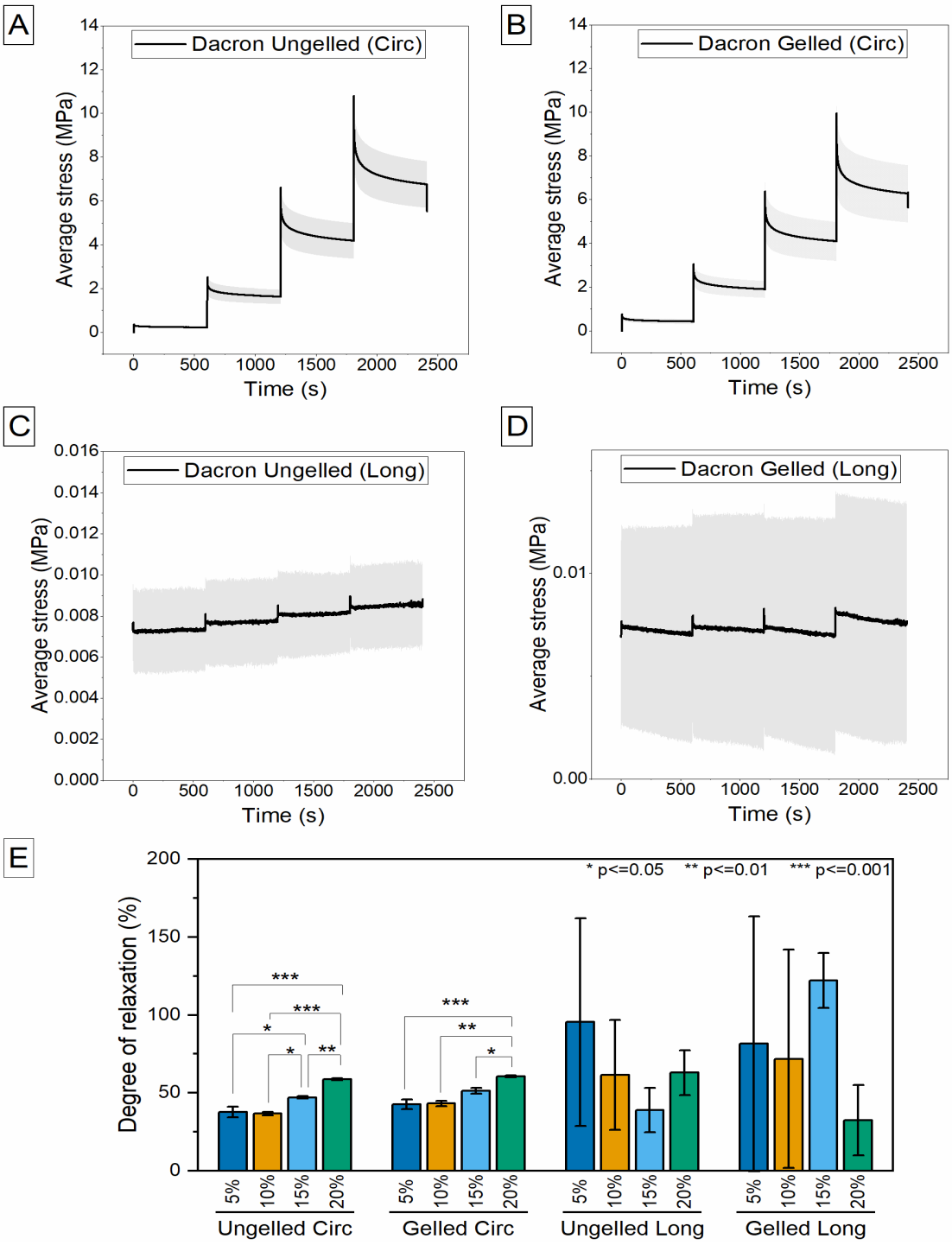


*Figure 4.4: Stress relaxation results. (A-D) stress response curves at 5% displacement increments for both (A, C) ungelled, and (B, D) gelled Dacron® graft specimens cut in the circumferential (Circ) and longitudinal (Long) directions to the crimp, and (E) the degree of relaxation calculated from the ratio of peak stress and equilibrium stress at each level of displacement (mean ±S.D.; n=3). Asterisks show a significant difference *p < 0.05, **p < 0.01, ***p < 0.001.*

### 4.4.3. Uniaxial tensile tests: dynamic measurements

The storage modulus (derived using Equation 3.6) versus loading frequency for both gelled and ungelled Dacron® graft specimens in the circumferential and longitudinal directions to the crimp are presented in Figure 4.5(A) and (C). In both directions and specimen types, dynamic testing revealed a decrease in storage modulus with increasing loading frequency. Similar to the stretch to failure test results, the crimped structure resulted in significantly lower storage modulus than the circumferential direction. The corresponding loss factor (or tan delta) values, calculated from the ratio of E'' and E', are presented in Figure 4.5(B) and (D) for the circumferential and longitudinal directions to the crimp, respectively. At specific frequencies, mostly up to 1 Hz, the loss factor is greater in the circumferential direction than the longitudinal direction.

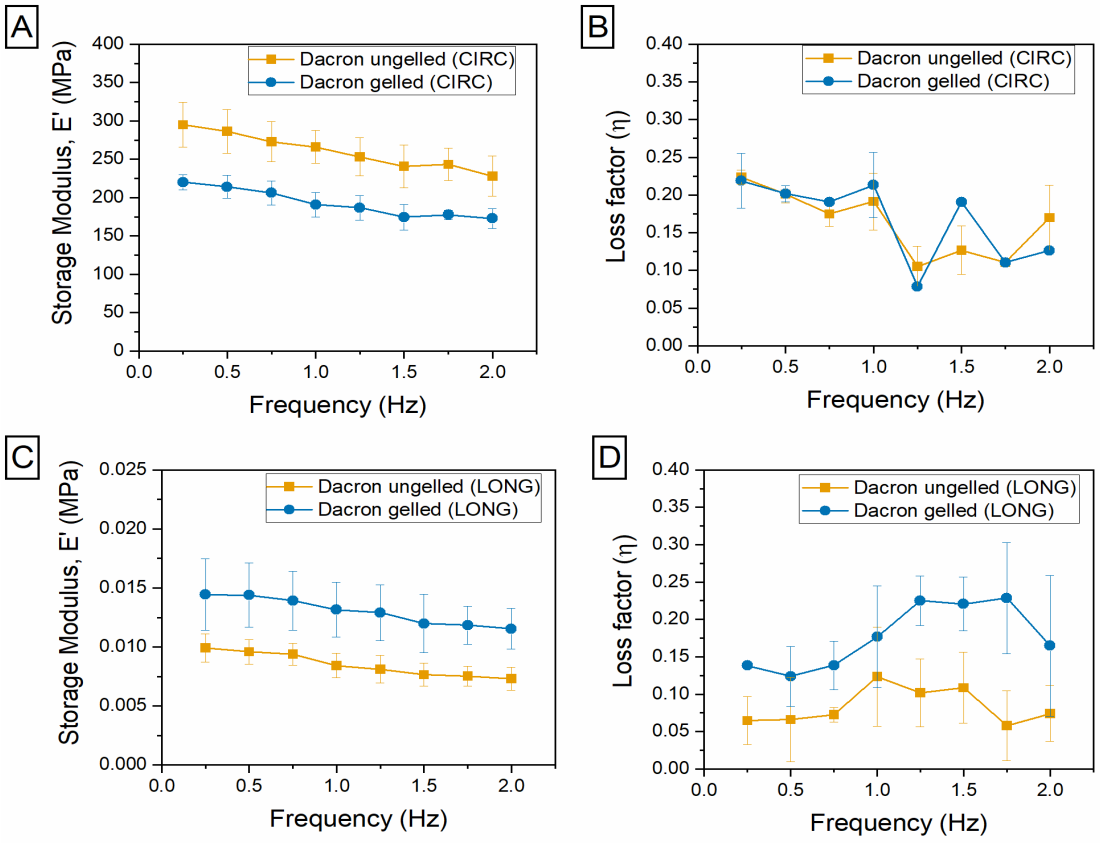


*Figure 4.5: Storage modulus (E') and loss factor (η) versus loading frequency (0.25 to 2.0 Hz) of Dacron® ungelled and gelled strips cut in the (A,B) circumferential (CIRC) and (C,D) longitudinal (LONG) directions to the crimp, respectively (mean ± S.D; n=3).*

## 4.5. Discussion

A uniaxial tensile setup was used to measure different properties of the widely utilised Dacron® vascular graft material. Vascular grafts are generally axially crimped in order to provide the implant flexibility, thereby facilitating insertion during surgery and kink resistance *in vivo.* To assess the crimping influence on the mechanical behaviour of vascular grafts, tensile measurements were performed on strips cut at various orientations to the crimp: longitudinal (along the crimp direction), circumferential (perpendicular to the crimp), and bias (at a 45-degree angle to the crimp).

Stretch to failure measurements were conducted to elicit static elastic properties. From Figure 4.2 it is evident that crimping in the longitudinal direction provides elongation to the graft, with elongation at break reaching values of 228.24 ±19.42% and 316.01 ±48.05% for gelled and ungelled Dacron® strips, respectively. The elongation in the other directions is significantly less, with the circumferential direction exhibiting the lowest elongation at break for both the ungelled and gelled Dacron® strips. This is because circumferentially the sample is stretched against the crimp direction limiting its ability to stretch (Figure 4.1(E)). Lower elongation corresponds to significantly higher strength values; 31.23 ±3.57 MPa and 41.65 ±4.02 MPa for the gelled and ungelled samples, respectively, showing great resistance to material rupture provided by the woven PET fibres. It is important to note that the circumferential direction to the crimp corresponds to the direction that the aorta expands to accommodate pulsatile flow. From these measurements, a degree of anisotropy could be observed; however, this is mostly due to the crimped structure of the graft material. Therefore, it would be interesting to investigate in future work whether the graft material would still exhibit a degree of anisotropy without the crimping effect, given that the crimped structure tends to lose its shape (flattens out) when implanted *in vivo*, and whether this would agree with previous

studies that have reported anisotropy originating from the fabric orientation of the Dacron graft material (Michael Lee and J. Wilson, 1986; Tremblay *et al.*, 2009)

The elastic modulus of the Dacron® material in the circumferential direction was also calculated from the slope of the stress-strain curve at the point of failure (MTM; Figure 4.3(B)). Despite offering an insight on graft endurance, rupture properties correspond to supraphysiological pressures. Therefore, in addition to this, the physiological modulus (PM) was measured at a range of circumferential stresses corresponding to physiological blood pressures (80 mmHg and 120 mmHg) derived using Laplace law for thin-walled pipes. It is important to note that this was employed by assuming that the vessel is a long, straight tubular structure with closed ends (Michael Lee and J. Wilson, 1986), which differs from realistic conditions. This resulted in PM (9.64 ±1.24 MPa and 9.92 ±0.56 MPa) around four times less than the MTM (43.15 ±2.19 MPa and 36.38 ±2.02 MPa) for both gelled and ungelled Dacron® strips. The significant difference between the MTM and PM is attributed to the non-linear stress-strain response, with an increase in stiffness observed as the material is stretched. Similar results were obtained by Lee and Wilson (1986), with PM values of 12 MPa (at 100 mmHg) for woven and knitted Dacron® in the circumferential direction to the crimp. Bustos *et al*. (2016) also assessed the failure properties of Dacron® grafts at different orientations to the crimp, similar to the work carried out here. When comparing the results of this present study to Bustos *et al*. (2016), the UTS in the circumferential direction differed considerably (31.23 ±3.57 MPa versus 74 MPa), but the impact of crimp orientation was essentially the same with the circumferential direction exhibiting greater UTS and less elongation than the other two orientations (longitudinal and bias). Therefore, a direct comparison of the results obtained in the present study with Bustos *et al*. (2016) was difficult to achieve primarily due to several differences in testing parameters between the two studies, including a slower strain rate, smaller specimen size, and different environmental

conditions, which influence the resulting mechanical properties. Nevertheless, as outlined in the literature review (Section 2.5.1 Table 2.1), the stiffness of aortic tissue measured via uniaxial tensile tests is approximately ten times less than the PM of Dacron® grafts, and it is this discrepancy that contributes to compliance mismatch. The introduction of a highly rigid tubular conduit as an aortic substitute that is unable to distend in a similar manner to the native artery has been linked with haemodynamic disruptions, and thus poor cardiovascular function including high blood pressure, heart strain, and reduced organ perfusion, leading to several long-term complications for the patient, such as the need for re-interventions due to graft failure (Spadaccio *et al.*, 2016; Lejay *et al.*, 2019).

In addition to the crimping effect, the impact of the gelatine sealant on the mechanical properties of vascular grafts was also investigated. Coating of vascular grafts via collagen, gelatine, or albumin impregnation was introduced as a sealant technology to reduce porosity and prevent post-operative blood loss (Chakfé *et al.,* 1999). As shown in Figure 4.2 and Figure 4.3 , the gelatine coating resulted in a significantly lower UTS in the circumferential direction (31.23 ±3.57 MPa versus 41.65 ± 4.02 MPa) yet a higher MTM and PM (36.38 ± 2.02 MPa and 9.64 ± 1.24 MPa versus 43.15 ± 2.19 MPa and 9.92 ± 0.56 MPa) than uncoated Dacron® strips. The increase in stiffness observed in the coated samples might be attributed to the drying of gelatine coating. This is because the samples were first immersed in PBS for 5 minutes prior to testing according to the instructions for use of Gelweave™ grafts, however the test itself was performed in air and not in an aqueous environment. Therefore, it is hypothesised that the soaking procedure might have rinsed out some of the glycerol (plasticiser) present in the gelatine coating, and the duration of sample loading between grips followed by the stretch to failure test might have led to the onset of drying resulting in a stiffer response than the uncoated samples. Thus, for future evaluations it would be ideal to test the gelatine-

coated Dacron® graft material in a hydrated environment, possibly submerged in DI water or PBS, to further mimic *in vivo* conditions and prevent the drying-out process.

Apart from the static tensile response, the time dependent properties of the graft material were also investigated via stress relaxation and dynamic oscillatory tests following similar protocols to Amabili *et al.,* (2018), with the exception that in the work reported here the stress relaxation tests involved incremental step displacements (5%, 10%, 15%, and 20%) as opposed to one level of displacement. However, when considering solely the 5% displacement level which is closest to the displacement used in Amabili *et al.,* (2018) (3%), similar peak stress values of gelled Dacron® grafts in the circumferential direction to the crimp were obtained when comparing both studies (0.73 ±0.07 MPa (Figure 4.4(B)) versus approximately 0.7 MPa). A direct comparison with the longitudinal strips could not be realised since in Amabili *et al.,* (2018) these samples were given a preload to eliminate the crimping effect. As shown in the stress response curve for longitudinal Dacron® strips where the crimping effect is dominant, the stress is much lower than the circumferential direction and contributed to less repeatable results as indicated by the larger error bars (shaded areas). Additionally, given that these tests were performed on a uniaxial tensile testing machine equipped with a 1 kN load cell, low load responses resulted in noisy data (Figure 4.4(C) and (D)). The degree of relaxation was quantified by considering the ratio of peak stress (i.e., the maximum stress at the end of each ramp) to equilibrium stress (i.e., the stress at the end of the hold phase). As shown in Figure 4.4(E), this increases with the level of displacement for the circumferential strips suggesting that higher strains resulted in faster relaxation. In contrast, varying responses were observed for the longitudinal strips with no significant differences observed at the different levels of displacement. Additionally, gelatine impregnation did not significantly impact the degree of relaxation in both directions to the crimp.

Given that the aorta is subjected to high pulsatile flow and pressures, any suitable aortic substitute must also be dynamically compatible. To investigate the dynamic response of Dacron® as a graft material, a frequency range from 0.25 Hz to 2 Hz was considered; primarily to include the frequency of a typical heart rate ranging from 60 to 100 beats per minute which is equivalent to a frequency range between 1.0 Hz and 1.7 Hz. Additionally, most pulsatile components at physiological conditions experience a frequency ranging from 0 Hz to 15 Hz (Dobrin, 1978). Dobrin (1978) reported that throughout this frequency range (0 Hz to 15 Hz) the dynamic elastic properties of arterial tissue in the circumferential direction often involve a dynamic modulus (E*) that: (1) increases with frequency up to 2 Hz and then remains unchanged as the frequency increases, and (2) has a magnitude of 1.5 to 2 times greater than the static modulus. From Figure 4.5 it is evident that the storage modulus, which indicates the elastic component of the dynamic modulus (Equation 3.14), is more than double the static elastic moduli (MEM and PM) presented in Figure 4.3, suggesting also that stiffness increases under dynamic conditions. A similar observation was made by Amabili *et al*., (2018), however E' was found to increase with frequency as opposed to that observed in the present work (Figure 4.5). This discrepancy might be attributed to: (1) the difference in range of loading frequencies investigated (1 Hz to 60 Hz), (2) the pre-strain employed to the grafts prior to dynamic testing, and (3) the oscillatory amplitude used (0.3% versus 5% strain used in this study). The range of E' for the circumferential strips obtained in this study lies within the range of 175 MPa to 300 MPa, which corresponds mostly to the range obtained in Amabili *et al.,* 2018 (150 MPa to 300 MPa). When performing a similar investigation of descending thoracic aorta trips, Amabili *et al.,* (2019) observed a much lower range of E' from 1.5 MPa to 3.0 MPa. The difference in E' between Dacron® and aortic tissue is significant indicating that mechanical property mismatch is not present solely in the static domain but also dynamically. Based on this, for optimal functionality, it is imperative that

novel aortic grafts are able to mimic the behaviour of the human aorta both in the static and dynamic (or elastic and viscoelastic) domain.

## 4.6. Conclusions

The aim of this chapter was to investigate the mechanical properties of the state-of-the-art Dacron® graft material in aortic surgical repair. Evaluating the mechanical behaviour is crucial in understanding the existing discrepancies between the graft material and human aortic tissue. Despite synthetic graft materials being well-renowned for their inability to mimic the mechanical properties of native aortic tissue, mechanical characterisation investigations comparing the two remain scarce in the literature.

Therefore, this work investigated the mechanical properties of Dacron® material via uniaxial tensile testing under static and dynamic conditions to elicit elastic and viscoelastic responses. Herein, particular attention was given to the effect of the axial crimp and the gelatine coating on the mechanical properties of the graft material. The crimped structure was found to provide flexibility to the graft in the longitudinal direction as indicated by the increase in elongation along the crimp. Given that testing was not performed in physiological environments (e.g., at 37°C in a physiologically aqueous solution), the gelatine coating was found to increase the elastic modulus (MTM and PM) in the circumferential direction to the crimp when compared with the ungelled graft material. Overall, similar results to other investigations were obtained where the mechanical properties in the circumferential direction are much higher than (1) the longitudinal direction, and (2) aortic tissue in the same direction. The dynamic modulus was also found to be drastically higher than the static modulus emphasising the importance of evaluating the mechanical response beyond the static domain especially when the graft is to be implanted in a highly pressurised region such as the aorta.

The results obtained in this study confirm that Dacron® does not mechanically match the human aorta. Therefore, alternative synthetic graft material substitutes are required, particularly designed to better mimic the biomechanical behaviour (elastic and viscoelastic) of the native aorta as this is hypothesised to reduce long-term graft related complications for the patient.

# Chapter 5 Synthesis and characterization of physically crosslinked alginate-based hydrogels towards the fabrication of aortic grafts

## 5.1. Introduction

In the previous chapter, it was demonstrated how existing synthetic graft materials such as Dacron® do not adequately mimic the mechanical behaviour of the native aorta. Therefore, alternative aortic graft technologies that address this mismatch in mechanical properties are required. In recent years, *in vitro* vascular graft research has been focussed on exploiting biomaterials to meet most of the biological and mechanical requirements for optimal *in vivo* graft functionality. However, this has been predominantly targeted at developing small diameter tubular constructs for vessels less than 6 mm in diameter, with little attention to larger-diameter grafts used in aortic surgical repair. In this chapter, focus will be on identifying a suitable material that is biocompatible and closely mimics the mechanical behaviour of aortic tissue.

Hydrogels have been widely investigated for the development of artificial blood vessel substitutes, particularly due to their high-water content, biocompatibility, and ease of fabrication and mechanical property tunability (Chapter 2: Section 2.6.2). The recent emergence of 3D-printing and the utilisation of hydrogels in the fabrication of tubular structures (Holland *et al.,* 2018) that could potentially act as blood vessel substitutes provide a promising approach towards developing patient-specific grafts that mimic the biomechanical behaviour of arterial tissue. However, for this approach to be realised, it is essential to first identify a suitable monomer, and obtain a fine balance between the target mechanical properties and the printability of the material.

Alginate, a natural anionic polysaccharide derived from the cell walls of brown algae (Lee and Mooney, 2012), has been widely used in the field of tissue engineering owing to its similarity to the extracellular matrix (ECM) of natural tissue, and various gel crosslinking

modalities that lead to controllable mechanical properties (Lee and Mooney, 2012; Piras and Smith, 2020). Structurally, alginate is a copolymer comprising of two types of uronic acid monomers: 1,4-linked β-D-mannuronic (M) and α-L-guluronic (G) arranged either as consecutive (GGGG or MMMM) or alternating block sequences (GMGM) as illustrated in Figure 5.1(A) (Lee and Mooney, 2012) – a structure that is highly similar to the glycosaminoglycans present in the ECM of native tissue (Gungor-Ozkerim *et al.,* 2018). In the presence of divalent cations, alginate rapidly transforms into a physically (or ionically) crosslinked 3D polymeric network, through the substitution of sodium ions present in the G blocks with the divalent cations present in the crosslinker. The G block of one polymer chain then forms a junction with the G block of adjacent chains – a mechanism best described via the 'egg-box' model, shown in Figure 5.1(B), forming a 3D hydrogel network.

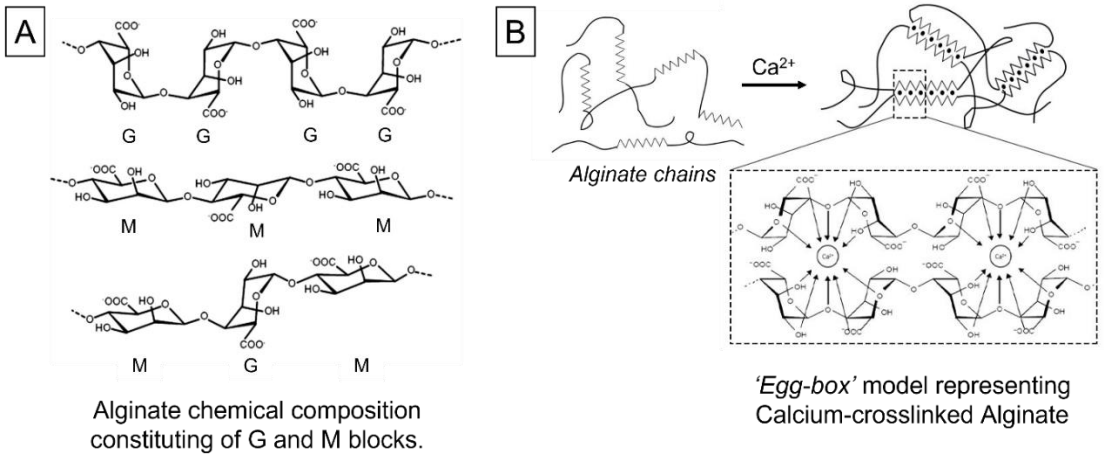


*Figure 5.1: Schematic illustrating (A) the chemical composition of alginate containing G and M blocks (Lee and Mooney, 2012) (reproduced with permission from Elsevier Ltd.), and (B) the ionic crosslinking mechanism of alginate hydrogels via calcium ions explained using the 'egg-box' model (Andersen, Auk-Emblem and Dornish, 2015).*

The ease of crosslinking and stability of ionically crosslinked alginate depend on the affinity (or ion binding) of the divalent cations to alginate which for G-blocks it has been shown to decrease in the following manner: Pb > Cu > Cd > Ba > Sr > Ca > Co, Ni, Zn > Mn, meaning that $Pb^{2+}$ ions exhibit the most

preferential binding to alginate while $Mn^{2+}$ ions exhibit the least (Haug *et al.*, 1970; Mørch *et al.*, 2006). Additionally, Mørch *et al*., 2006 demonstrated that this binding affinity is dependent on the sequences that make up the alginate monomer (i.e., GGGG, MMMM, and GMGM), for example $Ba^{2+}$ was found to bind to both G- and M- blocks, $Ca^{2+}$ binds more preferentially to G- and MG-blocks and $Sr^{2+}$ binds solely to G-blocks. This preferential binding may be attributed to variations in ionic radius and charge of the metal ions.

Typically, alginate is crosslinked via calcium ions using calcium chloride ($CaCl_2$) as the crosslinking agent. $CaCl_2$ is considered as an instantaneous gelling agent where the gelation mechanism is diffusion-based, hence the alginate immediately gels upon exposure to the crosslinker, initially creating an outer gelled skin around the volume of liquid alginate followed by the solidification of the inner volume through further diffusion (Nunamaker, Otto and Kipke, 2011). This rapid gelling behaviour restricts the crosslinker from being thoroughly mixed with the alginate solution resulting in an inhomogeneous distribution of crosslinks and gel-shape variabilities, which might adversely affect the mechanical properties of the gel (Nunamaker, Otto and Kipke, 2011). To overcome the limitations associated with $CaCl_2$, calcium carbonate ($CaCO_3$) or calcium sulphate ($CaSO_4$) may be used instead, which utilise an internal gelling mechanism (Nunamaker, Otto and Kipke, 2011; Freeman and Kelly, 2017; Kuo and Ma, 2001). $CaCO_3$ has low solubility in aqueous solutions, therefore the addition of a catalyst such as gluconic acid δ-lactone (GDL) is required to activate the release of calcium ions through the acidification of the alginate:$CaCO_3$ solution. This is a slow gelling method since it depends on the process of GDL hydrolysis and the consequent release of calcium ions, therefore allowing the alginate and crosslinker to be mixed together and poured into moulds prior to gelling (Kuo and Ma, 2001; Kuo and Ma, 2008; Growney Kalaf *et al.,* 2016). The calcium ions are released into the alginate solution in a controlled manner

resulting in uniform gel structures (Andersen, Auk-Emblem and Dornish, 2015; Growney Kalaf *et al.,* 2016).

One major limitation of calcium crosslinked alginate is the susceptibility of the alginate gel to lose its stability in physiological solutions due to the exchange and release of calcium ions with chelating agents (phosphates), monovalent ions (sodium or potassium) and non-crosslinking agents (magnesium) (Mørch *et al.,* 2006; Kuo and Ma, 2008). In order to overcome this limitation, various studies have investigated the effect of alginate crosslinking via other divalent cations, namely barium (Bajpai and Sharma, 2004; Sarker *et al.,* 2018; Mørch *et al.,* 2006), strontium (Sarker *et al.,* 2018; Mørch *et al.,* 2006; Place *et al.,* 2011) and zinc (Place *et al.,* 2011; Sarker *et al.,* 2018). Strontium and zinc have been specifically investigated for bone tissue engineering as the former tends to promote osteoblast activity while the latter is essential for alkaline phosphate production – an important enzyme for bone mineralisation (Place *et al.,* 2011). Barium has been mostly investigated as an alginate crosslinker for the fabrication of microbeads in drug delivery and cell encapsulation applications (Bajpai and Sharma, 2004; Mørch *et al.,* 2006; Mørch *et al.,* 2012) and as a secondary crosslinker in the development of tubular structures aimed at mimicking blood vessels (Ghanizadeh Tabriz *et al.,* 2015; Antunes *et al.,* 2021). In theory, barium crosslinked alginate should have superior mechanical properties than calcium crosslinked alginate since barium has a higher affinity to alginate (Mørch *et al.*, 2006; Jejurikar *et al.*, 2011). Yet, as previously noted, this affinity depends on the type of alginate being investigated, whether this is rich in M-blocks or G-blocks. In this chapter the differences, if any, in the mechanical properties of a readily available, inexpensive, high-M alginate (M/G ratio of 1.56) crosslinked with calcium (for both instantaneous and slow gelling agents) or barium were investigated via confined compression in order to determine which crosslinker is the most suitable for further investigations.

Moreover, although alginate is commonly used in tissue engineering applications, further modifications to its formulation are typically implemented due to its weak mechanical properties (Sun and Tan, 2013; Pereira and Bártolo, 2015; Yeh *et al.*, 2017; Wei *et al.*, 2023). Several investigations demonstrate changes in mechanical properties via the physical addition of secondary monomers creating a hydrogel blend (Annabi *et al.*, 2014; Wei *et al.*, 2023). Additionally, this strategy has also been exploited to promote cellular interactions in alginate hydrogels, since alginate's innate structure lacks mammalian cell recognition (Lee and Mooney, 2012). Monomers derived from tissue, such as collagen (Baniasadi and Minary-Jolandan, 2015), gelatine (Giuseppe *et al.*, 2018), and elastin (Silva *et al.,* 2018), promote cell adhesion through their inherent cell binding sites, and therefore have been widely explored in creating alginate hydrogel blends. To the author's knowledge, the use of alginate-based hydrogel blends for the generation of large-diameter blood vessels, such as the aorta, have not yet been investigated. Therefore, in this chapter, the mechanical properties of ionically crosslinked alginate hydrogels and alginate hydrogel blends (gelatine and elastin) were investigated to assess whether these hydrogels are sufficient to mimic the mechanical behaviour of the human aorta.

## 5.2. Aims and objectives

The aim of the study detailed in this chapter was to investigate the mechanical properties of physically crosslinked alginate-based hydrogels in comparison to the target properties of human aortic tissue, thereby allowing assessment of its potential as a material for the production of alternative aortic grafts.

The objectives of this chapter included the investigation of:

1. The mechanical properties of physically crosslinked alginate using different crosslinking agents ($CaCl_2$, $CaCO_3$, $CaSO_4$, and $BaCl_2$) at different concentrations of alginate (4% and 5 %(w/v)) and crosslinker molarities

(100, 200, and 300 mM), via confined compression. From this, a single hydrogel formulation was identified and taken forward for further investigation.

2. A 3-week incubation period to assess the mechanical and physical (degradation and/or swelling) properties of physically crosslinked alginate using different crosslinking agents at physiologically relevant conditions.
3. The tensile behaviour of physically crosslinked alginate-based hydrogels through stretch to failure tests, stress relaxation, and dynamic oscillatory measurements.
4. The effect of gelatine (2 %(w/v)) and elastin addition (0.5 %(w/v)) on the mechanical properties (compressive and/or tensile) of physically crosslinked alginate hydrogel.
5. Comparison of physically crosslinked alginate hydrogels with aortic tissue data obtained from the literature, to determine whether the selected hydrogel formulation is a suitable aortic graft material substitute or if it requires further modifications.

## 5.3. Materials and Methods

Briefly, sodium alginate was crosslinked using different crosslinking agents at different concentrations (Section 3.1.2) forming disc-shaped hydrogels in 24-well tissue culture plates. The gels were physically characterised by assessing mass and volume variations over a 21-day incubation period in calcium-supplemented phosphate buffered saline (1×PBS + 1.8 mM $CaCl_2$) at 37 °C. Mechanical characterisation was performed via confined compression after a 24 h gelation period and throughout the 21-day incubation period (Section 3.2.1). The alginate:crosslinker showing the highest compressive properties was then taken forward for tensile testing (Section 3.2.2). This required the gels to be prepared in dog-bone shaped structures according to the Standard Guide for Characterisation of Hydrogels used in Regenerative Medicine (ASTM F2900 (2011)), alongside other standards for tensile testing of polymers (ASTM D638 (2014) and ISO

37 (2017)), to ensure that specimen failure occurs mid-length of the specimen rather than at the clamp-specimen junction. Hydrogel specimens were prepared in dog-bone shapes by pouring the pre-hydrogel solution into a mould designed according to *ASTM D638 – Tensile properties of plastics* Type IV with a gauge length and width of 25 mm and 6 mm, respectively (Appendix A). Tensile testing involved stretch to failure, dynamic loading, and stress relaxation tests.

The mechanical characterisation methods and statistical analysis methods are described in Chapter 3.

## 5.4. Results

### 5.4.1. Visual observations

Figure 5.2 shows 4 %(w/v) alginate hydrogels prepared in 24-well tissue culture plates comparing both methods of gelation: instantaneous ((A) $CaCl_2$ and (B) $BaCl_2$) and slow gelling ((C) $CaCO_3$ and (D) $CaSO_4$). It is evident that shape uniformity depends on the type of crosslinking agent since slow gelling agents resulted in better gel shape structures than instantaneous gelling agents.

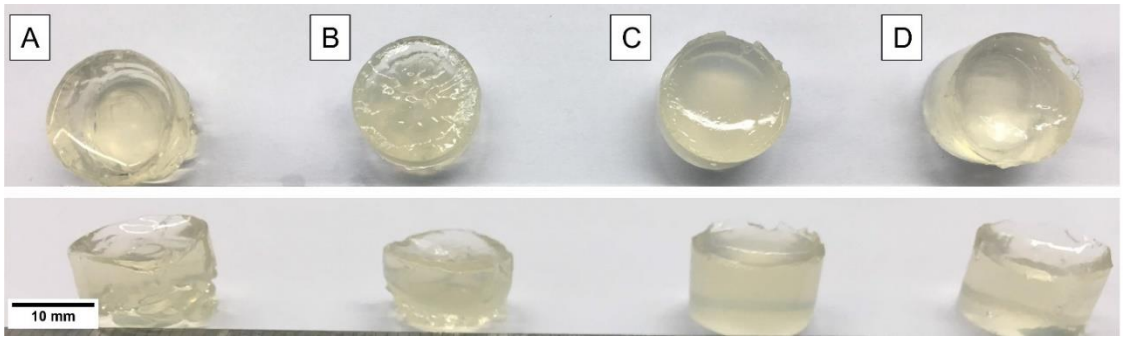


*Figure 5.2: 4% (w/v) alginate hydrogels prepared in 24-well plates for confined compression tests using different crosslinking agents at 100 mM (A)$CaCl_2$, (B) $BaCl_2$, (C) $CaCO_3$:GDL and (D) $CaSO_4$ –Top view (1st row) and Side view (2nd row).*

### 5.4.2. Confined compression measurements

Various alginate hydrogels were fabricated using two sodium alginate concentrations (4 %(w/v) and 5 %(w/v)), different crosslinking agents ($CaCl_2$, $BaCl_2$, $CaCO_3$:GDL, and $CaSO_4$) at different molar concentrations (100 mM, 200 mM, and 300 mM). The effect of these different parameters on the mechanical properties of the resulting hydrogel were investigated via compression testing in a confined set-up provided by the walls of a tissue culture well plate. The resulting stress response graphs exhibited a well-defined ramp, peak and hold phases for all samples. Figure 5.3(A) represents a typical stress versus time curve showing both the experimental response and the FEBio model curve fitting obtained as described in Chapter 3 Section 3.2.1. From the experimental curve, the peak stress can be easily determined since this is the maximum stress at the end of the ramp stage before the material begins its relaxation phase (marked in a red circle in Figure 5.3(A)). This parameter can be used to easily differentiate among various hydrogel concentrations tested in confined compression as shown in Figure 5.3(B). No significant differences were observed in samples grouped by alginate and crosslinker concentration, suggesting that the crosslinking agent type did not significantly affect the peak stress response of the alginate hydrogel. Increasing crosslinker concentration from 100 mM to 200 mM to 300 mM was also found to not significantly change the peak stress response for alginate crosslinked with different crosslinking agents. The highest peak stress was observed in 5 %(w/v) alginate: 200 mM $CaCO_3$ at 9.20 ± 0.16 kPa while the lowest peak stress was observed in 4 %(w/v) alginate: 100 mM $BaCl_2$ at 2.51 ± 0.77 kPa.

Using the confined compression model in FEBio, in combination with the parameter optimization routine, theoretical curves and suitable values for the unknown parameters, the aggregate modulus, $H_A$ (Figure 5.3(C)) and hydraulic permeability, $k$ (Figure 5.3(D)), were obtained. Similar to the peak stress results no significant differences were observed for $H_A$ and $k$ between crosslinker type, crosslinker concentration and alginate

concentration. The highest $H_A$ was observed in 5 %(w/v) alginate: 100 mM $CaCO_3$ at 73.42 ±0.77 kPa while the lowest $H_A$ was observed in 4 %(w/v) alginate: 300 mM $BaCl_2$. Herein, *k* is in the region of $10^{-10}$ $m^2$/Pa·s for all the different hydrogel formulations. The highest *k* was observed in 5 %(w/v) alginate: 300 mM $BaCl_2$ at 2.27 ±1.23 ×$10^{-10}$ $m^2$/Pa·s while the lowest *k* was observed in 5 %(w/v) alginate: 200 mM $BaCl_2$ at 0.51 ±0.07×$10^{-10}$ $m^2$/Pa·s.

`

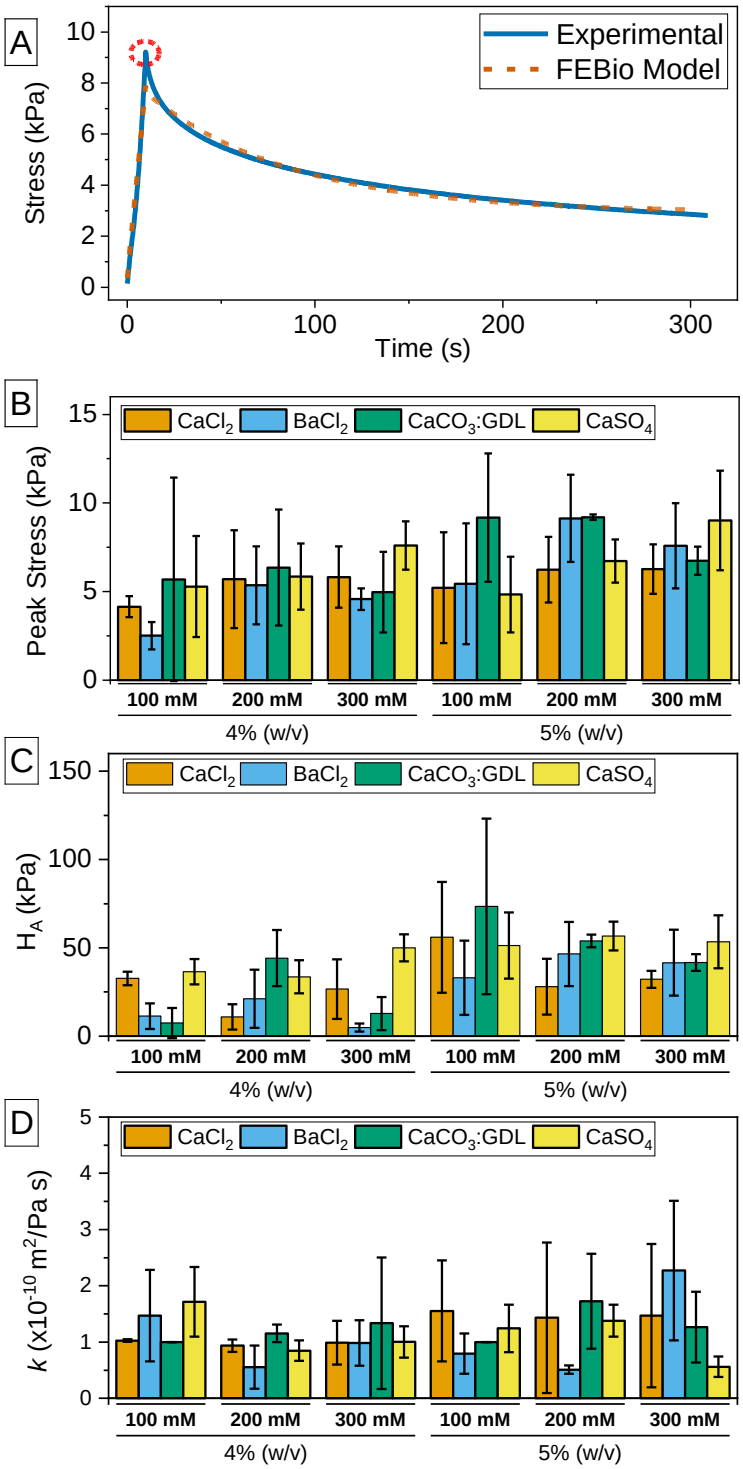


*Figure 5.3: Confined compression of alginate (4% (w/v) and 5% (w/v)) hydrogels prepared using different crosslinkers ($CaCl_2$, $BaCl_2$, $CaCO_3$:GDL, and $CaSO_4$) and concentrations (100 mM, 200 mM, 300 mM): (A) representative experimental and FEBio model stress-time curves, (B) average peak stress, (C) average aggregate modulus ($H_A$), and (D) average hydraulic permeability (k). Columns and error bars represent the mean ± S.D (n=3). No significant differences observed between any of the formulations (ANOVA, post-hoc Tukey, $p<0.05$).*

From these initial experiments, 5 %(w/v) alginate and 200 mM crosslinker concentration was taken forward for further investigations based on their high peak stress and aggregate modulus values. Alginate hydrogel discs were prepared once again using $CaCl_2$, $BaCl_2$, and $CaCO_3$:GDL for an incubation study where weight variations were analysed, and confined compression was carried out at different timepoints over a 21-day period (Figure 5.4). The gels were incubated in calcium-supplemented PBS (1×PBS + 1.8 mM $CaCl_2$) at 37°C.

Figure 5.4(A) shows the average change in mass of the three different alginate gels throughout the 21-day period. Percent mass change indicates the difference in hydrogel mass at each time point from the mass of the hydrogels prior to incubation. $CaCl_2$ gels exhibited a positive mass change indicating swelling whereas $CaCO_3$ and $BaCl_2$ exhibited a negative mass change indicating degradation. $CaCl_2$ gels swelled until day 7 (24% gain in mass), reached equilibrium between week 1 and 2, and exhibited a mass loss by week 3. No significant differences were observed between week 1, 2 and 3, however the mass at these time points were significantly different ($p < 0.05$) from the initial mass (day 0) and the mass after 24 hours. $BaCl_2$ gels exhibited significant mass loss (14%, $p < 0.05$) after 24 hours of incubation followed by significant gain in mass ($p < 0.05$) at each time point until day 21 (4%). When compared to the other two crosslinking agents, $CaCO_3$ exhibited the least percentage mass change (~5%) and no significant changes in mass from one time point to another, except for a significant mass loss between day 0 and day 21 ($p = 0.026$).

By measuring the diameter and thickness of the gels, volume variations were also noted throughout the incubation period (Figure 5.4(B)). Similar trends to the mass change in Figure 5.4(A) were observed. The volume increased steadily for the $CaCl_2$ crosslinked alginate gels and decreased for both $CaCO_3$ and $BaCl_2$ gels. The $CaCO_3$ crosslinked

alginate hydrogels exhibited minimal volume change when compared with the $BaCl_2$ gels, however at day 21 a significant decrease in volume change was observed.

Additionally, at each time point the alginate gels were subjected to confined compression and the compressive properties (peak stress, aggregate modulus, and permeability) were obtained. Figure 5.4(C) shows the variations in peak stress throughout the incubation period. $CaCl_2$ gels exhibited a decrease in peak stress until day 14, reaching a minimum of 2.83 kPa from the initial peak stress of 6.23 kPa, followed by an increase to 4.6 kPa at day 21. $BaCl_2$ gels exhibited a constant decline in peak stress until the end of the incubation period, from 9.13 kPa at day 0 to 3.58 kPa at day 21. $CaCO_3$ gels exhibited a decrease in peak stress until week 1, from 9.2 kPa to 4.03 kPa, followed by an increase in week 2 to 7.05 kPa and a decline once again in week 3 to 6.27 kPa. No significant changes were observed between time points for $CaCl_2$ and $CaCO_3$ gels, however, for $BaCl_2$ gels the peak stress at day 14 and day 21 was significantly lower ($p$> 0.05) than the peak stress at day 0.

Figure 5.4(D) shows the variations in $H_A$ throughout the 21-day incubation period. $H_A$ for both $BaCl_2$ and $CaCO_3$ gels followed the same trend as the peak stress in Figure 5.4(C), in fact both gel types exhibited a lower $H_A$ by the end of the incubation period (27.0 ±2.4 kPa and 40.5 ±2.5 kPa, respectively at day 21 as opposed to 46.5 ±10.5 kPa and 53.9±2.1 kPa, respectively at day 0) suggesting a decrease in mechanical properties due to the incubation environment. However, as can be observed in Figure 5.4(D), $H_A$ of $CaCl_2$ gels did not follow the same trend as the peak stress in Figure 5.4(C), the $H_A$ of $CaCl_2$ gel was maintained in the region of 30 kPa (day 0: 29.0 ±9.1 kPa and day 21: 30.1 ±2.6 kPa). The hydraulic permeability response is presented in Figure 5.4(E) and a downward trend is observed in $CaCO_3$ crosslinked alginate hydrogels as opposed to the upward trends exhibited by $BaCl_2$ and $CaCl_2$ crosslinked gels.

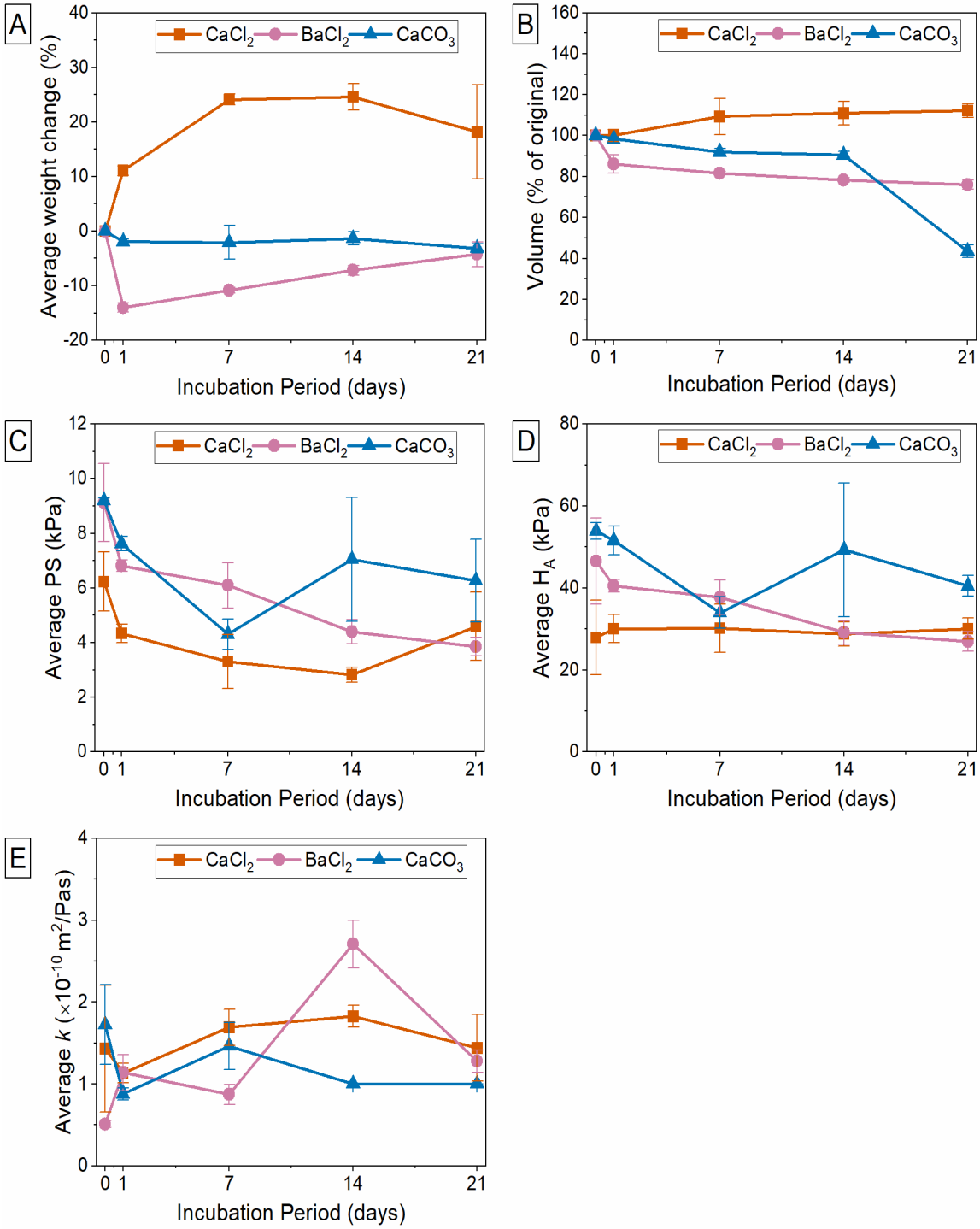


*Figure 5.4: Variations in (A) weight, (B) volume, (C) peak stress (PS), (D) aggregate modulus ($H_A$) and (E) hydraulic permeability (k) of alginate hydrogels (5% (w/v)) crosslinked using 200 mM $CaCl_2$, $BaCl_2$, or $CaCO_3$:GDL over a 21-day incubation period in calcium-supplemented PBS (1.8 mM $CaCl_2$ in 1× PBS) at 37°C. Data points represent the mean ± S.D (n=6) for the mass measurements, and the mean ± S.D (n=3) for the volume and confined compression measurements.*

The alginate solution (5 %(w/v)) when mixed with the $CaCO_3$: GDL (200 mM:400 mM) crosslinker in a 2:1 ratio, dilutes down to a final concentration of 3.3 %(w/v) alginate and 66.6 mM $CaCO_3$:133.2 mM GDL. Therefore, additional measurements were performed on lower concentrations of $CaCl_2$- and $BaCl_2$- crosslinked alginate hydrogels (3.3 %(w/v) alginate and 66 mM $CaCl_2$ and $BaCl_2$) for a direct comparison as shown in Figure 5.5. The $BaCl_2$ crosslinked hydrogels exhibited the highest peak stress, aggregate modulus, and permeability, yet no significant differences between the three crosslinker types were observed. Low variability (small error bars) was observed in $CaCO_3$:GDL crosslinked alginate hydrogels for all three mechanical properties, and this together with shape uniformity led to this hydrogel formulation being taken forward for further mechanical characterisation investigations.

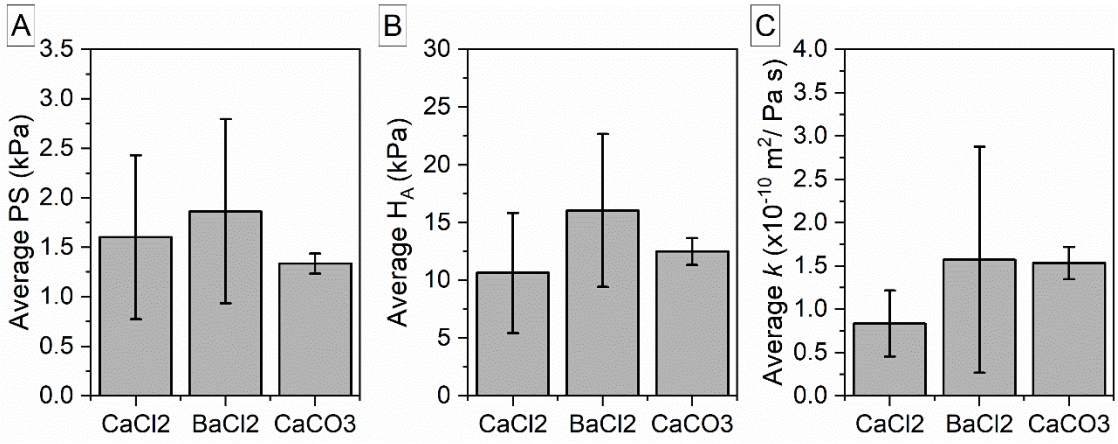


*Figure 5.5: Confined compression properties: (A) peak stress (PS), (B) aggregate modulus ($H_A$), and hydraulic permeability (k), of alginate (3% (w/v)) crosslinked with 66 mM $CaCl_2$, $BaCl_2$, and $CaCO_3$:GDL hydrogels. Columns and error bars represent the mean ± S.D (n=3).*

To investigate whether the addition of a secondary monomer that promotes cell adhesion influences the mechanical properties of alginate, gelatine and elastin were incorporated within the sodium alginate solution prior to mixing with the $CaCO_3$:GDL crosslinker. The initial concentration of gelatine and elastin was set at 2 %(w/v) and 0.5 %(w/v), respectively, in accordance with ongoing cell viability studies within the research group.

This resulted in final hydrogel formulations of 3.3 %(w/v) alginate:1.3 %(w/v) gelatine, and 3.3 %(w/v) alginate: 0.3%(w/v) elastin. The confined compression properties of these formulations are presented in Figure 5.6. No significant differences were observed among the three different formulations. The alginate:gelatine hydrogel resulted in the highest properties, although there was a high degree of sample variability within this particular formulation. The addition of elastin resulted in higher peak stress and aggregate modulus, and lower permeability than the alginate on its own, albeit not significant. Based on these results, the combination of alginate and elastin was taken forward for further characterisation.

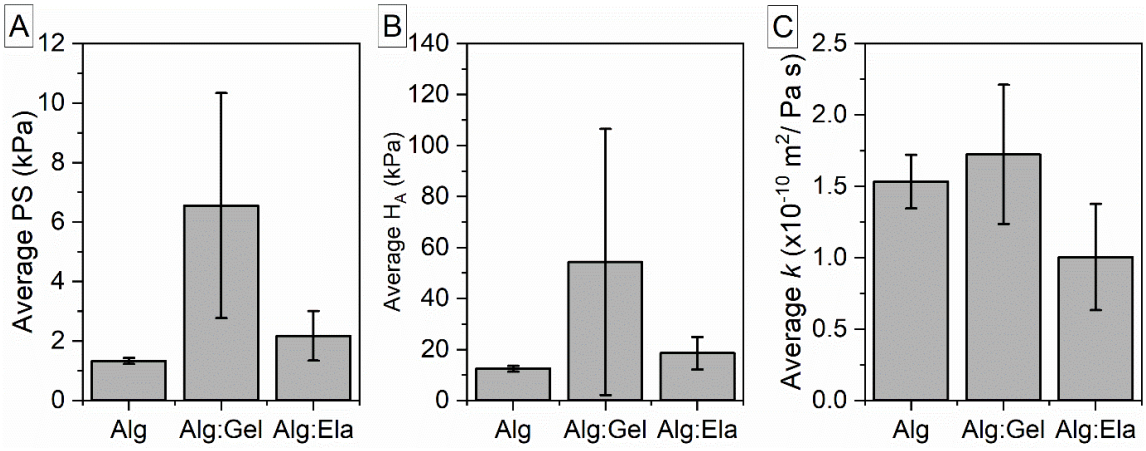


*Figure 5.6: Confined compression properties: (A) peak stress (PS), (B) aggregate modulus ($H_A$), and hydraulic permeability (k), of alginate hydrogels doped with gelatine (Alg:Gel) and elastin (Alg:Ela) in comparison with alginate alone (Alg). Columns and error bars represent the mean ± S.D (n=3).*

### 5.4.3. Uniaxial tensile tests: stretch to failure

Figure 5.7 shows the stretch to failure properties of alginate alone (3 %(w/v)) and alginate:elastin (3 %(w/v):0.3 %(w/v)) gels both crosslinked using $CaCO_3$:GDL (66mM:133.2 mM). The gels were stretched at two different crosshead speeds: 1 mm/min and 50 mm/min. The addition of elastin to alginate resulted in a significant increase in failure strain at both crosshead speeds (Figure 5.7(A)) indicating a higher degree of elongation than the alginate-alone hydrogel. An increase in strength and

stiffness between the two formulations was also observed as shown in Figure 5.7(B) and (C). However, this increase was only significant for the elastic modulus at a crosshead speed of 1 mm/min. A higher crosshead speed resulted in an increase in strength, although not significant, from alginate to alginate:elastin. A significant increase between crosshead speeds was observed in the stiffness of the alginate-alone hydrogel.

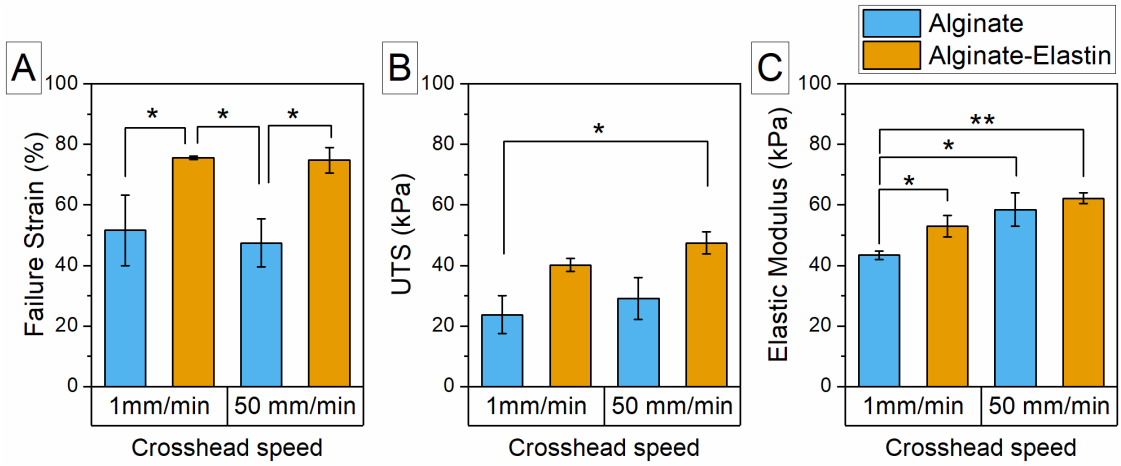


*Figure 5.7: Stretch to failure properties including (A) percentage failure strain, (B) ultimate tensile strength (UTS), and (C) elastic modulus of alginate and alginate:elastin hydrogels at two different crosshead speeds: 1 mm/min and 50 mm/min. Columns and error bars represent the mean ± S.D (n=3) and * represents $p < 0.05$ and ** $p < 0.01$.*

Given that the addition of elastin to alginate resulted in an increase in elastic properties, even although not always in a significant manner, these hydrogel formulations were investigated over a 72-hour incubation period to assess the impact of physiologically relevant conditions on the elastic properties of alginate-based hydrogels. The hydrogels were incubated in calcium-supplemented PBS (1×PBS + 1.8 mM $CaCl_2$) at 37°C. Figure 5.8 shows the stretch to failure properties of alginate and alginate:elastin at three time points (0h, 24h, and 72h). The failure strain, strength, and elastic modulus, all decreased significantly during incubation of the alginate:elastin hydrogel as shown in Figure 5.8. For the alginate-alone hydrogel a significant decrease in stiffness was observed but not in strength and elongation at break.

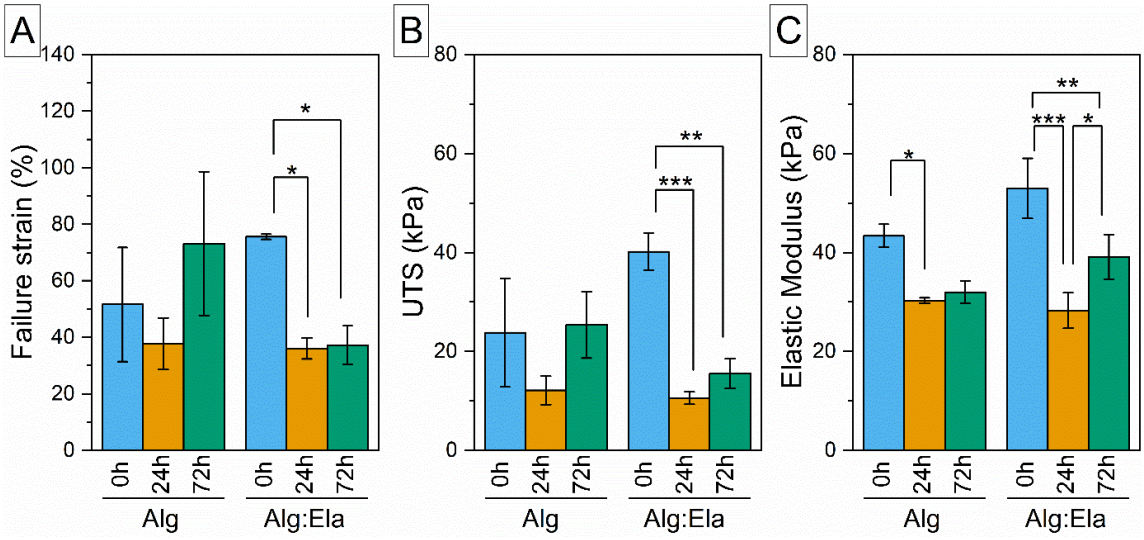


*Figure 5.8: Stretch to failure properties including (A) percentage failure strain, (B) ultimate tensile strength (UTS), and (C) elastic modulus of alginate (Alg) and alginate:elastin (Alg:Ela) hydrogels over a 72-hour incubation period. Columns and error bars represent the mean ± S.D (n=3). Statistical differences: *p < 0.05; ** p < 0.01; *** p < 0.001.*

### 5.4.4. Uniaxial tensile tests: stress relaxation

Figure 5.9(A) and (B) show the stress relaxation curves obtained at 4 levels of displacement (5%, 10%, 15%, and 20% relative to the sample's gauge length) for both alginate and alginate:elastin, respectively. At most levels of displacement, both hydrogels exhibited characteristic stress relaxation behaviour with a peak stress at the end of the ramp stage and an exponential decay in stress during the hold phase. However, a slight increase in stress at 5% displacement can be observed for the alginate:elastin hydrogel. The peak stress was observed to increase at each displacement level as shown in Figure 5.9(C). The alginate:elastin hydrogels displayed higher peak stress values yet the measurements within this sample group were highly variable (as indicated by the larger error bars in both Figure 5.9(B) and (C)). The decreasing trend in the degree of relaxation (Figure 5.9(D)) was observed in the alginate:elastin hydrogels, with the 5% level of displacement exhibiting a significantly higher degree of relaxation than the other displacement levels. Very little difference was observed in the alginate alone hydrogels for the first few levels of displacement, together

with a high degree of relaxation at the final step which was not found to be significantly higher than the other displacement levels.

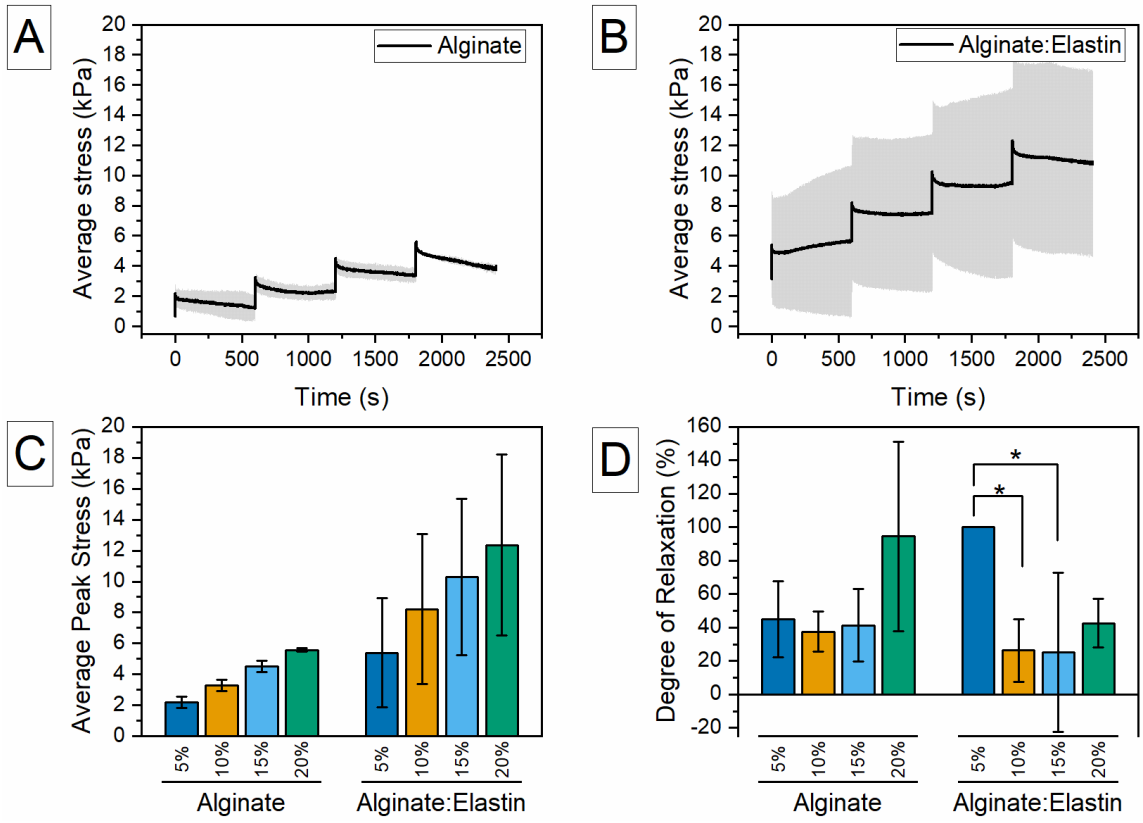


*Figure 5.9: Uniaxial tensile stress relaxation curves at 5% displacement increments for (A) alginate and (B) alginate:elastin, and (C) the average peak stress and (D) the percentage degree of stress relaxation calculated from the ratio of peak stress and equilibrium stress at each level of displacement. Data points represent the mean ± S.D. (n=3) and * implies a significant difference of $p < 0.05$ between each displacement step.*

### 5.4.5. Uniaxial tensile tests: dynamic measurements

The loss factor and storage modulus versus loading frequency are presented in Figure 5.10. The storage modulus (Figure 5.10(A)) for both the alginate alone and alginate:elastin hydrogel decreases gradually as the loading frequency increases. The corresponding loss factor (or tan delta) (Figure 5.10(B)) exhibits an overall downward trend with increasing loading frequency. The loss factor is greater than 0 at all

frequencies (except for the alginate:elastin at 1 Hz) which suggest that all materials exhibit a viscoelastic behaviour.

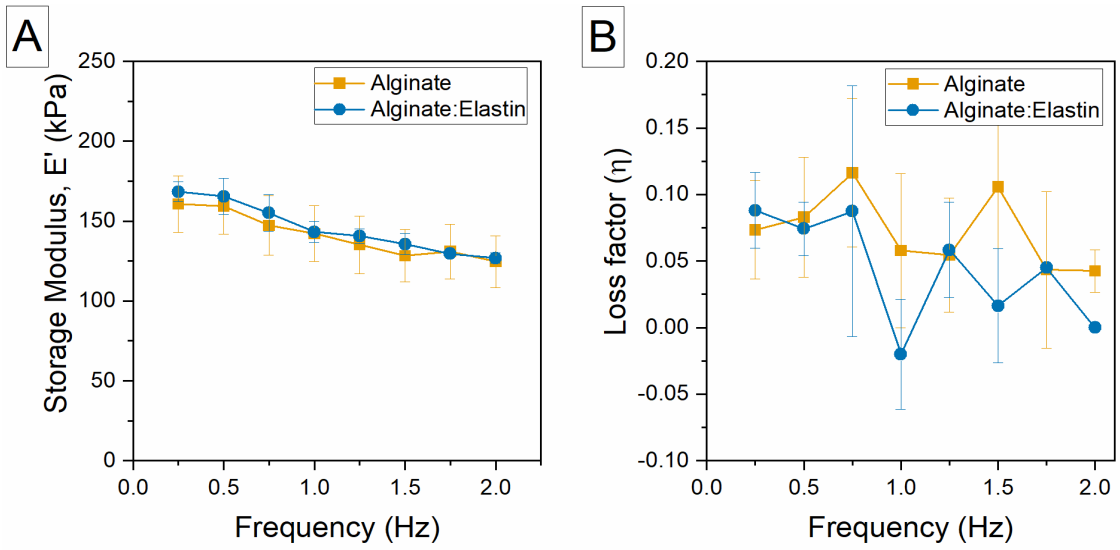


*Figure 5.10: Dynamic loading properties: (A) storage modulus (E') and (B) loss factor (or tan delta) versus loading frequency of alginate and alginate:elastin specimens. Data points represent the mean ± S.D. (n=3).*

## 5.5. Discussion

Alginate-based hydrogels have been widely explored in tissue engineering applications due to their biocompatibility and ease of gelation in the presence of divalent cations (Lee and Mooney, 2012; Cattelan *et al.*, 2020; Wei *et al.*, 2023). The principal aim of the work described in this chapter was to develop ionically crosslinked alginate hydrogels and assess their shape-forming ability and mechanical properties for the potential fabrication of tubular conduits for aortic grafts. The work presented here investigated the effect of different crosslinking agents ($CaCl_2$, $BaCl_2$, $CaCO_3$ and $CaSO_4$) at varying concentrations (100 mM, 200 mM, and 300 mM) on the compressive properties of alginate (4% and 5 %(w/v)) after a 24 h gelation period. The alginate: crosslinker formulations that showed the least variations in compressive properties and best hydrogel shape uniformity (5 %(w/v) alginate: 200 mM $CaCl_2$, $BaCl_2$, $CaCO_3$) were also assessed mechanically and physically throughout a 21-day incubation period. The

alginate: crosslinker agent and concentration (5 %(w/v) alginate: 200 mM $CaCO_3$) that showed stability during incubation was taken forward for tensile testing under static and dynamic loading.

### 5.5.1. Effect of crosslinking agent and concentration on alginate gel shape

From Figure 5.2 it is evident that the hydrogels prepared via instantaneous gelling crosslinking agents ($CaCl_2$ and $BaCl_2$) resulted in surface irregularities and did not maintain the characteristic uniform cylindrical shape of the well. In addition to this, upon increasing the crosslinking agent concentration, these hydrogels exhibited shrinkage, an effect most obvious in the 300 mM gels. To improve the hydrogel structure, the volume of crosslinking agent per well was halved. However, lowering the crosslinking volume for the 100 mM and 200 mM, resulted in poor gelation throughout the whole gel structure, most probably due to the lower number of calcium ions present in each well. Therefore, a lower crosslinker volume was only used when preparing the 300 mM gels, yet some degree of shrinkage still occurred. This phenomenon is known as syneresis whereby gels exude fluid as a result of a time dependent deswelling (Nunamaker, Otto and Kipke, 2011). Syneresis of ionically crosslinked alginate was thoroughly investigated by Nunamaker *et al.,* (2011), by observing the fluid level remaining in the moulds of gels prepared via different alginate concentrations, molecular weight, crosslinking agents and concentration ($CaCl_2$ - 50, 200, 680 mM and $CaCO_3$ – 20, 50, 100 mM). It was concluded that the syneresis level increases with an increase in $CaCl_2$ concentration since an increase in calcium concentration results in a higher crosslinking density. This is consistent with the shrinkage observed in the 300 mM $CaCl_2$ and $BaCl_2$ crosslinked hydrogels used in this study. This is also in agreement with the investigation of Growney Kalaf *et al.,* (2016), where the shrinkage of $CaCl_2$ crosslinked alginate gels was attributed to oversaturation of calcium and high density crosslinking.

Most studies have suggested the use of slow-gelling agents ($CaCO_3$ and $CaSO_4$) for better gel shape definition (Kuo and Ma, 2001; Kuo and Ma, 2008; Growney Kalaf *et al.,* 2016; Freeman and Kelly, 2017) since a homogenous structure leads to improved mechanical and physical integrity of the gel. Both $CaCO_3$ and $CaSO_4$ have low solubility in aqueous solutions, in fact, $CaCO_3$ requires the addition of a catalyst such as GDL to activate the release of calcium ions through the acidification of the alginate:$CaCO_3$ solution. This method results in uniform gel structures as it depends on the slow process of GDL hydrolysis and the consequent controlled release of calcium ions. As for $CaSO_4$, uniform gel structures can still be obtained without the addition of a catalyst, but this highly depends on thorough mixing of the crosslinker and alginate solution prior to the gelation period which still resulted in undissolved $CaSO_4$ particles. As expected, in the present study, alginate hydrogels prepared via $CaCO_3$ and $CaSO_4$ resulted in uniform cylindrical shapes with flat bottom surfaces (Figure 5.2) for all concentrations. Shrinkage of slow gelling gels was less prominent than the instantaneous gels, in fact, when investigating the syneresis level, Nunamaker *et al.,* (2011), concluded that $CaCl_2$ gels exhibit higher levels of syneresis (> 25%) than their $CaCO_3$ counterparts (< 10%).

### 5.5.2. Effect of crosslinking agent and concentration variations on the compressive properties of alginate gels.

The stress relaxation curves obtained from confined compression tests in response to a constant strain, demonstrate that physically crosslinked alginate gels exhibit a typical viscoelastic response characterised by a temporal decay in stress at a constant strain, similar to ECMs and several soft tissues including brain, skin, and arteries (Singh, Wong and Wang, 2015; Chaudhuri, 2017). On a molecular scale, once subjected to a stress or strain, ionically crosslinked alginate gels undergo a rearrangement of the 3D hydrogel network through unbinding of divalent cations (such as $Ca^{2+}$ or $Ba^{2+}$) from the anions present in the alginate chain that migrate over a molecular distance causing polymer flow

and then reattach to the alginate chains in the vicinity (Zhao *et al.,* 2010; Chaudhuri, 2017).

The confined compression stress relaxation parameters in this study comprised a displacement of 5% with respect to the original sample thickness and a strain rate of 0.5 %/s consistent with the protocol previously reported by Busby *et al.,* (2013) for the characterisation of collagen gels. For collagen gels, Busby *et al.,* (2013) concluded that the peak stress and aggregate modulus ($H_A$) increase with an increase in collagen content (0.2%, 0.3% and 0.4%). This is in line with most studies (Kuo and Ma, 2008; Chung *et al.*, 2013; Foss, Maxwell and Deng, 2014; Shi, Laude and Yeong, 2017; Giuseppe *et al.*, 2018; Sarker *et al.*, 2018) investigating the mechanical properties of ionically crosslinked alginate gels via compression testing, where the compressive properties increase with increasing alginate concentration. The confined compressive test properties obtained in the work presented here do not exhibit a significant increase with an increase in alginate and/or crosslinker concentration, however it can be concluded that concentration variation, although not significant, does have an impact on the mechanical properties of the gel (e.g., the increase in $H_A$ from 4% to 5% alginate (Figure 5.3(C)). Most gels exhibited an $H_A$ ranging between 40 and 50 kPa, depending on concentration and crosslinking agents. Similar results were obtained by Shi *et al.,* 2017 (6 – 65 kPa; increases with increasing alginate concentration from 2% to 10 %(w/v)), and Sarker *et al.,* 2018 (30 – 50 kPa; increases with increasing alginate concentration 2% to 4 %(w/v) and crosslinker concentration 50 to 150 mM). Variations in compressive properties between investigations may be attributed to the compression test performed whether it is confined or unconfined, or whether compression has been performed to a specific displacement with respect to sample thickness or until specimen failure; the hydrogel's condition whether it was tested immediately after gelation or if it

was tested in its swollen state; the type of alginate used whether it is composed of high G or high M blocks; and the crosslinker type and concentration, amongst other factors.

When comparing the confined compression results obtained in this study for instantaneous and slow gelling alginate gels, there are no indications that the latter significantly improves the compressive properties for all concentration variations. In addition to this, when comparing calcium crosslinked to barium crosslinked alginate, in theory barium crosslinked alginate is expected to yield hydrogels with superior mechanical properties than calcium crosslinked alginate. This is due to the greater affinity of barium to alginate than calcium, and its larger ionic radius (1.35 Å compared to 0.95 Å of calcium) which forms tighter crosslinks thus, stronger ionic bonds (Mørch *et al.*, 2006; Jejurikar *et al.*, 2011). However, when comparing $BaCl_2$ gels to the other crosslinking agents no significant differences were observed in mechanical properties (Figure 5.3(B)-(D)). When lowering the alginate concentration of $CaCl_2$ and $BaCl_2$ crosslinked hydrogels to 3.3 %(w/v) alginate for direct comparison with $CaCO_3$:GDL crosslinked hydrogels in Figure 5.5, an increase in compression properties was observed but this was not significant. In addition to this, the peak stress in Figure 5.3(B) exhibited lower values, although not significant, when increasing the crosslinking concentration from 200 mM to 300 mM $BaCl_2$. This might be due to the lower crosslinker volume (0.25 ml instead of 0.5 ml) used in the 300 mM concentrations, although this difference was not evident in the 300 mM $CaCl_2$. Another contributing factor might be due to the composition of the alginate used. In this study, the M to G ratio of alginate is 1.56 which suggests that the alginate has a higher M block than G block content. Mørch *et al.,* (2006) investigated the difference in gel stiffness between high G and high M block alginate crosslinked with different ions including calcium, barium, and strontium, where it was concluded that $Ba^{2+}$ ions have greater effect on the gel stiffness of high G alginate rather than high M alginate (for 1%(w/v) high G alginate crosslinked with 20 mM $BaCl_2$ the

stiffness under compression was reported to be around 30 kPa as opposed to 20 kPa for high M alginate).

Confined compression accompanied with FEBio analysis was also useful in evaluating the hydrogel's hydraulic permeability (*k*). This parameter is crucial in the design process of blood vessel substitutes; the graft's permeability describes the transport of fluid, nutrients, and oxygen through its porous structure (Whale, Grodzinsky and Johnson, 1996), it is also useful in assessing the graft's ability to prevent blood leakage (impermeable to blood), and its cell seeding efficiency and adhesion properties, amongst other factors (Rahbari *et al.,* 2017). Collagen studies such as Busby *et al.,* (2013) have shown that an increase in collagen concentration results in a decrease in permeability due to the increase in fibril density, and hence an increase in viscous drag on the fluid flow. Similarly, Gu *et al.,* (2003) reached the same conclusion when investigating agarose gels. Here, this was observed in some of the specimens when increasing the alginate concentration from 4% to 5 %(w/v) (Figure 5.3(D)) and when incorporating gelatine to alginate (Figure 5.6(C)), however the differences are not significant. The decrease in permeability due to a high monomer content correlates well with the increase in the gel's stiffness observed with higher $H_A$ values. A review of the literature revealed few studies investigating the hydraulic permeability of hydrogels, with most investigations reporting values for collagen and agarose. The permeabilities obtained in this study are within the same range of the collagen gels in Busby *et al.,* (2013) ($1\times10^{-10}$ $m^4/Ns$) but much higher than those reported by Gu *et al.,* (2003) for agarose gels ($1\times10^{-14}$ $m^4/Ns$). For porcine aortic tissue (with the endothelium removed), the permeability has been reported to be $7\times10^{-16}$ $m^4/Ns$ (Harrison and Massaro, 1976) which is orders of magnitude lower than that obtained for alginate gels in this work and the collagen and agarose gels cited here.

It should be noted that the addition of gelatine and elastin to alginate in this study was to biologically functionalise alginate and therefore add cell binding sites in the final hydrogel structure. The concentrations were in accordance with ongoing cell viability studies within the research group involving an initial concentration of gelatine and elastin in the precursor solution at 2 %(w/v) and 0.5 %(w/v), respectively. These secondary monomers were not crosslinked in any way, and this was reflected in the compressive test results (Figure 5.6), as their addition to alginate did not significantly improve the mechanical properties, contrary to other studies where the incorporation of gelatine at higher concentrations (Giuseppe *et al.*, 2018) and through various crosslinking strategies resulted in enhanced strength and stiffness of the gels.

### 5.5.3. Incubation effect on the physical and mechanical properties of ionically crosslinked alginate gels.

A major drawback of ionically crosslinked alginate gels is their lack of dimensional stability in long-term physiological conditions due to the susceptibility of the crosslinking ions to exchange with ions present in the surrounding media (Lee and Mooney, 2012). Hence, observing the behaviour of ionically crosslinked gels through an *in vitro* incubation study is critical to assess the effect of physiological conditions on both the physical and mechanical properties of the gel.

**Physical characterisation** involving hydrogel mass measurements at designated time points throughout the incubation period indicated swelling of $CaCl_2$ crosslinked alginate gels. The weight variation profile shown in Figure 5.4(A), indicates an increase in swelling until day 7 followed by a decrease from day 14 to day 21. This type of profile suggests that the gels experienced an initial (day 0 to day 7) ion-exchange involving the $Ca^{2+}$ ions bonded to the carboxyl ($-COO^-$) groups present in the alginate's M-blocks with the sodium ($Na^+$) and phosphate ($PO4^-$) ions present in the external solution (PBS) as a result of the weak electrostatic interaction between $Ca^{2+}$ ions and the M-blocks. This

results in an increase in the electrostatic repulsion between the now unbound negative $-COO^-$ groups, leading to alginate chain relaxation thereby allowing swelling to take place.

Maximum swelling at day 7 and day 14 suggest that the alginate gel attained maximum water uptake followed by gel dissolution as indicated by the decrease in swelling from day 14 to day 21. This decrease in swelling may be attributed to further ion-exchange this time involving the $Ca^{2+}$ ions bonded to the $-COO^-$ groups of the G-blocks with the $Na^+$ and $PO4^-$ ions in the buffer solution. The G-blocks contribute to tighter crosslinks and structural stability of ionically crosslinked alginate gels; therefore, disintegration of these crosslinks results in complete alginate gel dissolution. This type of profile is very similar to that obtained in the study by Bajpai and Sharma (2004) when investigating the swelling behaviour of alginate (4 %(w/v)) beads, however the swelling profile was observed over a shorter incubation period (420 minutes rather than 21 days), potentially due to the smaller size of gel being investigated (beads versus disc shape gels). Most studies investigating the swelling and/or degradation behaviour of ionically crosslinked alginate gels introduce a small amount of calcium ions in the incubation media to prevent rapid gel dissolution (Growney Kalaf *et al.,* 2016; Kuo and Ma, 2008; Ghanizadeh Tabriz *et al.,* 2015). In the present study, 1.8 mM $CaCl_2$ (Ghanizadeh Tabriz *et al.,* 2015) was added to the PBS media, which might have also contributed to the difference in dissolution periods between this study and Bajpai and Sharma (2004), since the latter did not include additional calcium ions in the incubation media.

Although both $CaCl_2$ and $CaCO_3$ alginate gels are crosslinked with $Ca^{2+}$ ions, the weight variation response of the two differed considerably, with the latter exhibiting weight loss rather than increase. In a study investigating the effect of calcium ion concentrations in the incubation media, when introducing 2 mM $CaCl_2$ to the PBS, Kuo and Ma (2008) obtained a similar profile to that in Figure 5.4(A) for $CaCO_3$-alginate gels. Moreover, Kuo

and Ma (2008) demonstrated that an increase in $Ca^{2+}$ concentration (up to 5 mM) leads to further shrinkage of the $CaCO_3$ alginate gels whereas a lower concentration (1 mM) results in swelling, similar to the $CaCl_2$ alginate gels obtained in the present study. Therefore, the supplementation of PBS with calcium ions has proved to be effective on the swelling and/or degradation profiles of alginate gels. One possible reason as to why $CaCl_2$ and $CaCO_3$ alginate gels exhibited a different response even though $Ca^{2+}$ ions were present in the incubation media, might be due to the difference in crosslinking methods. It could be speculated that since $CaCO_3$ alginate gels consist of highly ordered crosslinks due to the slow gelling mechanism of $CaCO_3$:GDL, they were less susceptible to decrosslinking thereby restricting swelling.

$BaCl_2$ alginate gels also displayed degradation throughout the incubation period. This might be attributed to the larger ionic radius of $Ba^{2+}$ ions when compared to $Ca^{2+}$ ions, which forms tighter junctions with the $-COO^-$ groups of both the M- and G-blocks of alginate gels thereby limiting ion-exchange, preventing water uptake, and swelling. The significant decrease in weight at day 1, is speculated to have originated from gel weight irregularities prior to incubation. Overall, weight variation was particularly evident in gels crosslinked via rapid crosslinking agents: $CaCl_2$ and $BaCl_2$.

**Mechanical characterisation** via confined compression at the designated time points throughout the incubation period yielded values for the peak stress, aggregate modulus, and permeability of the ionically crosslinked alginate gels. From the curves obtained in Figure 5.4, it is evident that immersion of the alginate gels in calcium-supplemented PBS decreases both the peak stress and aggregate modulus of most gels, except for $CaCl_2$ alginate gels where the aggregate modulus increased, although not significantly, ~3 kPa from day 0 to day 21. Considering that the alginate gels exhibited swelling and/or degradation throughout the incubation period, the decrease in compressive properties might be attributed to the loss in crosslink density. However, the increase in $CaCl_2$

alginate gel modulus together with the increase in both the peak stress and aggregate modulus of $CaCO_3$ alginate gels at day 14 and day 21, and the increase in peak stress at day 21 for $CaCl_2$ alginate gels might be attributed to the $Ca^{2+}$ ions present in the incubation media (1.8 mM) which resulted in further crosslinking, counterbalancing the loss in compressive properties. Periodic changing of the incubation media might have also contributed to a fresh availability of $Ca^{2+}$ ions resulting in further crosslinking. The effect of $Ca^{2+}$ ions in the incubation media on the compressive properties was also investigated in the study by Kuo and Ma (2008) where a significant reduction in both compressive strength and modulus was reported in the presence of 2 mM calcium supplemented media, however the mechanical properties significantly increased when higher calcium content (5 mM) in the surrounding media was used. Similarly in the study by Growney Kalaf *et al.,* (2016), incubation of $CaCl_2$ and $CaCO_3$ crosslinked alginate gels (1 %(w/v)) was carried out in calcium-supplemented PBS, although the concentration of calcium ions was not reported, and showed very little significant differences in peak stress and compressive modulus throughout a 28-day period, however there were timepoints (such as day 14 for $CaCl_2$ gels) that showed an increase in both peak stress and compressive modulus, similar to the curves obtained in this work, but the authors do not provide any reasoning to why this might have occurred. Overall, it may be concluded that immersion of alginate gels in physiological media for a time period of 21 days or more, consistently weakens the mechanical properties, which has also been reported in Growney-Kalaf *et al.,* (2016), and Sarker *et al.,* (2018), although there seems to exist a threshold where the reduction in mechanical properties slows down, within the first 2 weeks in Kuo and Ma (2008), and 3 weeks in Sarker *et al.,* (2018). Therefore, a longer *in vitro* incubation investigation (> 21 days) would be more representative of the physiological conditions if this material were to be implemented as vascular grafts.

### 5.5.4. The elastic properties of ionically crosslinked alginate hydrogels in comparison with aortic tissue.

Mechanical characterisation of ionically crosslinked alginate gels is typically carried out via compression and shear rheology tests, with little attention given to the elastic (tensile) properties. This is potentially due to their weak mechanical properties hence, the difficulty in preparing these gels in specific geometrical designs for tensile testing. In this work the slow crosslinking mechanism of $CaCO_3$:GDL allowed the fabrication of uniformly shaped dog-bone alginate and alginate:elastin hydrogel structures that were robust enough for tensile testing (Figure 5.11(A)). However, given that the tensile testing machine used in this investigation is equipped with high pressure pneumatic grips, specimen loading without crushing the dog-bone end tabs was found to be challenging. Several design methods (Figure 5.11(B-E)) to prevent the crushing effect of the pneumatic grips were considered prior to fabricating custom-made 3D-printed PLA grip adapters as shown in Figure 5.11(F-H).

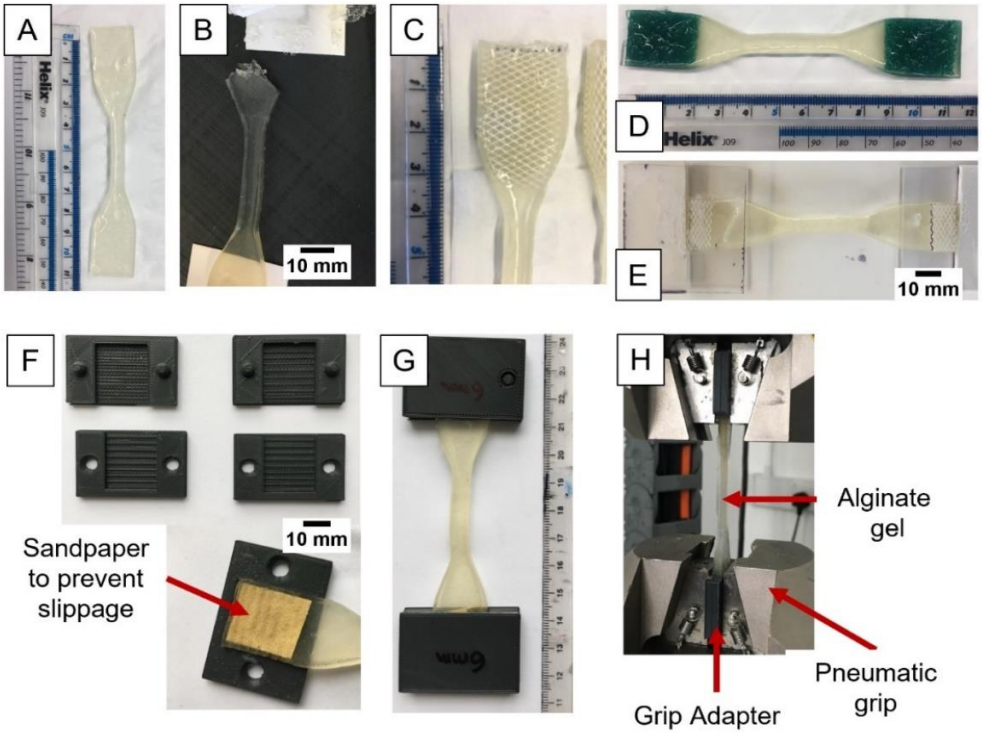


*Figure 5.11: Visual representation of the grip solution process: (A) alginate hydrogel dog-bone shaped specimen prepared for tensile testing, (B) first attempt to prevent the end tabs from damage using cardboard, (C) second attempt using a PVC mesh, (D) third attempt using scouring pads, (E) fourth attempt using a rubber sandwiched between two Perspex sheets, (F) fifth and successful attempt using a 3D-printed custom-design pin-hole grip adapter with the addition of sandpaper to prevent slipping during testing, (G) alginate hydrogel fit into the grip adapter ready for testing, and (H) the alginate hydrogel being successfully tensile tested.*

Drury *et al.,* (2004) presents an extensive assessment of the tensile properties of various alginate gel types using the slow crosslinker, $CaSO_4$. The closest alginate type (0.85 M/G ratio) to the one used in this work (1.56 M/G ratio), exhibited tensile strength and modulus less than 10 kPa, which is less than the values shown in Figure 5.7(B) for alginate-alone gels (UTS: 23.76 ±6.34 kPa, E: 43.37±1.33 kPa). There are several factors that need to be considered when comparing mechanical properties of hydrogels to studies such as Drury *et al.,* 2004, including tensile testing parameters (e.g., specimen dimensions, crosshead speed, preconditioning), environmental conditions (e.g., temperature, material hydration state), alginate gel preparation (e.g., alginate type, molecular weight, M/G ratio), data analysis (stress and strain calculations), amongst

other factors (Emmott *et al.,* 2016). Drury *et al.,* (2004) investigated the effect of most of these factors on the tensile properties of alginate hydrogels. By using different crosshead speeds (1%/s, 10%/s, and 100%/s relative to the specimen's gauge length) Drury *et al.,* (2004) concluded that failure strain, tensile strength and stiffness are all an increasing function of strain rate. In this work, although an increase in strength and stiffness of alginate gels was observed when changing the crosshead speed from 1mm/min to 50 mm/min, significant differences were only observed in the stiffness of the alginate alone hydrogels (Figure 5.7(C)).

In order to develop aortic grafts that closely mimic the biomechanical behaviour of the aorta, it is imperative to match the mechanical properties of the graft to healthy aortic tissue. Several investigations have focussed on identifying the mechanical properties of the aorta primarily to understand disease progression and the effect of aging (Sherifova and Holzapfel, 2019), nonetheless such engineering data is useful in the design process of the next generation of aortic grafts. The stretch to failure properties of the alginate-based hydrogels obtained via uniaxial tensile testing (Section 5.4.3) are presented once again in Table 5.1 but this time compared to aortic tissue data from the literature. It is evident that the alginate-based hydrogels are relatively weak in comparison with aortic tissue. Several studies suggest that hydrogel properties may be improved through the addition of a secondary polymer (Giuseppe *et al.*, 2018; Silva *et al.*, 2018; Seok *et al.*, 2019). Therefore, elastin, a naturally occurring ECM protein and an important functional component in arterial wall mechanics, was primarily incorporated within the alginate gel to improve cell adhesion properties (Silva *et al.*, 2018; Wang *et al.*, 2020b) and the overall mechanical properties of the hydrogel. Although the latter was achieved, as shown in Figure 5.7, the changes were not significant, and the strength was still inferior to that of aortic tissue (Table 5.1).

*Table 5.1: Comparing the mechanical properties of alginate-based hydrogels with aortic tissue data from the literature. Crosshead speed is at 1 mm/min for both the current work and Vallabhaneni et al., 2004. Data is presented as the mean ± S.D. (UTS: ultimate tensile strength, EM: elastic modulus, PM: physiological modulus, Circ: circumferential, and Long: longitudinal directions).*

| **Study** | **Specimen type** | **Mechanical Properties** | | | |
|---|---|---|---|---|---|
| | | **UTS (MPa)** | **Failure strain (%)** | **EM (MPa)** | **PM (MPa)** |
| Current work | Alginate (5%-200 mM $CaCO_3$) | 0.02 ± 0.006 | 51.60 ±11.66 | 0.05 ±0.004 | — |
| | Alginate:elastin (5%-0.5% 200 mM $CaCO_3$) | 0.04 ±0.002 | 75.55 ±0.54 | 0.06 ±0.004 | — |
| (Vallabhaneni *et al.,* 2004) | Abdominal Aorta (Human) Circ | 0.61 ±0.07 | 29.0 ±4.0 | — | 1.82 ±0.10 |
| | Abdominal Aorta (Human) Long | 1.30 ±0.11 | 33.0 ±4.0 | — | 1.38 ±0.12 |

As discussed in Section 5.5.3, ionically crosslinked alginate hydrogels are susceptible to ion exchange in physiological environments leading to weight and mechanical property variations. Therefore, a short study assessing the elastic properties of alginate and alginate:elastin hydrogels over a 72-hour incubation period in calcium-supplemented PBS at 37°C was conducted (Figure 5.8). A significant change in elastic properties at 24 h and 72 h timepoints was observed mostly in the alginate:elastin hydrogels. This might be attributed to some of the elastin that remains unblended, given that the elastin is not crosslinked in any way, that is released out from the hydrogel matrix during incubation, thereby lowering the mechanical properties (almost a 50% reduction for all three stretch to failure properties). Duan *et al.,* (2013) reported similar behaviour of alginate/gelatine blends where the elastic properties significantly decreased upon incubation in culture media. Silva *et al.,* (2018) also reported a loss in mechanical properties for alginate:elastin hydrogels after 3 days incubation. In both cases, gelatine and elastin were not crosslinked and the only crosslinked monomer in the hydrogel blend was alginate, corroborating the hypotheses that incubation resulted in the extra

secondary unblended monomer dissipating and weakening the hydrogel structure. Therefore, these results suggest that for long-term stability, alginate hydrogels require the addition of a secondary monomer that is preferably crosslinked and can withstand physiological conditions.

### 5.5.5. Comparing the viscoelastic properties of alginate-based hydrogels with aortic tissue

Viscoelasticity is a key characteristic of arterial tissue, and hydrogels have been particularly investigated in engineering vascular grafts due to their inherent viscoelastic properties. Herein, hydrogel viscoelasticity was measured via a mechanical tester under compression (confined compression stress relaxation) and tension (uniaxial tensile stress relaxation and dynamic oscillatory frequency sweep), Viscoelastic analysis of aortic tissue is limited in the literature, however the few investigations that report this have been performed using a uniaxial tensile setup (Amabili *et al.,* 2019; Faturechi *et al.,* 2019).

The uniaxial tensile stress relaxation conducted in this study involved a stepwise ramp-hold protocol based on the investigation by Lake and Barocas (2011) when characterising collagen-agarose hydrogels, and similar observations of increasing peak and equilibrium stress with increasing displacement levels were noted (Figure 5.10). Interestingly, in the present work some of the alginate:elastin hydrogel specimens did not exhibit the typical stress relaxation decaying response throughout the hold periods. On the contrary, the load increased with time as demonstrated by the large error bars on the stress relaxation curves and the percentage degree relaxation columns in Figure 5.10(B) and (D), respectively. This may be due to the lack of gel stabilisation prior to testing, which might be overcome by extending the initial hold period (> 1800 s) or by implementing an oscillatory preconditioning stage, to ensure more repeatable and reliable results. Although, both alginate and alginate:elastin hydrogels display typical

viscoelastic behaviour the magnitude of stress at a 5% displacement (peak stress) is considerably less than the stress corresponding to physiological pressure (approximately 0.7 MPa at a peak physiological pressure of 120 mm Hg (Amabili *et al.*, 2018)). As for dynamic loading, the loss factor of descending thoracic aorta strips in the circumferential direction was reported to be in the range between 0.09 and 0.1 (Amabili, Balasubramanian and Breslavsky, 2019) which is very similar to the hydrogel loss factor values reported in the present work. Comparing the storage modulus values (Figure 5.10(A) to the static stiffness obtained via the stretch to failure tests (Figure 5.8(C)) (40 kPa to 60 kPa), it is evident that a large increase in stiffness is obtained via dynamic loading for both hydrogel formulations (100 kPa to 160 kPa). Moreover, Amabili *et al.,* (2019) observed an increase in storage modulus with an increase in frequency, which is not the case in the present work. This might be due to the wider frequency range investigated (1-60 Hz) by Amabili *et al*. (2019).

## 5.6. Conclusions

The work presented in this chapter provided a comprehensive evaluation of ionically crosslinked alginate hydrogels as a first attempt at implementing such materials for the development of innovative aortic grafts.

The mechanical properties of ionically crosslinked alginate hydrogels were investigated using different concentrations and various crosslinking agents. Preliminary alginate hydrogel preparation using four different types of crosslinking agents demonstrated how the slow gelling crosslinkers ($CaCO_3$ and $CaSO_4$) resulted in more uniform hydrogel structures than instantaneous crosslinkers ($CaCl_2$ and $BaCl_2$). Mechanical characterisation via confined compression stress relaxation measurements showed that ionically crosslinked alginate hydrogels exhibit a typical viscoelastic response similar to ECMs and soft tissue. From the various concentrations and crosslinking agents, $CaCO_3$:alginate (200 mM:5 %(w/v)) was found to exhibit superior hydrogel shape

uniformity and compressive properties, immediately after gelation and throughout an incubation period. This stability rendered $CaCO_3$:alginate ideal for the fabrication of dog-bone shaped specimens for tensile testing, and therefore the tensile elastic and viscoelastic properties of ionically crosslinked alginate was also investigated.

Moreover, the influence of a secondary monomer incorporated within the alginate hydrogel on the mechanical properties was also investigated but given that both gelatine and elastin were not crosslinked in any way, significant changes to the overall hydrogel mechanical behaviour were not observed.

Finally, comparing the elastic properties of the ionically crosslinked alginate hydrogel to that of aortic tissue as reported in the literature, it is evident that changes in the hydrogel formulation are required in order to develop a graft that closely mimics the native aorta.

# Chapter 6 Enhancing the mechanical properties of physically crosslinked alginate-based hydrogels for aortic graft applications

## 6.1. Introduction

In the pursuit of developing a hydrogel that mimics the mechanical behaviour of aortic tissue, from Chapter 5, it is evident that ionically crosslinked, single-network alginate hydrogels lack the mechanical integrity and strength required for vascular graft applications, where it is crucial that the material withstands the surgical implantation procedure and pulsatile pressure *in vivo*. The weak mechanical properties of single network hydrogels originate from crosslinking inhomogeneity and lack of energy dissipation mechanisms (Costa and Mano, 2015; Chimene, Kaunas and Gaharwar, 2020). This has motivated the recent emergence of several reinforcement techniques such as monomer functionalisation and interpenetrating polymer networks (IPNs) briefly mentioned in Section 2.6.2, mostly targeted at incorporating energy dissipation within the gel to improve stiffness, strength, and fracture energy whilst maintaining extensibility (Chimene, Kaunas and Gaharwar, 2020).

Monomer functionalisation is one of the most common hydrogel-reinforcing strategies, where the monomer backbone is modified to incorporate acrylate functional groups rendering it suitable for covalent crosslinking via photopolymerisation (Yue *et al.*, 2015; Hasany *et al.*, 2021). The functionalised monomer transforms into a hydrogel in the presence of a photoinitiator and a light source, generally ultraviolet (UV) light. Following photon absorption, the photoinitiator either decomposes (Type I) or extracts hydrogen from donor molecules (Type II), both types creating free radicals that react with the functional groups of the monomer, thus initiating polymerisation (Han *et al.*, 2020; Tomal and Ortyl, 2020). One of the benefits of this crosslinking method is its controllability on the physical and mechanical properties of the final gel product by altering the photocrosslinking parameters, such as polymer and photoinitiator concentrations, and

light exposure intensity and duration (O'Connell *et al.*, 2018). A variety of natural and synthetic monomers have been modified to incorporate functional groups for photopolymerisation, primarily gelatine (gelatine methacrylate; GelMA)(Yue *et al.*, 2015), alginate (alginate methacrylate; AlgMA)(Hasany *et al.*, 2021), and polyethylene glycol (acrylate (PEGDA), or methacrylate (PEGDMA)). The incorporation of an acrylate side groups to monomers, for example alginate, allows for covalent photocrosslinking of the alginate monomer, thereby enhancing the resulting hydrogel's strength, durability, and stability in physiological solutions (no dissolution due to ion exchange) (Jeon *et al.*, 2009). Although monomer functionalisation improves the fracture energy of hydrogels due to the high bond energy associated with covalent crosslinking, it still lacks an energy dissipative mechanism, which may be achieved via IPN formation (Chimene, Kaunas and Gaharwar, 2020).

The addition of secondary polymers to alginate for composite hydrogel formation (or hydrogel blends) is another way of enhancing the mechanical properties. IPN formation falls under the category of hydrogel blends, with the hydrogel comprising two (or more) polymer networks that are crosslinked separately, meaning that the secondary polymer is crosslinked after the first hydrogel network has been formed and therefore, they are not covalently bound to one another (Parak *et al.*, 2019). In general, one of the polymer networks in IPNs is stiff and brittle whilst the other is soft and ductile; the former contributes to energy dissipation whilst the latter sustains large deformation upon stretching (Xu, Dai and Hong, 2019). Hence, this heterogeneous configuration exhibits an increase in fracture toughness and stiffness compared to either of the two parent monomers alone (Sun *et al.*, 2012).

Two common types of IPNs exist: double networks (DNs) and ionic-covalent entanglements (ICEs). In the former, the polymer networks are crosslinked separately via covalent bonding e.g., two photopolymerisable networks. Such polymer structures

have high bond energies, lack elasticity due to the two covalent networks, are independent of strain rate, less susceptible to environmental conditions but susceptible to fatigue since the breaking of covalent bonds is irreversible. On the other hand, in ICE networks the ionically crosslinked network act as sacrificial bonds that dissipate energy when stretched which can recover over time rendering the gel fatigue resistant; they are more sensitive to environmental conditions, display hysteresis at low strains, and are strain dependent (Chimene, Kaunas and Gaharwar, 2020). ICE polymer networks, particularly those comprising ionically crosslinked alginate, have gained popularity in 3D bioprinting applications due to their rapid fabrication process and recoverable mechanical properties (Chimene, Kaunas and Gaharwar, 2020). Several IPN investigations have combined ionically crosslinked alginate with synthetic polymers such as polyacrylamide (PAM) (Sun *et al.*, 2012; Bakarich *et al.*, 2013; Fitzgerald *et al.*, 2015; Deng *et al.*, 2017) and polyethylene glycol diacrylate (PEGDA) (Hong *et al.*, 2015; de Melo *et al.*, 2019; Zhang *et al.*, 2021). The PAM or PEGDA network is the first network formed via UV photocrosslinking followed by the alginate network that is typically crosslinked using calcium-based crosslinkers ($CaCl_2$ or $CaSO_4$) (Figure 6.1).

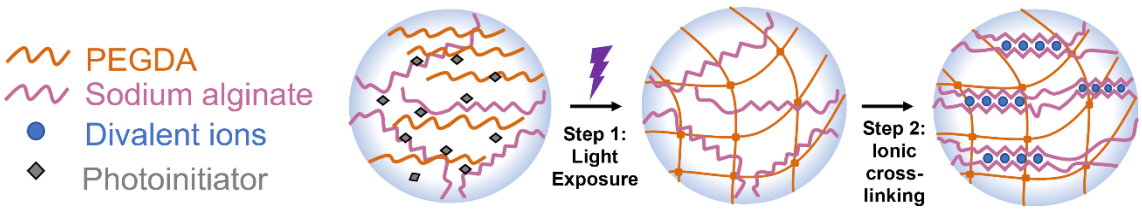


*Figure 6.1: Schematic representation of the alginate:PEGDA ICE IPN hydrogel formation where the PEGDA is crosslinked first via photopolymerisation in the presence of UV or visible light and a photoinitiator (Step 1) followed by ionic crosslinking of the alginate (Step 2) (de Melo et al., 2019; Zhang et al., 2021).*

This combination of alginate:PAM or alginate:PEGDA results in extremely tough and stretchable hydrogels despite their high water content (> 70 wt.%). Fracture toughness values of approximately 9000 J/m$^2$ were reported for alginate:PAM (*ca.* 36 times higher

than the individual components) (Sun *et al.*, 2012) and 1500 J/m$^2$ for alginate:PEGDA (*ca.* 7 times higher than PEGDA alone) (Hong *et al.*, 2015), and the alginate:PAM gels could be stretched to 20 times their original length (Sun *et al.*, 2012). Compressive testing demonstrated the alginate:PAM and alginate:PEGDA hydrogels ability to maintain their original shape following a compressive strain of over 90% (Darnell *et al.*, 2013; Hong *et al.*, 2015; Deng *et al.*, 2017). Despite the extensive research available on alginate:PAM, reports on the toxicity of acrylamide, the PAM monomer, makes PEGDA a more attractive option for tissue engineering, especially in cell encapsulation applications (Darnell *et al.*, 2013; Hong *et al.*, 2015).

PEGDA, a derivative of polyethylene glycol, is widely used in tissue engineering due to its hydrophilicity, biologically inert structure, and lack of toxic or immunogenic responses (Zhu, 2010; Hakim Khalili *et al.*, 2023). The mechanical and printability properties of alginate:PEGDA IPNs crosslinked with $CaSO_4$, the photoinitiator Irgacure 2959 (I2959) and 365 nm UV light were investigated by Hong *et al*., (2015), where the mechanical properties were found to be a function of the PEGDA's molecular weight and concentration. However, in Hong *et al*., (2015) the target application was to develop a tough hydrogel that mimics living tissue in general, and therefore the mechanical properties of the IPN formulation were not tailored specifically as an aortic substitute, yet it was demonstrated that by varying the parameters of this IPN (e.g., PEGDA molecular weight, and polymer concentration) the mechanical properties may be altered, thus showing great promise in implementing this to mimic the properties of native aortic tissue. Previous research on alginate:PEGDA based IPN hydrogels have mostly relied on conventional calcium-based crosslinkers ($CaCl_2$ or $CaSO_4$) to induce alginate gelation, and PEGDA monomers having molecular weights greater than 1000 Da.

In the work presented in this chapter, an alternative alginate:PEGDA IPN hydrogel fabrication strategy is proposed by using $CaCO_3$:GDL as the calcium-based

crosslinker whilst also investigating a barium-based alginate crosslinker ($BaCl_2$), and a lower molecular weight (Mn 575 Da or 700 Da), commercially-available, inexpensive PEGDA to mimic the mechanical properties of aortic tissue as reported in the literature.

## 6.2. Aims and Objectives

The aim of this chapter was to enhance the mechanical properties of physically crosslinked alginate hydrogels (developed in Chapter 5) by incorporating a synthetic secondary monomer, PEGDA. The mechanical properties of the alginate:PEGDA IPN hydrogel were investigated in comparison with physically crosslinked alginate hydrogels, and the target properties (i.e., human aorta) as a potential hydrogel towards the fabrication of alternative aortic grafts.

The objectives of this chapter included the investigation of:

1. Alginate:PEGDA IPN synthesis by varying PEGDA concentrations and molecular weight, and ionic crosslinker type ($CaCO_3$:GDL, $BaCl_2$) while evaluating photocrosslinking parameters (UV source intensity, exposure time).
2. The mechanical properties of alginate:PEGDA IPN at different concentrations of PEGDA (13.3 %(w/v) and 26.6 %(w/v)) and different molecular weights (Mn 575 and Mn 700) at a fixed PI (0.5 %(w/v)) via confined compression stress relaxation and tensile tests (stretch to failure).
3. The mechanical and physical (swelling and degradation) properties of alginate:PEGDA IPN over an incubation period at physiological conditions.
4. Alginate:PEGDA IPN in comparison to ionically crosslinked alginate single-network hydrogel and aortic tissue data (as reported in the literature) to determine whether the mechanical properties of the IPN hydrogel formulation have been sufficiently enhanced to be implemented as an aortic graft material substitute.

## 6.3. Materials and Methods

Most of the materials and methods used in this chapter are described in detail in Chapter 3. Briefly, hydrogel preparation involved the mixing of sodium alginate with PEGDA to prepare hydrogels with final concentrations of 3.3 %(w/v) and 13.3. %(w/v) or 26.6 %(w/v), respectively. The photoinitiator I2959 was also added to the alginate:PEGDA solution in order to initiate photopolymerisation of the PEGDA when exposed to UV light (365 nm). The alginate crosslinking agents investigated in this study included $CaCO_3$:GDL and $BaCl_2$ which were used at final concentrations of 66 mM :133.2 mM and 66 mM, respectively. Dog-bone shaped specimens were prepared for tensile testing using the customised mould (Appendix) and discs for confined compression were prepared using 24-well tissue culture plates.

The mechanical characterisation methods including tensile testing, confined compression stress relaxation, rheological analysis, physical characterisation, including swelling and degradation analysis, and SEM imaging, all follow the same protocols and parameters described in Chapter 3, unless otherwise specified.

To investigate the alginate:PEGDA IPN hydrogel suitability for vascular graft fabrication, tubular structures were prepared using an agarose hydrogel as a sacrificial cylindrical mould as illustrated in Figure 6.2. Agarose 2.5 %(w/v) stock solution was prepared by dissolving the powder in heated deionised water (DI water; T>80ºC). Once the agarose was fully dissolved, the hot solution was poured into 5 ml or 10 ml polypropylene syringes (BD PlastiPak™) and left at room temperature for the agarose to gel. The agarose gel cylinders were then placed into a larger diameter 10 ml or 20 ml syringe and the alginate:PEGDA precursor solution was poured in between the agarose and the syringe wall. The syringe containing the agarose gel surrounded by the alginate:PEGDA solution was then exposed to UV (Analytik Jena Short/long-wave UV lamp; 6 watts, 254/365 nm wavelength, Cole-Parmer, UK) for 20 minutes, followed by immersion in 66 mM $BaCl_2$.

Upon alginate:PEGDA hydrogel formation, the whole structure was immersed in a heated DI water bath (T>80ºC) for the agarose to shrink, leaving behind an alginate:PEGDA tubular structure.

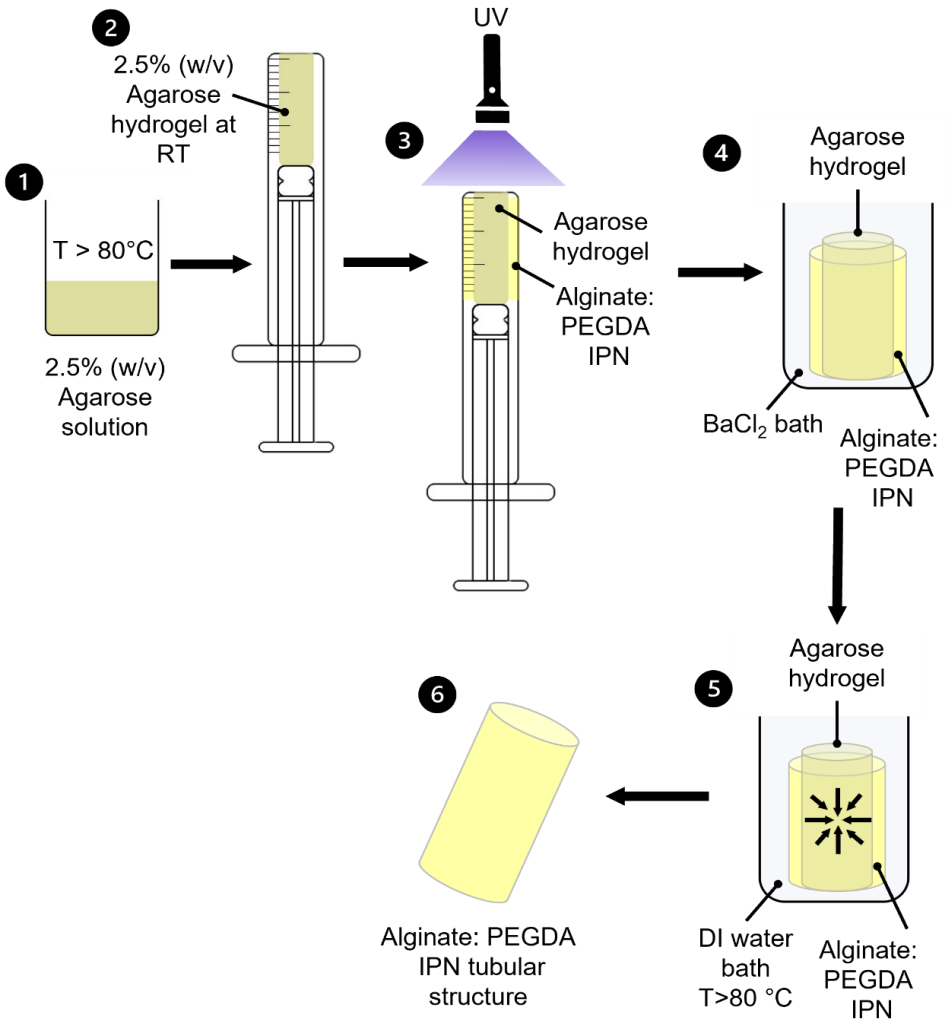


*Figure 6.2: Schematic representation of the tubular structure fabrication method using an agarose hydrogel sacrificial scaffold: Briefly. (1) the agarose solution (2.5% (w/v)) is prepared in heated DI water (T > 80°C), (2) then poured into a polypropylene syringe and left to gel at room temperature, (3) the agarose hydrogel cylinder is transferred into a larger polypropylene syringe and the alginate:PEGDA IPN solution is poured around it and exposed to UV light for PEGDA photopolymerisation, (4) the quasi-crosslinked alginate:PEGDA IPN together with the agarose hydrogel are transferred into a $BaCl_2$ bath for alginate crosslinking, (5) once the alginate:PEGDA IPN is fully crosslinked, the structure is transferred into a heated DI water bath (>80°C) and the agarose begins to shrink facilitating removal of the sacrificial mould, (6) leaving behind the alginate:PEGDA IPN hydrogel tubular conduit.*

## 6.4. Results

### 6.4.1. Fabrication of alginate:PEGDA hydrogel

#### 6.4.1.1. Preliminary alginate:PEGDA hydrogel fabrication using a UV torch

Three different single-network PEGDA (Mn 700) hydrogels were prepared at different concentrations (5%, 10%, and 20 %(w/v)) at a fixed I2959 concentration (0.05 %(w/v)) as shown in Figure 6.3(A). Using the same PEGDA concentrations, alginate:PEGDA IPN hydrogels were also prepared as shown in Figure 6.3(B). However, with the addition of $CaCO_3$:GDL crosslinker, the initial alginate, PEGDA, and photoinitiator concentrations diluted down to 3.3 %(w/v) alginate, 3.3 %(w/v), 6.7 %(w/v) and 13.3 %(w/v) PEGDA, and 0.03 %(w/v) I2959. From visual observations, in both the PEGDA alone and the alginate:PEGDA IPN, the hydrogels became more opaque with increasing PEGDA concentration.

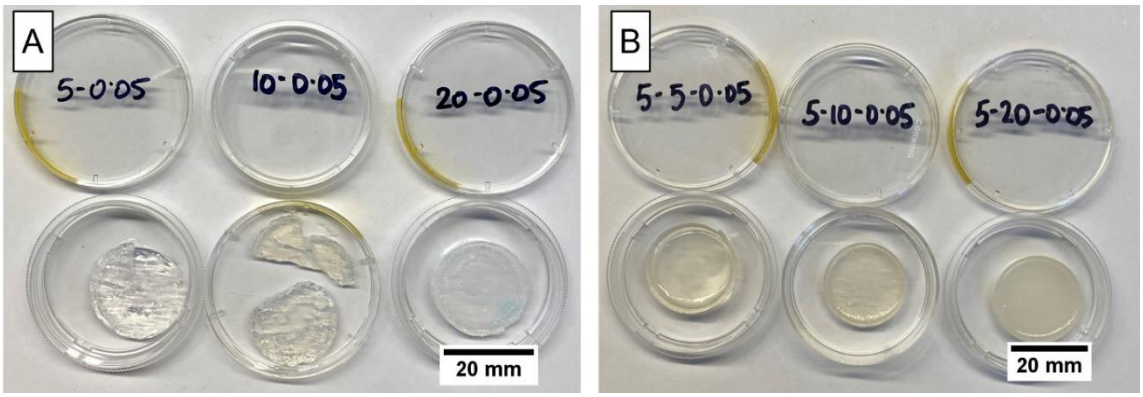


*Figure 6.3: Initial hydrogel preparation at different PEGDA700 concentrations using a UV torch (wavelength 365 nm, intensity 200 mW/cm$^2$, and 22 mm exposure area diameter) (A) PEGDA alone hydrogels, and (B) alginate:PEGDA IPN hydrogel.*

#### 6.4.1.2. Preparing dog-bone shaped samples for tensile testing

Due to the UV torch having an exposure area diameter of 22 mm, hydrogel samples could only be fabricated as discs, therefore, in order to prepare dog-bone shaped samples for tensile testing a different UV source was required. The first attempt was using the UV-KUB2, which is a UV-LED masking system specifically designed for soft

lithography (Figure 6.4(A)). However, as shown in Figure 6.4(E), despite a UV wavelength of 365 nm and a power intensity of 35 mW/cm$^2$, it was challenging to obtain a fully cured dog-bone specimen without breaking. Additionally, the dog-bone dimensions had to be altered for the mould to fit within the curing box whilst still being large enough to test using the same uniaxial tensile machine.

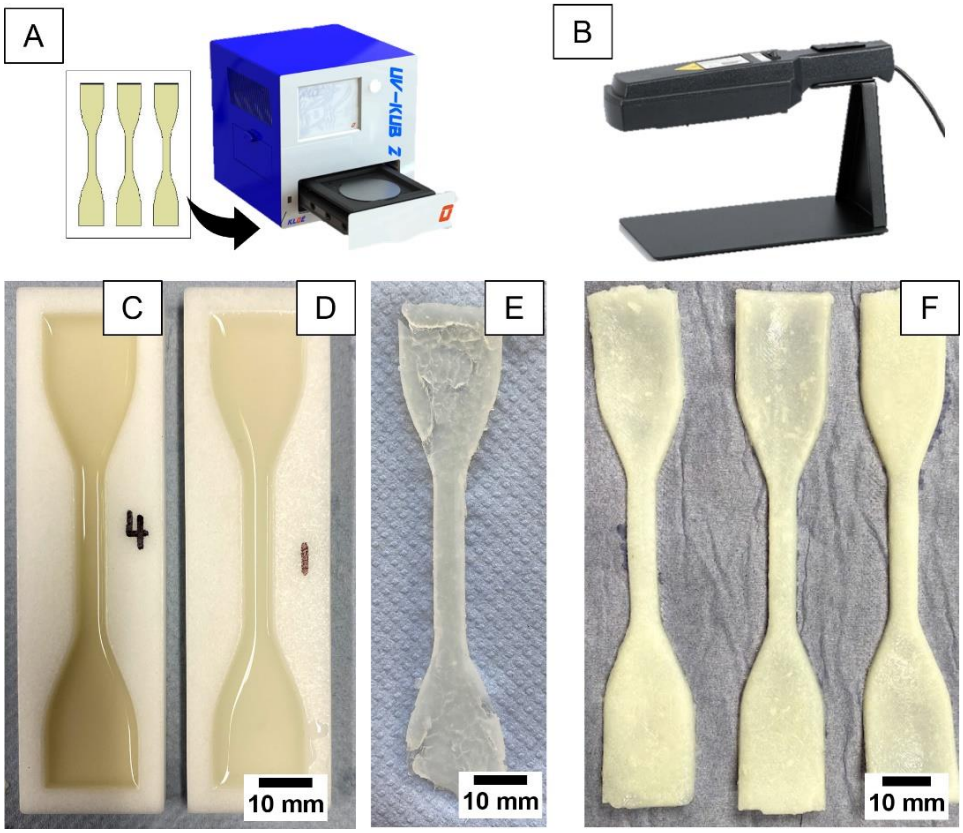


*Figure 6.4: Alginate:PEGDA IPN hydrogel dog-bone shaped samples for tensile testing. (A) schematic showing the sample mould and the UV-KUB2 used as a first attempt to prepare dog-bone sample, (B) the handheld UV lamp used to successfully crosslink the alginate:PEGDA hydrogels, (C) alginate:PEGDA pregel solution poured in mould, (D) alginate:PEGDA hydrogel after UV exposure via the UV-KUB2 system, and (E) the hydrogel once removed from the mould resulting in poor gelling behaviour despite long exposure times, and (F) successfully crosslinked algnate:PEGDA hydrogels using the handheld UV lamp.*

The second and successful attempt was using a hand-held UV lamp (Analytik Jena Short/long-wave UV lamp; 6 watts, 254/365 nm wavelength, 230 VAC/50 Hz, Cole-Parmer, UK) as shown in Figure 6.4(B). The exposure area was sufficient to cover the

whole dog-bone shape mould, however exposure time for a fully crosslinked hydrogel was 30 minutes for one dog-bone sample. Given that the manufacturer did not provide the information about the intensity of the lamp, this was measured using a UV light metre. First, the emission spectrum was measured to find the peak emission wavelength as shown in Figure 6.5. Then, setting the metre at this wavelength at a distance of 1 cm away from the lamp (which is the distance the lamp is set when crosslinking the hydrogels) an intensity of 2.2 mW/cm$^2$ was measured.

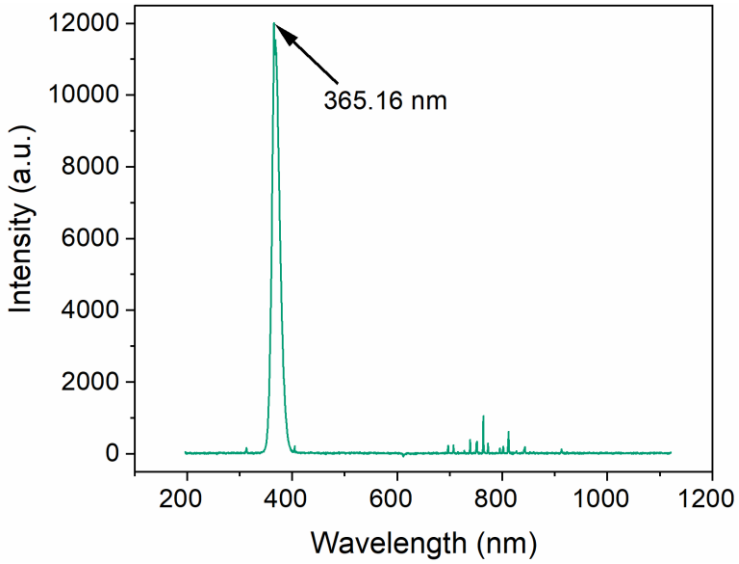


*Figure 6.5: UV lamp emission spectrum from 200 nm to 1120 nm exhibiting a maximum peak at 365.16 nm.*

### 6.4.2. Mechanical characterisation of alginate:PEGDA hydrogel

#### 6.4.2.1. Tensile testing: stretch to failure measurements

Initially, two PEGDA (Mn 700) concentrations (13.3 %(w/v) and 26.6 %(w/v)) were used to investigate the mechanical properties of the alginate:PEGDA IPN hydrogel. From Figure 6.6 it is evident that with increasing PEGDA concentration the elongation of the material significantly decreases, with a significant increase in both strength and stiffness.

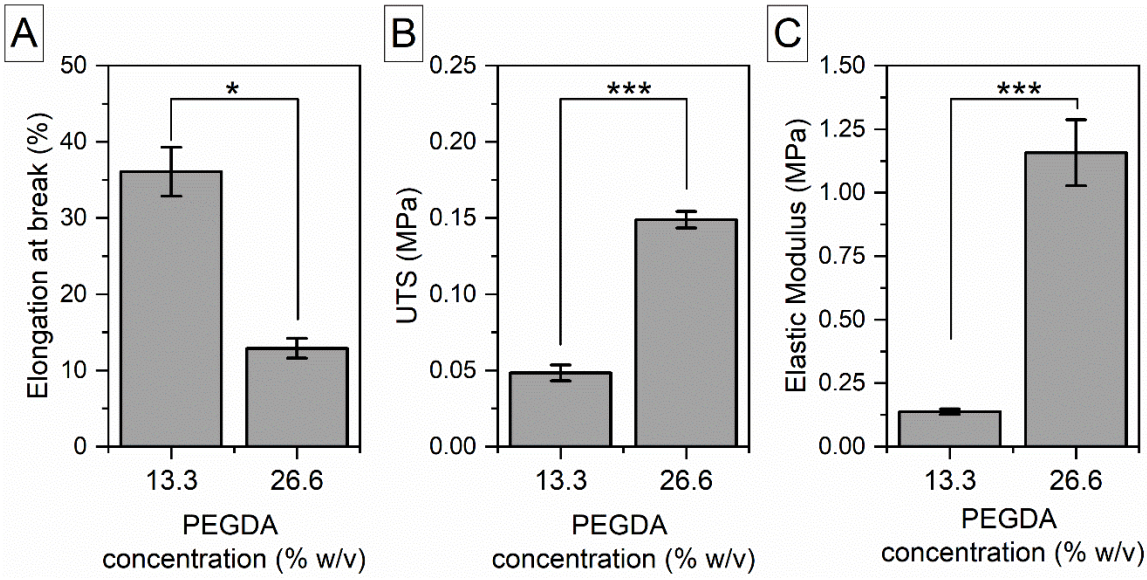


*Figure 6.6: Stretch to failure tensile properties of alginate:PEGDA IPN hydrogel at two different PEGDA concentrations (13.3% (w/v) and 26.6% (w/v)) and fixed alginate (3.3% (w/v)) photoinitiator (0.5% (w/v)) and $CaCO_3$:GDL (66 mM: 133.2 mM) concentrations. Columns and error bars represent the mean ± S.D (n=3) for 13.3% (w/v) and mean ± S.D (n=5) for 26.6% (w/v). Statistical significance measured via two sample t-test and represented graphically by * p<0.05, *** p<0.001.*

Given the high strength and stiffness obtained when using a higher percentage of PEGDA (Mn 700) i.e., 26.6 %(w/v), further stretch to failure tests were conducted to investigate the behaviour between two PEGDA molecular weights (Mn 575 versus Mn 700) and two alginate crosslinkers ($CaCO_3$:GDL versus $BaCl_2$) as shown in Figure 6.7. The $BaCl_2$ crosslinker resulted in a higher degree of elongation, higher strength, and higher stiffness than the $CaCO_3$:GDL for both molecular weights. The Mn 575 resulted in a higher elongation than the Mn 700 for both crosslinker types, but this was not significantly different ($p$ = 0.699 $BaCl_2$; $p$ = 0.449 $CaCO_3$). Contrarily, the Mn 700 resulted in a significantly higher strength ($p$ = 0.042) and stiffness ($p$ = 0.018) than the Mn 575 but only when $BaCl_2$ is used.

From this, the alginate:PEGDA IPN comprising PEGDA Mn 700 at a concentration of 26.6 %(w/v) with $BaCl_2$ as the alginate crosslinker was identified as the most suitable hydrogel formulation to be taken forward for further investigation.

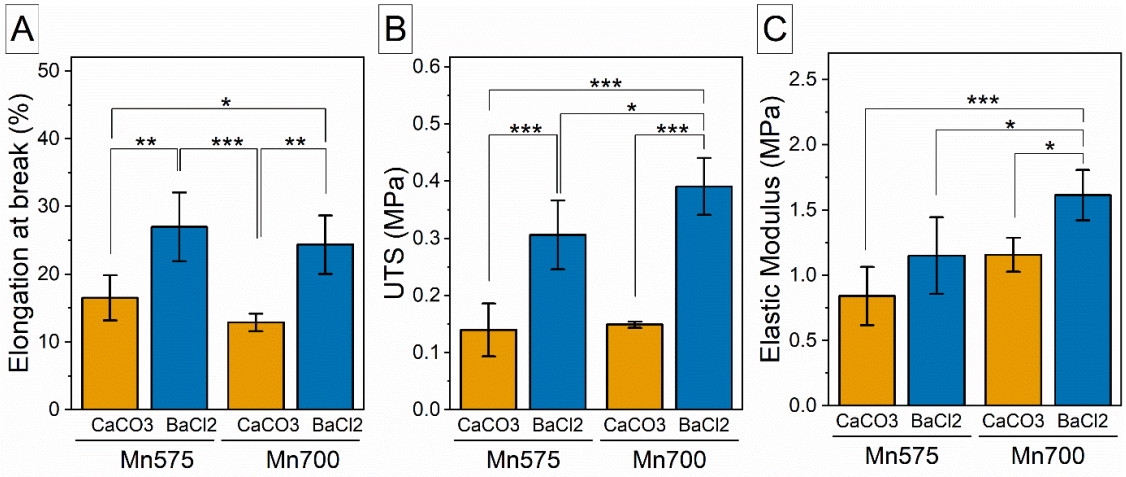


*Figure 6.7: Stretch to failure tensile properties of alginate:PEGDA IPN hydrogel at two different PEGDA molecular weights (Mn 575 and Mn 700) and two different alginate crosslinking agents ($CaCO_3$:GDL and $BaCl_2$). Alginate (3.3% (w/v)), PEGDA (26.6 % (w/v)), photoinitiator (0.5% (w/v)) concentrations were maintained constant. Columns and error bars represent the mean ± S.D (n=5). Statistical significance measured via one-way ANOVA with Tukey post-hoc analysis and represented graphically by * p<0.05, ** p<0.01, *** p<0.001.*

However, given that this hydrogel preparation process involves a two-step crosslinking method were the PEGDA is crosslinked first and then the semi-crosslinked hydrogel is removed from the mould and transferred to a bath of $BaCl_2$ for the alginate to crosslink, the lack of elasticity of the semi-crosslinked hydrogel resulted in several instances of dog-bone sample damage before the transfer to $BaCl_2$. Therefore, in an attempt to improve elasticity several modifications to the hydrogel formulation including the addition of glycerol at 3.5 %(w/v) and 5 %(w/v), and the addition of a higher molecular weight PEGDA (Mn 10000) were investigated. The stretch to failure properties for the different hydrogel formulations are presented in Figure 6.8. The highest elongation at break was observed in the alginate:PEGDA IPN comprising an 80:20 PEGDA 700 to PEGDA 10000 volume ratio. However, despite the increase in elongation this formulation resulted in

lower strength and stiffness values when compared to the alginate:PEGDA IPN hydrogel. The addition of glycerol did not enhance the elongation of the formulation and significantly lower strength values ($p$ = 0.036: 3.5 %(w/v), $p$ = 0.007: 5 %(w/v)) and stiffness ($p$ = 0.024: 3.5 %(w/v)) were observed when compared with the alginate:PEGDA IPN hydrogel. Therefore, due to the unsuccessful attempts at improving the elastic mechanical properties of the alginate:PEGDA hydrogel IPN, the initial hydrogel formulation was maintained as the most suitable formulation.

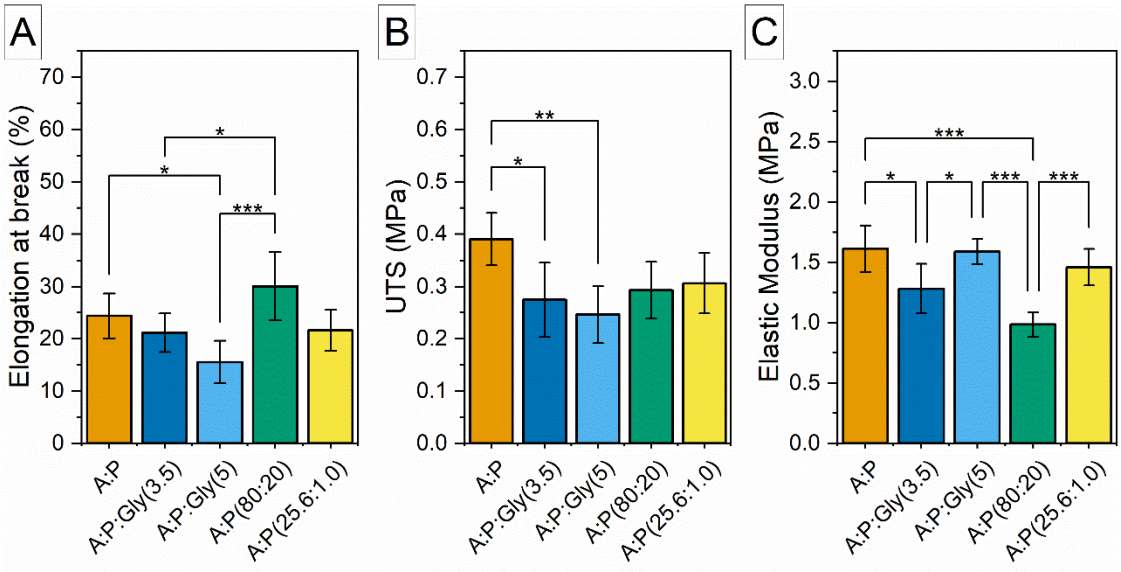


*Figure 6.8: Stretch to failure tensile properties of alginate:PEGDA IPN hydrogel crosslinked with $BaCl_2$ (A:P) in comparison with glycerol addition at 3.5% (w/v) (A:P:Gly(3.5)) and 5% (w/v) (A:P:Gly(5)), and PEGDA Mn10000 at an 80:20 volume ratio with PEGDA 700 (A:P(80:20)) and at 1.0% (w/v) (A:P(25.6:1.0)). Alginate (3.3% (w/v)), photoinitiator (0.5% (w/v)), and $BaCl_2$ (66 mM) concentrations were maintained constant. Columns and error bars represent the mean ± S.D. (n=5). Statistical significance measured via one-way ANOVA with Tukey post-hoc analysis and represented graphically by * p<0.05, ** p<0.01, *** p<0.001.*

### 6.4.2.2. Confined compression stress relaxation measurements

The effects of varying the PEGDA molecular weight and alginate crosslinker type on the mechanical properties of alginate:PEGDA IPN hydrogels were also investigated via confined compression stress relaxation tests. The stress relaxation curves for Mn 575 and Mn 700 are presented in Figure 6.9(A) and (B), respectively. Figure 6.9(C) shows

the peak stress i.e., the maximum stress at the end of the ramp stage, where all four formulations exhibit similar peak stress values. The maximum and minimum peak stress values were observed in PEGDA Mn 575 at 13.53 ±1.78 kPa ($CaCO_3$:GDL) and 10.76 ±3.44 kPa ($BaCl_2$), however none of these values were significantly different from each other ($p$ = 0.475). Similar to previous confined compression stress relaxation data analysis, the aggregate modulus ($H_A$) and the hydraulic permeability ($k$) were determined by utilising the FEBio model in combination with the parameter optimisation routine (Chapter 3 Section 3.2.1). Values for $H_A$ and $k$ are presented in Figure 6.9(D) and (E), respectively. Similar to the peak stress, no significant differences were observed in both the $H_A$ ($p$ = 0.427) and $k$ ($p$ = 0.873) when comparing the different molecular weights and alginate crosslinking agents together. The maximum and minimum $H_A$ values were observed in PEGDA Mn 700 at 156.58 ±1.84 kPa ($CaCO_3$:GDL) and 108.22 ±25.1 kPa ($BaCl_2$). $k$ is in the region of $10^{-11}$ $m^2/Pa{\cdot}s$ for all the different hydrogel formulations, with the $BaCl_2$ crosslinker exhibiting the highest $k$ at 2.67 ±0.56 $\times10^{-11}$ $m^2/Pa{\cdot}s$ (PEGDA Mn 700) and the lowest $k$ at 2.02 ±0.68 $\times10^{-11}$ $m^2/Pa{\cdot}s$ (PEGDA Mn 575).

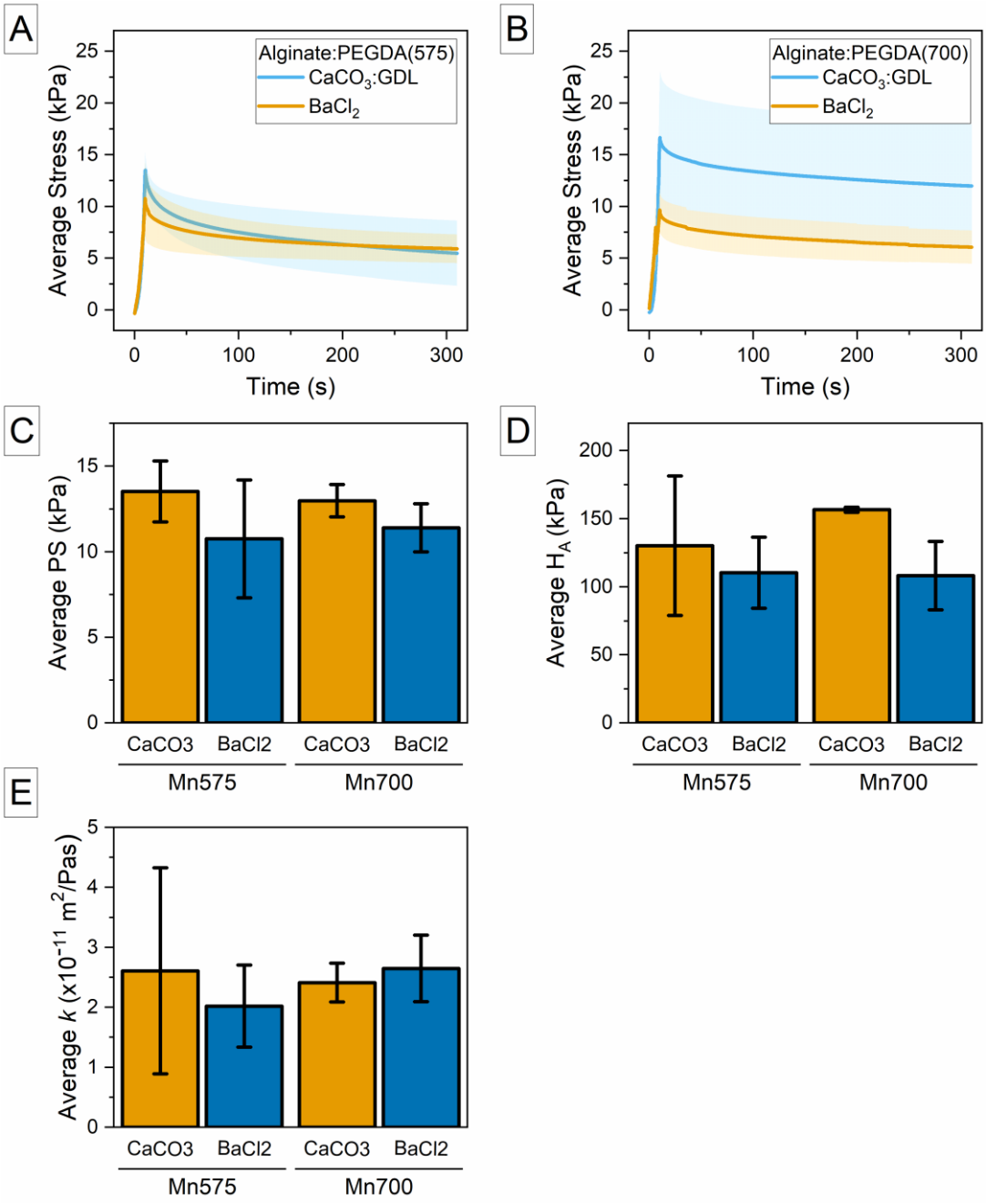


*Figure 6.9: Confined compression stress relaxation curves for alginate:PEGDA IPN hydrogels at two different PEGDA molecular weights: Mn 575 (A) and Mn 700 (B) and two different alginate crosslinking agents ($CaCO_3$:GDL and $BaCl_2$). Bar charts show confined compression properties including (C) average peak stress (PS), (D) average aggregate modulus ($H_A$)), and (E) average hydraulic permeability (k). Data is presented as mean ± S.D (n=3). Statistical significance measured via one-way ANOVA with Tukey post-hoc analysis resulted in no significant differences between molecular weights and alginate crosslinking agents.*

### 6.4.2.3. Mechanical behaviour of alginate:PEGDA IPN hydrogel following *in vitro* incubation in physiological media

To assess the mechanical behaviour of the alginate:PEGDA IPN at physiological conditions, uniaxial tensile stretch to failure (Figure 6.10) and confined compression stress relaxation (Figure 6.11) tests were conducted at consecutive timepoints over an incubation period in calcium-supplemented PBS at 37°C. Uniaxial tensile testing showed a significant decrease in hydrogel elongation (elongation at break, Figure 6.10(A)) ($p$= 0.009 between 0h and 186 h) and ultimate tensile strength (Figure 6.10(B)) ($p$= 0.005 between 0h and 186h, and $p$ = 0.008 between 0h and 336h) at later stages in the incubation period in comparison with the non-incubated hydrogels (0h). However, it should also be noted, that at these later stages variability between samples was quite high as evident from the large error bars. In contrast, no significant differences ($p$ = 0.778) were observed between the different timepoints for gel stiffness as shown in Figure 6.10(C).

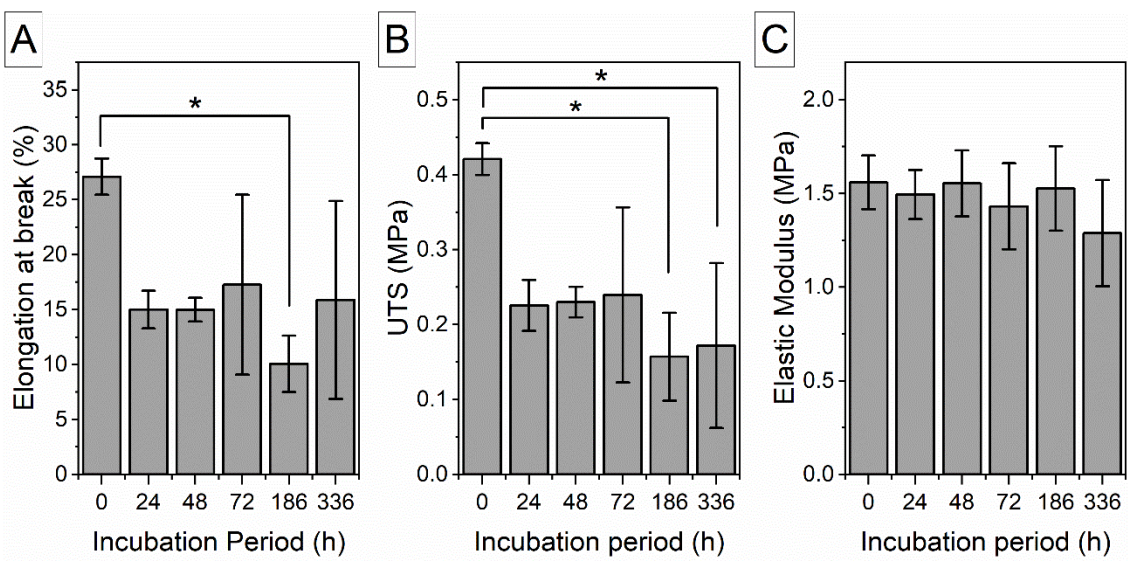


*Figure 6.10: Stretch to failure properties (A) elongation at break, (B) ultimate tensile strength (UTS), and (C) elastic modulus of alginate:PEGDA (3.3%(w/v):26.6%(w/v):66mM $BaCl_2$) over a 2-week incubation period in calcium supplemented PBS (1×PBS+1.8 mM $CaCl_2$) at 37°C. Columns and error bars represent mean ±S.D. (n=3). Statistical significance measured via one-way ANOVA with Tukey post-hoc analysis and represented graphically by * p<0.05.*

Confined compression stress relaxation peak stress, $H_A$, and *k* resulted in no significant differences among the investigated timepoints. A decreasing trend could be observed for peak stress values over the incubation period. However, a large variability among samples was observed for all three properties and at each timepoint.

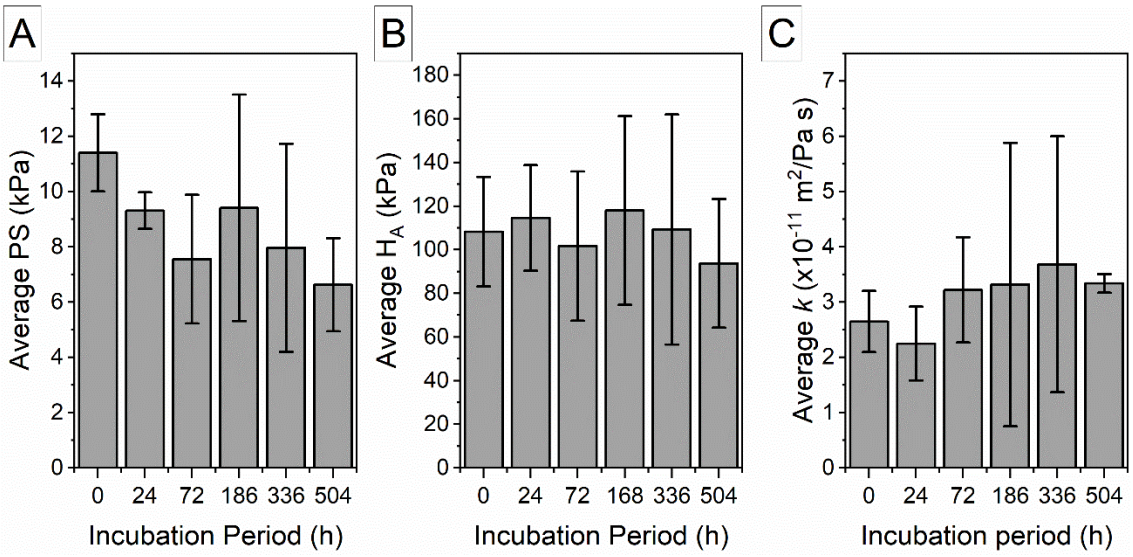


*Figure 6.11: Confined compression stress relaxation properties (A) peak stress (PS), (B) aggregate modulus ($H_A$), and hydraulic permeability (k) of alginate:PEGDA (3.3%(w/v):26.6%(w/v):66mM $BaCl_2$) over a 3-week incubation period in calcium supplemented PBS (1×PBS+1.8 mM $CaCl_2$) at 37°C. Columns and error bars represent the mean ±S.D.(n=3). Statistical significance measured via one-way ANOVA with Tukey post-hoc analysis resulted in no significant differences.*

### 6.4.2.4. Rheological measurements: amplitude and frequency sweeps

Another way of investigating the viscoelastic properties of hydrogels is via small amplitude oscillatory shear rheological measurements. Such tests, in comparison with the dynamic oscillatory frequency sweeps performed in Chapter 4 and Chapter 5, are much more convenient as they work better with soft materials, require smaller sample sizes (thin-disk shaped hydrogels), and offer quick and highly sensitive measurements (can cover a wide range of amplitudes and frequencies without significant vibrational effects) whilst also providing an insight into the hydrogel's architecture, including its degree of crosslinking and changes in its structural behaviour when subjected to a range

of shear stresses, strains or frequencies (Hyland, Taraban and Yu, 2013; Baby, 2020). These tests were performed on both the alginate:PEGDA IPN hydrogel and the single network alginate crosslinked with $CaCO_3$:GDL.

Amplitude sweeps for both hydrogel formulations are presented in Figure 6.12(A) and (C), respectively. The amplitude sweep identifies the linear viscoelastic region (LVER) i.e., the region where the moduli are independent of the input amplitude strain or stress. As shown in Figure 6.12(A), for alginate:$CaCO_3$ this region lies from 0.0001% to 0.05% shear strain, up until the point where the moduli change with increasing strain. Within this region, the storage modulus (G') is approximately 13 kPa whereas the loss modulus (G'') is approximately 1 kPa. The point of intersection where the G' and G'' meet is at 0.65% shear strain. For the alginate:PEGDA IPN hydrogel (Figure 6.12(A)) the LVER ranges from 0.0001% to 0.03%, beyond this the storage modulus decreases with increasing strain. G' within the LVER is approximately 60 kPa whereas G'' is approximately 4 kPa. The point where G' and G'' intersect lies at 34.2% shear strain.

By selecting a shear strain value within the LVER (0.01%), frequency sweeps were conducted to assess the modulus response to a frequency ranging from 0.1 Hz to 10 Hz. The frequency sweeps for both hydrogel formulations are presented in Figure 6.12(B) and (D). In both cases, the G' is greater than the G'' for all frequencies, which is a typical viscoelastic hydrogel behaviour. The G' exhibits a frequency dependent response, it increases with increasing frequency, from 12.7 ± 0.5 kPa at 0.1 Hz to 16.1 ± 0.2 kPa at 10 Hz for alginate alone and from 141.6 ±60.5 kPa at 0.1 Hz to 160.7 ±66.2 kPa at 10 Hz for the IPN hydrogel. The G'' exhibits a more stable response with 1.3 ± 0.2 kPa at 0.1 Hz and 1.5 ± 0.1 kPa at 10 Hz for the alginate alone and 24.2 ± 12.7 kPa at 0.1 Hz and 11.7 ± 5.3 kPa at 10 Hz.

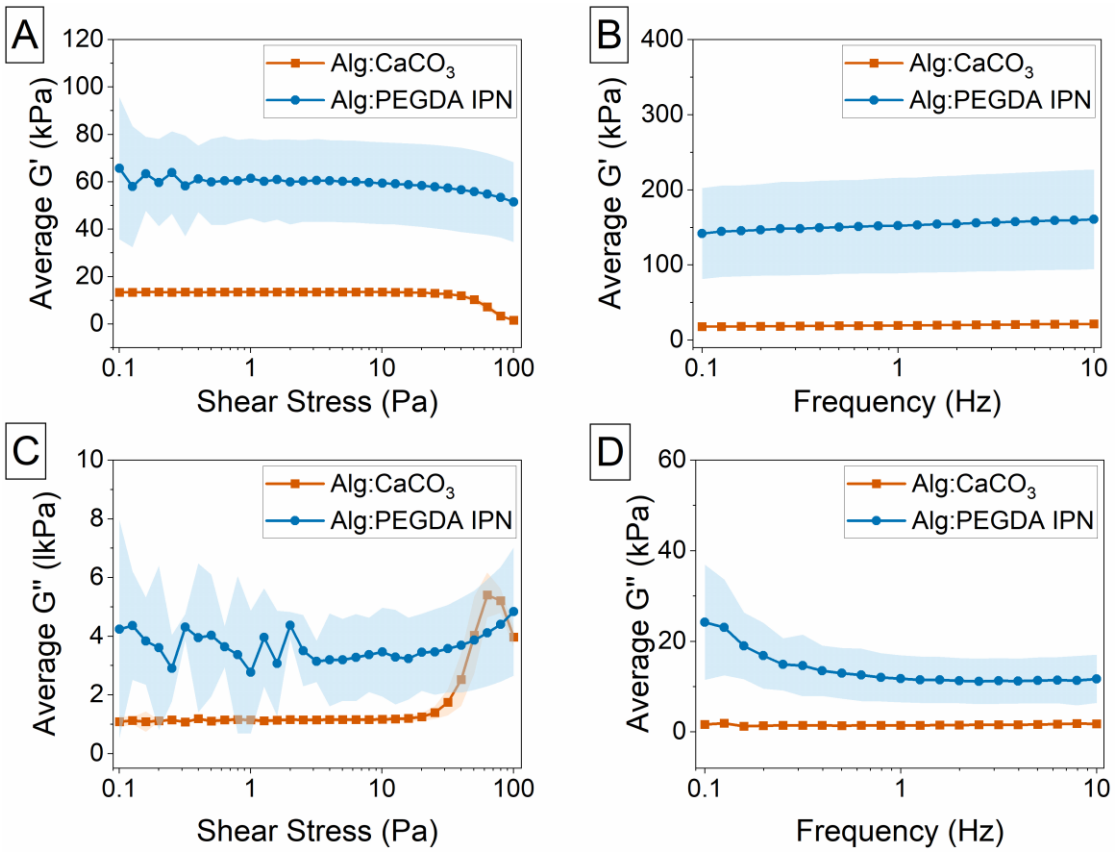


*Figure 6.12: Rheological measurements of single network alginate (3.3%(w/v) alginate: 66mM $CaCO_3$:133.3 mM GDL) and alginate:PEGDA IPN (3.3%(w/v):26.6%(w/v):66mM $BaCl_2$) including amplitude sweeps showing (A) storage modulus (G'), (C) loss modulus (G'') as a function of shear stress and frequency sweeps showing (B) storage modulus (G') and (D) loss modulus (G'') as a function of frequency. X-axes are in logarithmic ($log_{10}$) form. Data points and shaded error bars represent the mean ± S.D. (n=3).*

### 6.4.3. Physical characterisation

#### 6.4.3.1. Swelling and degradation profiles

In order to evaluate the hydrogel's behaviour in physiologically relevant conditions, fluid uptake and gel degradation studies were performed on both single-network alginate hydrogels (alginate:$CaCO_3$ and alginate:$BaCl_2$) and the alginate:PEGDA IPN hydrogel by measuring mass differences over an incubation period. For swelling analysis (Figure 6.13(A)), the hydrogels were first freeze-dried, then incubated in calcium-supplemented PBS at 37 °C for 21 days. From Figure 6.13(A), it is evident that the alginate:PEGDA IPN hydrogel exhibits the lowest degree of swelling when compared with the single-

network hydrogels and reaches equilibrium swelling at the 2-week timepoint (336 hours), beyond this no significant differences were observed in the water uptake ratio when comparing the means for week 2, 3, and 4 (*p = 0.472;* one-way *ANOVA* with Tukey post-hoc*)*. On the contrary, alginate:$CaCO_3$ and alginate:$BaCl_2$ both exhibit an increasing fluid uptake until the end of the incubation period.

For degradation, mass variations were observed over a 1-week incubation period as shown in Figure 6.13(B). From this, it is evident that alginate:$CaCO_3$ hydrogels exhibited the highest degree of mass loss with a maximum observed after 72 hours. The alginate:PEGDA IPN hydrogel exhibited a lower degree of mass loss than the alginate:$CaCO_3$. An increase in mass loss at the end of the incubation period could be observed, however, the variability between the samples at the 1-week timepoint is quite considerable as evident from the large error bar. On the contrary to the two other hydrogel formulations, alginate:$BaCl_2$ hydrogels exhibited a negative mass loss over the whole incubation period.

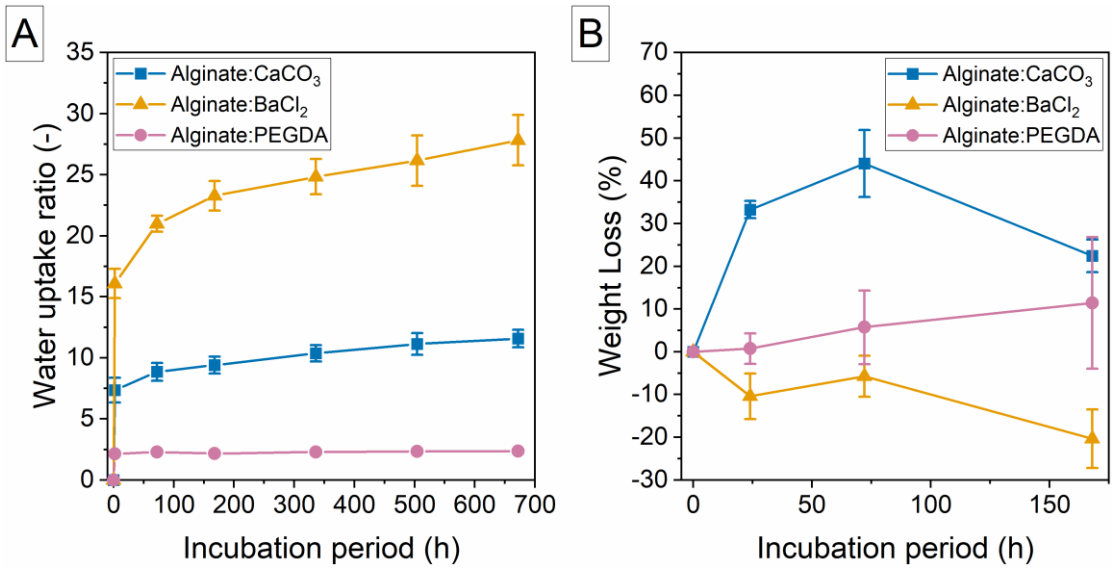


*Figure 6.13: Swelling (A) and degradation (B) profiles of single-network alginate (3.3% (w/v)) hydrogels crosslinked with 66 mM $CaCO_3$:GDL and $BaCl_2$, and alginate:PEGDA IPN (3.3% (w/v):26.6% (w/v):66mM $BaCl_2$) over an incubation period in calcium supplemented PBS (1×PBS+1.8 mM $CaCl_2$) at 37°C. Data points and error bars represent the mean ±S.D. (n=6).*

#### 6.4.3.2. Morphological analysis: Scanning Electron Microscopy (SEM) imaging.

The morphological structure of alginate alone (alginate:$BaCl_2$ and alginate:$CaCO_3$) and alginate:PEGDA IPN hydrogels was analysed via SEM by imaging both the surface and cross-sections of freeze-dried samples (Figure 6.14).

Surface images of alginate:$BaCl_2$ (Figure 6.14(A)) and the alginate:PEGDA IPN (Figure 6.14(E)) exhibited a relatively smooth and flat surface whereas for alginate:$CaCO_3$ a porous structure was evident at some surface sections as shown in Figure 6.14(C). Cross-sectional views showed that all three hydrogel formulations comprise a porous structure. Based on these cross-sectional images, the gel porosity varies from a highly open structure of alginate:$BaCl_2$ hydrogels (Figure 6.14(B)) to a slightly reduced pore structure of alginate:$CaCO_3$ (Figure 6.14(D) to tiny pores of alginate:PEGDA IPN (Figure 6.14(F)).

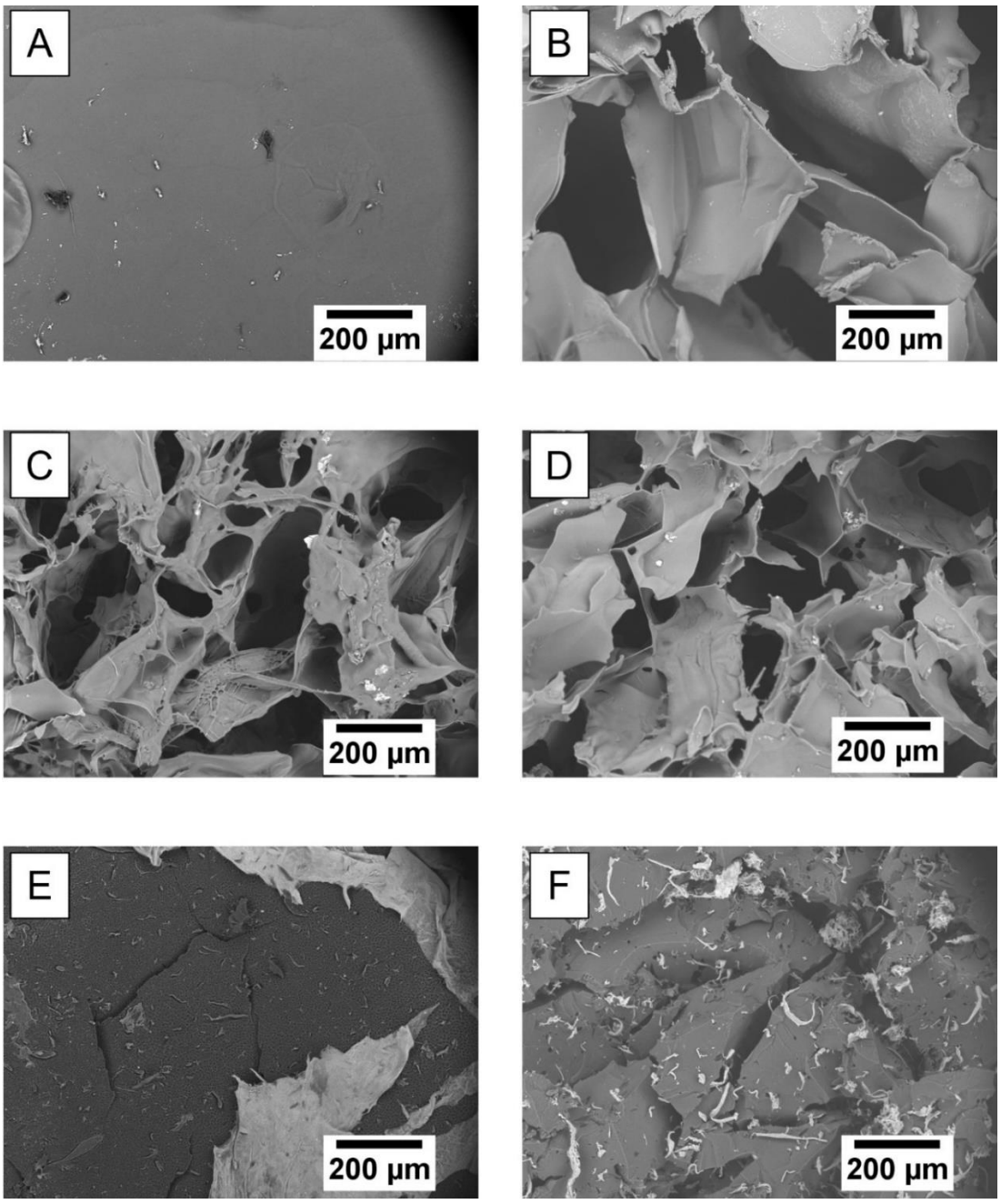


*Figure 6.14: SEM micrographs of freeze-dried single-network alginate (3.3% (w/v)) hydrogels crosslinked with 66 mM $BaCl_2$ (A,B) and $CaCO_3$:GDL (C,D), and alginate:PEGDA IPN (3.3%(w/v):26.6%(w/v):66mM $BaCl_2$) (E,F). (A, C, E) show surface images, and (B, D, F) show cross-sectional images.*

### 6.4.4. Tubular structure fabrication using an agarose sacrificial scaffold

#### 6.4.4.1. Moulding process: visual observations

An agarose hydrogel (2.5 %(w/v)) was used as a sacrificial cylindrical mould to fabricate alginate:PEGDA IPN hydrogel tubular structures. Two types of conduits with different dimensions were fabricated including a set with an average lumen diameter of 11.45 ±0.10 mm, average wall thickness of 1.68 ± 0.06 mm, and average length of 29.29 ±0.41 mm, referred to hereafter as small dimeter tubular structures (Figure 6.15), and another set with an average lumen of 14.43 ±0.36 mm, average wall thickness of 2.12 ±0.07 mm, and average length of 28.76 ±1.09 mm, referred to hereafter as large diameter tubular structures (Figure 6.16). From visual observations this moulding technique resulted in relatively straight, uniformly crosslinked, free-standing tubular structures for both set of dimensions.

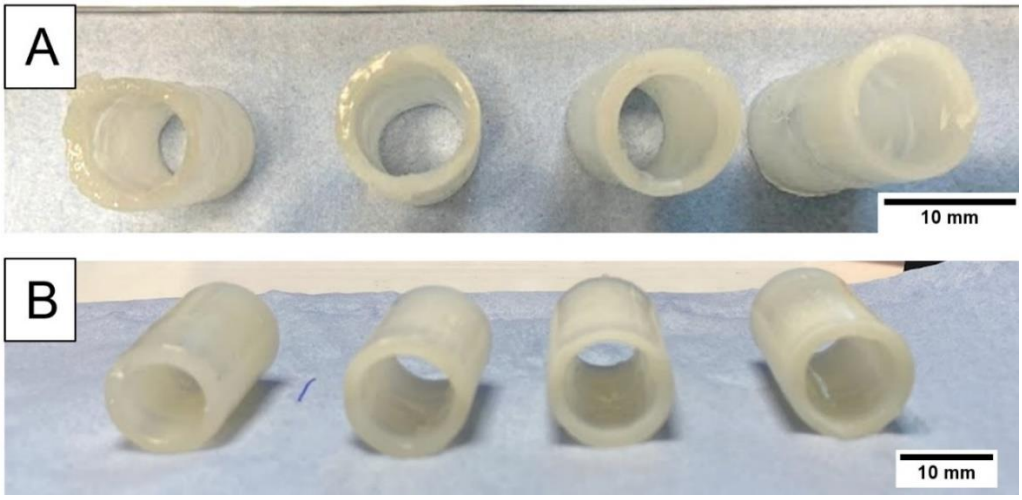


*Figure 6.15: Small diameter alginate:PEGDA IPN hydrogel (3.3 %(w/v):26.6 %(w/v):66 mM $BaCl_2$) tubular structures fabricated using an agarose sacrificial scaffold having an average lumen of 11.45 ± 0.10 mm, average wall thickness of 1.68 ± 0.06 mm, and average length of 29.29 ± 0.41 mm, (A) top view and (B) side view.*

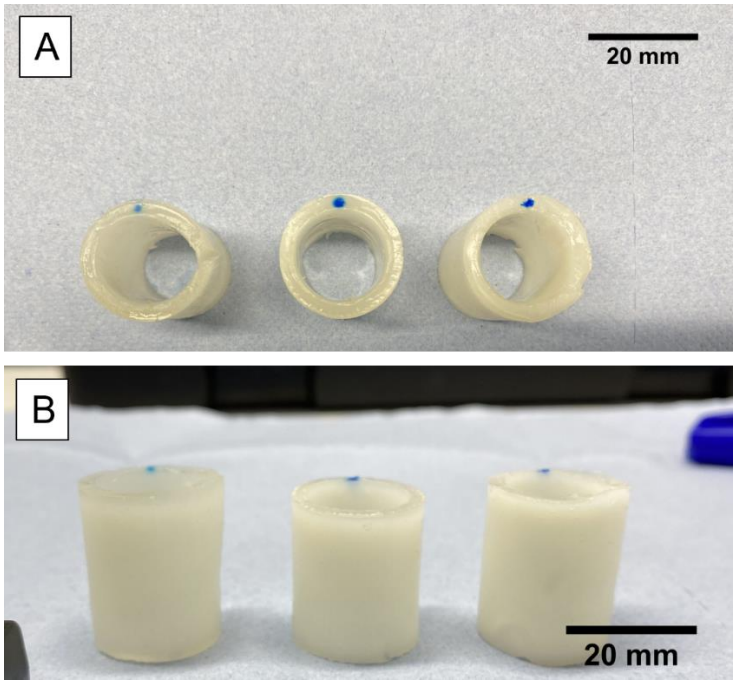


*Figure 6.16: Large diameter alginate:PEGDA IPN hydrogel (3.3 %(w/v):26.6 %(w/v):66 mM $BaCl_2$) tubular structures fabricated using an agarose sacrificial scaffold having an average lumen of 14.43 ±0.36 mm, average wall thickness of 2.12 ±0.07 mm, and average length of 28.76 ±1.09 mm, (A) top view and (B) side view.*

#### 6.4.4.2. Compression testing of tubular structures

To characterise the mechanical behaviour of the moulded tubular structures, samples were placed horizontally between two compression plates and compressed to the limit of the testing machine i.e., a total travel distance of 3.5 mm. This accounted to approximately 20% to 25% compression relative to the outer diameter of each tube. The load versus diameter reduction ratio of both sets of tubular structures are presented in Figure 6.17. Up to this displacement, no evidence of sample breakage could be observed as can be seen by the almost straight-line behaviour in both plots. The difference between the two sets of structures is the maximum load that they could withstand, where the large diameter structures exhibited a maximum load of 1.18 ±0.32 N whilst the small diameter structures exhibited a maximum load of 0.48 ±0.08 N.

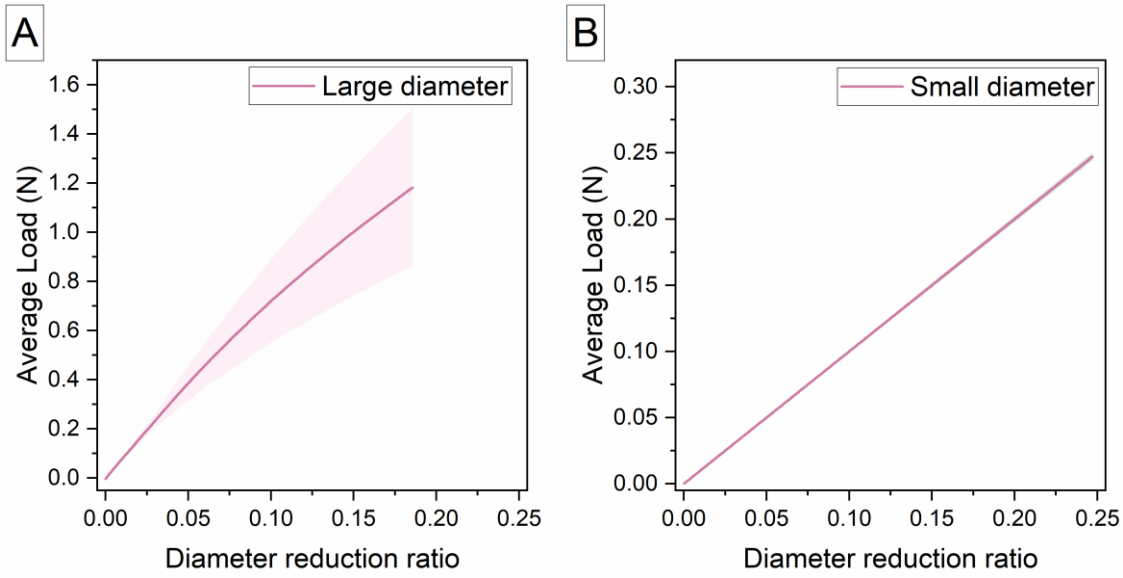


*Figure 6.17: Compression of alginate:PEGDA IPN hydrogel (3.3 %(w/v):26.6 %(w/v):66 mM $BaCl_2$) tubular structures (A) average lumen 14.43 ± 0.36 mm (large diameter) and (B) average lumen 11.45 ± 0.10 mm (small diameter) up to 3.5 mm relative to the outer diameter at a compression rate of 1 mm/min. Data represents the mean ± S.D. (n=3).*

## 6.5. Discussion

Single-network hydrogels such as ionically crosslinked alginate are mechanically weak and therefore require reinforcement to enhance their mechanical properties (Sun *et al.*, 2012; Costa and Mano, 2015; Xu, Dai and Hong, 2019; Chimene, Kaunas and Gaharwar, 2020). In this work, an alginate:PEGDA IPN hydrogel was developed by varying PEGDA concentration (13.3 %(w/v) and 26.6 %(w/v)) and molecular weight (Mn 575 and Mn700), and by utilising two types of alginate crosslinking agents ($CaCO_3$:GDL and $BaCl_2$) to obtain a hydrogel formulation with mechanical properties close to the human aorta. The mechanical properties of the hydrogel were characterised via tensile, confined compression stress relaxation, and rheological analysis. An incubation study was also performed to assess the hydrogel's stability in physiologically relevant environments. Finally, the hydrogel formulation that showed optimal mechanical behaviour was used to mould tubular conduits with similar dimensions to the human aorta as potential substitutes to existing aortic grafts.

### 6.5.1. Development of alginate:PEGDA IPN and the effect of composition and fabrication strategy on the hydrogel's elastic behaviour

The preparation method of alginate:PEGDA IPN hydrogels depends on several factors, primarily UV source parameters (e.g., intensity, wavelength, exposure area), photoinitiator, alginate crosslinker, and PEGDA molecular weight and concentration.

Herein, the light sources available for photocrosslinking of the PEGDA have a centred wavelength in the region of 365 nm, therefore a photoinitiator with an absorption spectrum that overlaps the UV light emission spectrum was considered (Fairbanks *et al.*, 2009). I2959 meets this criterion since it exhibits peak absorption at 276 nm in addition to a narrow range that overlaps 365 nm (as shown in Appendix 3: Absorption spectra of the photoinitiators and photoblocker used to fabricate the alginate:PEGDA hydrogels.: Figure 1). Together with its water solubility (< 2 %(w/v)), high compatibility with most photocurable polymers, and low cell cytotoxicity when used below 0.5 %(w/v) (Han *et al.*, 2020; Tomal and Ortyl, 2020; Xu *et al.*, 2020), I2959 has attracted significant interest in hydrogel fabrication for tissue engineering applications.

Visual observations in Section 6.4.1 demonstrated the importance of the UV light source, with different intensities resulting in different exposure times and gel shape formation. For instance, the UV torch used to prepare preliminary hydrogel discs has an intensity of 200 mW/cm$^2$ according to the manufacturer's data sheet, and therefore a low concentration of photoinitiator (0.05 %(w/v)) was sufficient in fabricating hydrogels within 10 minutes, parameters which were also reported in several investigations (Hockaday *et al.*, 2012; Hong *et al.*, 2015). However, due to its small exposure area (22 mm in diameter) this could not be used to fabricate large samples for tensile testing (110 mm × 19 mm), and different UV sources had to be explored. The intensity of the selected UV lamp was measured to be 2.2 mW/cm$^2$ at a distance of 1 cm from the sample (Section 6.4.1.2) hence, longer exposure times (30 minutes) to crosslink a single dog-

bone specimen for tensile testing were required. Additionally, the photoinitiator concentration had to be increased to the maximum cell compatible limit of 0.5 %(w/v) in order to maintain the UV exposure time within a 30-minute window.

This long exposure time resulted in another limitation when using $CaCO_3$:GDL as the alginate crosslinker, since despite being a slow-gelling crosslinker, the alginate was crosslinking at a faster rate (within 15 minutes) than the PEGDA. The $CaCO_3$:GDL crosslinking time could be controlled by lowering the concentration (less than a final concentration of 66 mM), but this has been reported to lower the mechanical properties of the hydrogel (Growney Kalaf *et al.*, 2016). However, despite $CaCO_3$:GDL being identified as the most suitable crosslinker to prepare alginate-alone and alginate:elastin hydrogels due to its shape retaining and gel uniformity abilities (Chapter 5), these properties were not essential anymore given that the quasi-crosslinked hydrogel (after PEGDA crosslinking) was able to maintain its shape. This enabled the use of fast gelling crosslinking agents, such as $CaCl_2$. However, $CaCl_2$ and other calcium-based crosslinkers have already been investigated in several alginate:PEGDA IPN hydrogel preparation protocols (Yu *et al.*, 2018; de Melo *et al.*, 2019; Krishnamoorthy, Zhang and Xu, 2019), therefore, in the present work $BaCl_2$ was investigated instead. This is mostly because as discussed in Chapter 5, in theory barium crosslinked alginate should enhance the mechanical properties due to its greater affinity to alginate (Mørch *et al.*, 2006), and its larger ionic radius forming tighter crosslinks thus, stronger ionic bonds (Mørch *et al.*, 2006; Jejurikar *et al.*, 2011). This was evident in the tensile test results (Figure 6.7) where the alginate:PEGDA(700) IPN crosslinked with $BaCl_2$ resulted in significantly higher strength ($p < 0.05$) and stiffness ($p = 0.02$) values (0.39 ±0.05 MPa and 1.61 ±0.19 MPa, respectively), than its $CaCO_3$:GDL crosslinked IPN counterpart (0.15 ±0.05 MPa and 1.16 ±0.13 MPa, respectively).

The mechanical properties of PEGDA-based hydrogels have been reported to be greatly influenced by PEG molecular weight and concentration (Mazzoccoli *et al.*, 2010; Nguyen *et al.*, 2012; Rekowska *et al.*, 2022). In this study, two molecular weights were investigated: Mn 575 and Mn 700, with tensile stretch to failure results showing a significant difference in both strength ($p$ = 0.042) and stiffness ($p$ = 0.018) between the two molecular weights when $BaCl_2$ was used as the alginate crosslinker. Contrarily, the elongation was not significantly affected by the change in molecular weight, contradicting studies which have reported an increase in extensibility with increasing molecular weight (Nguyen *et al.*, 2012; Hong *et al.*, 2015; Rekowska *et al.*, 2022). However, it should be noted that these investigations involved a wider range of PEGDA molecular weights (508 Da to 10 kDa (Nguyen *et al.*, 2012), 6 kDa to 20 kDa (Hong *et al.*, 2015), 4 kDa to 20 kDa (Rekowska *et al.*, 2022)) than the ones investigated here (Mn 575 versus Mn 700). Therefore, in an attempt to improve the alginate:PEGDA IPN elongation, following the study by Mazzaccoli *et al.,* (2010), a blend of PEGDA Mn 700 and PEGDA Mn 10000 (A:P(80:20) and A:P (25.6 %(w/v):1.0 %(w/v)) in Figure 6.8) was also considered and an increase in elongation at break was indeed observed, however at the expense of strength and stiffness.

The addition of a plasticizer such as glycerol was also considered in an attempt to preserve hydration of the hydrogel, and therefore facilitate the transfer of the semi-crosslinked hydrogel from the mould to the $BaCl_2$ bath. Alginate in combination with glycerol has been reported to interact with the alginate polymer chain by forcing them apart thereby enhancing hydrogel flexibility (Olivas and Barbosa-Cánovas, 2008; Pereira *et al.*, 2013). However, the tensile test results shown in Figure 6.8(A) contradict this since a significant decrease in elongation at break ($p$ = 0.047*)* was obtained when 5 %(w/v) glycerol was added to alginate:PEGDA IPN hydrogel. In addition to this, a significant decrease in strength for both 3.5 %(w/v) ($p$ = 0.036*)* and 5 %(w/v) ($p$ = 0.007*)* glycerol

was also observed (Figure 6.8(B)). Given that this is a multicomponent hydrogel formulation, with a much lower alginate concentration than PEGDA, the incorporation of glycerol to affect the overall mechanical properties might require further modifications in both concentrations and preparation method.

Contrary to the molecular weight, increasing the PEGDA (Mn 700) concentration from 13.3 %(w/v) to 26.6 %(w/v) contributed to a significant decrease in hydrogel elongation ($p = 0.019$) and a significant increase in both strength ($p < 0.05$) and stiffness ($p < 0.05$) (Figure 6.6). This may be attributed to the increase in acrylate end groups availability for polymerisation as a result of a higher monomer concentration which leads to a higher crosslinking density, resulting in stronger and stiffer hydrogels. This is consistent with most PEGDA hydrogel investigations including the study by Mazzaccoli *et al.,* (2010), where doubling the monomer concentration from 20% to 40% resulted in three times the mechanical strength.

### 6.5.2. The mechanical properties of alginate:PEGDA IPN hydrogel in comparison with ionically crosslinked alginate and aortic tissue

The key objective of this work was to enhance the mechanical properties of alginate-based hydrogels to closely resemble the mechanical properties of the native aorta. Comparing the elastic properties of ionically crosslinked alginate and alginate:elastin hydrogels (results from Chapter 5 Section 5.4.3) with the alginate:PEGDA IPN hydrogel at a 26.6 %(w/v) PEGDA Mn 700 concentration crosslinked with $BaCl_2$ (Table 6.1), it is evident that both the strength and stiffness increased considerably upon IPN formation, however at the expense of elongation. Despite this decrease in elongation at break, when comparing the alginate:PEGDA IPN stretch to failure properties with aortic tissue data from the literature (Table 6.1), similar elastic properties to the native aorta at physiological conditions (Vallabhaneni *et al.*, 2004) were obtained. Table 6.1 also includes Dacron® graft data from Chapter 4 which shows the discrepancy in mechanical

properties from native aortic tissue, where the elastic modulus in the circumferential direction i.e., the direction where the aorta must radially expand to accommodate changes in pulsatile pressure, is ten times stiffer than healthy aortic tissue. In addition to elastic properties, this alginate:PEGDA IPN hydrogel formulation (3.3 %(w/v) alginate: 26.6 %(w/v) PEGDA: 0.5 %(w/v) I2959) comprises a polymer content of approximately 30% which is within the range of dry weight content present in arterial tissue (Sommer, 2008)).

*Table 6.1: Comparing the tensile stretch to failure properties of alginate-based hydrogels and commercially available Dacron® grafts with aortic tissue data from the literature at a crosshead speed of 1 mm/min for alginate-based hydrogels and aortic tissue, and 50 mm/min for Dacron® grafts. Data is presented as the mean ± S.D. (UTS: ultimate tensile strength, $\varepsilon_B$: elongation at break, EM: elastic modulus, PM: physiological modulus, Circ: circumferential, and Long: longitudinal directions).*

| **Study** | **Material** | **Mechanical Properties** | | | |
|---|---|---|---|---|---|
| | | **UTS (MPa)** | **$\varepsilon_B$ (%)** | **EM (MPa)** | **PM (MPa)** |
| Current work | Alginate (3.3%:66 mM $CaCO_3$) | 0.02 ±0.006 | 51.60 ±11.66 | 0.05 ± 0.004 | — |
| | Alginate:Elastin (3.3%:0.3% 66 mM $CaCO_3$) | 0.04 ±0.002 | 75.55 ± 0.54 | 0.06 ±0.004 | — |
| | Alginate:PEGDA IPN (3.3%(w/v):26.6%(w/v): 66mM $BaCl_2$) | 0.39 ±0.05 | 24.4 ±4.33 | 1.61 ±0.19 | — |
| | Dacron® graft (Circ) | 31.23 ±6.17 | 84.11 ±1.85 | — | 9.92 ±0.56 |
| (Vallabhaneni *et al.*, 2004) | Abdominal Aorta (Human) Circ | 0.61 ±0.07 | 29.0 ±4.0 | — | 1.82 ±0.10 |
| | Abdominal Aorta (Human) Long | 1.30 ± 0.11 | 33.0 ±4.0 | — | 1.38 ±0.12 |

Given that the physiological loads on blood vessels are in a state of tension (Camasão and Mantovani, 2021), tensile testing of hydrogels is the most representative mechanical characterisation method of *in vivo* conditions. However, for comparative purposes,

confined compression stress relaxation tests were still performed on the alginate:PEGDA IPN to be able to assess any differences to the single network alginate hydrogel viscoelastic behaviour discussed in Chapter 5. Assessing viscoelasticity is essential in the material design process of vascular grafts, since blood vessels exhibit a viscoelastic response that is crucial in aortic biomechanics for the proper preservation of the Windkessel effect i.e., the dampening of pulsatile blood flow from the point of emergence to a continuous distal flow as it travels towards the extremities. From Figure 6.9(A) and (B), the alginate:PEGDA IPN hydrogel under confined compression displayed a typical stress relaxation behaviour irrespective of PEGDA molecular weight or alginate crosslinking agent. Contrary to tensile test results, confined compression properties including peaks stress, aggregate modulus, and hydraulic permeability resulted in no significant differences between PEGDA molecular weight and alginate crosslinker (Figure 6.9(C) –(D)).

Another way of characterising the viscoelastic behaviour of hydrogels is through shear rheology under small amplitude oscillatory sweeps whilst considering physiological frequencies (1 Hz). This method requires much less material than dynamic tensile testing (similar to the performed in Chapter 4 and Chapter 5 on Dacron® and ionically crosslinked alginate), however it does not represent the tensile conditions of blood vessel, but it could be related to the aortic wall shear stress as a result of blood flow. Figure 6.12 includes data for both single-network alginate hydrogel crosslinked with $CaCO_3$:GDL and the alginate:PEGDA IPN. The latter resulted in higher storage and loss moduli than the single-network alginate hydrogel in both amplitude (5 times increase) and frequency (10 times increase) sweeps. In frequency sweeps, both hydrogel formulations exhibited an increase in storage modulus with increasing frequency, therefore showing frequency-dependent mechanical properties which is a common characteristic of soft tissue mechanical behaviour (Zhijie, Mark and Naomi, 2016). Herein, the amplitude sweeps

were conducted at shear stresses ranging from 0.01 Pa to 100 Pa, and the alginate:PEGDA IPN showed no evidence of polymer network breakdown until the end of this range (Figure 6.12(A) and (C)). This suggest that the material is suitable to withstand physiological wall shear stresses present in the aorta which have been reported to be in the range between 1 and 2.5 Pa in the aortic arch - descending aortic regions (Callaghan and Grieve, 2018).

### 6.5.3. Incubation effect on the physical and mechanical behaviour of alginate:PEGDA IPN hydrogel

As discussed in Chapter 5 for ionically crosslinked alginate hydrogels, a major limitation of using an ICE IPN is the susceptibility of the alginate to lose its stability due to the exchange of divalent cations with sodium ions present in the surrounding physiological media (Lee and Mooney, 2012; Krishnamoorthy, Zhang and Xu, 2019). This would adversely impact the overall mechanical properties of the IPN, therefore assessing the mechanical properties over an incubation period under physiological conditions is essential in gaining insight on how vascular grafts made from this hydrogel formulation would potentially behave *in vivo*. In this work, both tensile tests and confined compression stress relaxation tests were performed on hydrogels incubated in calcium-supplemented PBS at 37°C over a 2-week and 3-week period, respectively. Uniaxial tensile test stretch to failure properties showed a decrease in hydrogel elongation and tensile strength throughout incubation, but no differences were observed in hydrogel stiffness (Figure 6.10). As for confined compression no significant differences in any of the parameters at each timepoint could be determined, however sample variability was an issue in this experiment as denoted by the large error bars (Figure 6.11). Despite showing an almost stable mechanical behaviour, this study is too simplistic in comparison to what goes on *in vivo*, where other factors might influence the material's overall mechanical behaviour.

Apart from evaluating the mechanical behaviour, swelling and degradation studies were also performed on alginate:PEGDA IPN hydrogel discs in comparison to single-network alginate crosslinked with $CaCO_3$:GDL or $BaCl_2$. It is important to note that the swelling experiments were performed on freeze-dried hydrogels, therefore the water content from the hydrogels was completely removed before measuring the dry mass ($m_d$). From Figure 6.13(A) it is evident that the single-network alginate hydrogels exhibit a larger degree of fluid uptake than the alginate:PEGDA IPN, and the latter maintained a stable absorption from the 2-hour timepoint onwards. This low fluid uptake may be attributed to the high crosslinking density arising from the higher polymer content of the IPN, which is approximately 30 %(w/v) as opposed to 3.3 %(w/v) for single-networked alginate (Zhang *et al.*, 2021; Asohan *et al.*, 2022). In line with this, SEM imaging of the freeze-dried samples prior to incubation, presented in Figure 6.14, also show a denser structure accompanied by smaller pores for the alginate:PEGDA hydrogel (Figure 6.14(E) and (F)) when compared with the alginate alone hydrogels (Figure 6.14(A)-(D)).

Additionally, degradation analysis (Figure 6.13(B)) also showed minimal mass loss for the alginate:PEGDA over a 1-week period suggesting that the IPN matrix is mostly preserved during incubation contributing to the low fluid absorption. At the 1-week time point a high degree of variability in sample mass was observed arising from the freeze-drying process which weakened the samples and proved challenging when handling. Interestingly, the single-networked hydrogels demonstrated contradictory degradation behaviour when compared with each other. Alginate:$CaCO_3$ exhibited mass loss over the incubation period, reaching a peak at the 72-hour timepoint, and then decreasing again at 1 week. This behaviour might be attributed to the dissolution of the alginate matrix due to the exchange of calcium ions with the surrounding chelating agents present in the PBS, but the calcium addition in the media might have promoted further crosslinking between the 72-hour and 1-week timepoints contributing to the decrease in

mass loss observed at week 1. On the contrary, alginate:$BaCl_2$ exhibited a negative mass loss throughout the 1-week period indicating an increase in mass. As discussed in Chapter 5, barium ions are bigger in size than calcium ions and can attach to both G and M residues, therefore producing tighter and stronger crosslinks between alginate chains. This slows down the alginate hydrogel dissolution that typically arises from calcium ion exchange, resulting in a more stable hydrogel in physiological media. Moreover, the additional calcium ions present in the incubation media (1.8 mM $CaCl_2$) might have promoted further crosslinking of the alginate hydrogel by acting as a type of secondary crosslinking stage, therefore contributing to the increase in hydrogel mass (Antunes *et al.*, 2021).

### 6.5.4. Alginate:PEGDA IPN hydrogel as a potential vascular graft material substitute: fabrication of tubular conduits

Apart from closely replicating the mechanical properties of aortic tissue, the hydrogel formulation must also be suitable in producing tubular structures to potentially be implemented as aortic graft substitutes. The use of a sacrificial mould or template to fabricate complex structures including tubular structures has been widely investigated (Gargava *et al.*, 2019; Lee *et al.*, 2019; Antunes *et al.*, 2021; Chen *et al.*, 2021). Therefore, this method was implemented by using a simple set-up comprising polypropylene syringes and an agarose hydrogel as the sacrificial mould (Figure 6.2). Agarose was selected due to its thermo-responsive properties that enable hydrogel dissolution at high temperatures, therefore facilitating tubular conduit formation. Moreover, according to the manufacturer's data sheet the agarose used in this work has a gel strength greater than 1200 g/cm$^2$ at 1 %(w/v), herein 2.5 %(w/v) was used resulting, indeed, in robust cylindrical hydrogels. This method was successful in fabricating free-standing, tubular conduits with different lumen and wall thickness dimensions, as shown in Figure 6.15 (small lumen: 11.45 ±0.10 mm) and Figure 6.16 (large lumen:

14.43 ±0.36 mm). The dimensions of both structures correspond with sections along the aortic tree. In the review by Humphrey and Holzapfel (2012), the *in vivo* lumen of the thoracic aorta and infrarenal aorta were reported to be in the range of 16 – 17 mm and 12 – 15 mm, respectively. The wall thickness of the tubular conduits for the smaller lumen vessel was at 1.68 ±0.06 mm and 2.12 ±0.07 mm for the larger lumen structures. According to Humphrey and Holzapfel (2012), the thoracic and infrarenal aorta have wall thicknesses between 1.6 – 1.7 mm and 1.4 – 1.5 mm, respectively. However, larger wall thicknesses closer to 2 mm and above (depending on age) have also been reported (Rosero *et al.*, 2011). Despite these dimensions being within range of native vessels, the dimensions of the tubular conduits fabricated using this method remain restricted by the size of polypropylene syringes used. Therefore, to accommodate various dimensions and thus potentially develop patient-specific grafts, a custom designed syringe would have to be developed. Another attractive option would be to move beyond traditional fabrication methods like moulding, and explore the option of advanced manufacturing techniques, namely 3D-printing.

In terms of vessel robustness, compression tests were performed to evaluate the maximum radial load that the vessel can withstand prior to rupture, similar to the investigation carried out by Zhou *et al.,* (2019). This is a crucial parameter since for optimal function of the aorta, the graft must exhibit durability and be able to withstand mechanical loading exerted by high pulsatile pressures. As shown in Figure 6.17 both vessels were able to withstand loading without breaking up to 3.5 mm compression with respect to the outer diameter, which corresponds to approximately 20% - 25% of the vessel size. However, this method was limited to the travel distance of the testing instrument, and therefore the load and displacement corresponding to failure could not be determined.

## 6.6. Conclusions

In this chapter, in order to enhance the mechanical performance of ionically crosslinked alginate, and thereby develop a biomaterial that closely mimics the mechanical behaviour of the native aorta, a secondary monomer, PEGDA, was successfully incorporated to produce an ionic covalent entanglement interpenetrating polymer network (ICE IPN) as a potential aortic graft substitute.

Different variants of the IPN hydrogel were investigated by altering (i) the PEGDA concentration (13.3 %(w/v) and 26.6 %(w/v)) and molecular weight (Mn 575 and Mn 700), and (ii) the alginate crosslinking agent ($CaCO_3$:GDL and $BaCl_2$). Overall, irrespective of these variations, the IPN hydrogels exhibited superior strength and stiffness to single-networked ionically crosslinked alginate. Moreover, when comparing the elastic properties of the IPN with aortic tissue data reported in the literature, the 3.3 %(w/v) alginate, 26.6 %(w/v) PEGDA Mn700, 0.5 %(w/v) I2959, and 66 mM $BaCl_2$ showed the closest strength, stiffness, and elongation at break (0.39 ±0.05 MPa, 1.61 ±0.19 MPa, and 24.4 ±4.33%, respectively) to the human aorta (0.61 ±0.07 MPa, 1.82 ±0.10 MPa, and 29.0 ±4.0%, respectively) (Vallabhaneni *et al.*, 2004). Further mechanical and physical evaluation of this formulation demonstrated viscoelastic behaviour, and stability in physiologically relevant environments with minimal differences in mechanical properties over incubation. Finally, this formulation was taken forward for the fabrication of tubular conduits via a sacrificial mould technique. The vessels were fabricated with similar dimensions to sections of the aorta, and compression tests demonstrated that the conduits could withstand a total compression of approximately 25% corresponding to loads ranging from 0.5 N to 1.0 N, depending on the dimensions of the structure.

Therefore, it can be concluded that this alginate:PEGDA IPN hydrogel shows great promise towards the development of alternative aortic grafts, however further

modifications to the fabrication process of tubular conduits is required, especially if the grafts were to be designed to match the patient's anatomical geometry.

# Chapter 7 Stereolithography (SLA) 3D-printing of alginate-based hydrogels towards the development of enhanced aortic grafts

## 7.1. Introduction

In previous chapters, the mismatch in mechanical properties between existing aortic synthetic grafts and the host vessel was emphasised, leading to investigations on potential material substitutes. Alginate reinforced with PEGDA to form an interpenetrating polymer network (alginate:PEGDA IPN) hydrogel was identified in Chapter 6 as a suitable material candidate with similar elastic properties to the human aorta, displaying viscoelastic behaviour, and stability under physiological conditions. However, in addition to material mechanical behaviour mismatch, another major concern related with state-of-the-art vascular prostheses is geometrical incompatibility. Despite enhancements in synthetic large-diameter graft design to closely mimic the implant site anatomy, including the introduction of multi-branched, fenestrated, and bifurcated grafts (Singh, Wong and Wang, 2015; Vahabli *et al.*, 2022), as shown in Chapter 2 Figure 2.5, these grafts still comprise a thin-walled, tubular configuration with limited variations in diameter. This lack of patient specificity has been linked with several complications including changes in blood flow and restricted organ perfusion (Juhyun, Matonick and Li, 2002; Obrien, Morris and McGloughlin, 2008; Vardoulis *et al.*, 2011).

In Chapter 6, the alginate:PEGDA IPN was successfully utilised to fabricate tubular constructs with similar diameters and wall thicknesses to the human aorta. However, this method is restricted by mould dimensions (in this case, syringe type). Consequently, changes to vessel geometry, including more complex designs that resemble the aortic tree, require the manufacture of new moulds. To impart customisation in the fabrication process of these grafts without the time-consuming and costly efforts of mould-making, attention in this chapter is directed towards 3D-printing, as this offers the potential of creating and/or modifying a computer-aided design (CAD) model according to the

patient's anatomy. Moreover, the use of 3D-printing in tissue engineering has become widely popular in recent years, mostly due to the continuous advancements in additive manufacturing technologies allowing the fabrication of complex, high-resolution structures whilst utilising soft biocompatible materials such as hydrogels (Holland *et al.*, 2018; Grigoryan *et al.*, 2019; Domingo-Roca *et al.*, 2022b; Asciak *et al.*, 2023). As outlined in the literature review (Chapter 2 Section 2.6.3), there are various forms of 3D-printing platforms. Among these, stereolithography (SLA) is a good candidate for this application given that it is a light-based printing technology (typically UV (365 nm) or visible light (405 nm)) that relies on photopolymerisation, and therefore suitable for printing photocurable materials like the alginate:PEGDA IPN. This would still require the presence of a photoinitiator, preferably one with an absorption spectrum that lies within the printer's emission wavelength, to form free-radicals and initiate photopolymerisation. As illustrated in Figure 7.1, the majority of SLA 3D printers utilise a bottom-up approach, where light passes through the transparent base of the tank (typically this is a fluoroethylene propylene (FEP) film) filled with the photocurable resin which is selectively cured according to the projected pattern.

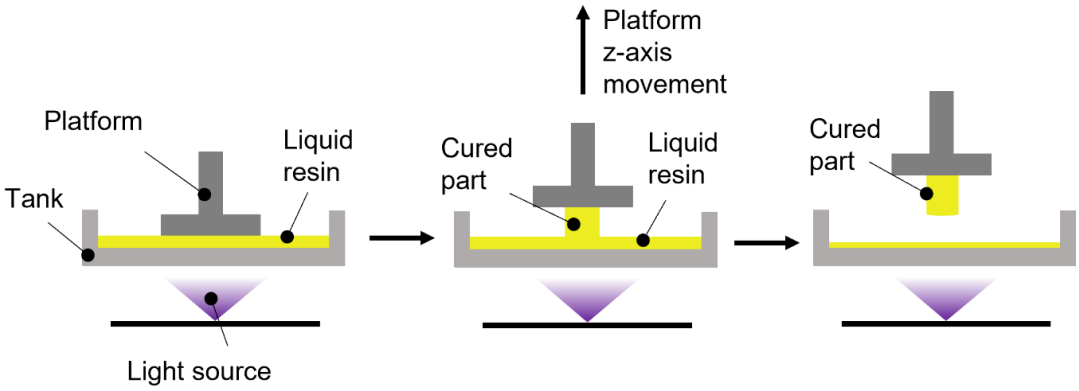


*Figure 7.1: Schematic representation of the stereolithography 3D-printing process.*

Initially, the platform (or print head) is lowered down at a one-layer distance from the bottom of the tank, the first layer is printed, and this moves upwards incrementally

according to layer thickness in the z-direction with the cured layer attached to it allowing the resin to rewet the area. This process is repeated for each layer until the whole part is attached to the platform. As more layers are printed, the light needed to cure new layers also passes through the printed ones which is beneficial for layer adhesion, however overexposure results in poor print resolution. Therefore, prior to printing it is essential to perform resin calibration to determine the critical exposure energy or time required to cure a single layer, known as cure depth ($C_d$), to obtain a fine balance between layer curing and adhesion. In most cases, $C_d$ within the range of standard printing exposure parameters is much thicker than the desired layer thickness owing to light scattering and subsequent overcuring beyond the focal plane. To address this, a light absorber (or photoblocker) is added to the resin to attenuate light, and this way the layer thickness can be reduced tenfold (Yu *et al.*, 2020). Typical photoblockers include pigments such as tartrazine, curcumin, chlorophyllin, Sudan I, and Quinolone yellow (Benjamin *et al.*, 2019; Yu *et al.*, 2020). When selecting a photoblocker it is important to consider the absorption wavelength as this has to be within the emission wavelength of the printer, and whether the printing process or application of the printed part requires a cytocompatible environment, since some photoblockers can be cytotoxic (Yu *et al.*, 2020). Moreover, the amount of photoblocker present in the resin must be carefully controlled to ensure that the degree of light attenuation still enables adhesion to the platform and between layers, and this is typically determined from $C_d$ analysis as a function of photoblocker concentration.

SLA 3D-printing of resins comprising PEGDA has been widely investigated for tissue engineering applications (Seo *et al.*, 2017; Benjamin *et al.*, 2019; Grigoryan *et al.*, 2019; Yang *et al.*, 2020; Huh *et al.*, 2021; Asciak *et al.*, 2023; Hakim Khalili *et al.*, 2023) particularly because of its photocuring ability, biocompatibility, mechanical property tunability, and limited swelling facilitating high resolution printing (Yu *et al.*, 2020).

Conversely, to date, 3D-printing of alginate:PEGDA IPN has only been reported via extrusion-based printing (Hong *et al.*, 2015; Cristovão *et al.*, 2019; de Melo *et al.*, 2019; Zhang *et al.*, 2021). Despite its successes, extrusion printing requires several printability evaluations, primarily via rheology to determine solution viscosity behaviour (6 - 30 $\times 10^7$ mPa·s) to obtain optimal material extrusion via the printer's nozzle and shape fidelity post-printing (Puza and Lienkamp, 2022). This is not the case in SLA printing, where resin viscosity is not restricted by the printing set-up and/or process, although low viscosity resins are recommended (less than 5 Pa·s) (Melchels, Feijen and Grijpma, 2009; Ni *et al.*, 2018) to allow for sufficient rewetting and uniform coverage of the tank surface, thereby facilitating the layer-by-layer printing process.

## 7.2. Aims and Objectives

The aim of this chapter was to investigate the printability of the alginate:PEGDA IPN hydrogel formulation identified in Chapter 6 using a commercially available, desktop SLA 3D printer towards the potential fabrication of patient-specific aortic grafts.

The objectives of this work included the investigation of:

1. The alginate:PEGDA pre-gel solution's printability by measuring its viscosity and the single-layer cure depth as a function of photoblocker.
2. 3D-printing various samples for mechanical characterisation including dog-bones for tensile testing and discs for rheological analysis and assess the differences in mechanical properties with the moulded hydrogel results in Chapter 6.
3. Evaluating the effect of the photoblocker on the mechanical properties of the 3D-printed hydrogel.
4. 3D-printing tubular structures of various dimensions similar to sections of the aorta while determining the maximum sample length that the printer can successfully produce.

5. 3D-printing representative structures based on the geometry of the human aorta as a ‘proof-of-concept’ that this mode of hydrogel fabrication might be potentially utilised for the production of personalised aortic grafts.

## 7.3. Materials and Methods

### 7.3.1. Preparation of the alginate:PEGDA IPN resin

The alginate:PEGDA IPN precursor solution (hereinafter referred to as resin) was prepared as described in Chapter 3, however 0.5 %(w/v) LAP (Lithium phenyl-2,4,6-trimethylbenzoylphosphinate) was used as the photoinitiator since this has better: (1) water solubility, (2) cell compatibility, and (3) absorption in the visible light range than Irgacure 2959 (Fairbanks *et al.*, 2009). The latter is essential to match the wavelength of the 3D printer’s LED panel (405 nm), and as demonstrated by the absorption spectrum in Appendix 3: Absorption spectra of the photoinitiators and photoblocker used to fabricate the alginate:PEGDA hydrogels., LAP absorbs within the visible light range (400 – 420 nm), albeit weakly. Moreover, a photoblocker, tartrazine, which is a synthetic yellow azo dye with high absorption in the visible light range as shown by the absorption spectrum in Appendix 3: Absorption spectra of the photoinitiators and photoblocker used to fabricate the alginate:PEGDA hydrogels. was incorporated within the resin at varying concentrations (0.01 %(w/v) to 0.03 %(w/v)) for optimal printing resolution.

### 7.3.2. Resin viscosity measurements

Viscosity measurements were performed using a rotational rheometer (Kinexus Pro+ rotational rheometer, NETZSCH, Germany) equipped with a cone (40 mm diameter; 4° cone) and plate (40 mm diameter) configuration. The solution was pipetted directly onto the bottom plate and a shear rate sweep was performed at shear rates ranging from 0.01 $s^{-1}$ to 100 $s^{-1}$ at ambient temperature.

### 7.3.3. Resin calibration via cure depth measurements

3D-printing was performed using a commercial desktop 3D printer (PRUSA SL1S, PRUSA Research, Prague, CR) equipped with a monochrome LCD screen with a resolution of 5.96” 2560 ×1620 pixels (equivalent to an x-y resolution of 50 µm) and a 405 nm UV LED panel. Printing exposure times were determined by performing cure depth measurements as a function of photoblocker concentration (0%, 0.01%, 0.025% and 0.03 %(w/v)). Single-layer disc samples (n=4; CAD model sliced at 0.05 mm layer thickness) were printed at four different exposure times (15 s, 25 s, 35 s, and 45 s) and the thickness for each sample was measured using a digital vernier calliper. The relationship between the cure depth ($C_d$) required to print a single layer and the photoblocker concentration ($c_b$) was determined from the Beer-Lambert Law (Seo *et al.*, 2017; Benjamin *et al.*, 2019), which states that the light absorbance of a solution is directly proportional to the concentration of the solution, defined via Equation (7.1):

$$A = \varepsilon D_p c_b \tag{7.1}$$

Where A is the absorbance of the solution, ε is the molar absorptivity, $D_p$ is the light penetration depth, and $c_b$ is the photoblocker concentration.

To implement this relationship to obtain printing parameters, the absorbance can also be defined in terms of intensity or exposure energy:

$$A = \log_{10}\left(\frac{I_0}{I_C}\right) = \log_{10}\left(\frac{E_0}{E_C}\right) \tag{7.2}$$

Where $I_0$ and $E_0$ are the intensity and exposure energy of the incident light, respectively, and $I_C$ and $E_C$ are the critical intensity and energy required for the material to solidify, respectively. Substituting Equation (7.2) into Equation (7.1) yields the following relationship:

$$\log_{10}\left(\frac{I_0}{I_C}\right) = \varepsilon D_p c_b \tag{7.3}$$

Given that the light penetration depth ($D_p$) for a single layer to solidify is equivalent to the cure depth ($C_d$), Equation (7.3) may be rearranged as a function of $C_d$ as follows:

$$C_d = \frac{1}{\varepsilon c_b}\log_{10}\left(\frac{I_0}{I_C}\right) = \frac{1}{\varepsilon c_b}\log_{10}\left(\frac{E_0}{E_C}\right) \tag{7.4}$$

Additionally, $C_d$ is also related to the exposure energy and $D_p$ (Benjamin *et al.*, 2019):

$$C_d = D_p \ln\left(\frac{E_0}{E_C}\right) \tag{7.5}$$

By substituting Equation (7.5) in Equation (7.4) and by changing the natural logarithmic base in Equation (7.4) to log base 10:

$$D_p = \frac{1}{\varepsilon c_b} \tag{7.6}$$

Therefore, Equation (7.4) may be rewritten into:

$$C_d = D_p \log_{10}\left(\frac{E_0}{E_C}\right) \tag{7.7}$$

By printing a single layer sample for resin formulations with different photoblocker concentrations at different energy or intensities, a semi-log plot of $C_d$ versus E or I (also known as Jacob's working curve (Jacobs, 1992)) is obtained.

Given that the printer used in this work is equipped with an LED screen with a fixed light intensity that cannot be altered, the working curves are obtained as a function of exposure time. However, exposure time (t) is related to the exposure energy (E) and intensity (I) as follows:

$$E = It \tag{7.8}$$

Therefore, by substituting Equation (7.8) into Equation (7.7), a relationship between $C_d$ and exposure time is obtained:

$$C_d = D_p \log_{10}\left(\frac{I_0 t}{I_c t_c}\right) \tag{7.9}$$

Moreover, given that the intensity of the LED screen is fixed: $I_0 = I_c$, therefore Equation (7.9) may be rewritten as:

$$C_d = D_p \log_{10}\left(\frac{t}{t_c}\right) \tag{7.10}$$

### 7.3.4. SLA 3D-printing of alginate:PEGDA IPN hydrogels

For material characterisation, discs and dog-bone shaped samples were 3D-printed at the same dimensions used to prepare moulded hydrogels (i.e., according to Type IV in the ASTM D638 standard). Prior to 3D-printing, the designed target models were prepared via a computer-aided design (CAD) software (Autodesk Inventor, Autodesk, Inc.) and exported as STL files. These were then imported into the printer's slicer software (PrusaSlicer 2.4.1) to convert the STL file in preparation for 3D-printing, including slicing the model at a specific layer thickness, in this case this was set at 0.05 mm. Following the 3D-printing process, the samples were transferred into a $BaCl_2$ bath (66 mM) for alginate to crosslink overnight.

To 3D-print tubular vessels that resemble human aortic dimensions, similar to the dimensions obtained by the moulding method in Chapter 6, initial prints included straight tubes of different wall thicknesses (0.5 mm, 1mm, and 2 mm), and fixed outer diameter (18 mm) or inner diameter (9 mm), and length (7.5 mm). The same wall thickness and outer diameter dimensions were then used to print longer constructs including 15 mm and 30 mm.

Moreover, to demonstrate the capability of this 3D-printing fabrication method in producing faithful replications of aortic geometries, a human abdominal aortic open-

source model (*The Biomedical 3D printing community, Embodi3D*, 2023) was used to 3D-print small segments of the aortic tree, including the renal and bifurcation areas. The STL model was modified to create a hollowed structure having a wall thickness of 2 mm for the renal part and 1mm for the bifurcation part. Exposure times varied depending on the geometry and dimensions of the design.

To investigate the geometrical deviation from the CAD model to the 3D-printed hydrogel part, the mean relative difference, both absolute and relative, was calculated according to Equation 7.11 and Equation 7.12:

$$mean\ absolute\ difference = 3D\ printed\ part\ dimension - CAD\ model\ dimension \tag{7.11}$$

$$mean\ relative\ difference\ (\%) = \frac{|3D\ printed\ part\ dimension - CAD\ model\ dimension|}{CAD\ model\ dimension} \times 100 \tag{7.12}$$

## 7.4. Results

### 7.4.1. Rheological properties of the resin: viscosity measurements.

The viscosity profiles of the alginate:PEGDA IPN resin, in comparison with alginate on its own (3.3 %(w/v)), are presented in Figure 7.2. The viscosity was evaluated over a range of shear rates: 0.1 $s^{-1}$ to 100 $s^{-1}$ based on similar investigations (González *et al.*, 2020; Sameni *et al.*, 2022). The alginate on its own was included for comparative purposes, and it showed a stable viscosity throughout the whole shear rate sweep. Conversely, the behaviour of both the alginate:PEGDA IPN solutions is very similar as they both exhibit a decrease in viscosity with increasing shear rate. The alginate:PEGDA with 0.03 %(w/v) photoblocker displayed a steeper decrease in viscosity than the solution without photoblocker. Moreover, both solutions displayed a viscosity less than 1 Pa·s across all shear rate, making them suitable for SLA 3D-printing.

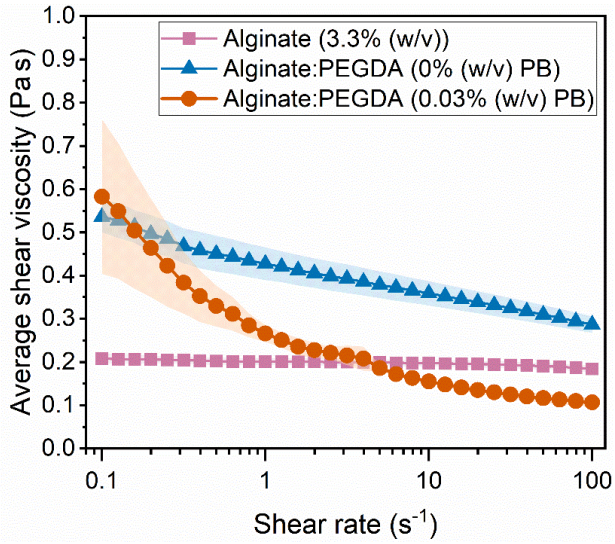


*Figure 7.2: Viscosity profiles of alginate (3.3% (w/v)) and alginate:PEGDA IPN solutions with (0.03% (w/v)) and without (0% (w/v)) photoblocker (PB) addition. Data points represent the mean ±S.D. (n=3). Measurements were performed at room temperature.*

### 7.4.2. Resin calibration and cure depth measurements

Figure 7.3 shows the semi-log plots of layer thickness versus exposure time for different photoblocker concentrations. In the absence of the photoblocker (Figure 7.3(A)), single layered prints resulted in thicknesses ranging from 1.63 ±0.11 mm to 2.23 ±0.08 mm, with layer thickness increasing with exposure time. However, once the photoblocker was introduced within the resin, a decrease in layer thicknesses was observed, ranging from 0.48 ±0.02 mm to 1.07 ±0.01 mm for all three different photoblocker concentrations (Figure 7.3(B) – (D)).

Equation 7.10 was rearranged as follows and fitted to the data points for each different concentration:

$$C_d = D_p \log_{10} t - D_p \log_{10} t_c \tag{7.11}$$

This corresponds to a semi-log fit where $D_p$ is the slope (A) and $D_p \log_{10} t_C$ is the intercept (B), therefore Equation 7.11 may be rewritten as:

$$C_d = A log_{10} t - B \tag{7.12}$$

To determine the exposure times required to cure different layer thicknesses according to the printer's layer slicing range i.e., 0.01 mm, 0.025 mm, 0.05 mm, and 0.1 mm, Equation 7.12 may be rewritten accordingly:

$$t = 10^{(C_d - B)/A} \tag{7.12}$$

The corresponding exposure times for the different layers at different photoblocker concentrations are presented for each plot in Figure 7.3.

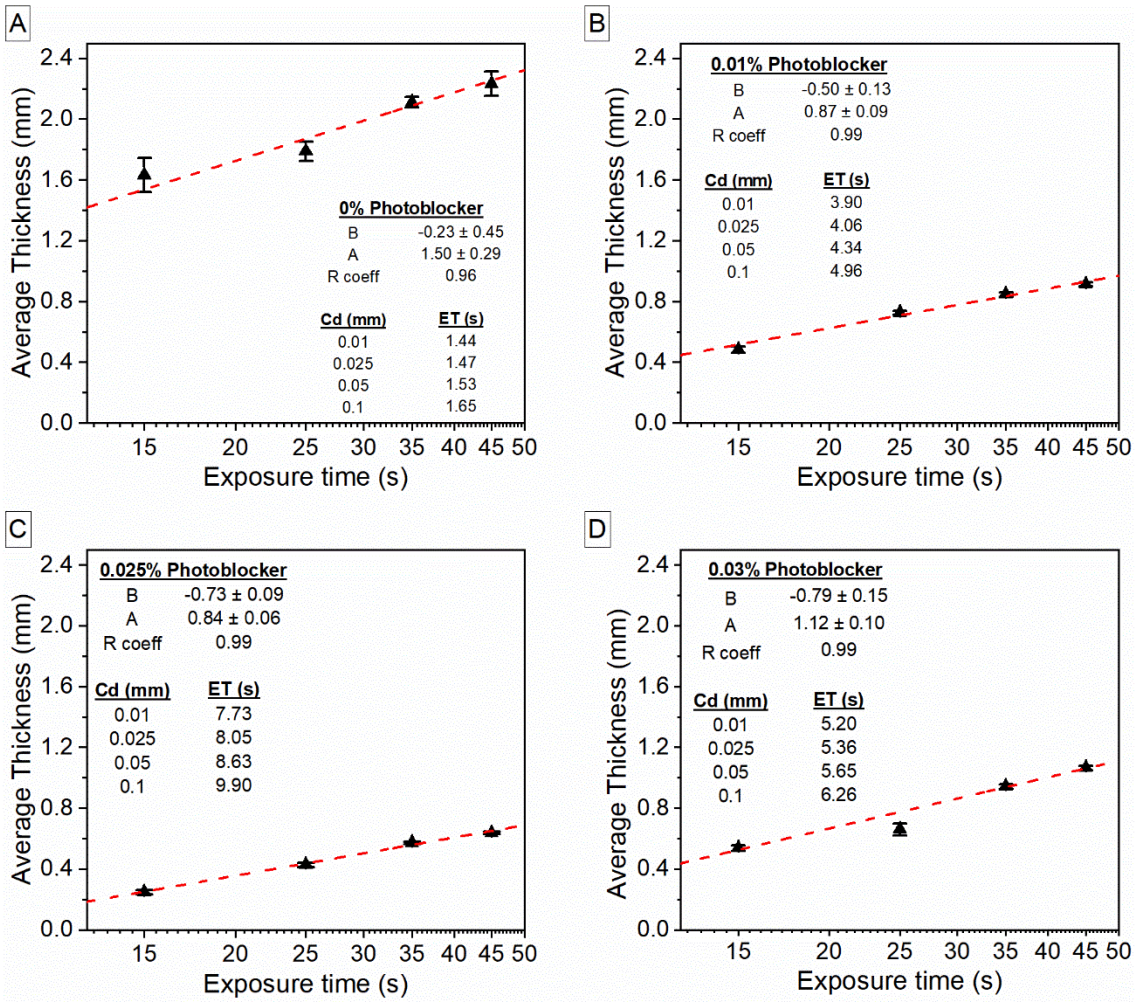


*Figure 7.3: Resin calibration curves as a function of photoblocker concentration: (A) 0% (w/v), (B) 0.01% (w/v), (C) 0.025% (w/v), and (D) 0.03% (w/v). X-axes are in logarithmic ($log_{10}$) form. Fitting curves (dashed red line) were obtained using Equation 7.10, where A is the slope and B is the intercept, and the corresponding exposure times (ET) for a given cure depth ($C_d$) are presented for each curve. R coeff represents the Pearson's correlation coefficient. Data points represent the mean ±S.D. (n=4).*

However, knowledge of $C_d$ is not enough to ensure optimal prints. The exposure times selected must also be long enough to provide layer adhesion, and ideally $C_d \geq$ layer thickness (Benjamin *et al.*, 2019). Therefore, if at a photoblocker concentration of 0.03 %(w/v) at a printing layer thickness of 0.05 mm, and the corresponding exposure time is 5.65 s, ideally this exposure time needs to be slightly increased to ensure layer adhesion. Additionally, the first couple of layers are generally printed at higher exposure times (*ca.* 3 times greater) than the rest of the print to ensure optimal adhesion to the print platform.

Therefore, the printing parameters implemented in this chapter include a first layer exposure time (FLET) of 30 s, exposure time (ET) depending on the photoblocker concentration used but this was set at 16 s, at a layer thickness of 0.05 mm, unless otherwise stated. To demonstrate whether this set of printing parameters result in faithful representation of the CAD model designs, dog-bone shaped alginate:PEGDA IPN hydrogel specimens were 3D-printed with similar dimensions to the moulded samples in Chapter 6, with (0.025% (w/v) and 0.03% (w/v)) and without (0% (w/v)) the addition of the photoblocker as shown in Figure 7.4. From Figure 7.4 it is evident that photoblocker addition results in higher resolution prints with sharper features and more accurate dimensions close to the CAD model design. Photoblocker addition is also evident from the difference in colour among prints, with the orange tint in Figure 7.4(B) corresponding to the tartrazine present in the hydrogel.

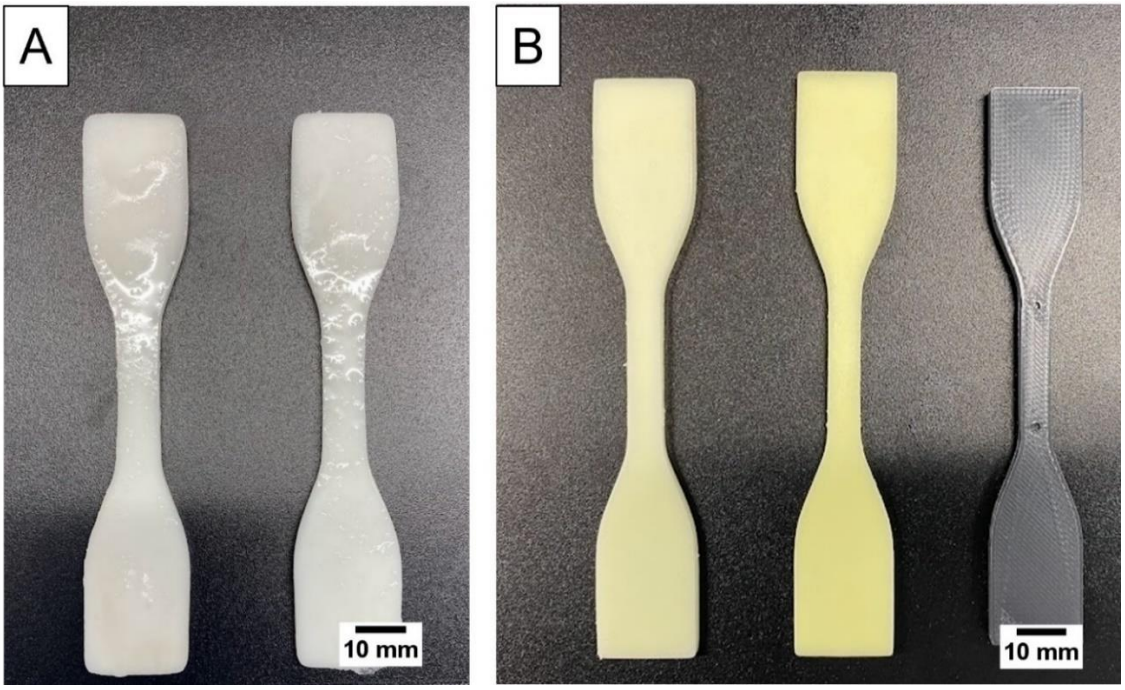


*Figure 7.4: Visual representation of 3D-printed alginate:PEGDA IPN hydrogel dog-bone specimens for uniaxial tensile testing: (A) without photoblocker addition, and (B) with photoblocker addition in comparison with a PLA 3D-printed specimen with accurate dimensions to the CAD model. Printing parameters were set at 30 s FLET, 16 s ET, and 0.05 mm layer thickness for all samples.*

Moreover, measurements of the gauge width i.e., the thin section (middle part) of the dog-bone specimen for all the four different conditions is presented in Table 7.1. This is primarily to emphasise the difference in printing resolution obtained via photoblocker addition and to quantify the degree of variation from the CAD design model via the mean differences, both absolute and relative. As expected, the highest difference was observed in the 3D-printed sample without photoblocker with a mean relative difference of 48.14 ± 2.22% while the moulded samples showed the least relative difference 3.62 ±1.12%. For the samples containing the photoblocker, the highest concentration demonstrated the closest gauge width measurements to the CAD model with a mean relative difference of 6.51± 0.51%.

*Table 7.1: Comparison of the gauge width measurements of tensile specimens (moulded and 3D-printed (3DP)) with respect to the mould or CAD file model gauge width (6 mm). Dimensions for 3D-printed parts include samples with and without photoblocker (PB). Gauge width values are presented as the mean ± standard error of the mean for n=5 for the moulded, 0.025% (w/v) and 0.03% (w/v) PB, and n=2 for the 0% (w/v) PB.*

| Specimen type | Gauge width (mm) | Mean absolute difference (mm) | Mean relative difference (%) |
|---|---|---|---|
| Moulded | 6.22 ± 0.03 | 0.22 ± 0.07 | 3.62 ± 1.12 |
| 3DP: 0 %(w/v) PB | 8.89 ± 0.19 | 2.89 ± 0.13 | 48.14 ± 2.22 |
| 3DP: 0.025 %(w/v) PB | 6.55 ± 0.02 | 0.53 ± 0.03 | 8.86 ± 0.46 |
| 3DP: 0.03 %(w/v) PB | 6.39 ± 0.03 | 0.39 ± 0.03 | 6.51 ± 0.51 |

### 7.4.3. Mechanical characterisation of 3D-printed alginate:PEGDA IPN hydrogels

#### 7.4.3.1. Uniaxial tensile testing: stretch to failure measurements

In order to assess whether 3D-printing of the alginate:PEGDA IPN results in changes in the elastic properties of the hydrogel, uniaxial tensile stretch to failure tests were performed on the 3D-printed hydrogels using the same testing parameters as in previous chapters. Figure 7.5 shows the elastic properties including elongation at break, ultimate tensile strength, and elastic modulus of 3D-printed alginate:PEGDA IPN hydrogels with 0.025 %(w/v) and 0.03 %(w/v) photoblocker in comparison with 3D-printed alginate:PEGDA without photoblocker addition (0 %(w/v)) and the results obtained for the moulded hydrogels in Chapter 6. Given that in the absence of photoblocker, the dimensions of the dog-bone specimen varied significantly from the moulded hydrogels, a limited number of samples were printed and tested, and Figure 7.5 only shows data for two samples.

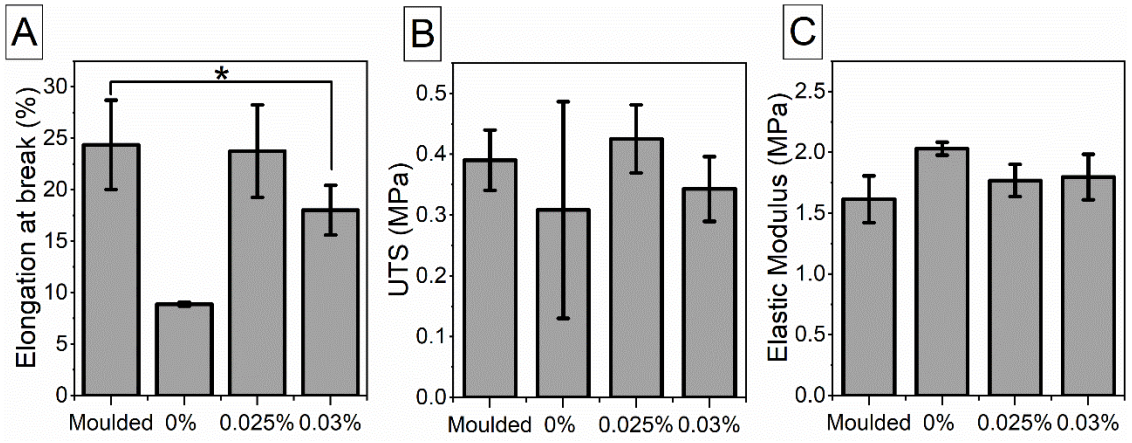


*Figure 7.5: Stretch to failure properties of 3D-printed alginate:PEGDA IPN hydrogels with (0.025%(w/v) and 0.03% (w/v)) and without (0% (w/v)) the addition of photoblocker in comparison with moulded hydrogels: (A) elongation at break, (B) ultimate tensile strength (UTS), and (C) elastic modulus. Columns represent the mean ± S.D. with n=5 for the moulded samples and photoblocker samples, and statistical significance between these sample groups was measured via one-way ANOVA with Tukey post-hoc analysis and represented graphically by * p<0.05. For the 0% (w/v), the columns represent the mean ± S.D. for n=2 and therefore this was not included in the statistical significance analysis.*

A decrease in elongation at break and ultimate tensile strength was observed for the higher photoblocker concentration (0.03 %(w/v); 18.02 ±2.42%, 0.34 ±0.05 MPa, respectively) when compared with the moulded (24.37 ±4.33% (*p = 0.046)*, 0.39 ±0.05 MPa (*p = 0.356)*, respectively) and 0.025 %(w/v) (23.27 ±4.05% (*p = 0.103)*, 0.42 ±0.05 MPa (*p = 0.115)*, respectively) samples. However, a significant decrease was only observed in the elongation at break between the 0.03 %(w/v) and the moulded samples ($p$ = 0.046). The elastic modulus of the moulded and photoblocker 3D-printed samples showed no significant differences ($p$ = 0.233).

#### 7.4.3.2. Rheological analysis

Alginate:PEGDA IPN hydrogel discs were 3D-printed for rheological analysis. The CAD model was designed to produce discs of 20 mm diameter and 2 mm thickness. Figure 7.6(A) shows the discs printed without photoblocker (0 %(w/v)) in comparison with a

moulded sample. Figure 7.6(B) compares the discs with (0.03 %(w/v)) and without photoblocker addition.

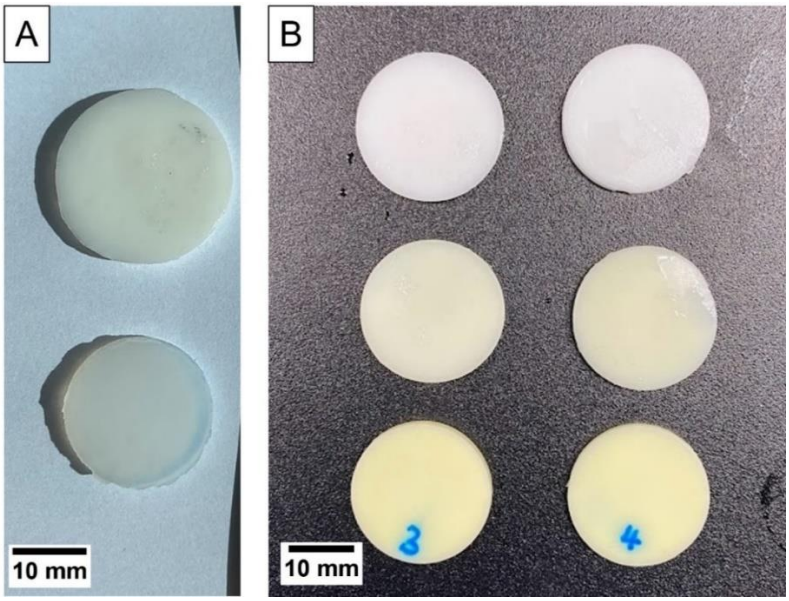


*Figure 7.6: Visual representation of 3D-printed alginate:PEGDA IPN hydrogel disc specimens for rheological analysis: (A) 3D-printed without photoblocker addition (top sample) versus moulded (bottom sample), and (B) 3D-printed with the addition of photoblocker (increasing concentrations of tartrazine from top to bottom).*

Figure 7.7 shows the rheological measurements obtained via amplitude and frequency oscillatory sweeps for 3D-printed alginate:PEGDA IPN hydrogel discs at different photoblocker concentrations (0%, 0.025%, 0.03%(w/v)) versus moulded alginate:PEGDA IPN hydrogels discs (results described in Chapter 6). By comparing both the amplitude and frequency sweeps of the moulded hydrogels (Figure 7.7(A) and (B)) with the 3D-printed hydrogels, it is evident that the storage modulus (blue line curve) increases with 3D-printing. Overall, similar responses were obtained for the 3D-printed hydrogels with different photoblocker concentrations.

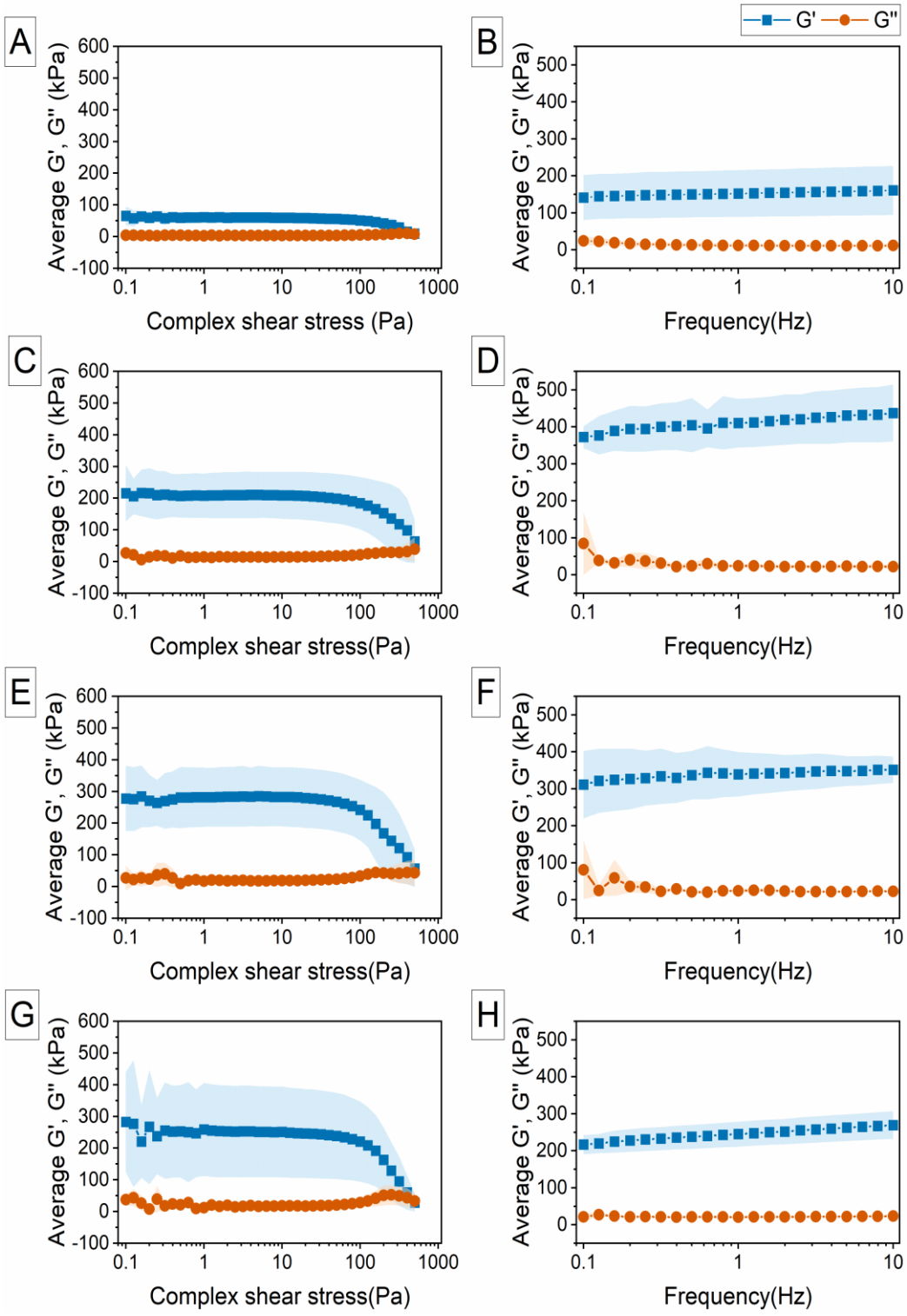


*Figure 7.7: Rheological analysis via amplitude (A, C, E, G) and frequency (B, D, F, H) sweeps of moulded alginate:PEGDA IPN hydrogel discs (A,B) versus 3D-printed alginate:PEGDA IPN hydrogel discs without photoblocker (C,D), and with 0.025% (w/v) (E,F) and 0.03% (w/v) photoblocker (G,H). G' is the storage modulus and G'' is the loss modulus. Data points represent the mean ± S.D. with n=3 for amplitude sweeps and n=5 for frequency sweeps.*

From the amplitude sweep plots, all different conditions resulted in higher storage modulus (G') than loss modulus (G') that remain stable until a G' and G'' crossover point at the end of the amplitude sweep i.e., at 500 Pa.

From the frequency sweeps performed at a fixed strain within the linear viscoelastic regime, a slight decrease in G' can be observed as the photoblocker concentration increases (Figure 7.7(D), (F), and (H)).

### 7.4.4. 3D-printing of alginate:PEGDA IPN hydrogel tubular constructs

#### 7.4.4.1. Straight, free-standing vessels

For the 3D-printed tubular structures, the photoblocker concentration was set at 0.03 %(w/v), the exposure times at 30 s FLET, and 16 s ET, with a layer thickness of 0.05 mm, unless otherwise stated. For the first attempt at 3D-printing tubular structures, the CAD model was designed with an outer diameter of 18 mm, wall thickness of 2 mm and a length of 7.5 mm. This was printed successfully as shown in Figure 7.8. The measured dimensions of the printed part resulted in 18.56 mm outer diameter, 2.26 mm wall thickness, and 7.62 mm length. A slightly tapered structure could be observed as shown in Figure 7.8(C).

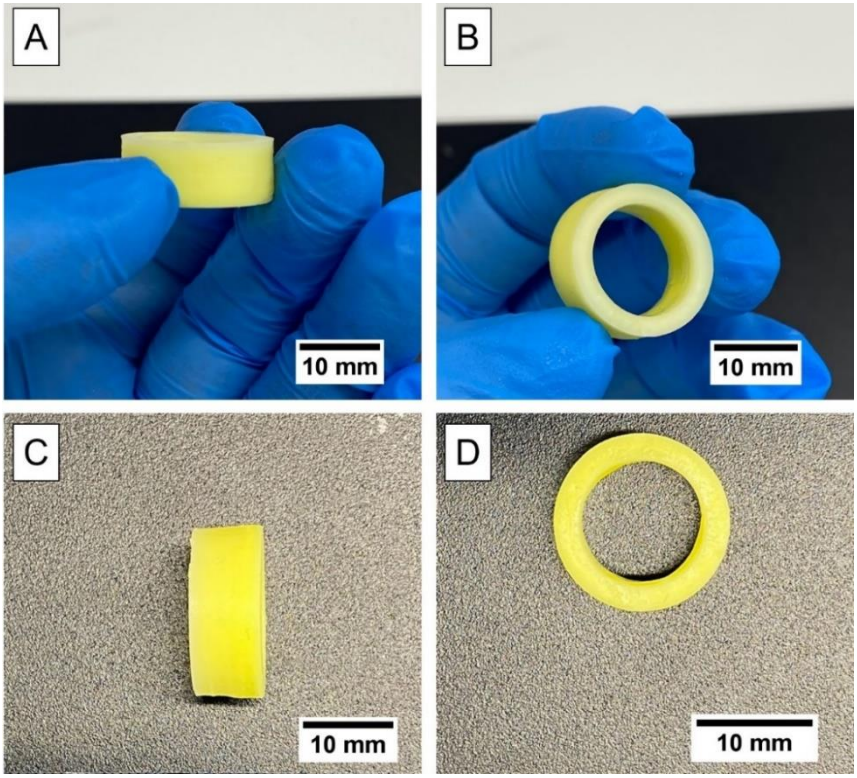


*Figure 7.8: Visual representation of the first attempt at printing tubular structures. Images (A) – (D) show the same sample at different angles. Sample dimensions: 2.26 mm wall thickness, 18.56 mm outer diameter, and 7.62 mm length.*

For the next set of samples, the length of the structure was maintained at 7.5 mm, but this time the inner diameter was fixed at 9 mm, and three different wall thicknesses: 0.5 mm, 1 mm, and 2 mm were selected. The three different structures were printed at the same time and due to the different wall thickness and therefore different sample weights, pulling forces during printing led to the 1 mm sample to break during printing, as can be observed in Figure 7.9(C). Despite this, the other two samples (the 0.5 mm and 2.0 mm wall thickness samples) were printed successfully.

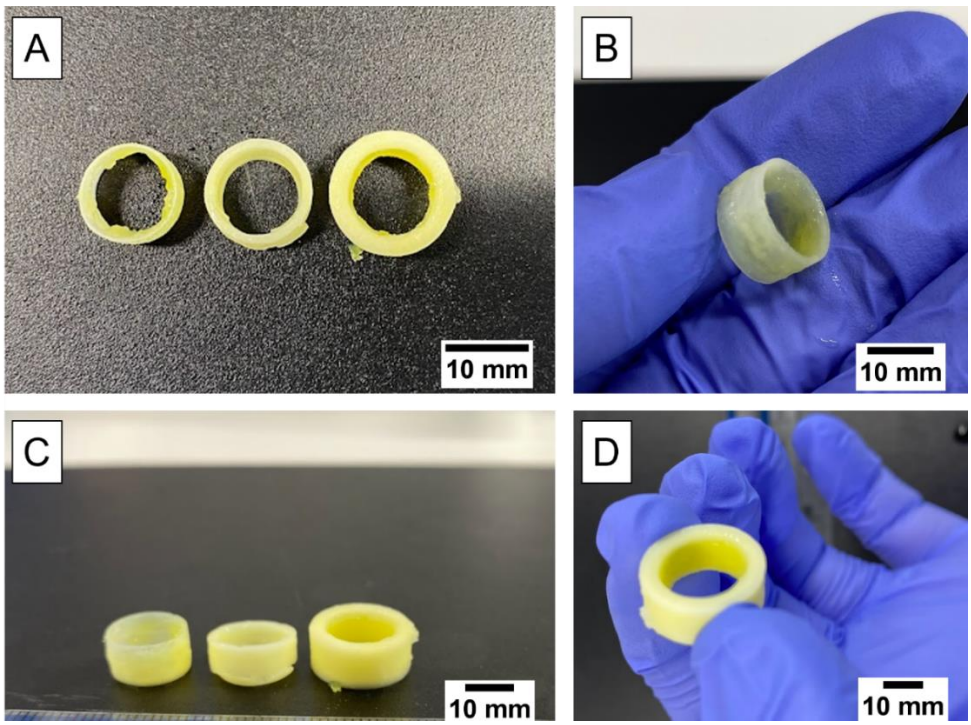


*Figure 7.9: Visual representation of tubular samples printed at different wall thicknesses (0.5 mm, 1 mm, and 2 mm) at a fixed length of 7.5 mm. (A) – (D) show the same set of samples at different angles.*

The inner diameter (9 mm) and wall thicknesses (0.5, 1, and 2 mm) remained unchanged for the next set of samples but the length was increased to 15 mm. All 3 samples were printed once again at the same time, and this time the print was successful as shown in Figure 7.10.

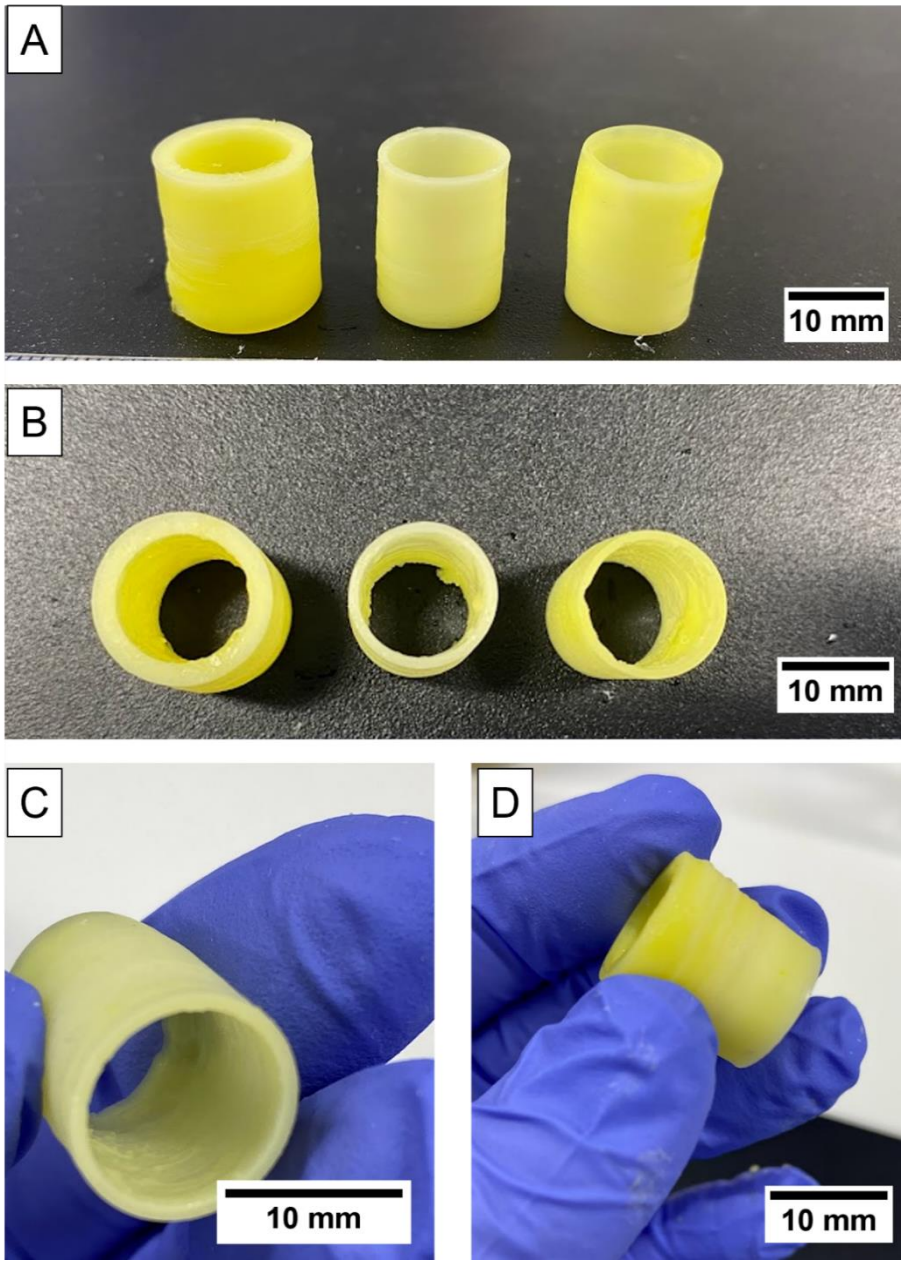


*Figure 7.10: Visual representation of tubular structures printed at a fixed length of 15 mm and different wall thicknesses (0.5 mm, 1 mm, and 2mm): (A) side view, (B) top view, (C) close-up of the 1 mm wall thickness vessel, and (D) close-up of the 2 mm wall thickness vessel.*

However, upon increasing the length to 30 mm, the print was unsuccessful as shown in Figure 7.11. Hydrogel dehydration could be observed because of the long printing time (*ca.* 3 hours). In addition to this, the sample having a 2 mm thick wall broke into two during printing possibly due to its weight and the lack of printing supports.

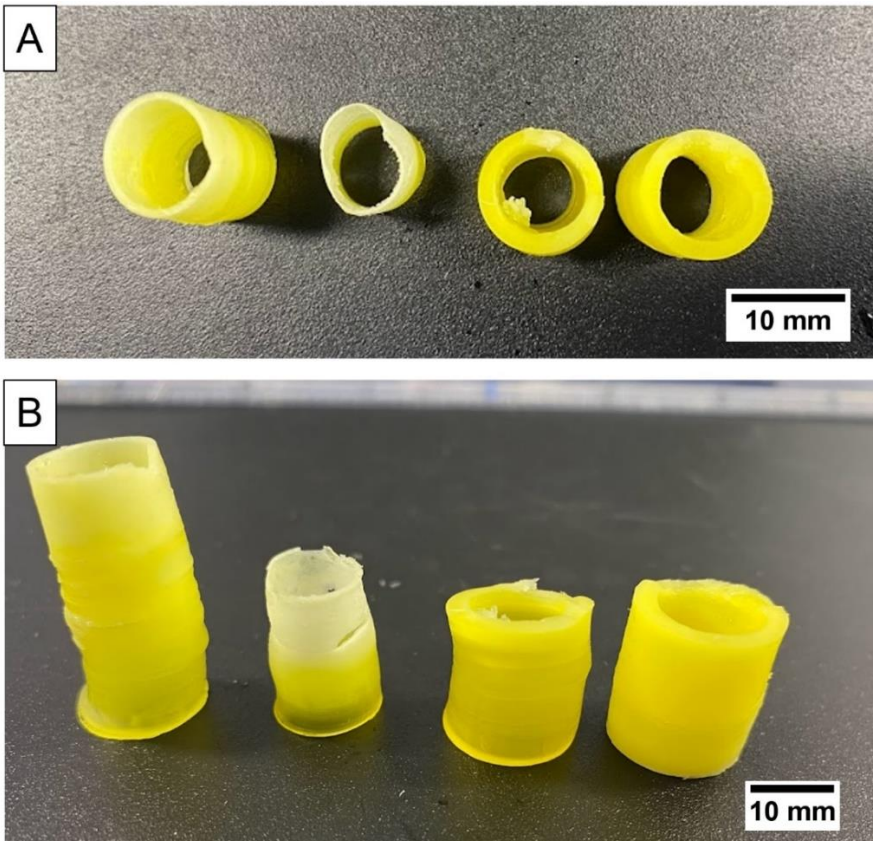


*Figure 7.11: Visual representation of the first and failed attempt at printing 30 mm long tubular structures of different wall thicknesses (0.5 mm, 1 mm and 2 mm): (A) top view, and (B) side view. Failure included hydrogel dehydration during printing, poor layer adhesion, and the breaking into two of the 2 mm wall thickness sample (far right).*

Therefore, in an attempt to obtain longer structures the CAD model was modified so that the structure could be printed at a 45-degree angle instead of vertically, with the addition of supports as shown in Figure 7.12(A). The structure's inner diameter and wall thickness were maintained at 9 mm and 1 mm, respectively. This was printed successfully, however the printing parameters require optimisation, since overexposure could be observed by the poor print resolution. The dimensions of the printed structure were: 2.41 mm wall thickness, 9.11 mm inner diameter, and a total length of 32.5 mm.

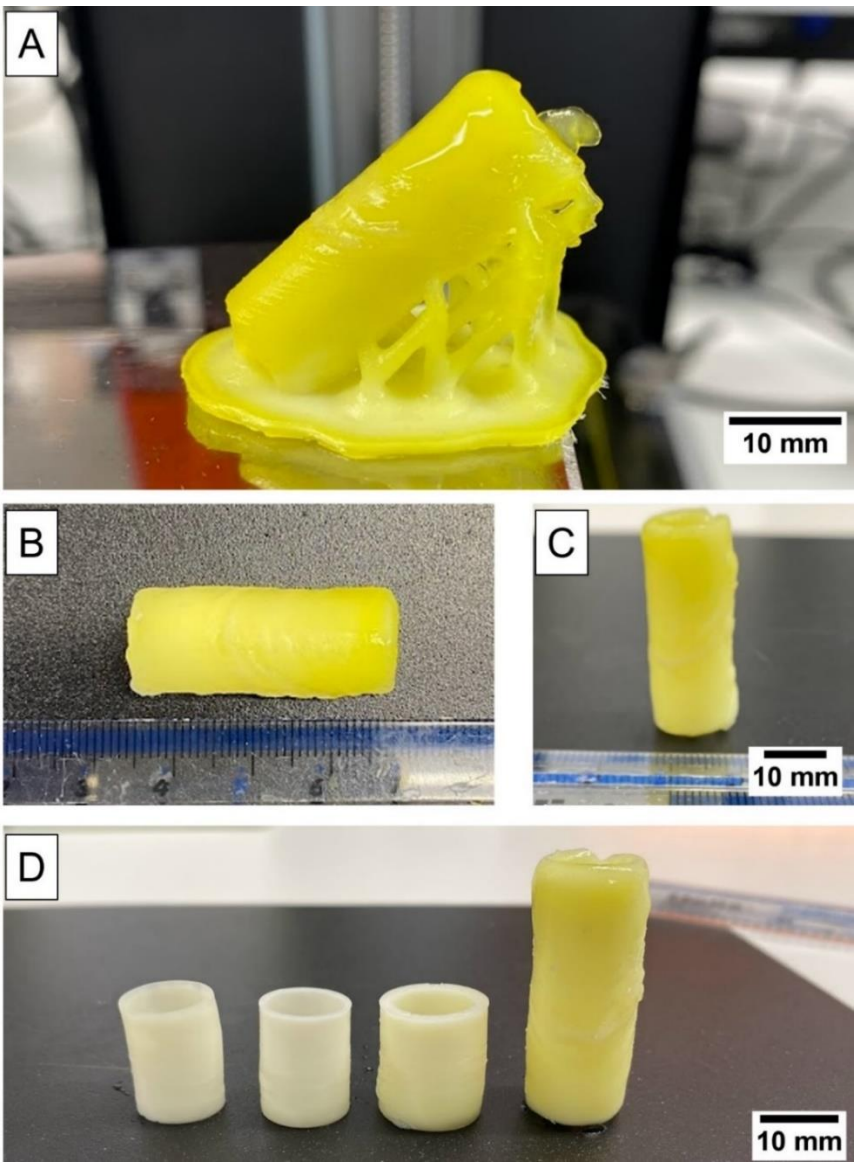


*Figure 7.12: Visual representation of the attempt at printing 30 mm long tubular structures at 45° with supports (A), top view (B), side view (C), and 30 mm long structure in comparison with 15 mm long vessels of different wall thicknesses (0.5 mm, 1 mm, and 2 mm).*

Therefore, in an attempt to improve print accuracy by utilising the calibration curve for 0.03 %(w/v) photoblocker a lower exposure time was selected (7 s) but the FLET was maintained at 30 s in order to ensure print adhesion to the platform and successful printing of the supports. However, poor layer adhesion could be observed in Figure 7.13(B). Therefore, printing of long structures (> 20 mm) requires further investigation when utilising this printer and hydrogel formulation.

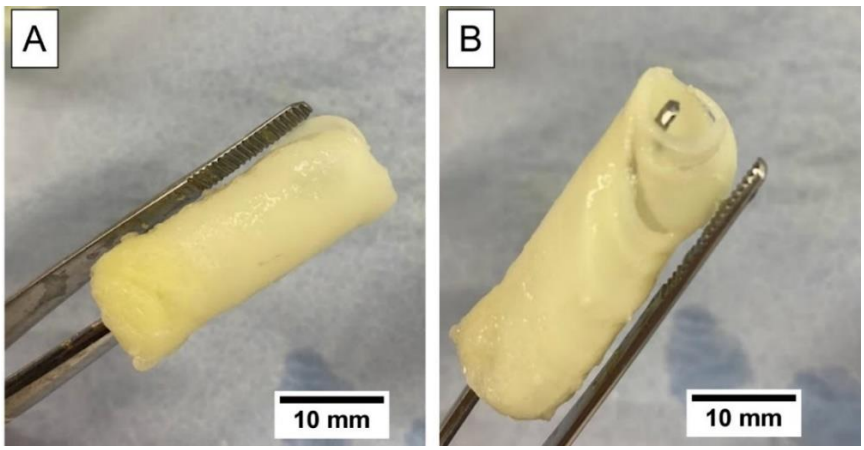


*Figure 7.13: Reprint of 30 mm long tubular structure at 45° using a lower exposure time. (A) and (B) show the same sample at different angles.*

### 7.4.4.2. Mechanical characterisation of straight, free-standing vessels

For comparative purposes with the moulded structures in Chapter 6, the dimensions that resulted in successful prints (2 mm wall thickness, 18 mm outer diameter, and 15 mm length) were used to fabricate tubular structures for radial load evaluation as shown in Figure 7.14.

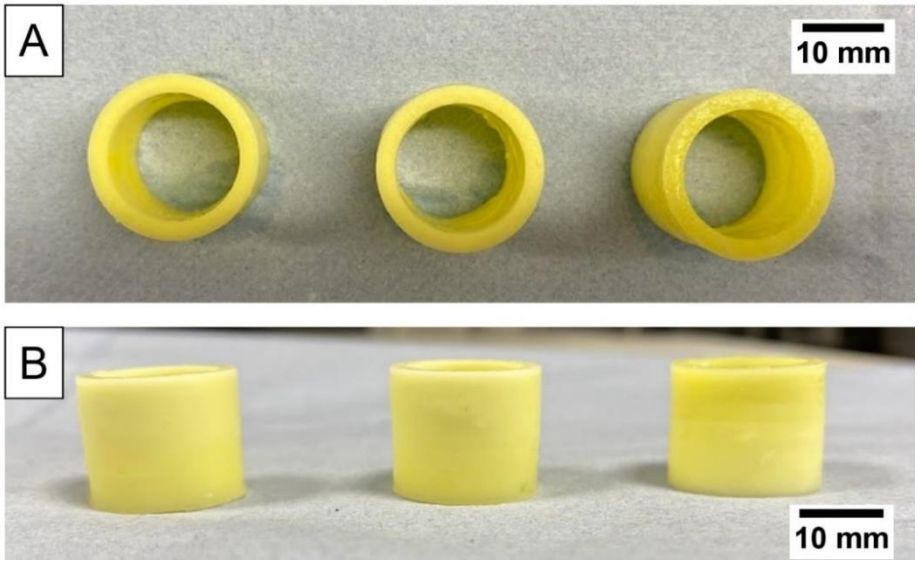


*Figure 7.14: Visual representation of 3D-printed tubular structures (15 mm long, 2 mm wall thickness, and 18 mm outer diameter). Printing parameters used for these prints involved lower exposure times of 25 s FLET and 7.5 s ET.*

The samples were placed horizontally between two compression plates and were compressed by a displacement of 50% relative to the outer diameter i.e., 9 mm, as shown in Figure 7.15(A) – (C). The resulting load versus diameter reduction ratio curves are shown in Figure 7.15(D). Out of 3 samples, 2 samples did not fail following the 50% compression and exhibited shape recovery by returning to their pre-deformed shape once the load was removed. Sample 1 exhibited a maximum load of 2.89 N while sample 2 exhibited a maximum load of 2.48 N. The third sample failed at 42.2% displacement relative to the outer diameter equivalent to a maximum load of 2.17 N.

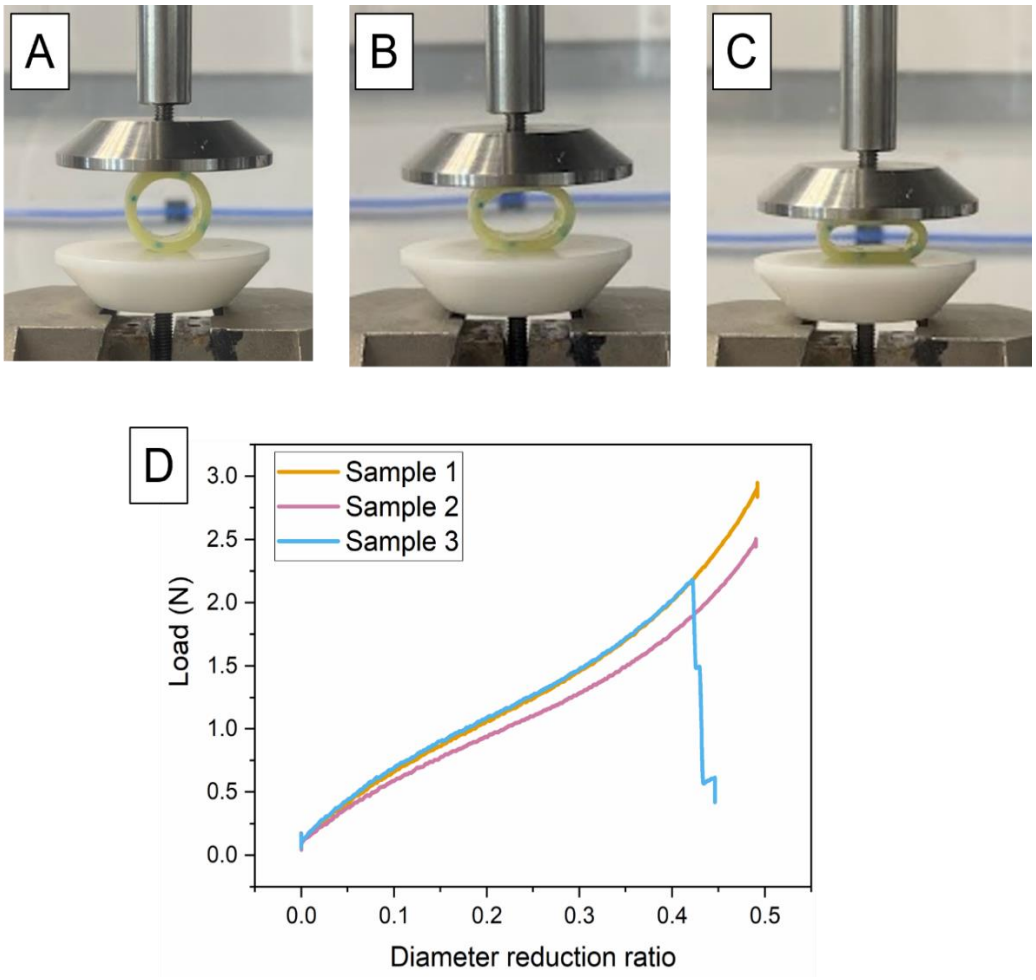


*Figure 7.15: Radial compression of 3D-printed tubular structures (15 mm length, 2 mm wall thickness, 18 mm outer diameter) to 50% relative to their outer diameter: (A) - (C) show the compression process at different stages, and (D) the load versus diameter reduction ratio for 3 replicate samples.*

#### 7.4.4.3. Vessels based on human aorta geometry towards the potential development of personalised aortic grafts.

To demonstrate the use of this 3D-printing technique for the fabrication of alternative aortic grafts that are also patient-specific, an open-source human aorta model was used to 3D-print anatomically relevant parts of the aortic tree. The model used is shown in Figure 7.16(A) and the sections printed including the part of the aorta that branches out to the renal arteries and the part that bifurcates into the iliac arteries are highlighted by dashed black boxes. First, the part that branches out to the renal arteries was printed. The overall length of this part was 18.6 mm, and the wall thickness was set at 2 mm. The printing parameters were set at a FLET of 25 s and ET of 7 s at a layer thickness of 0.05 mm. As can be seen in Figure 7.16(D) and (E) the part was printed successfully, faithfully representing the CAD model (Figure 7.16(B) and (C)).

The second part to be printed was the bifurcation into the iliac arteries as shown by the CAD model in Figure 7.16(F) and (G). The overall height of the structure was 21.96 mm, and the wall thickness was set at 1 mm throughout. The printing parameters were set at a FLET of 40 s and ET of 11 s. Once again, the resulting structures faithfully replicated the CAD model as shown in Figure 7.16(H) and (I).

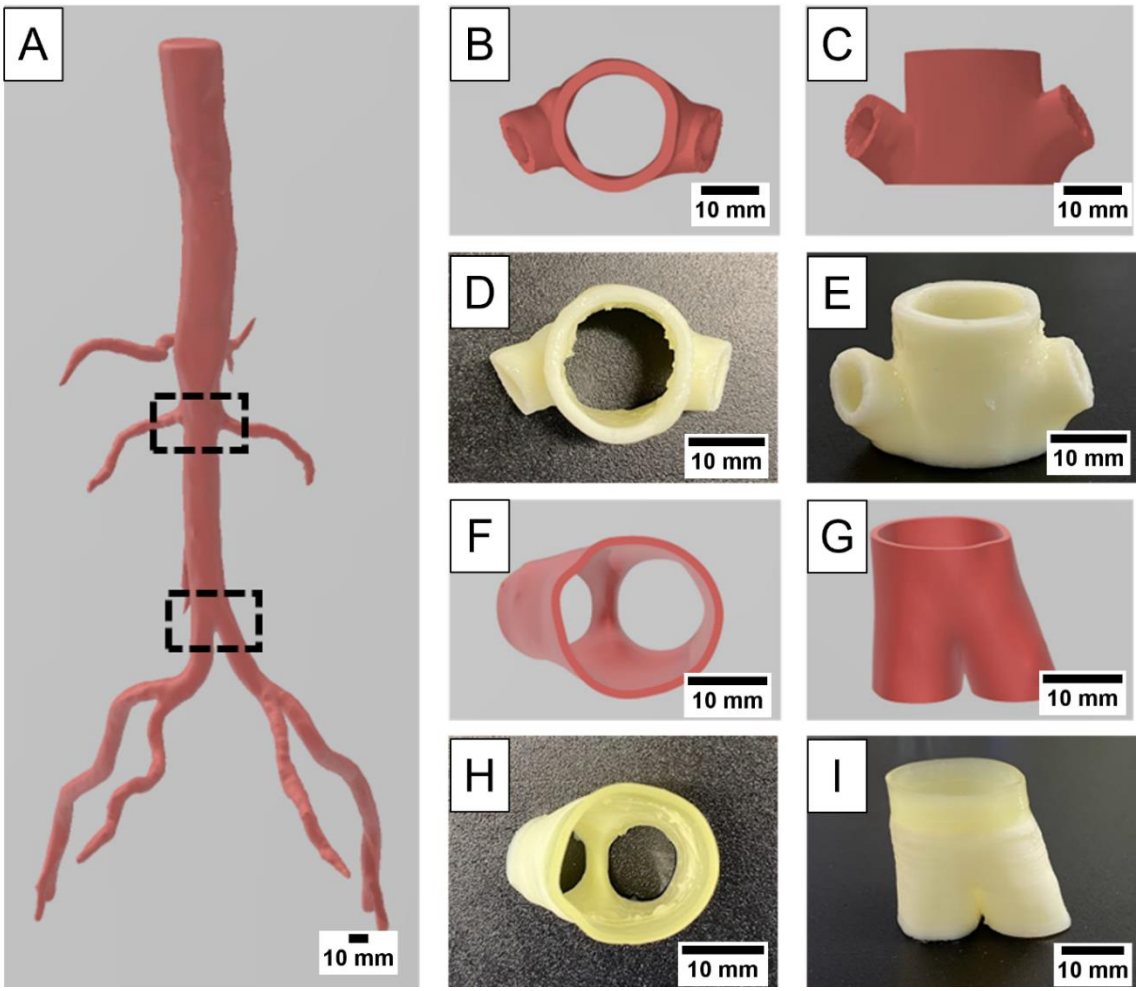


*Figure 7.16: 3D-printing of an anatomically relevant aortic structure: (A) open source human abdominal aorta model (The Biomedical 3D printing community, Embodi3D, 2023) with target model segments marked in dashed boxes, (B) top and (C) side view of the aortic segment target model that branches into the renal arteries, corresponding (D) top and (E) side view of the 3D-printed branched vessel, (F) top and (G) side view of the aortic bifurcation target model, and corresponding (H) top and (I) side view of the 3D-printed aortic bifurcation.*

## 7.5. Discussion

The use of 3D-printing for the fabrication of aortic grafts opens up the possibility of developing constructs that geometrically match the intricate design of the human vasculature whilst also offering the potential of design customisation depending on patient needs (Skoog, Goering and Narayan, 2014; Melchiorri *et al.*, 2016; Robinson *et al.*, 2018). Herein, stereolithography was selected as the 3D-printing method of choice due to its photocuring ability, rapid fabrication times, and potential of printing multiple

constructs simultaneously (Yu *et al.*, 2020). However, prior to implementing this fabrication method for the production of aortic-like vessels, the alginate:PEGDA resin was characterised to assess its printability and optimal print resolution. Additionally, given that 3D-printing involves a layer-by-layer crosslinking process as opposed to bulk crosslinking of the material during moulding, any changes to the mechanical properties (both elastic and viscoelastic) between 3D-printing and moulding were evaluated. Finally, a series of tubular constructs with dimensions similar to the native aorta were fabricated.

### 7.5.1. Evaluating alginate:PEGDA resin properties for optimal printability via SLA

Printability is a key characteristic in 3D-printing analysis. This determines whether the resin can be easily printed, and its ability in producing structures that: (1) faithfully represent the target model, and (2) possess structural integrity to be utilised in the desired application. Herein, the first step involved the evaluation of the resin's printability by assessing it viscous behaviour. For the SLA printer used in this work, prior to the printing of each layer, the tank comprising the resin tilts to ensure that the whole printing area is sufficiently recoated in preparation for the following layer. To assess whether the resin can flow easily inside the tank with every tilt movement, resin viscosity analysis via shear rheology is typically performed. Low viscosity resins (< 5 Pa·s) have been reported to facilitate SLA printing as these can spread evenly over the tank surface (Mondschein *et al.*, 2017; Ni *et al.*, 2018; González *et al.*, 2020; Schwab *et al.*, 2020). As shown by the flow curves in Figure 7.2, the alginate:PEGDA resin with and without photoblocker addition exhibits a viscosity less than 1 Pa·s which is within the flowable range required for SLA 3D-printing. In addition to this, the viscosity profile is non-Newtonian given that the viscosity decreases with increasing shear rate, also known as a shear-thinning solution. This behaviour typically occurs due to microstructural rearrangements such as the disentangling and stretching or aligning of polymer chains resulting in more free

space within the solution contributing to a reduction in viscosity (Panalytical, 2016). Therefore, from these curves it can be concluded that shear rates up to 100 $s^{-1}$ that may be imposed on the resin due to the tilting movement does not increase the viscosity of the resin but instead it decreases and remains sufficient for tank recoating.

In addition to viscosity analysis, the resin's printability was also investigated by 3D-printing single-layered samples at different exposure times. From this, as shown extensively in other light-based 3D-printing investigations (Seo *et al.*, 2017; Benjamin *et al.*, 2019; Hisham, Saravana Kumar and Deshpande, 2022) working curves as a function of photoblocker concentration were obtained (Figure 7.3). In the absence of a photoblocker, light scattering was dominant as can be observed in Figure 7.3(A) where the thickness of a single-layered print was measured to be greater than 1.4 mm with increasing exposure times. This was also evident when 3D-printing dog-bone shaped specimens for tensile testing without photoblocker, where the gauge width was much larger (48.14 ± 2.22 % difference) than the designed CAD model (Table 7.1).

By maintaining the same printing parameters, upon the addition of a photoblocker, single layer thickness was almost halved as shown in Figure 7.3(B) – (C). Moreover, tensile specimens were printed with dimensions closer to the CAD design model, with the difference between 3D-printed parts and the design model decreasing with increasing photoblocker concentration (Table 7.1). However, given that the samples were not measured immediately post-print, but following immersion in $BaCl_2$ for the alginate crosslinking and immersion in water to rinse out non-crosslinked residues, the difference in gauge width to the CAD model might also be due to swelling of the hydrogel. When comparing the hydrogels containing the photoblocker, the difference in gauge width when compared with the CAD model was much less in the 0.03 %(w/v) photoblocker sample than the 0.025 %(w/v). It is important to note, given that the structures produced here are on the order of millimetres and do not consist of complex, microarchitecture

features, such as internal channels or overhangs, photoblocker controllability is not as crucial, provided that $C_d$ ≥ layer thickness (Benjamin *et al.*, 2019). However, it is still important that the printed structure dimensions do not vary significantly from the CAD model design as in the case of samples printed without photoblocker. Therefore, despite a 6.51 ± 0.51% relative difference to the designed model, the 0.03 %(w/v) photoblocker concentration was taken forward for further evaluations.

In the present work, tartrazine was used as the photoblocker. Several investigations have reported the use of tartrazine as a photoblocker in SLA 3D-printing for biomedical applications, particularly due to its biocompatibility, low toxicity in humans, and widespread use as a food additive approved by the Food and Drug Administration agency (Benjamin *et al.*, 2019; Grigoryan *et al.*, 2019; Yang *et al.*, 2020; Yu *et al.*, 2020). However, it has been reported that tartrazine can be easily washed out by immersing the 3D-printed sample in an aqueous solution, with elution time highly dependent on the dimensions of the 3D-printed part (Grigoryan *et al.*, 2019). This can be observed in Figure 7.17 which shows the 3D-printed aortic segment that branches out into the renal arteries straight after removal from the printer's platform (Figure 7.17(A)) and after 3 days immersion in DI water (Figure 7.17(B)).

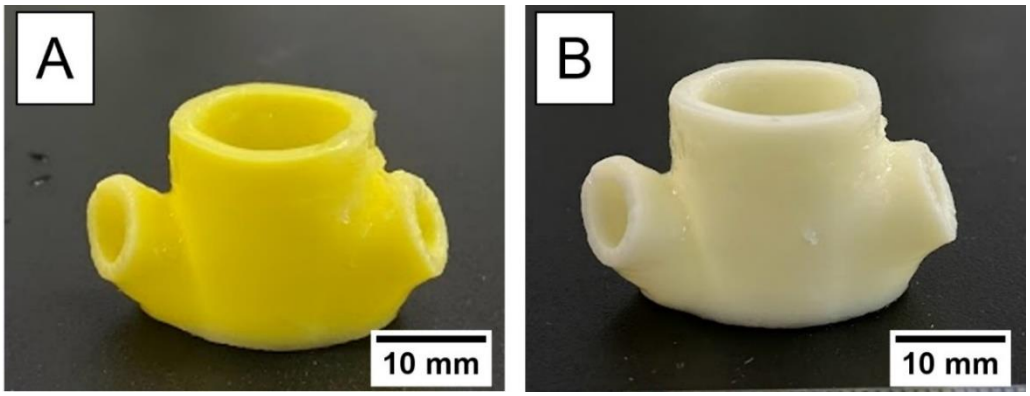


*Figure 7.17: 3D-printed aortic-like vessel after removal from the printer's platform (A) and after 3 days immersion in DI water (B), showing tartrazine release from the sample.*

The latter is almost completely white in colour indicating that most of the tartrazine had been released. This correlates well with the study by Grigoryan *et a*l., (2019), where 70% of the tartrazine present in small gels was reported to have been released after a 3-hour immersion in an aqueous solution. Therefore, if these constructs were to be implanted *in vivo,* a period for tartrazine release must be considered prior to implantation to minimise excessive release in the patient's body. In light of this, for future work, an *in vitro* release study would provide better insight on what would happen physiologically.

### 7.5.2. Comparing the mechanical properties of moulded versus 3D-printed alginate:PEGDA IPN hydrogels

The 3D-printed hydrogels were mechanically characterised via uniaxial tensile stretch to failure tests and rheological measurements to assess the impact of the fabrication process on the mechanical properties of the alginate:PEGDA IPN hydrogel. Interestingly, the mechanical properties, both elastic (Figure 7.5) and viscoelastic (Figure 7.7), of the 3D-printed hydrogels (FLET: 30 s, and ET: 16 s) showed good agreement with the moulded samples, except for a significant decrease in elongation at break when 0.03 %(w/v) photoblocker was incorporated in the 3D-printing resin (Figure 7.5(A)). Moreover, the range of storage modulus (G') over varying frequencies, was also found to decrease with increasing photoblocker concentration (G' at 1 Hz for 0 %(w/v): 410.03 ±66.02 kPa, 0.025 %(w/v): 339.43 ±60.25 kPa, and 0.03 %(w/v): 245.13 ±33.73 kPa as shown in Figure 7.7). This variation in mechanical properties might be attributed to the increase in light attenuation as a result of a higher photoblocker concentration which restricts photocrosslinking of the PEGDA within the focal plane. Consequently, throughout the printing process, the previously printed layers are not overexposed as in the absence of a photoblocker or at lower concentrations (0.025 %(w/v)), therefore exhibiting inferior mechanical properties (Seo *et al.*, 2022). A similar behaviour was observed by Burke *et al*., (2020) when comparing the tensile

properties of moulded and SLA printed polyethylene glycol dimethacrylate (PEGDMA) hydrogels, where the latter exhibited lower tensile strength but similar elastic modulus to their moulded counterparts. Burke *et al.*, (2020) suggested that this might be due to (1) potential structural imperfections originating from the layer-by-layer 3D-printing process where sections within the printed part might not have been fully cured, and (2) printing orientation, in particular along the z-axis, which has been reported to have a great impact on mechanical properties (Unkovskiy *et al.*, 2018; Saini *et al.*, 2020; Farkas, Galatanu and Nagib, 2023). In this work, as shown schematically in Figure 7.18(A) the dog-bone samples were printed horizontally i.e., in parallel with the build platform without any supporting structures, with one layer on top of each other in the z-direction. Therefore, when subjected to tensile testing, the load exerted to stretch the sample is parallel to the printed layers. It is likely that changes to the print direction, which would essentially change the way the printed object is layered, would result in variations in the alginate:PEGDA IPN hydrogel mechanical properties. However, this caters for further investigations to justify whether the elastic properties would be enhanced or not due to print orientation.

Moreover, both the use of a photoblocker and the different exposure times between the initial layers (FLET: 30 s; equivalent to the first 14 layers which is ~25% of dog-bone sample thickness) and the rest of the printed layers (ET: 16 s) create a crosslinking gradient within the hydrogel contributing to variations in mechanical performance in comparison with the bulk material (Uzcategui *et al.*, 2018; Galarraga *et al.*, 2023), as schematically explained in Figure 7.18(B).

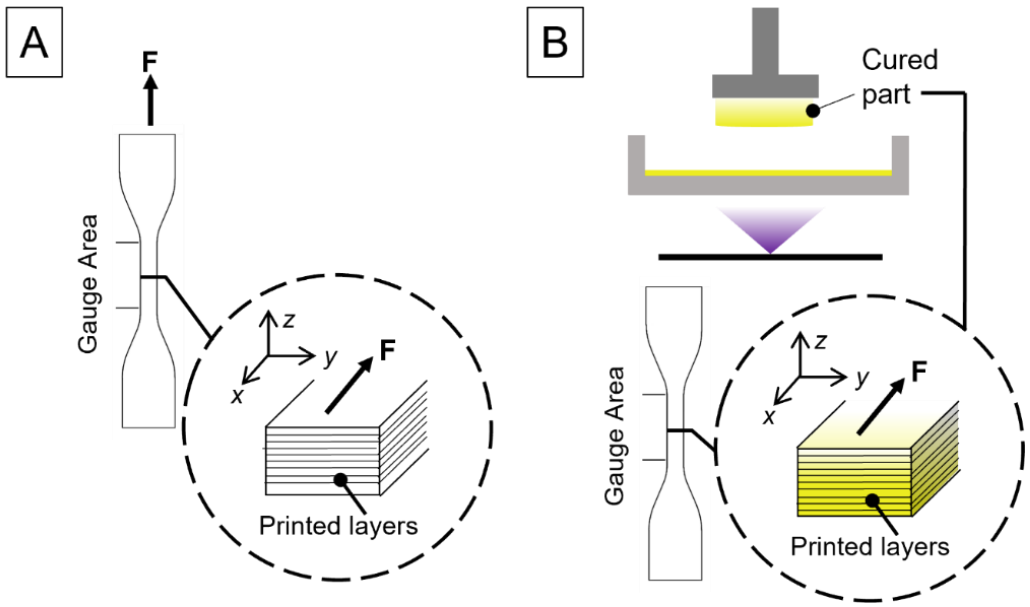


*Figure 7.18: Schematic representation of (A) the load exerted on the 3D-printed dog-bone sample during uniaxial tensile testing with cross-sectional view of the gauge area illustrating stretching along the printed layers, and (B) the photoblocker and exposure time gradient on the printed structure and its effect on the tensile specimen during loading.*

Despite the change in elongation at break between the 3D-printed alginate:PEGDA IPN hydrogel comprising 0.03 %(w/v) photoblocker and the moulded hydrogels, the strength and stiffness were still within range of the elastic properties reported for aortic tissue, as presented in Table 7.2. Additionally, as shown by the gauge width measurements, the 0.03 %(w/v) photoblocker concentration provides closer shape fidelity to the CAD model than the lower photoblocker concentrations. Therefore, this hydrogel formulation in combination with SLA 3D-printing was taken forward to print aortic-like conduits.

*Table 7.2: Comparing the tensile stretch to failure properties of alginate:PEGDA IPN moulded, and 3D-printed with aortic tissue data from the literature at a crosshead speed of 1 mm/min. Data is presented as the mean ± S.D. (UTS: ultimate tensile strength, $\varepsilon_B$: elongation at break, EM: elastic modulus, PM: physiological modulus, Circ: circumferential, and Long: longitudinal directions).*

| **Study** | **Material** | **Mechanical Properties** | | | |
|---|---|---|---|---|---|
| | | **UTS (MPa)** | **$\varepsilon_B$ (%)** | **EM (MPa)** | **PM (MPa)** |
| Current work | Alginate:PEGDA IPN **Moulded** (3.3%(w/v):26.6%(w/v):66mM $BaCl_2$) | 0.39 ±0.05 | 24.4 ±4.33 | 1.61 ±0.19 | — |
| | Alginate:PEGDA IPN **3D-printed** (3.3%(w/v):26.6%(w/v):0.03%(w/v) PB:66mM $BaCl_2$) | 0.34 ±0.05 | 18.02 ±2.41 | 1.79 ±0.19 | — |
| (Vallabhaneni *et al.*, 2004) | Abdominal Aorta (Human) Circ | 0.61 ±0.07 | 29.0 ±4.0 | — | 1.82 ±0.10 |
| | Abdominal Aorta (Human) Long | 1.30 ± 0.11 | 33.0 ±4.0 | — | 1.38 ±0.12 |

### 7.5.3. 3D-printed alginate:PEGDA IPN hydrogels towards the fabrication of alternative aortic grafts

Given the success in printing samples for material mechanical characterisation, the alginate:PEGDA resin comprising 0.03 %(w/v) photoblocker was taken forward to 3D-print tubular structures of varying dimensions. Using 3D-printing for the production of aortic-like structures has numerous benefits over the moulding technique described in Chapter 6. Primarily, with 3D-printing, the use of moulds, including the polypropylene syringes and the sacrificial agarose hydrogel, were not required anymore thereby facilitating variations in tubular structure dimensions, including inner and outer diameters, wall thicknesses, and lengths. However, sample length proved to be problematic when printing vertically (layers parallel to the build platform). Consequently, straight tubular conduits were initially printed at a length of 7.5 mm (Figure 7.8 and Figure 7.9), which was then increased to 15 mm (Figure 7.10), followed by 30 mm (Figure 7.11), to assess the point up to which the printer can print successfully in the vertical direction.

Print failures were observed when printing several constructs of different wall thicknesses at the same time, and when the structure length was set beyond 20 mm. The former could be attributed to the weight of the printed structures; as the wall thickness increases the weight of the constructs increases, creating poor load distribution on the build platform leading to sample failure, especially for the thinner walled structures. Therefore, it is ideal when printing multiple parts simultaneously that they are of the same geometrical dimensions to prevent failure due to pulling forces.

Failure due to object length, was primarily due to the printing time which was extended to almost 3 hours for a 30 mm construct. This resulted in numerous issues, including dehydration of the previously printed layers as shown in Figure 7.11, separation of the alginate:PEGDA resin in the tank which required either resin change or top-up mid-print, and pulling forces due to the structure's length possibly requiring a higher FLET to ensure structure adhesion to the build platform. In an attempt to successfully produce 30 mm long vessels, or even longer, given that aortic sections requiring grafts are typically much longer than this, the printing orientation was changed to 45° and supports were included to prevent structure collapse. The first attempt was carried out using the same exposure time conditions (FLET: 30 s and ET: 16 s) as the previous prints, however this resulted in a long printing time (~ 3 hours 40 minutes) and overexposure as could be observed by the poor fidelity to the CAD model in Figure 7.12. A second attempt was made using lower exposure times (FLET: 30 s and ET: 7 s) but this resulted in layer separation (Figure 7.13). From this, it was demonstrated that longer structures may be obtained by changing the print orientation, but further investigations are required in order to obtain better printing accuracy. Additionally, as already mentioned in the previous section, printing orientation influences greatly the mechanical behaviour of the final product, and therefore evaluation of the mechanical properties of alginate:PEGDA IPN hydrogels printed at different angles to the build platform would be necessary.

The radial load of the 3D-printed tubular structures was also investigated by placing the vessels horizontally between two plates and exerting a compressive displacement relative to the outer diameter. Contrary to Chapter 6, for this experiment a different mechanical characterisation instrument was used equipped with a larger load cell and a greater travel distance, allowing for the assessment of a 50% compressive displacement relative to the tube's outer diameter. Table 7.3 compares the dimensions and radial compression results of the 3D-printed and moulded structures.

*Table 7.3: Comparison of the 3D-printed and moulded alginate:PEGDA IPN tubular structures characterised by radial compression measurements. (OD: outer diameter, WT: wall thickness, L: length).*

| **Tubular Structure fabrication** | **Dimensions (mm)** | | | **Maximum Load (N)** | **Maximum diameter reduction ratio** |
|---|---|---|---|---|---|
| | **OD** | **WT** | **L** | | |
| 3D-printed | 18.34 ±0.01 | 2.08 ±0.02 | 15.50 ±0.22 | 2.71 ±0.34 | 0.491 ±0.001 |
| Moulded: smaller lumen | 14.09 ±0.05 | 1.68 ±0.06 | 29.29 ±0.41 | 0.48 ±0.08 | 0.247 ±0.002 |
| Moulded: larger lumen | 18.85 ±0.15 | 2.12 ±0.07 | 28.76 ±1.09 | 1.18 ±0.32 | 0.186 ±0.003 |

Direct comparison between 3D-printed and moulded vessels could not be made because of the difference in length (15.5 ±0.22 mm versus 28.76 ±1.09mm, respectively). Additionally, the maximum load for the 3D-printed samples corresponds to a diameter reduction of 49.1 ±0.10% as opposed to a diameter reduction of 18.6 ±0.25% for the moulded samples with a larger lumen. However, considering a diameter reduction ratio around 18.6% from the 3D-printed plots, this corresponds to a load of 0.98 N, which is less than that of the moulded samples. This does not necessarily mean that the 3D-printed samples are radially weaker than their moulded counterparts given that the plate to specimen contact area is much less for the 3D-printed samples due to their smaller length. Ideally, further tests would have been performed by 3D-printing structures of

similar dimensions to the moulded samples to be able to effectively compare the maximum load that these constructs are able to withstand. Interestingly, at a 50% displacement, two out of the three 3D-printed samples were able to withstand the load after reaching a 50% displacement and return to their original configuration once the load was removed. This indicates that the alginate:PEGDA IPN hydrogel has shape recovery characteristics consistent with the results reported by Hong *et al.,*(2015), where an alginate:PEGDA IPN hydrogel was developed and demonstrated a compressive strain of 95% prior to returning to its original shape. This work, however, requires further research to assess shape recovery properties, particularly using a greater sample size.

In addition to straight, tubular structures, aortic-like vessels based on an open-source human aortic model were also fabricated to demonstrate that this hydrogel formulation and fabrication method may be taken forward for the development of patient-specific aortic grafts. 3D-printed models of the vasculature based on imaging modalities such as CT and/or MRI scans have gained recent interest as teaching tools and for surgical planning (Torres and Luccia, 2018; Sun, Wong and Yeong, 2023). However, this typically utilises materials that are not biocompatible or mechanically matched to the native tissue and has yet to be translated for the fabrication of grafts that can be surgically implanted for aortic reconstruction. Herein, both fabricated structures resulted in a faithful representation of the target model (Figure 7.16). Once again, when printing these structures, the length of the sample was limited to approximately 20 mm (Figure 7.16). Some dehydration was visible in the bifurcated sample (Figure 7.16(H) and (I)), which might be attributed to the longer printing time, since the FLET and ET were increased to 33 s and 11 s, (accounting to an overall printing time of approximately 2 hours) when compared with the renal branching section. However, adding extra resin mid-print might have helped in preventing this. Nevertheless, this proof-of-concept 3D-printing of slightly more complex aortic geometries (branched and bifurcated) has demonstrated the ability

of this method towards patient-specific 3D-printing. Therefore, for future work it would be interesting to obtain actual patient 3D CT or MRI scans of the aorta and transform these into CAD models for SLA 3D-printing using the alginate-PEGDA IPN hydrogel.

## 7.6. Conclusions

3D-printing offers a wide-range of benefits over existing vascular graft manufacturing methods, primarily the option of obtaining patient-specific geometries. Therefore, in this chapter, stereolithography 3D-printing via a commercially-available desktop 3D printer was investigated for the production of alginate:PEGDA IPN hydrogels in the pursuit of developing anatomically-relevant tubular vessels as aortic graft substitutes.

The 3D-printing resolution was controlled by the addition of a photoblocker (tartrazine dye) that strongly absorbs the wavelength emitted by the printer (405 nm). The 3D-printed material was mechanically characterised via uniaxial tensile stretch to failure and rheological measurements to assess differences between the moulded material characterised in Chapter 6, and the printed material fabricated in a layer-by-layer manner. A significant difference in elongation at break was observed when using 0.03 %(w/v) photoblocker. The 3D-printed hydrogels maintained their viscoelastic behaviour, yet a decrease in storage modulus could be observed with increasing photoblocker concentration.

By considering both geometrical fidelity and mechanical behaviour, the 0.03 %(w/v) photoblocker concentration was taken forward to print tubular structures. The vessels were fabricated with similar dimensions to sections of the aorta (outer dimeter: 18 mm and wall thickness: 2mm), and compression tests showed that the conduits could withstand a displacement up to 50% of their outer diameter, with some vessels also showing signs of shape recovery. In addition to straight, tubular structures, vessels based on human aortic geometry were also fabricated demonstrating potential that this method could be used towards the development of patient-specific grafts.

# Chapter 8 Introducing cell binding sites to alginate-based hydrogels via the incorporation of an RGD peptide

## 8.1. Introduction

As demonstrated in previous chapters, the alginate:PEGDA IPN hydrogel formulation exhibits similar elastic properties to the native aorta and shows good printability properties capable of producing aortic-like structures. However, despite the relative biocompatibility of alginate and PEG, both monomers lack intrinsic cell binding sites, and therefore additional modifications to the hydrogel formulation are required for optimal biological compatibility.

Once implanted *in vivo*, vascular grafts are recognised by the human body as foreign objects, triggering the blood coagulation and inflammatory pathways, leading to non-specific plasma protein adsorption on the graft's lumen, culminating in thrombosis (Ren *et al.*, 2015; Kizhakkedathu and Conway, 2022). Hence, ideal vascular grafts should favour rapid endothelialisation of the lumen by ensuring that the material is responsive to endothelial cells (Ren *et al.*, 2015). A common strategy to achieve this on synthetic hydrogel matrices involves the incorporation of extracellular matrix (ECM)-based proteins (collagen, elastin, laminin, fibronectin) within the precursor hydrogel solution. However, given that these proteins are of animal origin, their use in implantable medical devices such as vascular grafts, may elicit an immunological response whilst increasing the risk of infection (Hersel, Dahmen and Kessler, 2003; Andersen, Auk-Emblem and Dornish, 2015), consequently introducing complications in the regulatory pathway and clinical translation of the implant. Moreover, proteins may also accelerate the degradation process of the material *in vivo* due to their susceptibility to proteolytic enzymes (Hersel, Dahmen and Kessler, 2003). Therefore, to address these limitations and maintain a completely synthetic synthesis process, several investigations have opted for the incorporation of short peptide sequences, such as the widely investigated

arginine-glycine-aspartate (RGD) motif present in most ECM proteins. This is recognised by cell integrins (namely, $\alpha_5\beta_1$ and $\alpha_v\beta_3$) as a ligand, thereby facilitating cell adhesion and proliferation (Ren *et al.*, 2015).

The primary advantage of using peptides is that they are chemically defined, providing a great degree of precision and controllability during synthesis and conjugation with biomaterials (Collier and Segura, 2011). Peptides are generally produced synthetically via solid phase peptide synthesis (SPPS), as schematically described in Figure 8.1. Briefly, this method involves a stepwise assembly of amino acids (residues) via a series of alternating reactions for amino acid (AA) coupling and protecting group (PG) removal, while the AA sequence is covalently attached to an insoluble polymer (resin) as support. Once the sequence is synthesised, the crude peptide is released from the resin via a cleavage reaction generally using a strong acid, and purified (Fields, 2001). The peptide is then conjugated with the biomaterial through either physical (deposition onto a material or blending) or chemical (covalent bonding through coupling agents or crosslinkers) methods (Perlin, MacNeil and Rimmer, 2008).

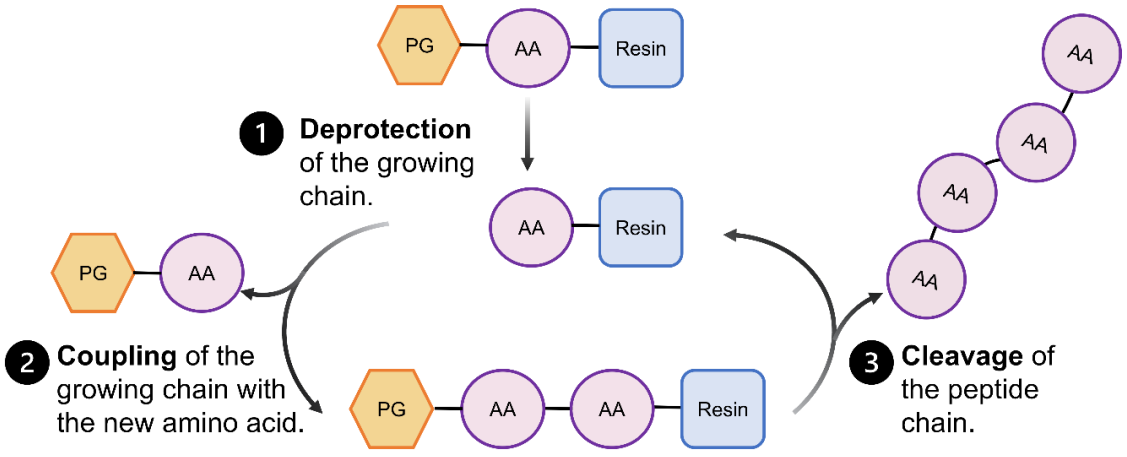


*Figure 8.1: Schematic representation of the solid phase peptide synthesis process (AA: amino acid, PG: protecting groups). Schematic created using BioRender.com.*

Several investigations have addressed the lack of cell binding sites in alginate and PEG monomers via the incorporation of an RGD peptide (Rowley, Madlambayan and Mooney,

1999; Yu *et al.*, 2009; Bidarra *et al.*, 2011; Jia *et al.*, 2016a; Yan, Chen and Amsden, 2016; Della Sala *et al.*, 2020). The RGD peptide is typically synthesised or introduced to biomaterials as more than just a tripeptide, with various variants involving several flanking amino acids at both sides of the sequence (e.g., GRGDY, RGDSP, GGGGRGDSP) to improve cell adhesive strength (Hersel, Dahmen and Kessler, 2003; Bellis, 2011). Alginate is traditionally functionalised with RGD via aqueous carbodiimide chemistry, as outlined in the well-established protocol by Rowley *et al.,* (1999). The ability of this alginate:RGD combination to support cell adhesion and viability has been investigated in several cell types, including endothelial cells (Yu *et al.*, 2009; Bidarra *et al.*, 2011). Similarly, RGD-functionalised PEG has been extensively investigated and synthesised using various conjugation methods, with the most common strategy involving initial functionalisation of the RGD peptide with reactive groups, such as acrylates, to enable covalent bonding between the peptide and PEG-based polymer (Zhu, 2010; Jia *et al.*, 2016a). Despite the introduction of cell binding sites in single-network alginate and PEG hydrogels separately, to the author's knowledge there have been no reports on the incorporation of an RGD peptide within an alginate:PEGDA ionic covalent entanglement interpenetrating polymer network (ICE IPN). Similar work was reported by Aldana *et al.,* (2021), however this involved a double network hydrogel comprising oxidised alginate, crosslinked via a Schiff base reaction (specific for aldehyde groups), and PEGDA, crosslinked via photopolymerisation. The RGD peptide was modified to contain aminooxy functional groups and was covalently bonded to the aldehyde groups present in the oxidised alginate. Other alginate:PEGDA IPN hydrogels have undergone biofunctionalisation via the incorporation of cell-recognising monomers, such as collagen (Hong *et al.*, 2015), fibronectin (Huang *et al.*, 2022) and polyphosphate (Zhang *et al.*, 2021).

## 8.2. Aims and Objectives

The aim of this chapter was to synthesise and incorporate an RGD-based peptide using solid phase peptide synthesis to the alginate:PEGDA ICE IPN (developed in Chapter 6 and Chapter 7) as a way of enhancing the material's biological activity and suitability as a potential alternative to existing aortic graft technologies.

The objectives of this work included the investigation of:

1. The synthesis of a $G_4$RGDSP peptide via Fmoc solid phase peptide synthesis.
2. The incorporation of a $G_4$RGDSP peptide to sodium alginate using a protocol based on aqueous carbodiimide chemistry.
3. The functionalisation of the $G_4$RGDSP peptide with an acrylate end group at the N-terminus to allow incorporation with the PEGDA monomer, thus forming a PEGDA:RGD hydrogel.
4. The production of an RGD-modified alginate, PEGDA, and alginate:PEGDA IPN hydrogels, and evaluation of endothelial cell attachment and viability via brightfield and fluorescence imaging.

## 8.3. Materials and Methods

### 8.3.1. Fmoc Solid Phase Peptide Synthesis (SPPS) of $G_4$RGDSP peptide

#### 8.3.1.1. Materials

All reagents and solvents were purchased from Merck-Sigma Aldrich, UK at reagent grade or higher unless otherwise stated. H-Pro-2-ClTrt resin (0.87 mmol/g), Rink Amide MBHA resin (0.36 mmol/g, Novabiochem), Rink Amide MBHA resin HL (0.89 mmol/g, Novabiochem), Fmoc-L-Pro-OH, Fmoc-L-Ser(tBu)-OH, Fmoc-L-Asp(OtBu)-OH, Fmoc-Gly- H, Fmoc-L-Arg(Pbf)-OH, *N,N*-Diisopropylethylamine (DIPEA*), N,N,N′,N′*-Tetramethyl-O-(1H-benzotriazol-1-yl)uranium hexafluorophosphate (HBTU), Benzotriazole-1-yl-oxy-tris-pyrrolidino-phosphonium hexafluorophosphate (PyBOP), 1-

Hydroxybenzotriazole (HOBt), Piperidine, dichloromethane (DCM), *N,N*-Dimethylformamide (DMF), 1-Methyl-2-pyrrolidinone (NMP), *N,N'*-Diisopropylcarbodiimide (DIC), acrylic acid (AAc), trifluoroacetic acid (TFA), triisoproylsilane (TIPS), Ether Diethyl ether, acetonitrile, isopropanol, and methanol.

#### 8.3.1.2. Peptide synthesis

Three $G_4$RGDSP peptide sequences were synthesised. Peptide 1 was prepared at a scale of 0.3 mmol using the H-Pro-2-ClTrt resin and coupling of Fmoc amino acids using HBTU together with DIPEA and HOBt. Peptide 2 was prepared at a scale of 0.3 mmol using the Rink Amide MBHA resin, and PyBOP as the coupling reagent together with DIPEA and HOBt. Peptide 3 was prepared in a similar manner to Peptide 2, however using the Rink Amide MBHA resin HL (high loading) and at a higher synthesis scale (1.5 mmol), without the addition of HOBt. This sequence was also capped at the N-terminus with an acrylation step prior to cleavage.

#### 8.3.1.3. Resin preparation

For both resin types, H-Pro-2-ClTrt and rink amide, the resin powder was weighed according to the synthesis scale and swelled in DCM (3 times the bed volume) for 20 minutes. The DCM was then aspirated via vacuum, and the dried resin was washed twice in DMF.

#### 8.3.1.4. Fmoc amino acids coupling and deprotection steps

Following resin swelling, the first Fmoc amino acid was coupled. For the H-Pro-2-ClTrt this was Fmoc-L-Ser(tBu)-OH (Serine, S) because the resin contained C-terminal Proline (P) as shown in Figure 8.2(A). 0.5 M Fmoc amino acid was first dissolved in DMF at 4 molar excess. 1.0 M HBTU, 0.5 M HOBt, and DIPEA at 4 molar excess, were also dissolved in DMF, and then combined all together with the Fmoc amino acid. The same coupling process was employed for the rink amide resin (Figure 8.2(B)), however the first Fmoc amino acid to be coupled was the Fmoc-L-Pro-OH (Proline, P), and 1.0 M PyBOP,

and DIPEA at 2 molar excess were used instead. The combined Fmoc-coupling agent cocktail was added to the respective resin and the reaction was allowed to proceed for 1 hour. The resin was then rinsed 4 times with DMF, and twice with the solvent of the next reaction (NMP).

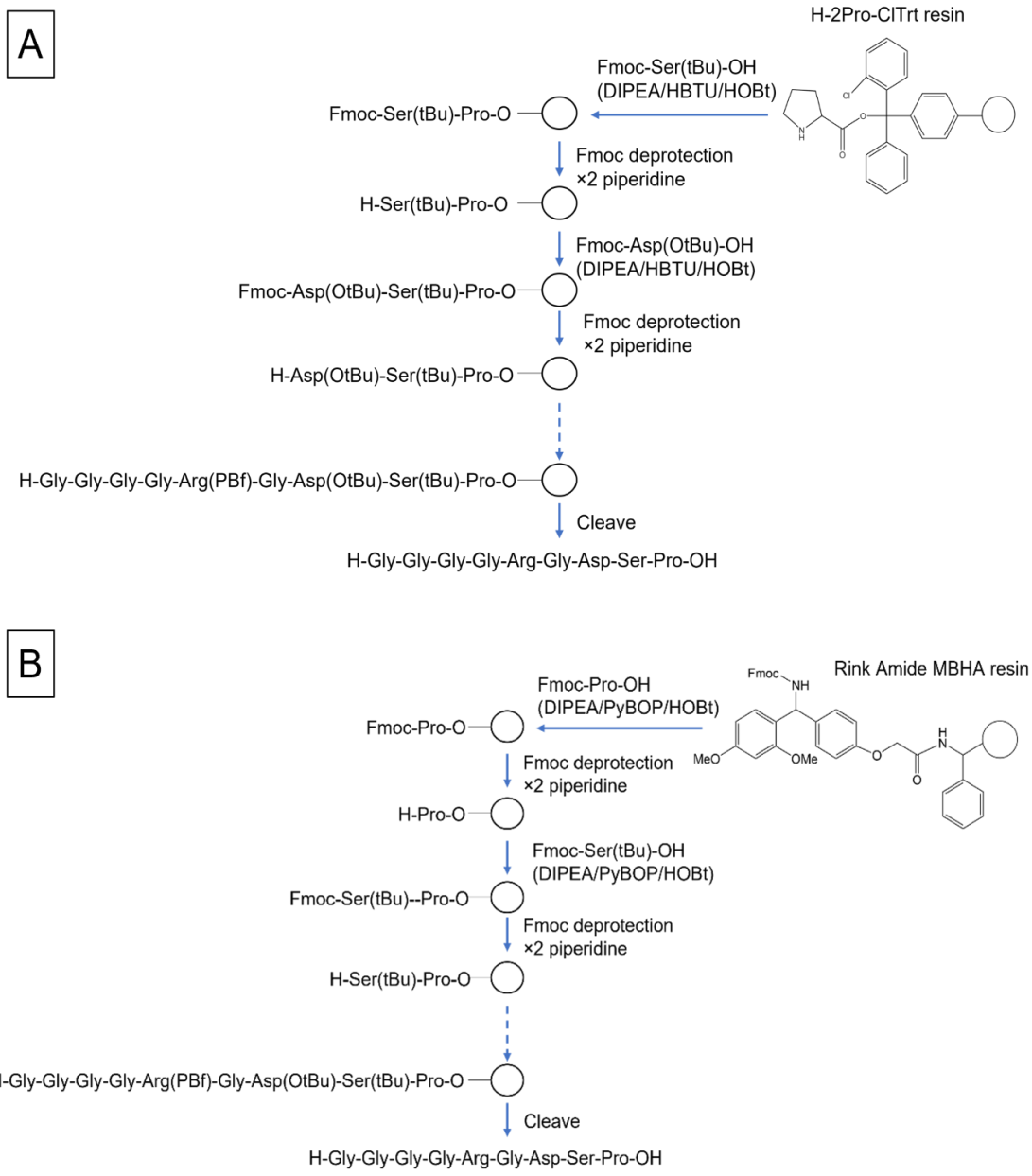


*Figure 8.2: Schematic representation of the general method of peptide synthesis through SPPS using (A) the H-Pro-2-ClTrt resin, and (B) Rink Amide MBHA resin, showing the Fmoc amino acid coupling and deprotection steps to obtain the final $G_4$RGDSP peptide product.*

Following Fmoc coupling, the resin was treated with piperidine to remove the Fmoc protecting groups. 20% (v/v) piperidine in NMP was added to the resin (2 times the bed volume) and the resin was agitated for 20 minutes, drained, and the piperidine step was repeated. The resin was then rinsed in NMP for 3 times and rinsed twice with the solvent of the next reaction (DMF). These coupling and deprotection steps were repeated until all 8 residues were coupled to the resin (Figure 8.2).

Fmoc amino acid coupling and deprotection steps were monitored via colorimetric tests: Kaiser (or Ninhydrin) and/or Chloranil. The Kaiser test involves the combination of 2 to 3 drops of each of the following reagents to a small sample (10 to 15 beads) of the resin: Reagent A (potassium cyanide (KCN) in DI water diluted in pyridine), Reagent B (ninhydrin in n-butanol), and Reagent C (phenol in n-butanol). The test tube containing the sample was heated to 110°C in a heating block for 5 minutes and changes in colour of the solution were noted. This test is mostly sensitive to primary amines, as the ninhydrin reacts with the deprotected N-terminal amine group of the peptide producing an intense blue colour (Figure 8.3(A)). No colour change implies that the Fmoc amino acid coupling was complete (Figure 8.3(B)). This test is not suitable to detect secondary amines and is not accurate when the N-terminal amino acid is proline, therefore the Chloranil test was used instead when deprotecting Fmoc-Pro-OH.

The Chloranil test comprises two reagents: Reagent A (acetaldehyde in DMF) and Reagent B (p-chloranil in DMF). The test was carried out by adding a drop of both reagents to a small sample of the resin in an Eppendorf tube. The reaction was allowed to proceed at room temperature for 5 minutes and changes in colour of the beads were observed. A blue colour suggests that secondary amine is present indicating successful deprotection of Fmoc-Pro-OH, whereas no colour changes suggest that the coupled Fmoc-Pro-OH still retained the Fmoc group. After coupling the following Fmoc-AA, the Chloranil also revealed whether any remaining chains terminating in Pro still remained

due to incomplete coupling. Moreover, given that the as-received rink amide resin is Fmoc protected, a deprotection step is first performed prior to the coupling of the Fmoc-Pro-OH, therefore, a chloranil test was also performed following the deprotection of the rink amide resin to test for the primary amine.

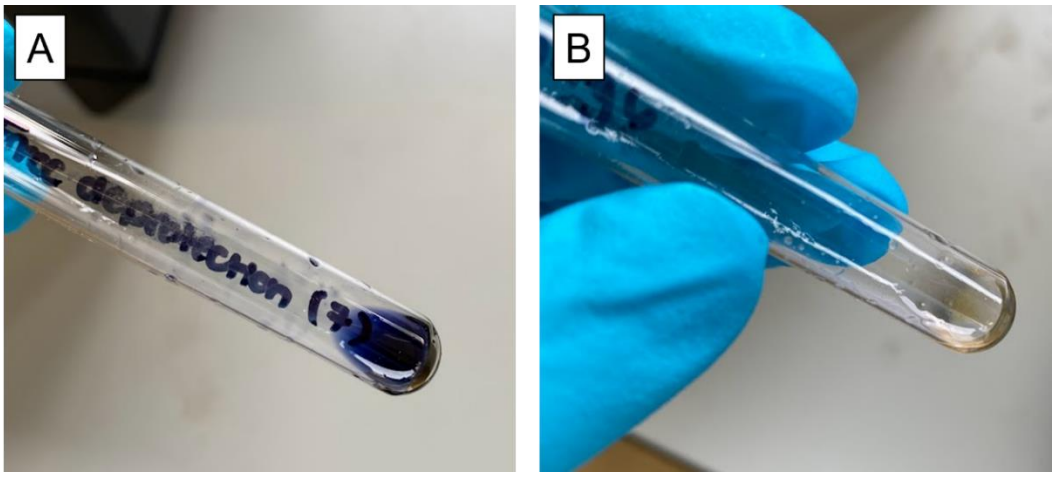


*Figure 8.3: Kaiser test: (A) after Fmoc deprotection step showing an intense blue colour, and (B) after Fmoc amino acid coupling showing no changes in colour.*

#### 8.3.1.5. Peptide cleavage

Test cleaves were performed at different stages of the peptide synthesis process. This involved the preparation of 1 ml cleavage cocktail comprising 95% (v/v) TFA, 2.5% (v/v) TIPS, and 2.5% (v/v) DI water. A small sample of resin was transferred to the cleavage cocktail, and this was agitated for 1 hour. Samples for HPLC and LCMS analysis (Section 8.3.1.6) were prepared containing 20 µl of the cleavage solution and 80 µl of acetonitrile in DI water (1:1).

Once the whole peptide sequence was complete and the N-terminal Fmoc group was deprotected, a full peptide cleave was carried out. A higher volume cleavage cocktail enough to cover the bed volume twice was prepared, comprising 95% (v/v) TFA, 2.5% (v/v) TIPS, and 2.5% (v/v) DI water. The cleavage cocktail was mixed with the resin and allowed to agitate for 1 hour. The solution was filtered to remove the resin and the

filtered liquid collected in a round-bottom flask (RBF) (Batch 1). The remaining resin was rinsed again in fresh TFA cocktail and allowed to agitate for another hour, the filtered liquid was collected in another RBF (Batch 2). Using a rotavapor, any remaining TFA in the solution was evaporated from both batches leaving behind an oily residue corresponding to the remaining peptide. Cold diethyl ether was added to the RBFs to precipitate the peptide, and the precipitate was transferred into centrifuge tubes. Centrifugation at 2000 rpm for 3 minutes was performed to separate the precipitate. Once spun down, the supernatant was removed. The peptide was resuspended in acetonitrile:DI water (1:1) and transferred into glass vials. This was followed by first freezing at -80° C and then lyophilisation at -50° C.

#### 8.3.1.6. Peptide analysis: Analytical High Performance Liquid Chromatography (HPLC) and Liquid Chromatography – Mass Spectrometry (LCMS)

Analytical HPLC was carried out on a Dionex P680 HPLC system equipped with a C-18 column (EC 250/4.6 Nucleocil 100-5 C18), mobile phase A comprising $H_2O$ and 0.1% (v/v) TFA, and mobile phase B comprising acetonitrile and 0.1% (v/v) TFA. HPLC runs were conducted at a flow rate of 1 ml/min at an acetonitrile eluting gradient of 5% to 95% over 47 minutes, and UV detection was set at four different wavelengths: 210 nm, 220 nm, 254 nm, and 280 nm.

Mass spectroscopy was carried out using the Agilent HPLC-MS (Agilent Technolgies 6130 Quadrupole LC/MS with ESI/SPCI Multiple mode Ionisation) equipped with a Reverse Phase C18 column (Poroshell 120 4.6 × 7.5 2.7 µm). LCMS runs were conducted in an ammonium acetate buffer (5 mM) at a flow rate of 1 ml/min and an acetonitrile eluting gradient of 5% to 95% over 18 minutes. UV detection was set at 214 nm with masses detected up to 2000 Da.

#### 8.3.1.7. Peptide purification

The resulting peptides were purified using preparative High Performance Liquid Chromatography (prep-HPLC) (Dionex Ultimate 3000) following analytical HPLC and LCMS analysis of the crude product. The use of different columns in the analytical and prep-HPLC results in peaks being eluted at different acetonitrile percentages, therefore the first run on the prep-HPLC was performed at a low sample concentration (5 mg/ml). The acetonitrile eluting gradient was adjusted according to the analytical HPLC data (2% to 100%), and samples were collected every 60 s for the first run to ensure that the peaks obtained contain the correct mass. Following the first run, the peak of interest was identified on the prep-HPLC graph as the one corresponding to the fraction with the target peptide mass. The acetonitrile percentage where the peak of interest appeared was then calculated, and a new gradient based on this was identified for the following purification runs, which were performed at higher sample concentrations (20 mg/ml and 50 mg/ml). With higher concentrations, fraction collection was changed to 20 s. The fraction collections of the peak of interest, mainly the fraction corresponding to the top of the peak, was combined for all runs. Analytical HPLC was performed to test the purity of the different combinations and LCMS to analyse the mass. Finally, centrifugal evaporation (Genevac™ Centrifugal Duo and Quattro Concentrator) was performed to reduce the solvent volume (acetonitrile:water) to not more than 5 ml. The sample solution was transferred to glass vials, frozen at -80°C and then lyophilised at -50°C.

### 8.3.2. Conjugating G4RGDSP peptide to PEGDA

Prior to cleavage of Peptide 3, an acrylate group was coupled to the N-terminus of the $G_4$RGDSP peptide using acrylic acid and DIC. First, 1.5 M acrylic acid was dissolved in DMF. To ensure successful coupling, the acrylic acid solution was run through a basic alumina plug to remove the MEHQ inhibitor. Briefly, the alumina column was prepared by packing a column with basic alumina and oven dried potassium carbonate ($K_2CaCO_3$)

(Figure 8.4). DIC was dissolved in DMF in a 1:1 volume ratio. The purified acrylic acid in DMF was then combined with DIC:DMF. The subsequent acrylic acid:DIC solution was added to the peptide resin and the reaction was allowed to proceed for 30 minutes. The resin was rinsed 6 times in DMF prior to cleavage and purification according to Sections 8.3.1.5 and 8.3.1.7. HPLC and LCMS analysis were carried out according to Section 8.3.1.6.

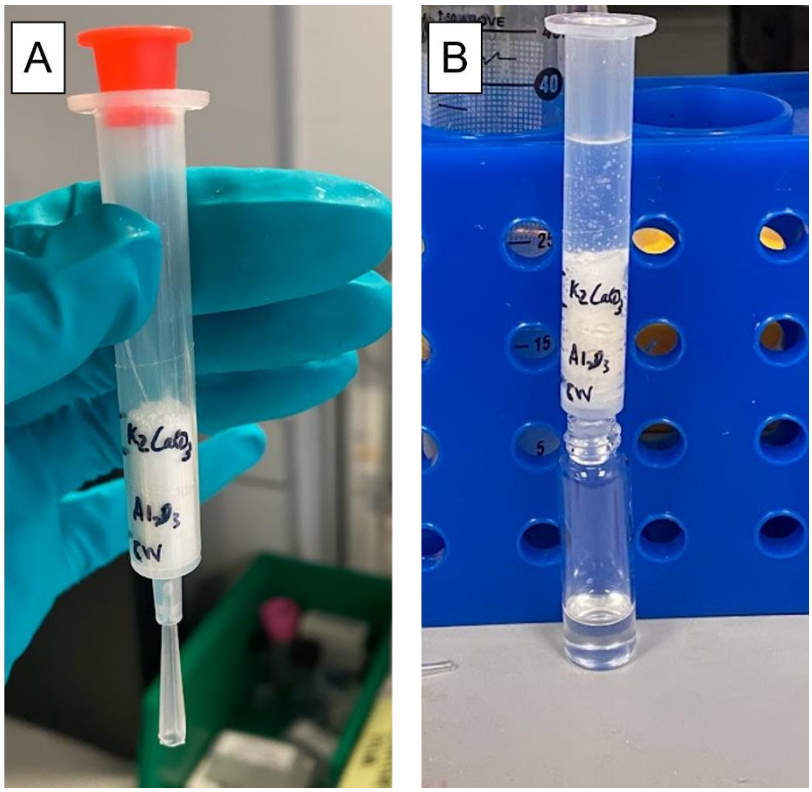


*Figure 8.4: Visual representation of (A) the packed alumina column comprising basic alumina at the bottom and oven dried potassium carbonate on top, and (B) the acrylic acid being passed through the alumina plug with the purified solution collected in a glass vial.*

### 8.3.3. Conjugating G4RGDSP peptide to alginate

#### 8.3.3.1. Materials

MES Buffer (1.0 M buffer solution, pH 6.5, Thermo Fisher Scientific, UK), EDC (3-Ethyl-3-(3-dimethylaminopropyl) carbodiimide HCl, Thermo Scientific, UK), Sulfo-NHS (N-Hydroxysulfosuccinimide, Thermo Scientific, UK), Hydroxylamine hydrochloride (ACS

reagent, Thermo Fisher Scientific, UK), sodium chloride, and dialysis membrane tubing (Spectra Por).

#### 8.3.3.2. Conjugation method

Alginate was modified with the $G_4$RGDSP peptide via aqueous carbodiimide chemistry according to the protocol outlined in Charbonier *et al*., (2021). First, sodium alginate powder was mixed with the MES buffer (0.1 M, pH 6.5) (1 g alginate per 100 ml MES buffer) overnight to ensure a homogeneous solution. Sulfo-NHS was dissolved into the alginate mixture in a 1:2 molar ratio to EDC, followed by EDC, and finally the $G_4$RGDSP peptide (2.87 mg peptide per 200mg alginate). The reaction was allowed to proceed for 20 hours and then quenched with 18 mg hydroxylamine hydrochloride per 1 g of alginate. The solution was then poured into dialysis tubes and dialysed in NaCl-supplemented DI water for 3 days. The salt solution was changed 2 to 3 times a day whilst decreasing the salt solution with every change. Following dialysis, the alginate: $G_4$RGDSP solution was poured into 50 ml centrifuge tubes, frozen at -80°C overnight, and then lyophilised at -50°C for approximately 3 days until completely dry. The resulting alginate: $G_4$RGDSP powder was stored at -20°C until further use.

#### 8.3.3.3. Proton Nuclear Magnetic Resonance (1H NMR) analysis

$^1$H NMR was carried out to determine whether the $G_4$RGDSP peptide was successfully conjugated to the sodium alginate powder. $^1$H NMR spectra were conducted with a Bruker Avance 3 NMR spectrometer. Samples (sodium alginate on its own, and alginate: $G_4$RGDSP) were prepared at 10 mg/ml in deuterium oxide ($D_2O$). Spectral data was collected and analysed using TopSpin 3.6.5.

### 8.3.4. In vitro cell culture studies

#### 8.3.4.1. Materials

Versene (EDTA), Dulbecco's Phosphate Buffered Saline (DPBS) (Oxoid™ Thermo Fisher Scientific), TrypLE™ (Gibco® Thermo Fisher Scientific), Human Umbilical Vein

Endothelial Cells (HUVECs) single donor, cryopreserved (PromoCell, UK), Human Endothelial Cell Growth Basal Medium (PromoCell, UK), Endothelial Cell Growth Medium Supplement Mix (PromoCell, UK), Penicillin/Streptomycin (Gibco® Thermo Fisher Scientific), and Opti-MEM™ reduced serum media (Gibco® Thermo Fisher Scientific).

#### 8.3.4.2. Preparation of Human Umbilical Vein Endothelial Cell (HUVEC) medium

A supplement mix, comprising primarily of foetal calf serum (2% (v/v)), endothelial cell growth supplement, epidermal growth factor, basic fibroblastic growth factor, heparin, and hydrocortisone, as provided by PromoCell was added to the endothelial cell growth basal medium and gently mixed until a homogenous mixture was formed. Penicillin and streptomycin were also added to the growth medium at 1% (v/v).

#### 8.3.4.3. HUVEC culture

HUVECs used in this research were kindly provided by Dr Junxi Wu (Biomedical Engineering, University of Strathclyde) and Dr Roger Domingo-Roca (Electrical and Electronic Engineering, University of Strathclyde). After reaching sub-confluency (approximately 70%), HUVECs were subcultured (passaged) first by washing twice with Versene (EDTA) in PBS to remove any traces of growth media, then the cells were detached using TrypLE. Following detachment of the cell monolayer, the cell suspension was transferred into a centrifuge tube containing growth media to stop the reaction and spun down at 220g for 5 minutes until a cell pellet was formed. The supernatant was aspirated and replaced by growth medium, cells were counted, and then seeded either onto gels or replated in flasks, depending on whether an experimental study was to be carried out or if the cells were to be maintained for further use. Cells were incubated in a humidified atmosphere of 5% $CO_2$ at 37°C with media changes performed every second day.

#### 8.3.4.4. Cell seeding on hydrogels

Cell adhesion experiments were carried out using HUVECs from passage 1 to passage 6. A range of hydrogels were prepared in 48-well tissue culture plates and/or 35 mm petri dishes: alginate (3.3 %(w/v) sodium alginate, 66mM $CaCO_3$:133.2 mM GDL), alginate:RGD (3.3 %(w/v) alginate:RGD, 66mM $CaCO_3$:133.2 mM GDL), and alginate:RGD:PEGDA (3.3 %(w/v) alginate:RGD. 13.3 %(w/v) PEGDA Mn700, 0.5 %(w/v) LAP, 66 mM $BaCl_2$), PEGDA (26.6 %(w/v)), and PEGDA:RGD (26.6 %(w/v): 13.3 mM). Sterile DI water was used as the solvent to prepare stock solutions of both the monomers and the crosslinkers. All solutions were mixed under the safety cabinet to ensure a sterile environment. Each well or petri dish contained 200 µl or 2 ml of pre-gel solution, respectively. The alginate and alginate:RGD solutions were mixed with the crosslinker ($CaCO_3$:GDL) and allowed to gel overnight at 4°C. The hydrogels comprising PEGDA were cured in a UV photocuring box (405 nm, Asiga Flash) for 2 minutes. Following hydrogel formation, the samples were UV sterilised for 1 hour. Cell growth media was added in each well or petri dish and the hydrogel samples were incubated at 37 °C in 5% $CO_2$ for 24 hours. Prior to cell seeding, the hydrogels were first checked under the microscope to ensure that no contamination was present, and the cells were seeded onto the hydrogel samples at a seeding density of 10,000 cells/$cm^2$. To allow the cells to adhere to the gel, additional growth media was added after 1 hour incubation. The media was then changed every second day until the end of the incubation period. For positive and negative controls, cells were seeded onto tissue culture plastic (TCP). The positive control was prepared in a similar manner as the cell-seeded hydrogels using the same endothelial cell growth medium (2% (v/v) as recommended for optimal endothelial cell growth) while the negative controls were supplemented with Opti-MEM serum-free media.

#### 8.3.4.5. Characterisation of cell behaviour on hydrogels

Cell adhesion of HUVECs on the hydrogels was assessed visually via a light-inverted microscope (Motic AE31) at designated time points post-seeding. At the end of each experiment, live/dead staining was carried out to assess cell viability. For live/dead, the cell seeded hydrogels were first washed twice in Dulbecco's Phosphate Buffered Saline (DPBS), then stained with propidium iodide (PI; 2% (v/v) in DPBS) and incubated in the dark for 1 minute. After three DPBS washes, the samples were stained with Calcein-AM (5 μM in DPBS), followed by three DPBS washes. The samples were then imaged using a ZOE$^{TM}$ fluorescent cell imager (BIO-RAD, UK) under the green (excitation wavelength: 480/17 nm) and red (excitation wavelength: 556/20 nm) channels.

## 8.4. Results

### 8.4.1. Preparation of the G4RGDSP peptide via SPPS

The chemical structure of the $G_4$RGDSP peptide is shown in Figure 8.5. Different resins yield different C-termini; peptide 1 synthesised using the H-Pro-2-ClTrt resin comprises the natural C-terminal acid (Figure 8.5(A)) and peptide 2 synthesised using the Rink Amide resin comprises the synthetic C-terminal amide (Figure 8.5(B)). Both peptides were synthesised according to the SPPS process described in Figure 8.2.

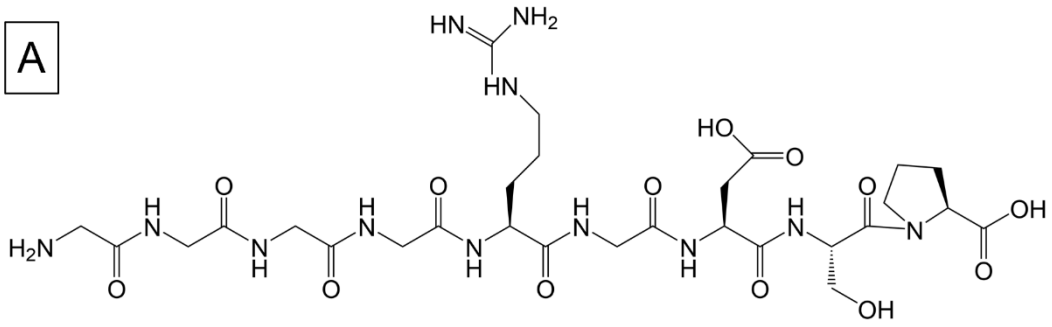


Chemical Formula: $C_{28}H_{46}N_{12}O_{13}$
Exact Mass: 758.33
Molecular Weight: 758.75
m/z: 758.33 (100.0%), 759.33 (35.2%), 760.34 (4.7%), 760.33 (4.1%), 761.34 (1.3%)
Elemental Analysis: C, 44.32; H, 6.11; N, 22.15; O, 27.41

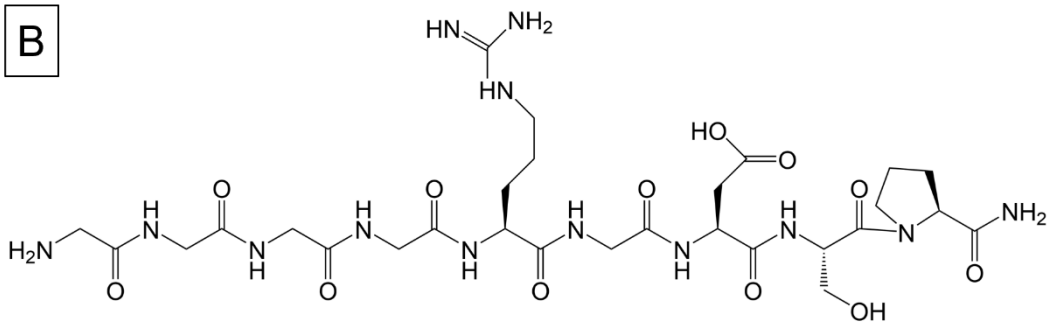


Chemical Formula: $C_{28}H_{47}N_{13}O_{12}$
Exact Mass: 757.35
Molecular Weight: 757.76
m/z: 757.35 (100.0%), 758.35 (31.3%), 759.35 (8.5%), 758.34 (4.7%), 760.35 (1.1%)
Elemental Analysis: C, 44.38; H, 6.25; N, 24.03; O, 25.34

*Figure 8.5: (A) Chemical structure and exact mass of the $G_4$RGDSP peptide 1 and (B) peptide 2, illustrating the difference in C-termini. Schematic generated using ChemDraw 21.0.0.*

To assess successful residue coupling and deprotection steps, resin samples were analysed via analytical HPLC and LCMS. The analytical HPLC spectra at different stages during synthesis are shown in Figure 8.6. Figure 8.6(A) shows the peptide synthesised with the H-Pro-2-ClTrt resin (peptide 1) while Figure 8.6(B) shows the peptide synthesised with Rink Amide resin (peptide 2). The tops of a number of peaks in the chromatograms are “chopped off” due to the high concentrations and corresponding high absorbances. Nonetheless, these are analysed according to their retention times.

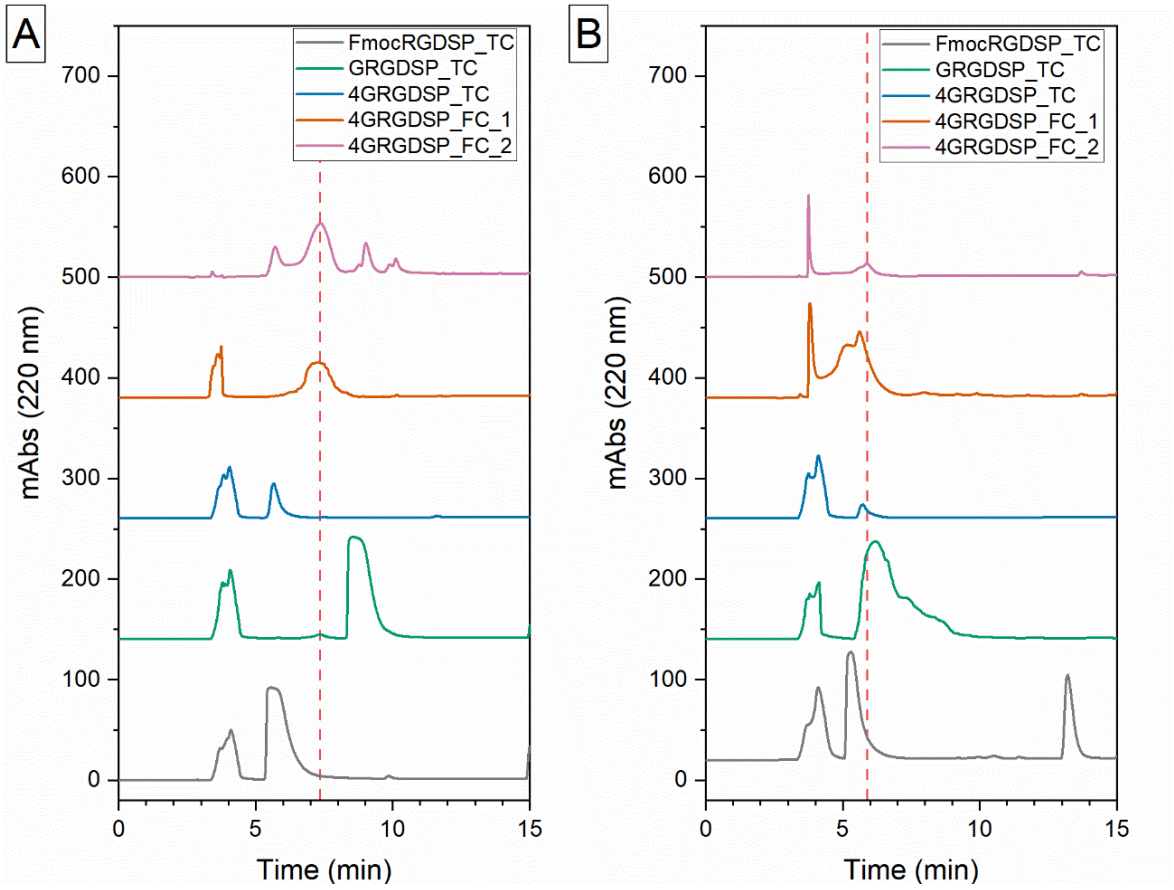


*Figure 8.6: Analytical HPLC spectra showing the crude products at different stages of synthesis for (A) peptide 1 using the H-Pro-2-ClTrt resin and (B) peptide 2 using the rink amide MBHA resin. The spectra presented were detected at 220 nm. Analytical HPLC measurements were performed at different stages throughout the synthesis process denoted by TC (test cleave), and after the full cleave (FC). Red dashed line indicates the peptide elution peak after full cleave.*

The full cleave chromatograms (4GRGDSP_FC_1 and 4GRGDSP_FC_2) for peptide 1 and peptide 2, show peptide elution at around 7 min and 6 min, respectively as indicated

by the red dashed line in Figure 8.6. For both peptides, a higher peak could be observed in batch 1 (4GRGDSP_FC_1) than batch 2 suggesting that almost all the peptide was already cleaved during batch 1. The peak observed in both the test cleave and full cleave chromatograms at an earlier retention time at around 4 minutes is potentially the TFA from the cleavage cocktail.

LCMS was used to verify the peptides obtained at different stages throughout synthesis. Figure 8.7 shows the LCMS UV trace together with the corresponding mass spectrum for batch 1 of both peptides. The mass obtained for both peptides include 759.4 ($[M+H]^+$) for peptide 1 and 758.4 ([M]) for peptide 2, which is within range of the expected mass for the $G_4$RGDSP peptide ([M]: 758.3 as shown in Figure 8.5). Masses were eluted at the initial stages of the LCMS measurements (1.22 min for peptide 1 and 1.24 min for peptide 2), corresponding to the high abundance peak of the HPLC spectrum in Figure 8.6.

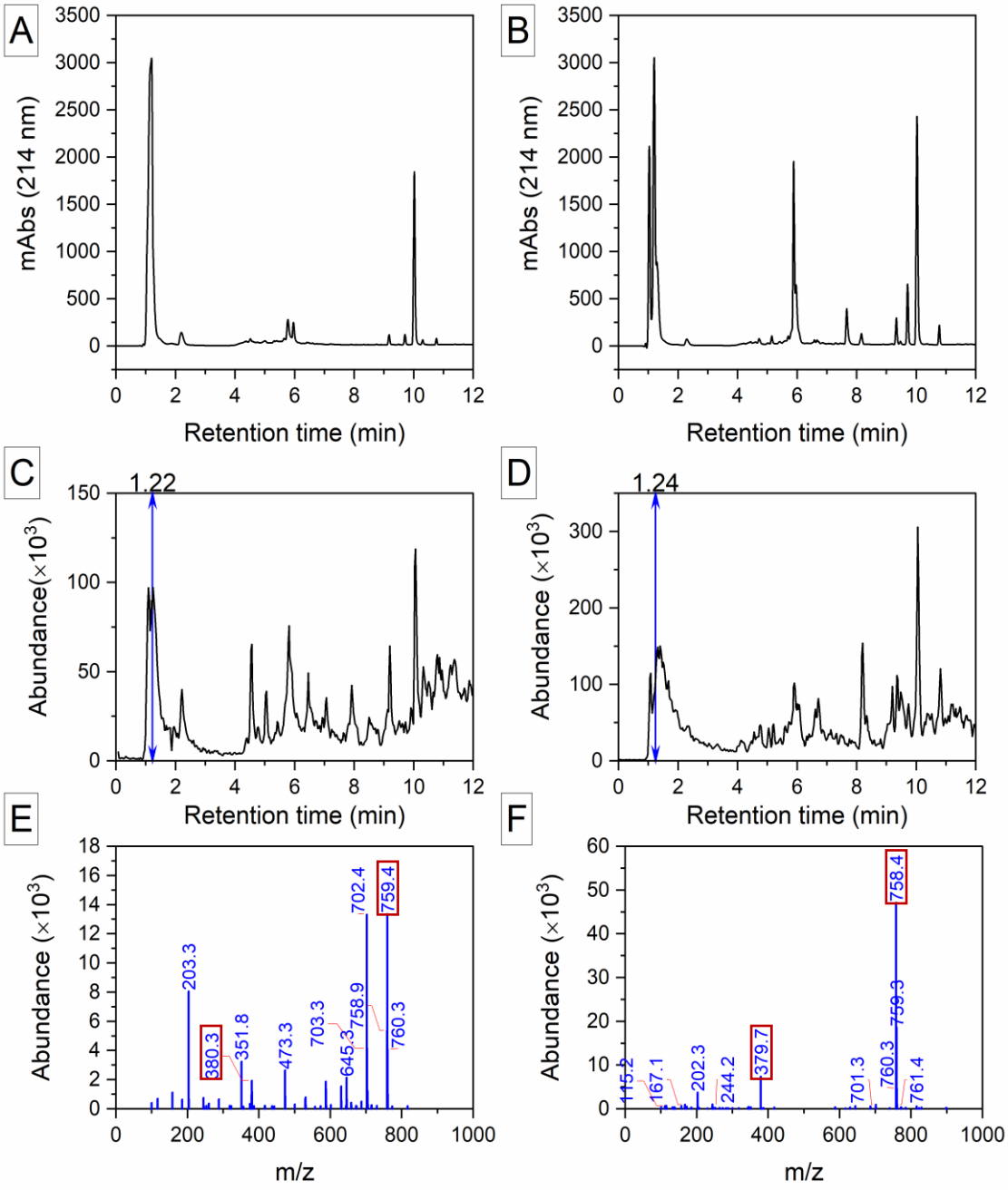


*Figure 8.7: LCMS results of peptide 1 (Batch 1) (A, C, E) and peptide 2 (Batch 1) (B, D, F) including the UV trace (A, B) and the corresponding LC (C, D) and m/z spectra (E, F). The peptide elution time is marked by blue arrows (C, D). The peaks corresponding to [M] (759.4 for peptide 1, and 758.4 for peptide 2) and $[M+2H]^+$ (380.3 for peptide 1, and 379.7 for peptide 2) are marked by red boxes (E, F).*

Following cleavage of the peptide chain, the next step involved purification of the peptide via prep-HPLC. Figure 8.8(A) shows the different spectra at different peptide 1 concentrations in acetonitrile:water. The flat peaks indicate a high abundance of material, which become more evident as the concentration increases since the column becomes increasingly saturated. The corresponding fractions are displayed in Figure 8.8(B). The different peaks in Figure 8.8(B) were analysed to determine where most of the peptide material lies. Once again, a high concentration of material results in the column becoming increasingly saturated which in turn contributes to earlier peak elution, as can be observed by fractions 4 (F04), 5 (F05), and 6 (F06). Despite F04 showing the same compound as F05 and F06, this was discounted due to the impurities as shown by small side peaks next to major peak. F08 and F09 were also disregarded due to the narrow area under the peak in F08, and the low peak in F09, both suggesting that peptide abundance is low. Fractions 5, 6, and 7 showed the highest peaks suggesting that the peptide material mostly lies within these fractions, although F07 seemed to contain some slight impurities as indicated by small peaks on both sides of the major peak. From this analysis, fractions 5 to 7 were combined. LCMS analysis was performed on all three fractions prior to the combination step. Figure 8.8(C) – (E) show the LCMS data obtained for fraction 6. The obtained mass (m/z: 759.3 equivalent to $[M+H]^+$) matches the expected mass of the $G_4$RGDSP peptide ([M]: 758.3). The mass spectrum also shows the corresponding half mass $[M+2H]^+$ (380.1).

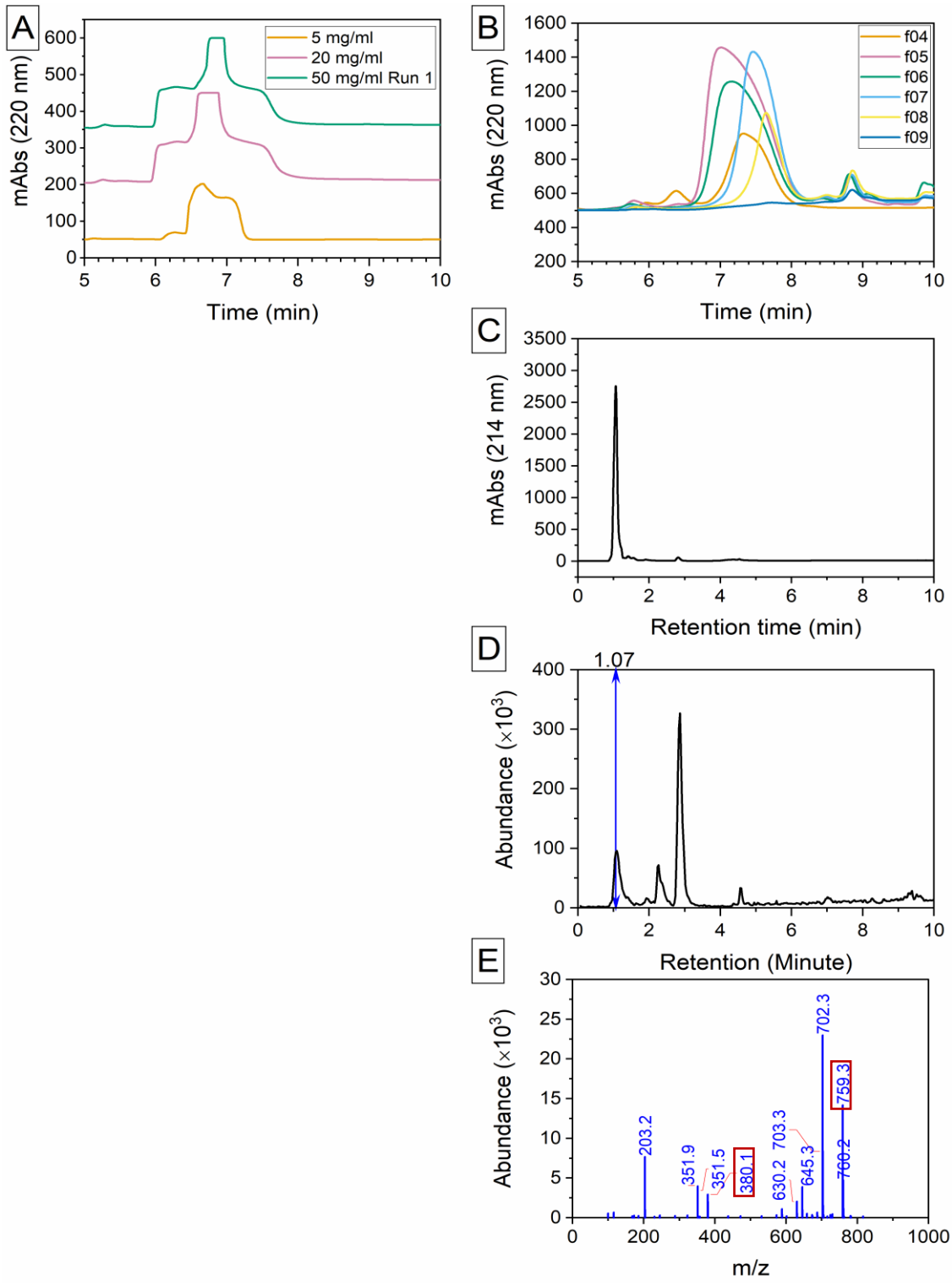


*Figure 8.8: Purification stage of peptide 1 with (A) showing the multiple runs at different concentrations (5 mg/ml, 20 mg/ml, and 50 mg/ml) performed on the prep-HPLC, (B) the collected fractions for the 50 mg/ml concentration, LCMS analysis of fraction 6 including the UV trace (C), the LC trace (D) and the corresponding m/z spectra at the time of peptide elution. Masses are marked by red boxes.*

For the rink amide resin i.e., peptide 2, prep-HPLC runs for the crude peptide diluted in acetonitrile:water are present in Figure 8.9(A) and the corresponding fractions in Figure 8.9(B). Analysis of these fractions showed that fractions 8 and 9 contained very little material as indicated by the low peaks. Fractions 4 to 7 seemed to contain most of the peptide material, and therefore these fractions were combined. Figure 8.9(C) – (E) show the LCMS data for fraction 6. The obtained mass (m/z: 758.2) matches the expected mass of the $G_4$RGDSP peptide ([M]: 758.3). The mass spectrum also shows the corresponding half mass $[M+2H]^+$ (379.7).

Once purified, the peptides were analysed via analytical HPLC to quantify the degree of purification by assessing the area under the highest peak. Figure 8.10 shows the spectra of both peptides after purification. From this, the degree of purity was calculated to be 86.66% for peptide 1 and 98.33% for peptide 2. Moreover, the peak elution time of the purified peptides matches the elution time of the full cleave chromatograms presented in Figure 8.6.

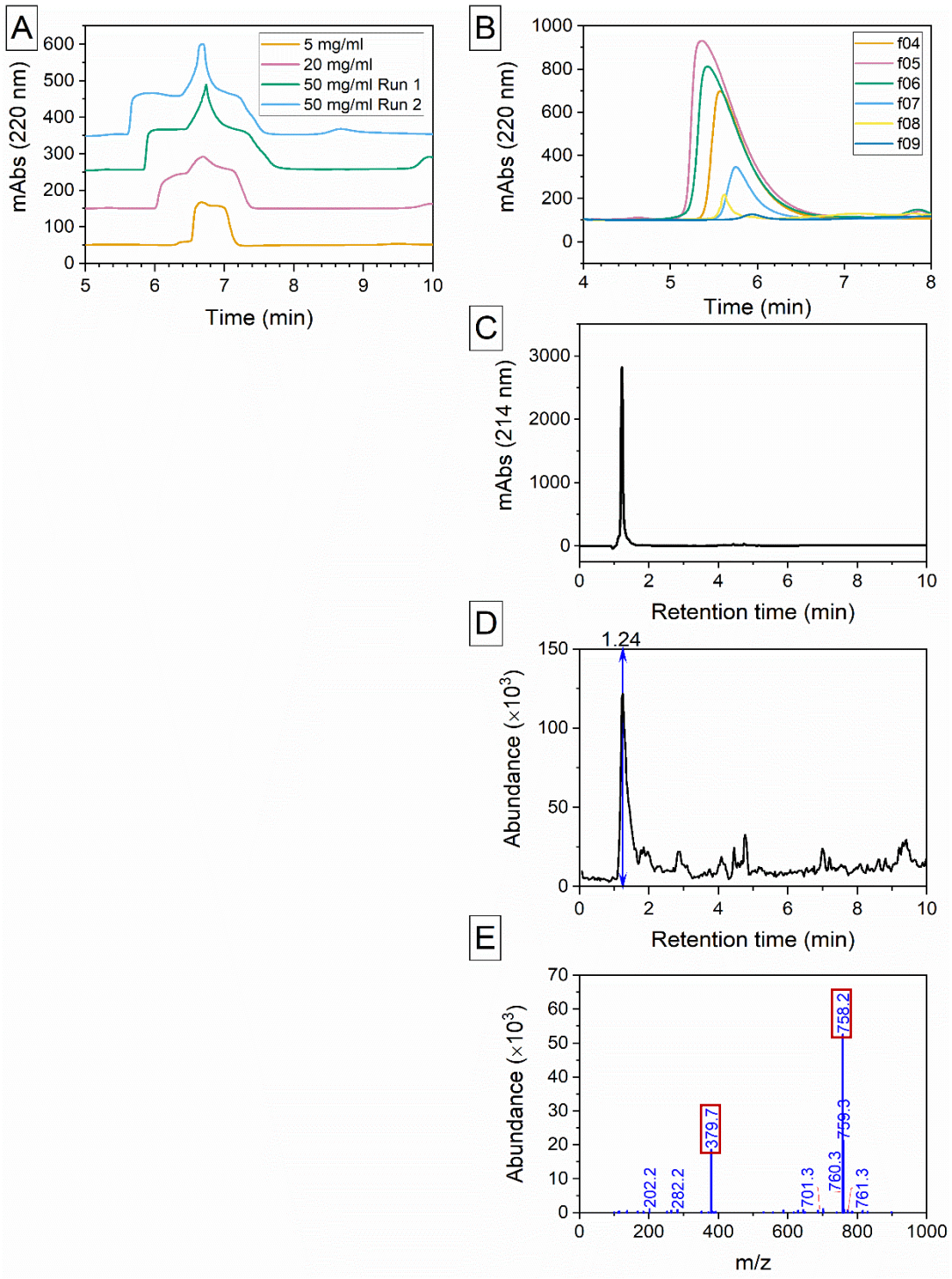


*Figure 8.9: Purification stage of peptide 2 with (A) showing the multiple runs at different concentrations (5 mg/ml, 20 mg/ml, and 50 mg/ml) performed on the prep-HPLC, (B) analytical HPLC of the collected fractions for the 50 mg/ml concentration prep elution, (C) LCMS analysis of fraction 6 including the UV trace, (D) the LC trace and (E) the corresponding m/z spectra at the time of peptide elution. The target masses are marked by red boxes. Other masses are related fragments.*

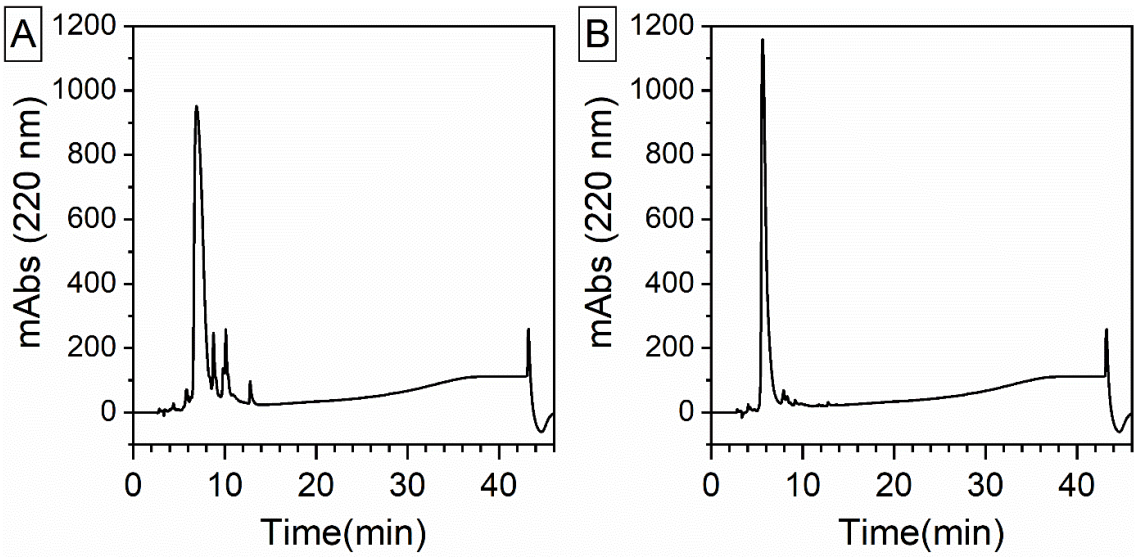


*Figure 8.10: Analytical HPLC spectra showing (A) peptide 1 and (B) peptide 2 after purification. The spectra presented were detected at 220 nm.*

### 8.4.2. Introducing an acrylate group to the $G_4$RGDSP peptide

In order to be able to conjugate the RGD peptide to PEGDA, peptide 3 was synthesised in a similar manner peptide 2, note that both have the same C-terminus (Figure 8.5(B)), however at the end of the of the fourth glycine coupling an acrylate group was coupled to the N-terminus of peptide 2 using acrylic acid, as represented by the chemical structure in Figure 8.11.

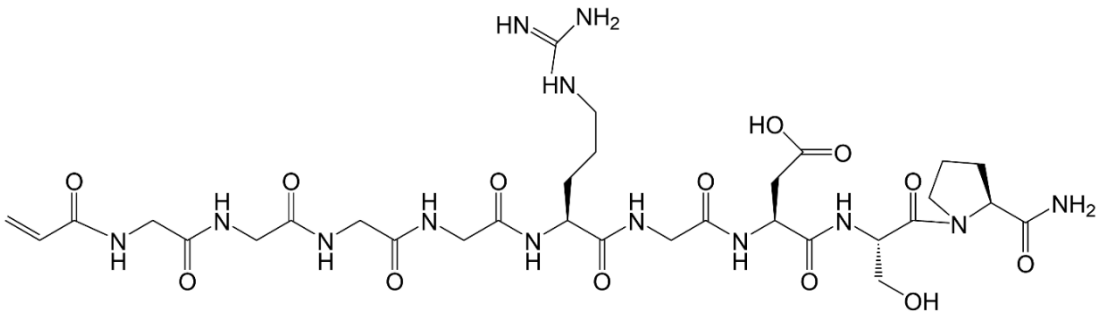


*Figure 8.11: Chemical structure and exact mass of the $G_4$RGDSP with acrylate side chain at N-terminus (Peptide 3). Schematic generated using ChemDraw 21.0.0.*

To assess residue coupling and deprotection steps, resin samples were analysed via analytical HPLC and LCMS. Figure 8.12 shows the analytical HPLC spectra before and after the addition of the acrylate group at the N-terminus. Although there is no obvious shift in retention time in the test cleave sample (4GRGDSP_TC and 4GRGDSP_Aac_TC both elute around 5.9 min, at the same time as indicated previously in Figure 8.10(B) showing the purified peptide 2), the full cleave sample shows large shifts to later elution times from around 9 min onwards (4GRGDSP_Aac_TC_Batch_1). “Batch 2” shown also in Figure 8.12 (4GRGDSP_Aac_TC_Batch_2) is simply the same resin left in the TFA cleavage cocktail for an extended time and, in this case, the peaks are very small, indicating that almost all the peptide was already cleaved during Batch 1.

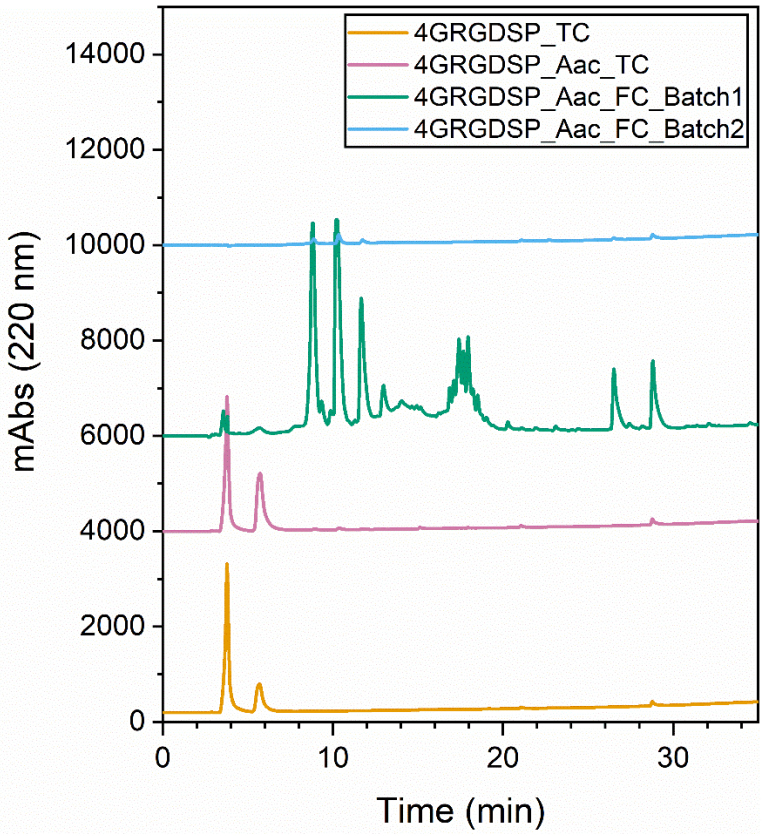


*Figure 8.12: Analytical HPLC spectra showing the synthesis process of peptide 3 using the rink amide MBHA resin before and after the addition of acrylic acid. The spectra presented were detected at 220 nm. Analytical HPLC measurements were performed at different stages throughout the synthesis process denoted by TC (test cleave), and after the full cleave (FC).*

The exact mass of peptide 3 as shown in Figure 8.11 is 811.36. The mass obtained via LCMS is the $[M+H]^+$ at m/z 812.4 (Figure 8.13(C)). Two other smaller fragments with main peaks at m/z = 698.2 and 755.4 were also found. These correspond to acrylated sequences missing one and two glycine residues, respectively. It is assumed that these series of masses correspond to the series of peaks appearing in the HPLC (i.e., at 9 min, 10 min, and 11 min in Figure 8.12). Despite having inserted 4 glycines before the terminal acrylate to facilitate presentation of the RGD, peptides with 2 or 3 glycines are also expected to functionalise PEGDA well. A longer glycine linker region introduces more amides for hydrogen bonding and may act to better solubilise the sequence. Therefore, the peaks appearing later may indicate successively fewer glycines.

In LCMS (Figure 8.13), the target mass(es) are most easily found at an elution time of around 2 min, which is earlier than the main series of peaks presumed to correspond to the acrylate peptide appearing at 4.3 to 7.5 min in LCMS. It is observed that after prep-HPLC (Figure 8.14(A)) and successful isolation of the main peak in re-analysis of the HPLC fractions (Figure 8.14(B)), an earlier and later peak also appeared in the LCMS traces (Figure 8.14(C)-(D)). Thus, both peaks may belong to the same peptide, with earlier peak indicating a more soluble species, e.g., arising from deprotonation of the aspartic acid residue.

The fractions were re-analysed in analytical HPLC (Figure 8.14(B)) to determine in which fractions the peptide is most abundant, which were fractions 5 and 6. Therefore, the other fractions (F04, F07, F08, and F09) were disregarded. In this case, fraction 6 for each run was combined together and dried. Unfortunately, upon final re-analysis in analytical HPLC (Figure 8.15), peaks at around both 9 min and 10 min were detected, indicating 4GRGDSP_Aac and 3GRGDSP_Aac species, respectively. The area under the highest peak at 9 min (indicated by the orange arrow) was calculated to be 58%. The 3GRGDSP_Aac impurity may have been introduced because of shifts in elution time

between purification runs (each fraction differs only by 20 s). Nonetheless, since both glycine linker lengths are useful for RGD functionalisation, the combined peptide product was applied to the cell culture experiments.

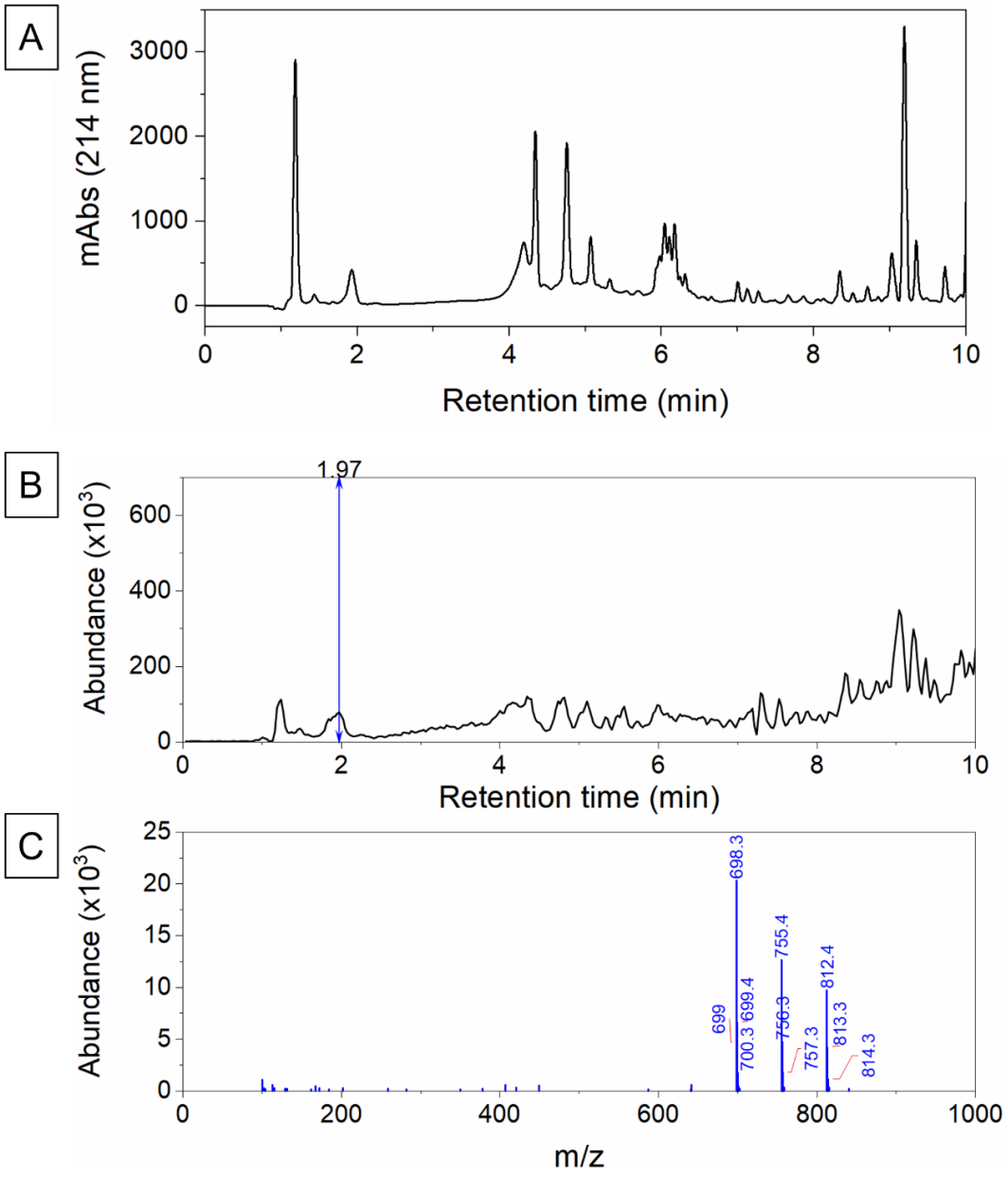


*Figure 8.13: LCMS results of peptide 3 (Batch 1): (A) UV trace, (B) LC trace with the peptide elution time marked by a blue arrow, and (C) the corresponding mass spectrum with the peak showing peptide mass marked by a red box.*

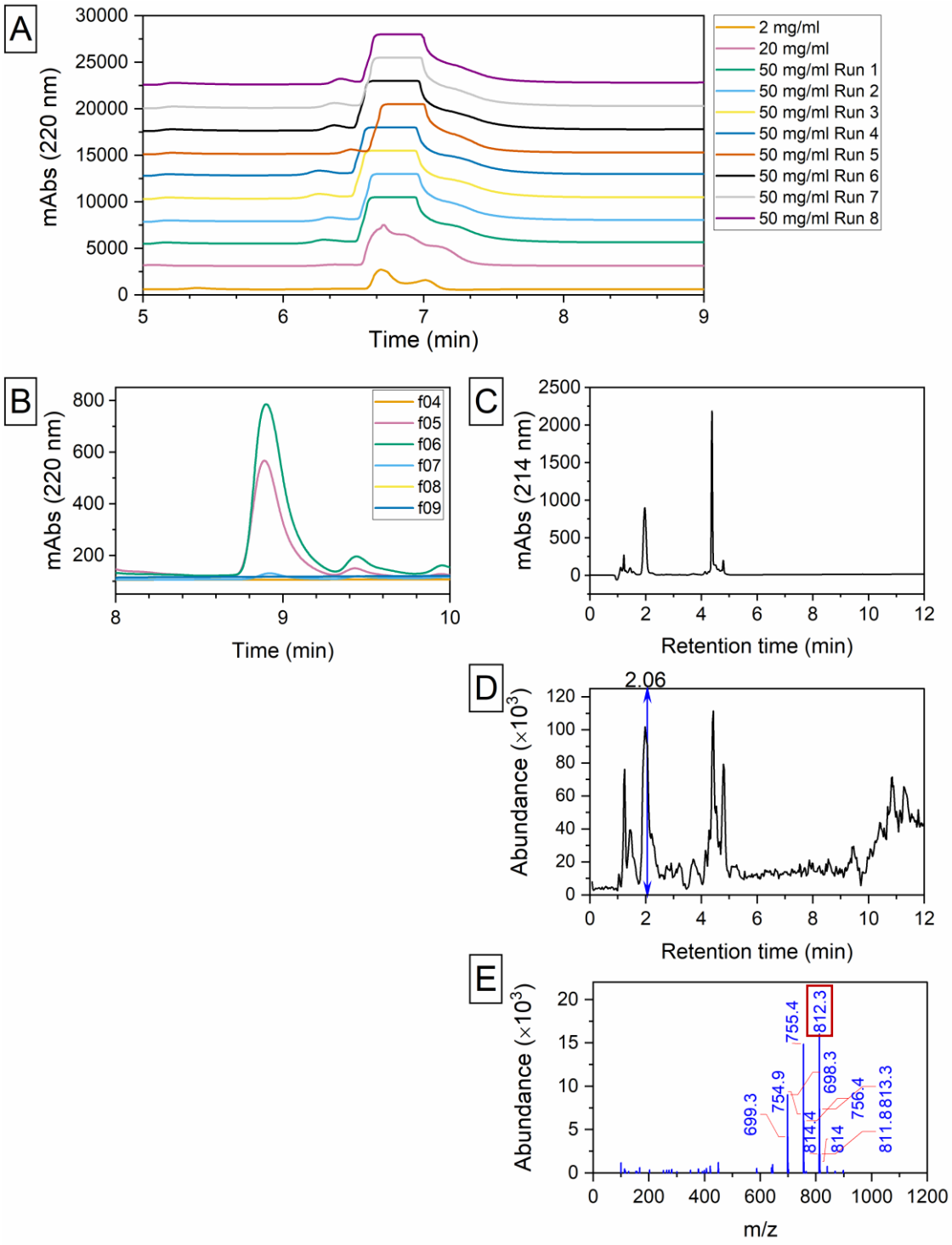


*Figure 8.14: Purification stage of peptide 3 with (A) showing the multiple runs at different concentrations (2 mg/ml, 20 mg/ml, and 50 mg/ml) performed on the prep-HPLC, (B) analytical HPLC of the collected fractions for the 50 mg/ml concentration prep elution, (C) LCMS analysis of fraction 6 including the UV trace, (D) the LC trace and (E) the corresponding m/z spectra at the time of peptide elution. The target mass id marked by red boxes. Other masses are related fragments.*

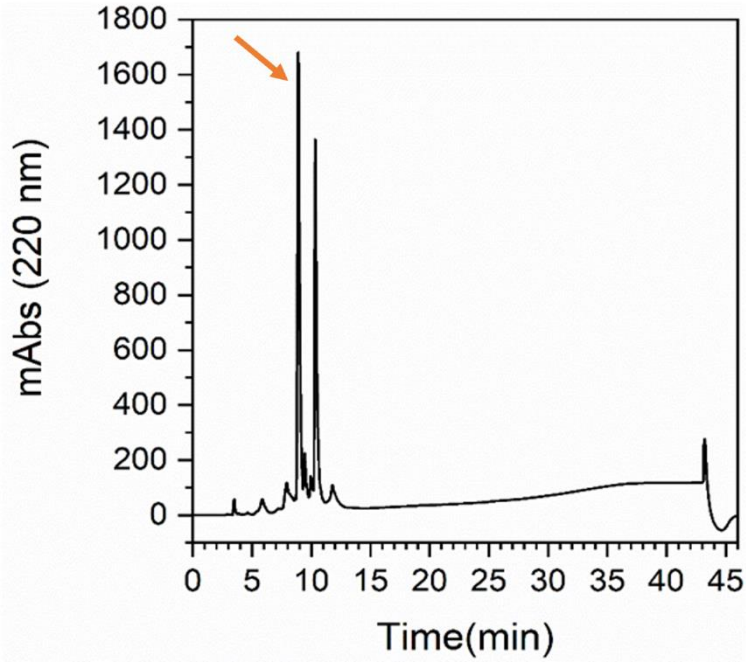


*Figure 8.15: Analytical HPLC spectrum showing peptide 3 after purification. Orange arrow indicates the peak corresponding to the peptide. The spectrum presented was detected at 220 nm.*

### 8.4.3. Synthesis characterisation of RGD-coupled alginate via $^{1}$H NMR

Figure 8.16(A) shows the chemical structure of the RGD peptide coupled with sodium alginate. The conjugation of the $G_4$RGDSP peptide to alginate was verified via $^{1}$H NMR spectroscopy, and the spectra of both the RGD-coupled alginate and sodium alginate on its own are shown in Figure 8.16(B). The two main sodium alginate single peaks corresponding to H1 of the M unit block and H1 of the G unit block were noted at a chemical shift, δ, of 4.4 ppm and 5 ppm, respectively, and were observed in both samples. In the alginate:$G_4$RGDSP sample, newly formed peaks could be observed, especially within the 1.0 ppm to 3.2 ppm region, suggesting successful coupling reaction.

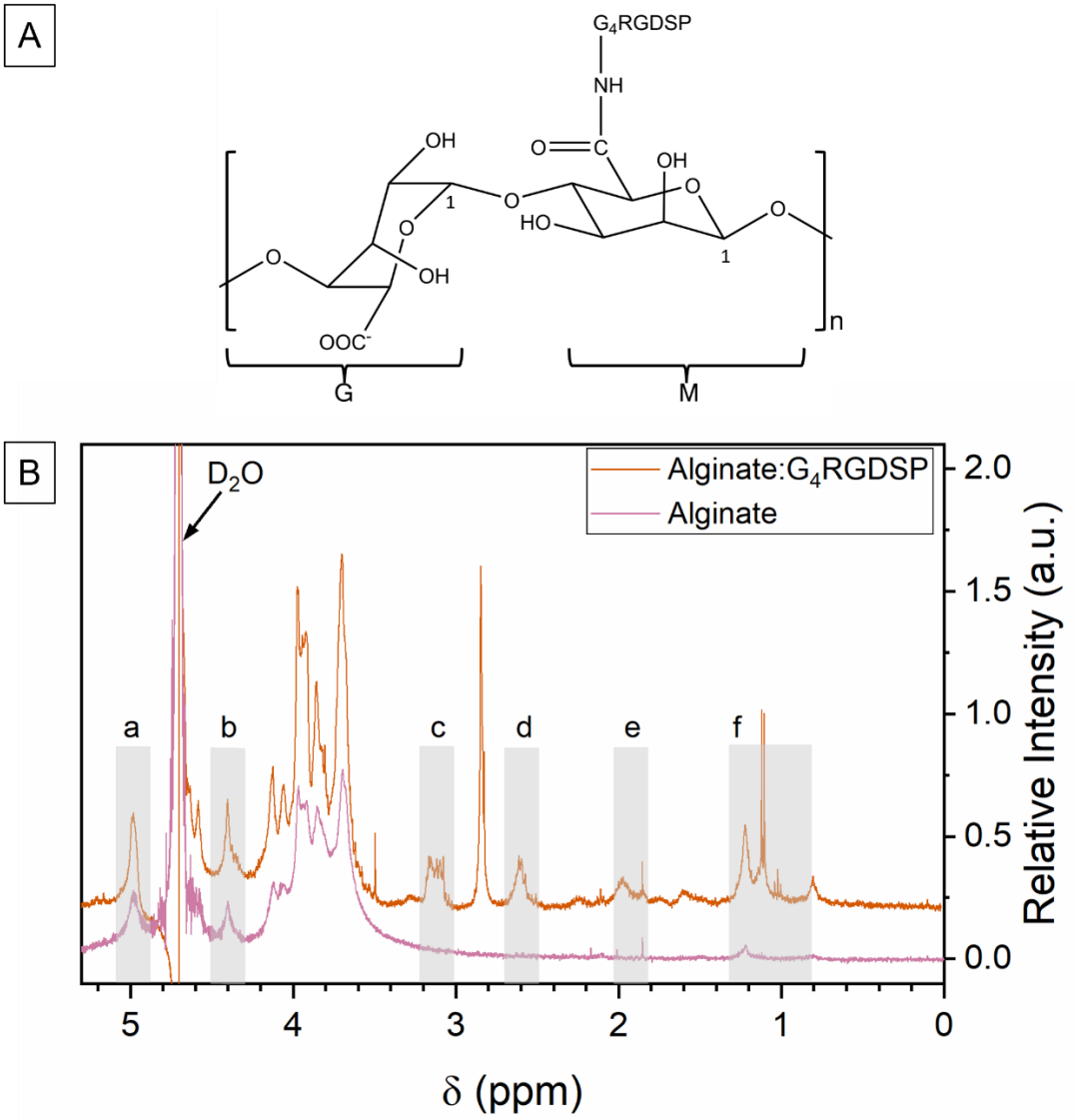


*Figure 8.16: (A) Chemical structure of RGD-coupled alginate showing the $G_4$RGDSP peptide conjugated to sodium alginate and the G and M block units of sodium alginate, and (B) Zoomed in $^1$HNMR spectra of RGD-modified alginate (orange line) and sodium alginate (purple line) in deuterium oxide ($D_2O$). The highlighted regions indicate the significant proton peaks including (a) H1 of G residue, (b) H1 of M residue, (c) arginine, (d) aspartic acid, (e) proline, and (f) possible by-products from coupling reaction.*

To calculate an estimate of the number of RGD peptide sidechains per disaccharide repeating unit of alginate, peaks corresponding to the RGD peptide such as the group of peaks ranging from 1.4 ppm to 2.0 ppm (possibly arising from the R and P amino acids in the peptide) were normalised against the single peak at 5 ppm corresponding to H1 of

the guluronic residue in each alginate repeating unit (peak (a) in Figure 8.16). The integrated area under the specified peaks correspond to 1 and 4.4696, respectively (refer to Appendix 2: NMR and MS spectra for full spectrum with integrated peaks). Considering a total of 4 protons within the 1.4 ppm and 2.0 ppm region, this would give 0.895 less RGD than a 1:1 alginate repeating unit to RGD. In other words, the actual measured ratio is 1.1162 alginate repeating units per RGD peptide available.

### 8.4.4. *In vitro* cell characterisation of hydrogels

To assess whether RGD-functionalisation of alginate, PEGDA, and alginate:PEGDA IPN hydrogels was successful in providing cell binding sites, and therefore attachment and proliferation, HUVECs were seeded onto the hydrogel's surface and cultured with endothelial cell media (supplemented with 2% (v/v) serum). Cells were assessed microscopically as shown in Figure 8.17 (day 2 of culture) and Figure 8.18 (day 6 of culture). The lack of transparency of the alginate:PEGDA IPN hydrogel limited the use of brightfield imaging to assess cell attachment and viability and therefore this formulation was not included in Figure 8.17 and Figure 8.18. Cells seeded on single-networked alginate (Figure 8.17(B) and Figure 8.18(B)) and PEGDA (Figure 8.17(D) and Figure 8.18(D)), exhibited very poor attachment, and a rounded morphology with no evidence of spreading at both time points.

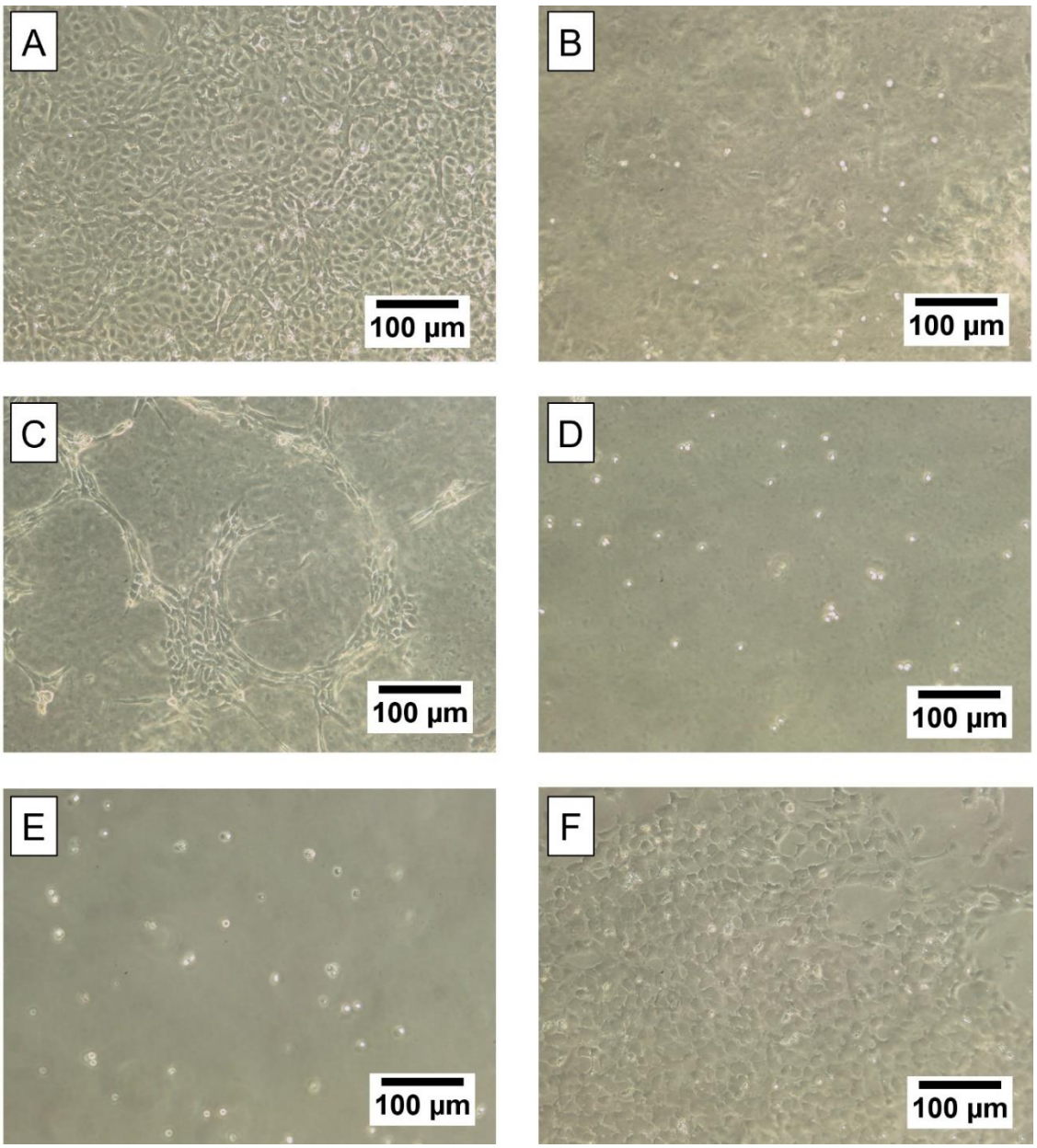


*Figure 8.17: Attachment and viability of HUVECs on (A) Tissue Culture Plastic (TCP; positive control), (B) alginate, (C) alginate:RGD, (D) PEGDA, (E) PEGDA:RGD, and (F) TCP (negative control), after day 2 of culture, evaluated through brightfield imaging. Images captured at 100x magnification.*

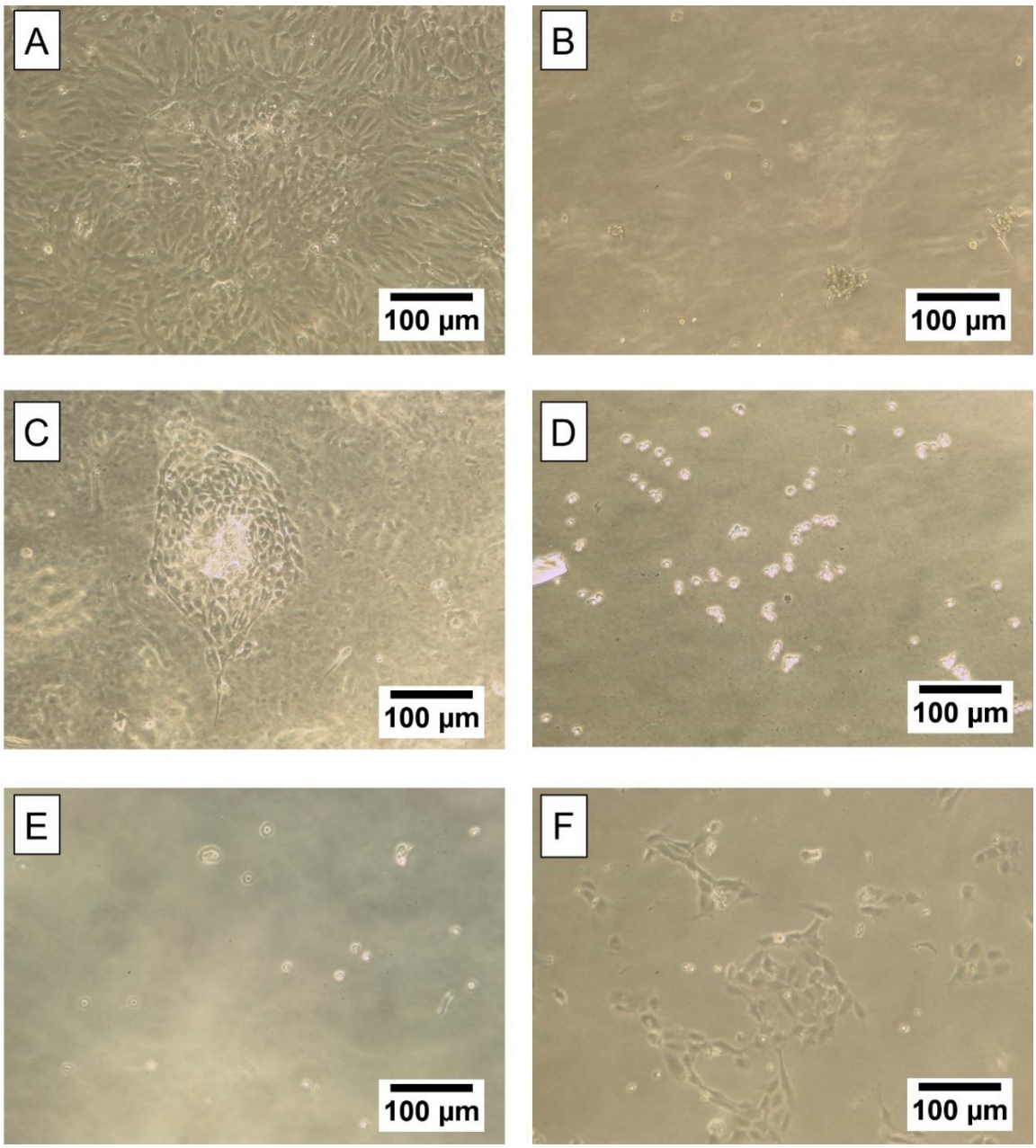


*Figure 8.18: Attachment and viability of HUVECs on (A) Tissue Culture Plastic (TCP; positive control), (B) alginate, (C) alginate:RGD, (D) PEGDA, (E) PEGDA:RGD, and (F) TCP (negative control), after day 6 of culture, evaluated through brightfield imaging.*

Cell attachment improved with the introduction of the RGD peptide to alginate as shown in Figure 8.17(C) and Figure 8.18(C), and Figure 8.19, with cells spreading creating areas of relatively high cell coverage. However, this was not the case when RGD was introduced to the PEGDA, where similar cell behaviour to the unmodified PEGDA could be observed as shown in Figure 8.17(E) and Figure 8.18(E)). Positive (with serum in

culture media; Figure 8.17 (A) and Figure 8.18(A)) and negative (without serum in culture media; Figure 8.17(F) and Figure 8.18(F)) controls showed good cell adhesion and coverage on tissue culture plastic with less cell growth for the negative control especially at day 6 (Figure 8.18(F)).

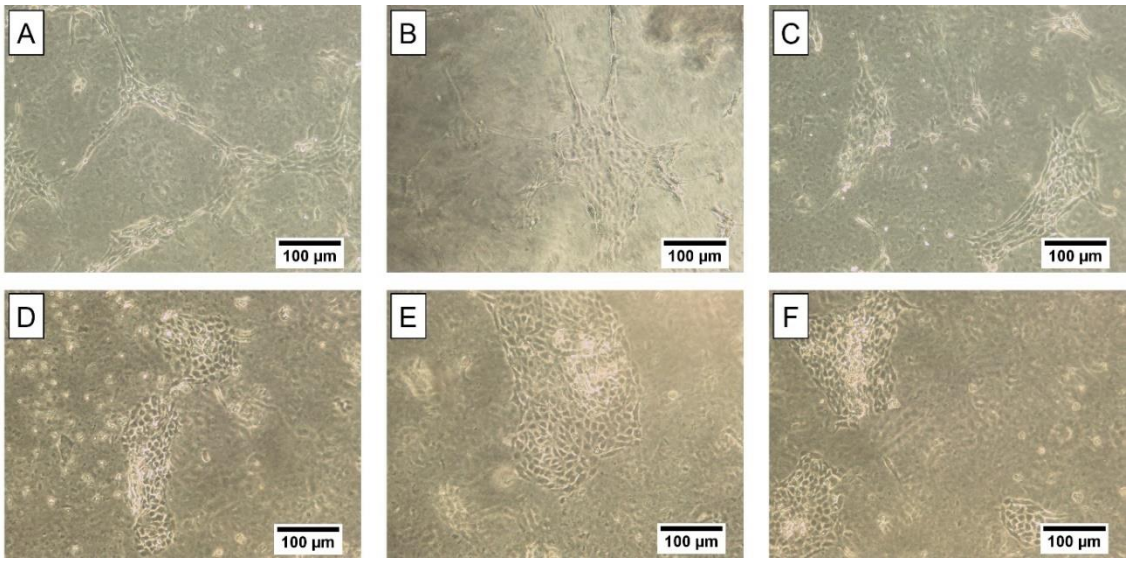


*Figure 8.19: Additional images showing the attachment and viability of HUVECs on alginate:RGD, after (A, B, C) day 2 and (D, E, F) day 6 of culture, evaluated through brightfield imaging.*

In addition, a Live/Dead assay, staining viable cells in green (Calcein-AM) and dead cells in red (Propidium Iodide), was implemented to investigate cell viability after 1 week of culture. Fluorescence images for alginate and alginate:RGD hydrogels are presented in Figure 8.20. The positive and negative controls shown in Figure 8.20(A) and Figure 8.20(B) both show live cells, with the number of cells on the negative control being substantially less. Viable cells were detected on both the alginate:RGD (Figure 8.20(C) and (D)) and alginate (Figure 8.20(E) and (F)) hydrogels. Clusters of live cells could be observed on the surface of the alginate:RGD hydrogels whereas alginate hydrogels revealed single, rounded live cells.

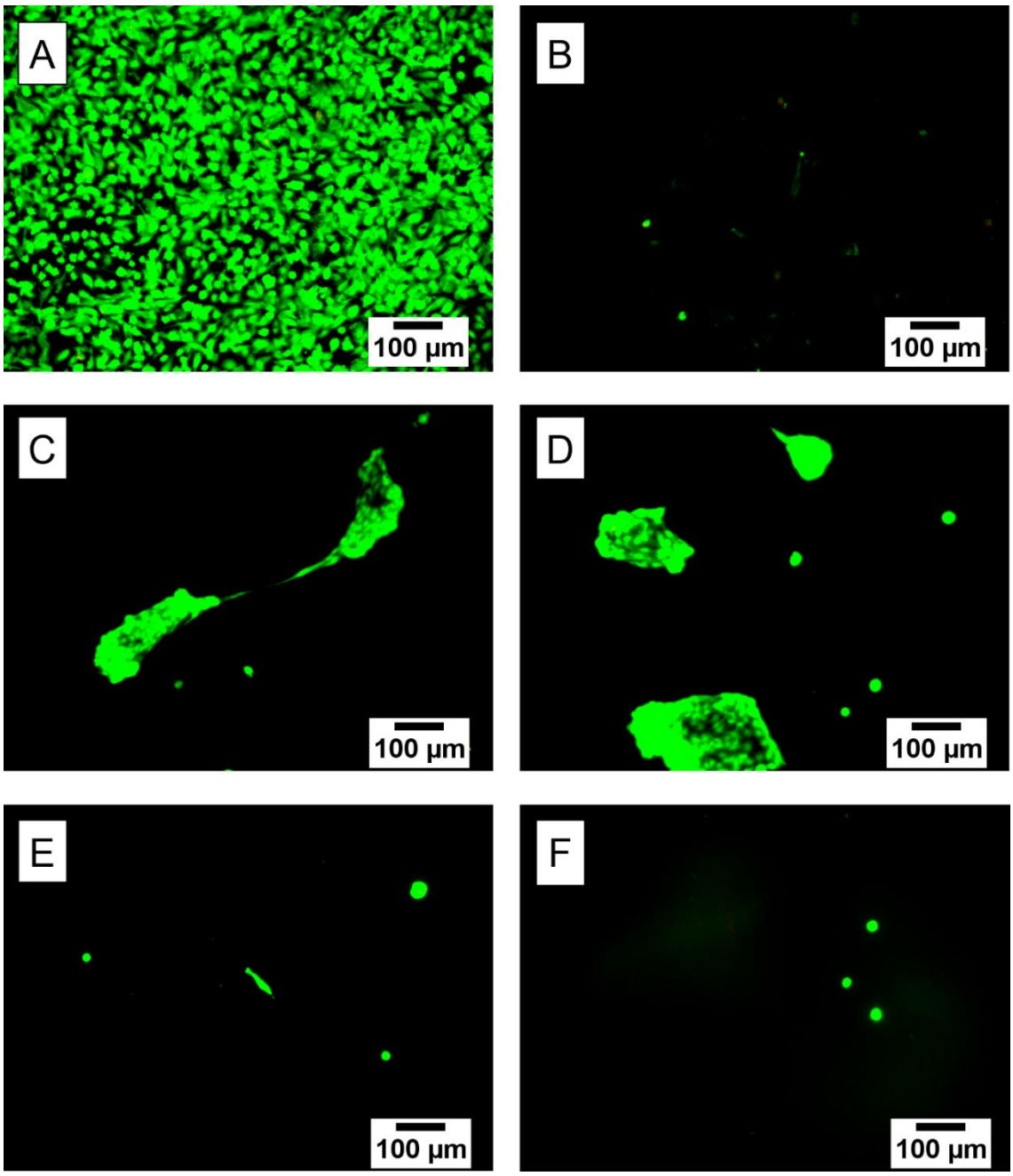


*Figure 8.20: Cell viability of HUVECs on (A) Tissue Culture Plastic (TCP, positive control), (B) TCP (negative control), (C) alginate:RGD sample 1, (D) alginate:RGD (sample 2), (E) alginate (sample 1), (F) alginate (sample 2), after day 7 of culture, evaluated through Live/Dead imaging.*

Live/Dead staining was also performed on alginate:RGD:PEGDA IPN hydrogel, however with a lower concentration of PEGDA (13.3 %(w/v)) than that used in previous chapters. Fluorescence images are presented in Figure 8.21. Clear images were difficult to obtain.

However, cell-like structures with a rounded morphology could be observed (Figure 8.21(C) and Figure 8.21(D)).

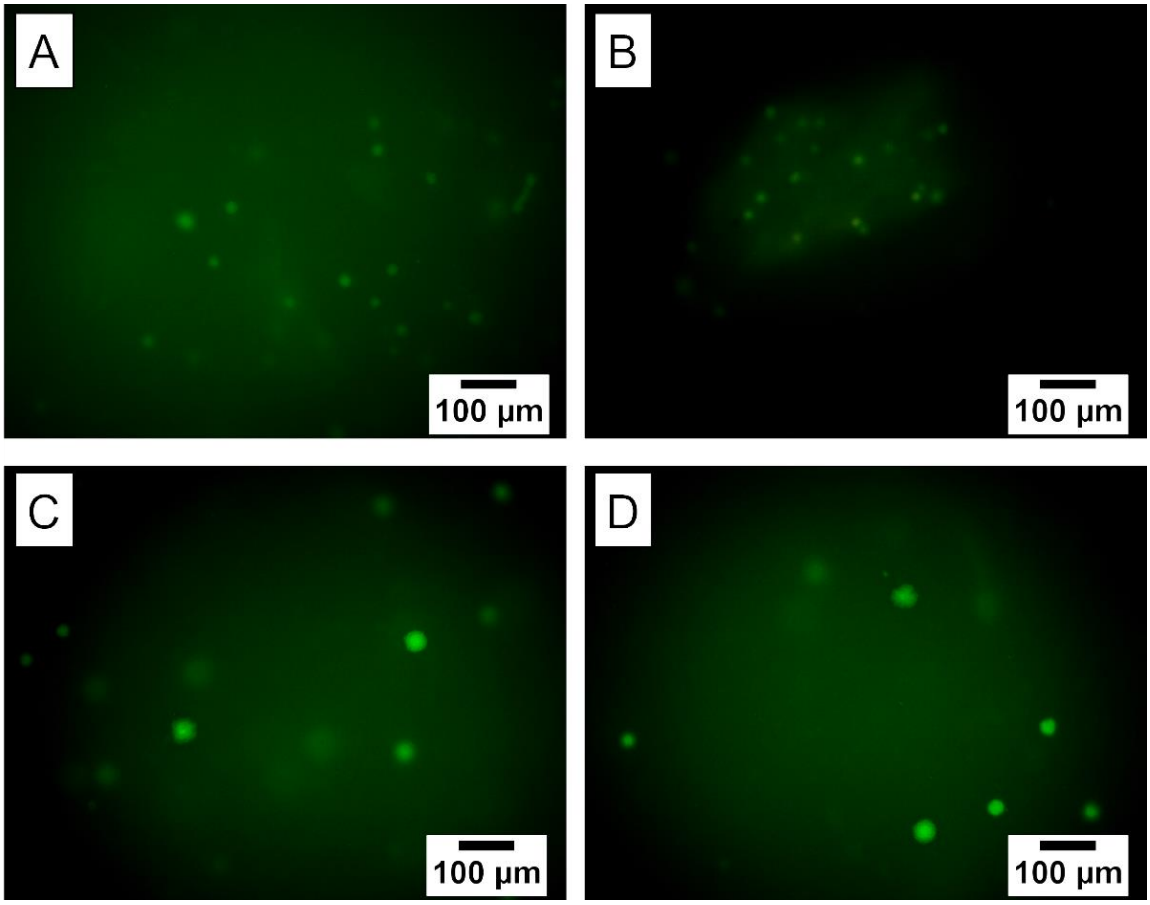


*Figure 8.21: Cell viability of HUVECs on alginate:PEGDA (3.3% (w/v):0.25 mM alginate:RGD, 13.3% (w/v) PEGDA) after day 7 of culture ((A-D) show different areas within the same sample in a petri dish), evaluated through Live/Dead imaging.*

## 8.5. Discussion

The incorporation of an RGD peptide as a way of introducing cell binding sites within materials that generally show poor cell adhesion has been demonstrated to be an effective strategy in enhancing biointegration (Hersel, Dahmen and Kessler, 2003; Perlin, MacNeil and Rimmer, 2008; Bellis, 2011). Moreover, the ability to synthetically synthesise such peptides presents a degree of controllability that is lacking in other cell compatibility promoting methods, such as the addition of proteins within a hydrogel matrix (Bellis, 2011). Therefore, in this work an RGD-based peptide ($G_4$RGDSP) was

synthetically synthesised via SPPS and coupled with both sodium alginate and PEGDA, separately. The alginate and PEGDA hydrogels together with the alginate:PEGDA IPN hydrogel containing a certain amount of the synthesised $G_4$RGDSP peptide were produced, and their cell compatibility behaviour investigated by seeding endothelial cells on the hydrogel's surface.

Herein, three versions of the $G_4$RGDSP peptide were synthesised via conventional Fmoc SPPS; (1) using different resins, H-Pro-2-ClTrt and Rink amide to produce peptide 1 and peptide 2, respectively, and (2) by modifying the N-terminus with an acrylate group to produce peptide 3. In SPPS, overall success of the synthesis process highly depends on each individual step, and therefore colorimetric tests (Kaiser and Chloranil) and test cleaves were performed at different stages to confirm coupling of amino acids and removal of protecting groups (Fmoc and side groups). Similar HPLC spectra were observed for the two peptides prepared using the two different resins (Figure 8.6) and the masses obtained matched the theoretical exact mass of the peptide (Figure 8.7). One of the main differences between the two peptides is the degree of purification, with peptide 2 exhibiting a higher purity percentage than peptide 1 (98.33% and 86.66%, respectively). This can be observed in the analytical HPLC spectra in Figure 8.10, where peptide 1 (Figure 8.10(A)) revealed several peaks on either side of the major peak confirming the presence of impurities. Consequently, peptide 2 was taken forward for the functionalisation of alginate via carbodiimide chemistry.

### 8.5.1. RGD-modified alginate hydrogel formation and its effect on HUVEC attachment and viability

Peptide 2 was conjugated to sodium alginate by following the step-by-step protocol outlined in Charbonier *et al*., (2021), based on the original protocol by Rowley *et al*., (1999). When using carbodiimide chemistry, EDC concentration is crucial since large amounts contribute to a side reaction involving the internal rearrangement of the O-

acylurea activated ester to a *N*-acylurea which covalently bonds to the alginate backbone, and therefore may hinder its ionic crosslinking ability (Rowley, Madlambayan and Mooney, 1999). Consequently, once the alginate:$G_4$RGDSP conjugation was performed and the solution was freeze-dried to obtain the powdered product, the first test performed was to assess whether the alginate:$G_4$RGDSP solution made with a 1:2 ratio of NHS:EDC, can be gelled, and Figure 8.22 shows the successful production of an alginate hydrogel crosslinked with $BaCl_2$.

*Figure 8.22: Alginate:$G_4$RGDSP hydrogel (3.3% (w/v):0.25 mM) crosslinked via $BaCl_2$ (66 mM).*

Once gelling capability was confirmed, RGD-conjugation success was evaluated by NMR spectroscopy (Figure 8.16). Comparing NMR spectra with the literature is complex because different investigations use different alginate types (high M or high G content), varying peptide sequences (length and flanking amino acids), different NMR solvents ($D_2O$ versus DMSO), different measurement temperatures, and varying sample dilutions, amongst other factors. Despite this, some similarities to other RGD-modified alginate NMR spectra could be made (Jeon *et al.*, 2010; Sandvig *et al.*, 2015; Yan, Chen and Amsden, 2016). Similar peaks to that reported by Sandvig *et al*., (2015) could be noted between δ of 1.0 ppm and 1.2 ppm, and at 2.9 ppm, which may be attributed to carbodiimide reaction by-products, such as the *N*-acylurea covalently bound to the alginate backbone. Additionally, the peaks corresponding to the $G_4$RGDSP peptide

residues including proline (P), aspartic acid (D), and arginine (R) could be observed at δ of 1.9 ppm, 2.6 ppm, and 3.1 ppm, respectively. It is also noteworthy, that additional peptide peaks potentially overlapped with alginate peaks, as could be observed by the differences in the δ region ranging from 3.6 ppm to 5 ppm.

Apart from conjugation confirmation, and key structural information, NMR spectroscopy allows for quantitative analysis of the degree of substitution, i.e., the amount of RGD peptide available for alginate repeating units. In this work, this was estimated by considering the arginine and proline peaks between 1.4 ppm and 2.0 ppm (Appendix 2: NMR and MS spectra: $^{1H}$ NMR spectra relevant to Chapter 8), amounting to approximately a 1:1 alginate repeating units to RGD. Despite following similar protocols, RGD-modified alginate investigations via carbodiimide chemistry have reported a wide range of coupling efficiencies, with Rowley *et al*., 1999 reporting a reaction yield greater than 80%, and Sandvig *et al*., (2015) a 2% – 4%. This demonstrates the sensitivity of the overall process, with multiple factors affecting reaction efficacy, including pH of MES buffer, EDC concentration, and the type and length of the RGD sequence used (Rowley, Madlambayan and Mooney, 1999).

Ultimately, the conjugation efficiency in RGD-modified alginate should be enough to enable ionic crosslinking for hydrogel formation whilst providing sufficient cell binding sites for appropriate cell adhesion. The latter was investigated here via *in vitro* cell experiments involving the seeding of HUVECs on the surface of the hydrogel. The alginate:$G_4$RGDSP hydrogel was successful in promoting endothelial cell adhesion as shown by the brightfield light microscopy images in Figure 8.17 and Figure 8.18. A contrasting difference between the behaviour of endothelial cells on alginate:$G_4$RGDSP and alginate without the RGD peptide could be observed, with the former showing cell spreading and growth, while the latter revealing rounded up cells. Similar behaviour was observed in a study by Bidarra *et al*., (2011) where HUVECs on RGD-modified alginate

hydrogels showed adherence and good coverage just after 24 hours of culture while HUVECs on unmodified alginate showed poor adherence and formed rounded cell clusters.

However, despite showing cell adhesion and growth, HUVEC coverage on alginate:$G_4$RGDSP did not exhibit the same behaviour as that observed on the positive control (tissue culture plastic), with many large empty spaces evident on the alginate:$G_4$RGDSP hydrogel surface at both day 2 and day 6 (Figure 8.17 and Figure 8.18). Figure 8.19 shows more images of an additional alginate:$G_4$RGDSP sample imaged at different areas to further illustrate the way HUVECs attached on to the hydrogel surface. Given that cell adhesion on the surface of RGD-modified alginate hydrogels highly depends on peptide availability and distribution (Sandvig *et al.*, 2015), it is hypothesised that in this work, the way the HUVECs grow on the alginate:$G_4$RGDSP hydrogel surface is potentially due to areas being rich in RGD and other areas that are not. Live/Dead viability staining after 1 week of culture also showed clusters of cell growth on the alginate:$G_4$RGDSP hydrogel surface as shown in Figure 8.20(C) and Figure 8.20(D).

### 8.5.2. RGD-modified PEGDA hydrogel formation and its effect on HUVEC attachment and viability

Peptide 3 was prepared in the same way as peptide 2 using the rink amide resin with an additional step after coupling all 8 residues of the sequence, involving a reaction with acrylic acid to introduce an acrylate group at the N-terminus (Figure 8.11). Through this, it is hypothesised that the acrylate end of the peptide would tether to one of the acrylate end groups of the PEG, whilst the other PEG acrylate end group would still be available for photocrosslinking to form the PEGDA:RGD hydrogel (Chen *et al.*, 2018). LCMS analysis confirmed peptide functionalisation with the mass obtained as detailed in Section 8.4.2. However, several impurities were detected via HPLC analysis of the

peptide post-purification (i.e., fraction 6), with the purity percentage measured at 58%. This is evident in the HPLC spectrum in Figure 8.15 which shows a large peak next to the peak of interest (indicated by orange arrow in Figure 8.15) and additional tiny peaks on either side of this. These impurities may have originated during the SPPS process from incomplete Fmoc and side group deprotection steps, or inefficient activation during the amino acid coupling steps, although test cleaves in Figure 8.12 do not suggest this. Newly formed HPLC peaks could be observed following full cleave of the peptide coupled with the acrylate group at the N-terminus (green trace in Figure 8.12) suggesting potential reactions occurring during the full cleave process.

Despite the presence of impurities, this peptide was mixed with the PEGDA (Mn 700) and photoinitiator (LAP) to produce hydrogels for cell attachment analysis. These hydrogels were photocured successfully suggesting that the PEG acrylate end groups were available for polymerisation. HUVEC seeding on the hydrogel surface of both RGD-modified PEGDA and unmodified PEGDA resulted in poor cell attachment as shown in Figure 8.17 and Figure 8.18, where cells rounded-up and showed no signs of spreading. This suggests that the RGD presence in the PEGDA hydrogel was not successful in providing sufficient binding sites for HUVECs to grow. Moreover, despite brightfield imaging showing rounded cells on both unmodified PEGDA and PEGDA:RGD as shown in Figure 8.17 and Figure 8.18, attachment of these cells to the hydrogel surface was poor, with Live/Dead imaging (images not presented here) showing no signs of cells on the hydrogel surface. It is hypothesised that any viable cells were washed away during the staining process which involves several DPBS washes.

Several factors might have contributed to this lack of cell adhesion. Assuming that the RGD functionalisation was successful, the ratio of peptide to PEGDA might not have been sufficient for cells to attach and proliferate. In a study by Zhu *et al*., (2012), 1 %(w/v) RGD-modified PEG methacrylate (PEGMA) (prepared by conjugating, at an equal molar

ratio, GRGDSP with acryloyl-PEG-NHS) copolymerised with 9 %(w/v) PEGDA, was found to initiate endothelial cell attachment just after 4 hours of culture with cell spreading observed after 24 hours. However, in the work presented here, as described in the Section 8.3.4.4, a considerably higher PEGDA concentration was used (26.6 %(w/v)) while a similar amount of functionalised peptide was incorporated within the PEGDA solution (13.3 mM, equivalent to approximately 1 %(w/v) of the total solution). Therefore, the poor cell behaviour observed in Figure 8.17(E) and Figure 8.18(E) may be associated with high PEGDA concentration, however given the limited amount of peptide material obtained from the synthesis process (a total of 86.6 mg), the effect of a higher concentration of RGD in the PEGDA hydrogels could not be investigated further.

When comparing cell behaviour on PEGDA hydrogels with other studies in the literature, several other parameters come into consideration, making direct comparisons challenging. Given that the molecular weight of PEGDA has been associated with changes in the mechanical behaviour of hydrogels (Mazzoccoli *et al.*, 2010; Nguyen *et al.*, 2012), consequently this has been found to impact cell adhesion and growth. Della Sala *et al*., (2020) investigated two types of PEGDA molecular weights (700 Da and 3400 Da) both conjugated with an RGD peptide (again using acryloyl-PEG-NHS), and cells were observed to prefer the higher molecular weight PEGDA after 24 hours of culture. This behaviour is possibly due to the lower stiffness values of high MW PEGDA which was observed in this work too, as discussed in Chapter 6 and as shown in Figure 6.8, the introduction of PEGDA Mn10000 in an 80:20 volume ratio with PEGDA 700 resulted in an elastic modulus of 0.99 ± 0.10 MPa compared with the 1.6 ± 0.19 MPa of the Alginate:PEGDA IPN containing just PEGDA 700. However, Della Sala *et al*., (2020) still reported cell adhesion on PEGDA 700 which is the same molecular weight used in this work. Concentrations of PEGDA (10%, 20%, and 40 %(w/v)) in Della Sala *et al*., (2020) were also similar to that investigated here, yet RGD concentrations were

considerably lower (0.5, 1.0, and 5.0 mM) and still cell adhesion was reported. An important difference lies with the type of cell line investigated, where Della Sala *et al*., (2020) used NIH 3T3 cells as opposed to the HUVECs used in this work. It has been reported that certain cell lines respond better to specific peptides, with endothelial cells showing preference to the REDV (arginine-glutamine-aspartic acid-valine) peptide (Wang *et al.*, 2015). Here, RGD was selected because it is considered to promote adhesion and migration for all types of cells, however a more specific peptide, such as REDV, might have promoted better behaviour in the case of PEGDA hydrogels.

It may also be possible that the peptide was not functionalised adequately using acrylic acid prior to cleavage. Several studies have reported the use of acryloyl-PEG-NHS as a way of functionalising peptides for incorporation with PEGDA monomers (Yang *et al.*, 2005; Guarnieri *et al.*, 2010; Zhu *et al.*, 2012; Della Sala *et al.*, 2020). This is simply a linear PEG chain with an acrylate group on one end and an NHS (succinimidyl ester) group on the other, which is used as a linker to covalently bind the peptide with PEGDA. Another way of functionalising RGD peptides, with similarities to the process implemented here, was reported by Jia *et al*., (2016a), where 2-isocyanatoethyl methacrylate was used to functionalise the amine group of the peptide chain prior to cleavage. This shows potential optimisation routes that may be explored in future work.

### 8.5.3. The effect of RGD peptide incorporation on the alginate:PEGDA IPN hydrogel formation and HUVEC attachment and viability

The ultimate goal of this work was to be able to incorporate cell binding sites within the alginate:PEGDA IPN hydrogel. Therefore, following the attempts at functionalising both alginate and PEGDA separately with the $G_4$RGDSP peptide, the next step involved combining either alginate:RGD to PEGDA or PEGDA:RGD to alginate. However, this proved to be challenging. When mixing alginate:RGD to PEGDA or PEGDA:RGD to alginate while maintaining the same concentrations of alginate and PEGDA used in

Chapter 5 and Chapter 6, i.e., 3.3 %(w/v) alginate and 26.6 %(w/v) PEGDA, macro-phase separation between the two monomers in solution could be observed (Figure 8.23).

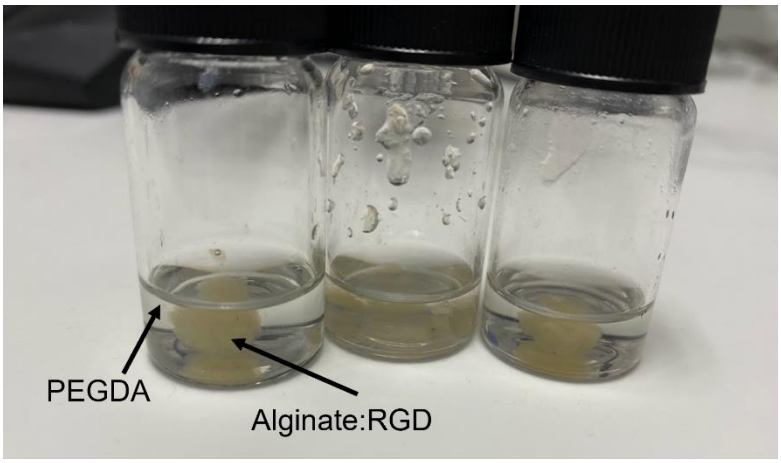


*Figure 8.23: Solution of alginate:RGD:PEGDA after mixing showing phase-separation of the two monomers.*

Initially, this behaviour was thought to be a result of buffer pH given that the monomers were being dissolved in DI water. Therefore, attempts at using more basic buffers including endothelial cell growth medium (pH 7.4) and HEPES buffer (pH 8) to ensure protonation of the aspartic acid and the alginic acid for higher water solubility were made, and yet this resulted in the same outcome, possibly due to the resulting immiscibility with PEGDA. Due to limited RGD material, this was not investigated further, and instead changes in monomer concentration were made.

Interestingly, decreasing the PEGDA concentration to 13.3 %(w/v) minimised the separation issue and allowed the formation of alginate:RGD:PEGDA IPN hydrogels. However, this was at the expense of mechanical properties. As discussed in Chapter 6, at 13.3 %(w/v) PEGDA the strength and stiffness of the IPN hydrogel (Figure 6.6) exhibits a significant decrease in comparison with the 26.6% PEGDA (UTS: 0.05 ±0.01 MPa and E: 0.14 ±0.01 MPa for 3.3 %(w/v) alginate: 13.3 %(w/v) PEGDA, and UTS: 0.15 ±0.01 MPa and E: 1.16 ±0.13 MPa for 3.3 %(w/v) alginate: 26.6 %(w/v) PEGDA). The IPN

hydrogel comprising 13.3 %(w/v) PEGDA and alginate:RGD was fabricated for cell adhesion evaluation, but its lack of transparency rendered it difficult to image via brightfield microscopy. Media was changed every other day, and a Live/Dead stain was attempted after 1 week of culture expecting that fluorescence imaging of viable cells would be a better imaging technique of opaque hydrogels. This proved to be challenging as well, as can be observed in Figure 8.21 poor images were obtained. Despite this, possible viable cells were noticeable as shown in Figure 8.21(C) and Figure 8.21(D). However, these images are inconclusive and further investigations of cell attachment and growth on RGD-modified alginate:PEGDA IPN hydrogels is required.

## 8.6. Conclusions

In order to ensure optimal physiological behaviour, aortic substitute materials must also promote endothelialisation. In this chapter, an attempt to enhance cell adhesion of the alginate:PEGDA IPN hydrogel was made to ultimately develop a bioactive, mechanically-matched, patient-specific aortic graft by synthesising and incorporating an RGD-based peptide ($G_4$RGDSP).

The peptide was produced via Fmoc solid phase peptide synthesis, and following purification this was conjugated with single-network alginate via aqueous carbodiimide chemistry. An additional peptide was produced with a modified N-terminus to incorporate an acrylate group and facilitate crosslinking with the PEGDA. Successful synthesis of peptides was confirmed by HPLC and LCMS, while peptide to alginate conjugation was confirmed via NMR spectroscopy.

Hydrogel-endothelial cell interaction was analysed by seeding HUVECs onto the hydrogel surface, and cell attachment and viability were evaluated via brightfield imaging and Live/Dead staining. Cells attached and showed favourable growth on alginate:RGD hydrogels with good cell coverage observed after day 2 and day 6 of culture, while live/dead imaging showed viable cells after 1 week. The incorporation of RGD with

PEGDA was not as successful, with cells exhibiting a rounded morphology at both day 2 and day 6 of culture, similar to the unmodified PEGDA hydrogel. Mixing of the alginate:RGD or PEGDA:RGD with alginate or PEGDA to produce an RGD-modified alginate:PEGDA IPN hydrogel proved to be challenging when maintaining the PEGDA concentration at 26.6 %(w/v) due to macro-phase separation of the alginate and RGD from the PEGDA. Reducing the PEGDA concentration by half solved the issue of solution separation, however at the expense of the elastic properties, primarily strength and stiffness. A robust analysis of cell growth on the RGD-modified alginate:PEGDA IPN hydrogel could not be made visually via brightfield imaging due to the hydrogel's lack of transparency. Live/Dead imaging showed hints of viable cells but further investigations on this are required.

Nonetheless, these results provide important insights to inform future work to optimise the alginate:PEGDA RGD functionalisation methods that would prevent phase separation whilst maintaining similar mechanical properties to the unmodified alginate:PEGDA IPN hydrogel.

# Chapter 9 General Discussion

## 9.1. Summary

At present, state-of-the-art synthetic vascular grafts used in the surgical repair of the aorta fail to mimic the biomechanical behaviour and intricate morphology of the host vessel. Despite this, the post-operative outcomes of such grafts are deemed acceptable, and consequently, research on improving their mechanical performance has been limited (Spadaccio *et al.*, 2016; Pennel and Zilla, 2019).

In the work presented here, the discrepancies in mechanical properties between existing aortic graft materials (in this case, Dacron®) compared with abdominal aortic tissue data reported in the literature were confirmed via tensile tests in Chapter 4. Ultimate tensile strength (UTS) and physiological modulus (PM) of gelatine-coated Dacron® graft material in the circumferential orientation (the direction that the aorta expands to accommodate pulsatile flow) were measured to be 31.23 ±3.57 MPa and 9.64 ±1.24 MPa, respectively (Figure 4.2 and Figure 4.3). Both values are significantly higher than those observed in human aortic tissue (UTS: 0.61 ±0.07 MPa, and PM: 1.82 ±0.10 MPa, (Vallabhaneni *et al.*, 2004)). Even under dynamic conditions, the storage modulus (E') of the Dacron® material investigated here (Figure 4.5) is 100 times greater than that reported for the descending thoracic aorta (1.5 MPa – 3.0 MPa (Amabili, Balasubramanian and Breslavsky, 2019)). Such discrepancies in mechanical behaviour have been associated with the disruption of cardiovascular homeostasis leading to long-term complications for the patient, often requiring several surgical reinterventions, and increased mortality (Spadaccio *et al.*, 2016; Pennel and Zilla, 2019; Lejay *et al.*, 2019). This has raised concerns over the suitability of such grafts in large vessel repair, emphasising the need for novel vascular graft technologies. This body of work has sought to address the limitations associated with existing vascular grafts by investigating alternative materials and fabrication methods that could potentially produce more compliant and anatomically-

relevant conduits. To achieve this, an analysis of research literature on small-diameter tissue engineered blood vessels (Pashneh-Tala, Macneil and Claeyssens, 2016; Wang *et al.*, 2020a) and artificial tissue-mimicking vasculature structures (Grigoryan *et al.*, 2019; Chen *et al.*, 2022; Domingo-Roca *et al.*, 2022b; Asciak *et al.*, 2023), has helped identify hydrogels to be used as the graft material in combination with 3D-printing as the fabrication method.

Several monomers have been investigated towards the development of blood vessel substitutes; alginate in particular has emerged as a promising material candidate due to its biocompatibility, and ease of hydrogel formation in the presence of inorganic salts, such as $CaCl_2$ (Ghanizadeh Tabriz *et al.*, 2015; Ghanizadeh Tabriz *et al.*, 2017; Antunes *et al.*, 2021; Xie *et al.*, 2021). One of the disadvantages of utilising single-networked, ionically crosslinked alginate hydrogels is their poor strength and stiffness in comparison to the human vasculature, a factor that is often overlooked in synthetic blood vessel development investigations involving this type of alginate hydrogel. Here, the discrepancy in mechanical properties of single-networked, ionically crosslinked alginate hydrogels to human aortic tissue is demonstrated in Chapter 5. Tensile tests were performed on alginate crosslinked with $CaCO_3$:GDL owing to its shape retention ability. This resulted in an ultimate tensile strength (UTS), elastic modulus (E), and elongation at break ($\varepsilon_B$) of 23.76 ±6.34 kPa, 43.37 ±1.33 kPa, and 52.53 ±14.35%, respectively (Figure 5.7), with both strength and stiffness being significantly less than that reported for aortic tissue (Vallabhaneni *et al.*, 2004). The incorporation of a secondary, non-crosslinked monomer within the alginate hydrogel (alginate:elastin) revealed a significant increase in elastic properties (UTS: 39.42 ±9.39 kPa, E: 54.10 ±5.18 kPa, $\varepsilon_B$: 73.94 ±5.88%) when compared to alginate on its own (Figure 5.8). This suggested that the incorporation of additional monomers to the alginate hydrogel matrix could potentially enhance its mechanical behaviour to the desired range. Hence, a

reinforcement strategy comprising an ionic-covalent entanglement interpenetrating polymer network (ICE IPN) was developed, where the alginate remained ionically crosslinked but the additional monomer, PEGDA, was covalently crosslinked via photopolymerisation. Following several optimisation steps, involving variations in PEGDA concentration (13.3 %(w/v) and 26.6 %(w/v)), molecular weight (Mn 575 and Mn 700), and alginate crosslinker type ($CaCO_3$:GDL and $BaCl_2$), a hydrogel formulation (3.3 %(w/v) alginate: 26.6 %(w/v) PEGDA (Mn 700) and 66 mM $BaCl_2$) with significantly higher strength and stiffness than single-network alginate, and elastic properties (UTS: 0.39 ±0.05 MPa, E: 1.61 ±0.19 MPa, and $\varepsilon_B$: 24.4 ±4.33%) within the range of aortic tissue was obtained (Figure 6.8).

Most studies investigating the combination of alginate and PEGDA towards IPN hydrogel formation utilise higher molecular weight PEGDA (greater than 1000 Da) (Hong *et al.*, 2015; Mistry *et al.*, 2017; Zhang *et al.*, 2021; Huang *et al.*, 2022) than the one presented here, and the alginate is typically crosslinked using either $CaCl_2$ (Zhang *et al.*, 2021) or $CaSO_4$ (Hong *et al.*, 2015). Higher molecular weight PEGDA monomers have been associated with greater extensibility, however such monomers are typically synthesised via a laborious in-house process or purchased at a costly price for just a few milligrams (Mazzoccoli *et al.*, 2010; Hong *et al.*, 2015; Della Sala *et al.*, 2020; Rekowska *et al.*, 2022). The work reported here addresses these limitations by using PEGDA with a molecular weight of 700 Da, which is commercially-available and inexpensive. When used in combination with barium-crosslinked alginate, it is demonstrated to be sufficient to provide similar elastic properties to the human aorta, the first time this has been achieved with this combination of materials. Moreover, the use of a barium-based crosslinker ($BaCl_2$) over a calcium-based one ($CaCO_3$:GDL), was found to significantly enhance the elastic properties of the alginate:PEGDA IPN hydrogel

(UTS: 0.39 ±0.05 MPa and E: 1.61 ±0.19 MPa for $BaCl_2$ versus UTS: 0.15 ±0.05 MPa and E: 1.16 ±0.13 MPa for $CaCO_3$:GDL) (Figure 6.7).

As outlined in the literature review Section 2.2.2, the aorta is also inherently viscoelastic, a characteristic that is especially important for optimal functionality of the Windkessel effect (i.e., the dampening of pulsatile pressure in the arterial system). Hence, the graft material should also exhibit a similar degree of viscoelasticity. All hydrogel formulations investigated in the present study, be it single-networked alginate or alginate:PEGDA IPN exhibited viscoelastic behaviour, as demonstrated by typical stress-relaxation curves (Figure 5.3 and Figure 6.9), and the characteristic storage and loss modulus behaviour obtained via rheological measurements (Figure 6.12). Rheological analysis also showed that these hydrogel formulations exhibit frequency-dependent mechanical behaviour, which is a common behaviour associated with vascular tissue (Zhijie, Mark and Naomi, 2016).

In the pursuit of developing aortic graft substitutes, the alginate:PEGDA IPN hydrogel formulation was used to produce tubular conduits with diameters and wall thicknesses based on segments of the human aorta. This was achieved using a combination of polypropylene syringes and an agarose sacrificial mould (as described in Chapter 6, Figure 6.2). Tubular vessels were successfully fabricated, however the range of dimensions that could be obtained with this method were limited to the dimensions of the moulds used. Therefore, a more customisable approach was required to be able to produce patient-specific vascular grafts. Consequently, the hydrogel fabrication process was shifted towards the direction of 3D-printing, since this manufacturing technique allows for the rapid production of components according to a CAD model that could also be based on patient CT/MRI imaging.

One major advantage of incorporating a functionalised monomer such as PEGDA within the hydrogel matrix is its compatibility with light-based 3D-printing such as

stereolithography (SLA) 3D-printing, in the presence of a photoinitiator. Investigations involving alginate:PEGDA IPN hydrogels have mostly involved either moulding (Asohan *et al.*, 2022; Huang *et al.*, 2022) or extrusion-based 3D-printing (Hong *et al.*, 2015; Mistry *et al.*, 2017; de Melo *et al.*, 2019; Zhang *et al.*, 2021) as the mode of hydrogel fabrication. The present work explores for the first time the fabrication of alginate:PEGDA IPN hydrogels via SLA 3D-printing (Chapter 7), given the several advantages of this technology over extrusion-based 3D-printing, including faster fabrication times and enhanced resolution (Levato *et al.*, 2023). Using the optimised alginate:PEGDA IPN hydrogel formulation that resulted in similar elastic properties to the human aorta (3.3 %(w/v) alginate: 26.6 %(w/v) PEGDA (Mn 700) and 66 mM $BaCl_2$), compatibility of this resin with SLA 3D-printing was evaluated by assessing the process parameters (photoblocker concentration, and printing exposure times) that would allow conduits to be printed at high resolutions. This was performed via cure depth measurements as a function of layer thickness which was then applied to the Beer-Lambert law (Figure 7.3) (Seo *et al.*, 2017; Benjamin *et al.*, 2019; Hisham, Saravana Kumar and Deshpande, 2022).

Moreover, the mechanical properties of the 3D-printed alginate:PEGDA IPN hydrogels were evaluated to assess whether the printing process alters the mechanical behaviour of the hydrogel formulation. Slight variations could be noted when comparing the elastic properties of the 3D-printed hydrogels versus the moulded ones, especially through the addition of the tartrazine photoblocker. A 0.03 %(w/v) photoblocker concentration resulted in an acceptable print resolution with the closest geometries to the CAD model, yet this contributed to a significant decrease in $\varepsilon_B$ (18.02 ±2.41%) when compared with the moulded samples (24.4 ±4.33%) (Figure 7.5). Despite this, no significant changes in strength and stiffness were observed, and thus, this hydrogel formulation comprising 0.03 %(w/v) tartrazine was used to 3D-print tubular conduits mimicking the human aorta.

SLA 3D-printing proved to be successful in producing aortic-like structures. The primary challenge encountered in this work, involved the production of conduits longer than 20 mm. This was mostly due to pulling and peeling forces exerted on the structure during printing leading to failures mid-print. Another key factor stems from the fact that longer structures required longer printing times, and the alginate:PEGDA resin was observed to potentially exhibit macro phase separation, where the alginate separated from the PEGDA at long periods in the printer tank contributing to inhomogeneous prints (as evident from the discolouration when printing the bifurcation aortic section in Figure 7.16(I)). To address these issues, attempts at printing at an angle with additional supports whilst adding fresh resin mid-print were made (Figure 7.13), however further optimisation of the printing parameters is required to achieve a high-resolution print in this manner.

Finally, having established a hydrogel formulation that could be 3D-printed to produce mechanically relevant structures to the human aorta, the cell-compatibility of the material was investigated under static culture conditions. When designing synthetic arterial substitutes, endothelialisation is key to prevent unwanted build-up of plasma proteins that could ultimately contribute to thrombus formation (Ren *et al.*, 2015). The use of PEGDA for such an application is highly desirable due to its bio-inertness that helps in repelling protein adhesion (Munoz-Pinto *et al.*, 2015). Since both alginate and PEGDA are widely known for their lack of biological cues required for endothelialisation, biofunctionalization of the material was required.

A considerable number of investigations have shown that the introduction of cell binding motifs, such as RGD-based peptides, to synthetic materials could enhance cell adhesion and proliferation (Hersel, Dahmen and Kessler, 2003; Bellis, 2011; Rowley, Madlambayan and Mooney, 1999; Bidarra *et al.*, 2011; Jia *et al.*, 2016a; Della Sala *et al.*, 2020). Therefore, in the present work, as detailed in Chapter 8, an RGD-based

peptide ($G_4$RGDSP) was produced via Fmoc solid phase peptide synthesis and conjugated with either alginate or PEGDA in an attempt to biofunctionalise the alginate:PEGDA IPN hydrogel. Initial cell assessment findings showed that the RGD-modified alginate was successful in promoting cell adhesion and proliferation over the course of a 1-week culture period (Figure 8.17(C), Figure 8.18(C) and Figure 8.19). Unfortunately, this was not the case for the RGD-modified PEGDA (Figure 8.17(D) and Figure 8.18(D)), which exhibited the same response as the unmodified PEGDA, where the cells assumed a rounded-up morphology and attachment was poor. Endothelial cell assessment on RGD-modified alginate:PEGDA IPN proved to be challenging as a result of phase separation when incorporating one of the RGD-modified monomers to the other (Figure 8.23). This phase separation phenomenon is hypothesised to have resulted from the high concentration of PEGDA whose inherent bioinert characteristics repelled the peptide causing the alginate:RGD to agglomerate. In fact, upon decreasing the PEGDA concentration to 13.3 %(w/v) instead of 26.6 %(w/v), the phase separation issue was minimised, however proper cell assessment was difficult to achieve due to the hydrogel's poor optical transparency which rendered it difficult to image (Figure 8.21).

Nevertheless, this study has successfully identified a hydrogel formulation that could be: (1) tailored to mimic the elastic properties of the human aorta whilst also showing viscoelastic behaviour, and (2) 3D-printed to produce personalised aortic-like structures. This combination of materials and advanced manufacturing technology represents a novel approach for large-diameter grafts, which has not been previously reported in the literature and has achieved key mechanical properties that closely match those of the native aorta.

## 9.2. Research limitations and recommendations for future work

Despite achieving most of the research aims and objectives outlined in Chapter 2 Section 2.8 and 2.9, this work still presents some limitations whilst also providing several opportunities for future work.

### 9.2.1. Hydrogel formulation development

For the development of the alginate:PEGDA IPN hydrogel formulation, this work focussed on just one form of acrylate-based PEG: PEGDA. One of the main reasons this was selected as the secondary monomer to alginate, is due to it being widely investigated in the 3D-printing of PEG-based hydrogels for biomedical applications, especially through the use of vat-based 3D printers (Benjamin *et al.*, 2019; Grigoryan *et al.*, 2019; Yang *et al.*, 2020; Hisham, Saravana Kumar and Deshpande, 2022; Asciak *et al.*, 2023). Moreover, for comparative purposes, the alginate:PEGDA hydrogel formulation investigated in this work was designed based on the previously published work by Hong *et al.,* 2015, where they also investigate PEGDA in combination with alginate, but at higher molecular weights than 700 Da, whilst using a calcium-based alginate crosslinker ($CaSO_4$ instead of $CaCO_3$:GDL and $BaCl_2$) and extrusion-based 3D-printing instead of light-based 3D-printing (SLA). Other linear variations of acrylate-based PEG exist, including PEGDMA, which is very closely related to PEGDA in chemical structure, with the only difference being the methyl groups near the carbon double bonds. Kalakkunnath *et al*., (2006) reported both monomers to exhibit similar mechanical behaviour following dynamic mechanical analysis. Hence, based on these observations, PEGDMA was not considered in this work. Indeed, for future work it would be interesting to investigate whether the use of PEGDMA over PEGDA as the secondary monomer for the alginate:PEG-based IPN hydrogel would yield an improved graft material, considering that PEGDMA has been reported to demonstrate better hydrogel transparency than PEGDA (Kadry *et al.,* 2019), which could potentially solve the issue of imaging during

cell adhesion investigations. Moreover, Asawa *et al.,* (2018) reported that PEGDMA exhibits a degree of stem cell adhesion without the need for chemical modification. In light of this, it would be useful to investigate whether a similar behaviour could be observed with endothelial cells, hence opening up the possibility of developing an alginate:PEGDMA hydrogel without the need for the addition of an RGD peptide.

One of the major advantages of using a hydrogel-based graft material is the potential of incorporating additional components to the hydrogel matrix. This was attempted in Chapter 8 via the synthesis and addition of an RGD peptide as a way to incorporate biological cues within the material. However, this was not entirely successful with challenges encountered when adding RGD to the IPN hydrogel as demonstrated and discussed in Chapter 8 Section 8.5.3, and thus the overall aim of this research i.e., to biologically functionalise the material for enhanced endothelial cell interactions was not fully achieved. Therefore, future work should aim to first address the issue of phase separation when using alginate:RGD for the preparation of an RGD-modified alginate:PEGDA IPN hydrogel. Moreover, as discussed in Chapter 8, the PEGDA:RGD method used in this work might not have been successful as evident from the rounded cell morphology and poor attachment. Therefore, alternative methods to conjugate the RGD-based peptide to the PEGDA monomer should be explored; including modifications to the functionalisation process of the RGD peptide, such as constraining the RGD within the crosslinking chain by adding polyglycines at both ends to potentially improve integrin binding, or by changing the conjugation method, for example by utilising carbodiimide chemistry to ensure covalent bonding between the peptide and the monomer (similar to the acryloyl-PEG-NHS described in Chapter 8 Section 8.5.2).

Moreover, due to time-restrictions, a limited amount of $G_4$RGDSP peptide was synthesised, and therefore the effect of RGD modification on the mechanical properties of alginate or PEGDA hydrogels was not evaluated here. Studies have reported that

through the incorporation of an RGD-based peptide the mechanical properties of the hydrogel can be significantly altered (Ochbaum, Davidovich-Pinhas and Bitton, 2018; Della Sala *et al.*, 2020). Therefore, another future work recommendation would involve the mechanical characterisation, preferably using the same testing methods utilised in this work, of RGD-modified alginate or PEGDA hydrogels.

The addition of bioactive peptides within the hydrogel matrix also opens up the possibility of incorporating other biological components, such as angiogenic molecules (vascular endothelial growth factors (VEGFs)) which also encourage endothelial cell adhesion (Yuan *et al.*, 2020). Moreover, this method is not solely restricted to biological components, but other chemical compounds may be introduced including antimicrobial drugs which could be useful in preventing the occurrence of graft infection, especially since aortic graft infection remains a significant challenge in the field of vascular surgery. It is associated with significant morbidity and mortality despite the low incidence rates (0.3% to 4.5% of aortic repairs depending on the type of surgery (endovascular versus open surgery)) (Shiraev *et al.*, 2019). Therefore, there is a need for graft infection prevention strategies, and the graft developed in this work might provide a suitable platform to address this challenge.

### 9.2.2. Hydrogel material mechanical characterisation

In this work, the target mechanical properties for this novel, hydrogel 3D-printed aortic graft were based on the elastic properties of non-aneurysmatic human abdominal aortic tissue as reported in the literature from *ex vivo* testing, i.e., a stiffness of around 1.8 MPa in the circumferential direction and ultimate tensile strength of approximately 0.6 MPa (Vallabhaneni *et al.*, 2004). However, as outlined in Chapter 2 Section 2.5.1 in Table 2.1, these properties change with aging and the on-set of disease. Therefore, by matching the mechanical properties of this novel graft material to healthy, non-aneurysmatic tissue it is assumed that this graft would be implemented in open surgery and anastomosed to

healthy tissue. Consequently, future work should also consider whether the target properties are to be altered according to the patient's age and surgical repair type, which would possibly require a range of hydrogel formulations with varying mechanical properties from which the surgeon can then decide which one would best match the patient's needs.

Another major limitation of the work presented here, includes the limited mechanical characterisation evaluation tests performed on the moulded (Chapter 6) and 3D-printed (Chapter 7) tubular structures. Here, the structures were radially compressed to a certain level of displacement with respect to their outer diameter, in order to evaluate their radial load capacity. This type of measurement is typically performed on stent-graft structures used in endovascular repair surgeries (de Oliveira, da Silva and de Oliveira, 2021). Hence, a more representative testing method of *in vivo* conditions, such as radial load evaluation under tensile conditions, is highly recommended for future work. Additional mechanical testing recommendations that emulate better the behaviour of aortic grafts *in vivo*, include burst pressure analysis, dynamic compliance testing, and suture retention strength evaluation. Ideally, these tests should be performed according to the ISO standard for tubular vascular grafts (ISO7198, 2016). In addition to this, some review papers in the literature, such as the one by Camasão and Mantovani (2021), provide strategic plans that can be implemented for a more profound analysis of the mechanical behaviour of the proposed vascular graft substitutes, which could also be implemented to the aortic region.

Other limitations encountered in this work are related to the mechanical testing equipment, specifically the Instron tensile tester which is equipped with a 1 kN load cell. This, in comparison with the loads exhibited by these hydrogels (approximately 0.8% of load cell capacity) is too high thereby contributing to noisy data that requires filtering or smoothing, potentially decreasing the accuracy of the results reported here. However,

due to unavailability of lower load cells or other types of mechanical characterisation equipment within the research group, the tensile tests were carried out on this machine, accepting that some inaccuracies might be present. Moreover, since this machine comprises two highly pressurised pneumatic grips, the sample geometry required for testing is quite large in comparison with the ones used for compression or rheological measurements. Therefore, a large amount of material was required, and sample size was limited to n = 3 for most experiments. Despite not needing large sample geometries for confined compression, a sample size of n = 3 was still employed, this time due to the long stabilisation period (approximately 2 hours) required prior to running the confined compression test. However, a large variation in sample measurements could be observed as indicated by the error bars in some hydrogel formulations e.g., the alginate:gelatine presented in Figure 5.6. This suggests that a larger sample number might have been required to provide a more accurate representation of the confined compression properties of the hydrogels, and it would be beneficial in future work to increase this at least to a sample number of 5. Furthermore, all of the mechanical characterisation tests were performed under ambient conditions, which differs from physiological environments. Therefore, for future research it is recommended that such tests be performed in physiologically mimicking solutions (such as PBS) at body temperature (37 °C).

### 9.2.3. *In vitro* cell characterisation of hydrogels

In terms of cell-hydrogel interaction experiments (Chapter 8 Section 8.4.4), the cell adhesion evaluation presented here is only preliminary. The cell-seeded hydrogels were imaged via brightfield microscopy after day 2 and day 6 of culture, and finally live/dead staining was conducted at day 7 to assess viability. A more in-depth evaluation including fluorescence staining for the visualisation of the cytoskeleton and nucleus, and quantification of cell adhesion (i.e., number of cells per $mm^2$) through microscopy might

provide a better insight into cell behaviour and morphology on the RGD-modified hydrogels, especially on the PEGDA hydrogels where imaging seemed to show poor cell adhesion and growth. Given the lack of cells at day 7 for the live/dead staining and imaging of PEGDA and PEGDA:RGD hydrogels due to the possibility of cells not adhering well and being washed away during the staining process, an alternative characterisation method might be more useful. For example, in this case, even the use of a live/dead kit which does not require several PBS washes might have been more beneficial in not disturbing any live cells that were poorly attached. Additionally, for future work, the use of assays, such as the MTT or cell counting kits (CCK8) to assess cell proliferation, viability, and cytotoxicity is recommended. Moreover, given that this hydrogel material is intended for the fabrication of vascular grafts where the *in vivo* environment involves contact with blood, a natural progression of this work would be to investigate how this hydrogel formulation, with and without the incorporation of an RGD peptide, interacts with such an environment through hemocompatibility tests. Further research might also explore the development of an *in vitro* platform that involves dynamic blood circulation in order to be able to assess haemodynamic effects, such as shear stress on the lumen. This work is especially important if endothelialisation is successful to investigate the robustness of this inner layer and whether it would delaminate over time.

### 9.2.4. Hydrogel physical characterisation

In an attempt to assess the long-term stability of the alginate:PEGDA IPN hydrogel, water uptake and degradation analysis were also conducted (detailed in Chapter 6). These experiments were performed according to protocols reported by several hydrogel development investigations (Krishnamoorthy, Zhang and Xu, 2019) which suggest freeze-drying of the samples prior to incubation (for water uptake studies) and at different time points throughout the incubation period (for degradation analysis). However, this is

not representative of physiological conditions since at no point will the graft material be lyophilised prior to implantation. Therefore, a more representative swelling and degradation measurements should be considered in the future, potentially without the lyophilisation steps. Additionally, the degradation study presented here only evaluates weight changes over a 1-week period of moulded samples. If this graft were to be clinically translated, an additional incubation investigation on 3D-printed constructs at a longer period would be required to assess *in vitro* degradation behaviour and how this would impact the mechanical performance of the hydrogel in the long-term. If such a technology were to be investigated further for clinical use, a crucial assessment would be to perform *in vivo* animal studies which would include implanting the graft for a period of time, explant it, and assess its physical and mechanical properties post-implantation.

Freeze-drying was also implemented to prepare hydrogels for visualisation using SEM as shown in Figure 6.14. However, this method is inherently biased since the drying process may alter the native microarchitecture of the hydrogel leading to an inaccurate representation (Martinez-Garcia *et al.*, 2022). Therefore, despite being able to visualise the porous structure of the different hydrogel formulations, the effect of the drying process should be considered when interpreting such images. Given that all hydrogel formulations have been prepared and imaged using the same method, and thus have sustained the same processing error, this method can still serve as a comparative measure between the formulations as shown in Figure 6.14. For future work, other imaging techniques that do not require a drying process may be useful to explore, for example environmental SEM which allows the presence of water vapour inside the vacuum chamber thereby allowing the hydrogel samples to remain in their native, hydrated states (Koch and Włodarczyk-Biegun, 2020).

### 9.2.5. Aortic graft construct design

This research successfully demonstrated the 3D-printing of aortic-like constructs as potential graft substitutes using the alginate:PEGDA IPN hydrogel in combination with SLA. Figure 7.16 specifically demonstrates the ability of this method to fabricate complex aortic structures based on human anatomical dimensions. Thus, moving forward the next step for this work would be to base the 3D-printing CAD model on CT or MRI scan images from actual patients to demonstrate further the ability to develop personalised aortic grafts. This would provide a great opportunity to collaborate with clinicians.

One major limitation related to this part of the work, is that despite the hydrogel formulation demonstrating similar elastic properties to human aortic tissue (Chapter 6 and Chapter 7) and success in fabricating tubular conduits, the morphology of these 3D-printed constructs does not accurately represent the native tissue architecture. As highlighted in Chapter 2 Section 2.2.1, the aortic wall comprises three distinct layers with layers of elastic lamina in between, and each layer imparts different mechanical properties to the whole artery. Therefore, future research should aim to reproduce this triple-layered vessel wall structure. The optimisation process may take into consideration the possibility of using different hydrogel formulations for the different layers to closely resemble aortic wall tissue. This would open-up the possibility of multi-material 3D-printing to produce the different layers. However, to the author's knowledge multi-material 3D-printing via vat polymerisation methods have only been performed in the horizontal direction (i.e., parallel to the build plate), meaning that layers are first 3D-printed using one type of resin, the 3D-printing process is paused allowing for the resin in the tank to be swapped with a different resin type, followed by additional 3D-printing of the remaining layers (Asciak *et al.*, 2023). Therefore, 3D-printing via light-based methods might prove challenging in fabricating multiple layers in a concentric manner

that mimic the aortic wall structure. Nevertheless, it would be an interesting research direction to explore in the future.

Moreover, it is well-established that microscale topographical modifications influence cell adhesion, shape, alignment, and proliferation (Nikkhah *et al.*, 2012; Ermis, Antmen and Hasirci, 2018). Consequently, it would be interesting for future studies to exploit the potential of the 3D-printing method proposed in this work by incorporating micropatterns, such as micro-pits and micro-grooves, within the lumen of the hydrogel tubular conduits and observe how these topographical changes, in combination with biological cues within the material (RGD peptide), impact endothelialisation.

## 9.3. Key contributions of the research

The aim of the present research was to develop a synthetic aortic graft with similar biomechanical behaviour and morphology to the human aorta whilst also promoting a degree of bioactivity for endothelialisation. A review of the literature highlighted the lack of existing investigations that address the biomechanical and geometrical mismatches between large-diameter vascular grafts and aortic tissue – mismatches that have been associated with the development of graft-related complications, ultimately leading to surgical reinterventions. Hence, the primary contribution of this thesis was addressing this gap in the literature. To the author's knowledge this is also the first investigation to propose the use of 3D-printed hydrogels for the fabrication of more compliant, patient-specific aortic grafts, thus laying down the groundwork for future research.

By collaborating with Terumo Aortic, a world leading vascular graft technology company, this work is a prime example of knowledge exchange between academia and industry. For the company, this project was one of the first to investigate alternative biomaterials for graft production fitting well within its advanced material strategic research theme. Ultimately, the company envisages to build-up on this work through similar academic collaborations as it gradually moves towards its long-term goal of developing a

mechanically-relevant, clinically-available, personalised vascular graft. Moreover, the proposed technology is not just a contributor towards the development of alternative grafts but given its similarities in mechanical behaviour to the human aorta, it could also be used as an in-house bench-top testing system for aortic stents, as an alternative to animal tissue or standard silicone materials that are currently in use.

To this end, this research focussed on developing a hydrogel-based aortic graft material that could also be 3D-printed, thus opening up the possibility of a personalised fabrication approach. The hydrogel material comprising an interpenetrating polymer network of ionically crosslinked alginate and photopolymerisable PEGDA was developed and optimised to reveal elastic properties within the range of that reported for aortic tissue. Consequently, this work presents a methodological contribution to biomaterial research through the extensive mechanical characterisation approach applied to the hydrogel formulations developed. Hydrogel mechanical characterisation was performed using three different testing methods: confined compression, tensile stretch to failure, and rheological measurements, whereby the protocols used here are not limited to just these hydrogel formulations (alginate and alginate:PEGDA IPN) but can also be implemented to other hydrogel types, as demonstrated in (Domingo-Roca *et al.*, 2022a; Asciak *et al.*, 2023). Moreover, to the author's knowledge, this work presents for the first-time modelling of the confined compression stress relaxation measurements on ionically-crosslinked, single-networked alginate and alginate:PEGDA IPN hydrogels using FEBio, and the use of SLA 3D-printing for the fabrication of alginate:PEGDA IPN hydrogels, as opposed to existing literature on similar IPN hydrogels limited to extrusion-based 3D-printing (Hong *et al.*, 2015; Mistry *et al.*, 2017; Zhang *et al.*, 2021) or moulding techniques (Asohan *et al.*, 2022).

The use of light-based 3D-printing allowed for the fabrication of aortic-like structures based on an open-source to-scale human aorta model, thereby demonstrating

encouraging potential towards the development of patient-specific aortic grafts. By using CT or MRI patient scans this proposed technology could provide future collaborations with clinicians. Through this, in combination with mechanically-relevant materials, it is envisaged that more compliant and anatomically-matched grafts can be developed, thus minimising the existing complications typically associated with graft failure due to the rigidity of the Dacron® material. Moreover, it is widely-acknowledged that blood vessels, including the aorta, differ in morphology, structure, and thickness, based on gender and age (Zia, Liu and Wu, 2022). For instance, female aortic geometry typically involves smaller diameters and lengths than males (Rylski *et al.*, 2014). Therefore, the ability to produce a graft based on patient scans would potentially contribute towards addressing complications that arise when using the same graft design for both male and female patients.

Ultimately, the long-term goal of this technology is to minimise surgical reinterventions and hospitalisations, thus alleviating clinical and economic burdens on the healthcare system, but also enhancing the post-operative quality of life of patients. Therefore, from a global perspective, this work contributes to the United Nation's Sustainable Development Goals (SDG), in particular goal 3 which aims to reduce premature mortality from non-communicable diseases (which includes cardiovascular disease) by 2030 through prevention and treatment. If this technology were to be clinically translated in the future, the use of inexpensive materials to develop the hydrogel formulation, and affordable, desktop 3D-printers such as the one used in this work, could also offer access to personalised grafts to middle-, and possibly even low-income areas, thereby ensuring access to quality healthcare worldwide (SDG3).

## 9.4. Concluding remarks

This research set out to address the existing mechanical and geometrical mismatches between clinically-available synthetic aortic grafts and human aortic tissue, whilst attempting to promote endothelialisation. This was achieved by investigating different alginate-based hydrogel formulations as the proposed novel graft material. Through a series of mechanical characterisation methods (compressive, elastic, and rheological), the hydrogels' mechanical properties were compared with that of aortic tissue data reported in the literature. Following the identification of a suitable hydrogel formulation (alginate:PEGDA IPN) with elastic properties within range of the human aorta, the fabrication of large-diameter tubular conduits based on human aortic dimensions, both through moulding and 3D-printing, were investigated. Light-based 3D-printing (SLA) facilitated the production of rapid, more precise, and complex conduits, than the moulding technique, whilst also demonstrating encouraging results towards the development of patient-specific grafts in the future. To biofunctionalise the hydrogel and in turn promote endothelialisation, an RGD-based peptide was synthesised and introduced within the hydrogel matrix. Despite not achieving a fully-functionalised alginate:PEGDA IPN hydrogel, this work still demonstrates a promising approach towards the introduction of cell binding sites within otherwise bioinert monomers, whilst also providing opportunities for optimisation in future projects.

# References


Abdal-Hay, A., Bartnikowski, M., Hamlet, S. and Ivanovski, S. (2018) 'Electrospun biphasic tubular scaffold with enhanced mechanical properties for vascular tissue engineering', *Materials Science & Engineering C,* 82, pp. 10-18.

Aldana, A. A., Morgan, F. L., Houben, S., Pitet, L. M., Moroni, L. and Baker, M. B. (2021) 'Biomimetic double network hydrogels: Combining dynamic and static crosslinks to enable biofabrication and control cell-matrix interactions', *Journal of Polymer Science,* 59(22), pp. 2832-2843.

Aldridge, A., Desai, A., Owston, H., Jennings, L. M., Fisher, J., Rooney, P. and Kearney, J. N. (2018) 'Development and characterisation of a large diameter decellularised vascular allograft.(Report)', *Cell and Tissue Banking: International Journal for Banking, Engineering and Transplantation of Cells and Tissues,* 19(3), pp. 287.

Amabili, M., Balasubramanian, P., Bozzo, I., Breslavsky, I. D. and Ferrari, G. (2019) 'Layer-specific hyperelastic and viscoelastic characterization of human descending thoracic aortas', *Journal of the Mechanical Behavior of Biomedical Materials,* 99, pp. 27-46.

Amabili, M., Balasubramanian, P. and Breslavsky, I. (2019) 'Anisotropic fractional viscoelastic constitutive models for human descending thoracic aortas', *Journal of the Mechanical Behavior of Biomedical Materials,* 99, pp. 186-197.

Amabili, M., Balasubramanian, P., Breslavsky, I., Ferrari, G. and Tubaldi, E. (2018) 'Viscoelastic characterization of woven Dacron for aortic grafts by using direction-dependent quasi-linear viscoelasticity', *Journal of the Mechanical Behavior of Biomedical Materials,* 82, pp. 282-290.

Amabili, M., Prabakaran, B., Isabella, B., Ivan, D. B., Giovanni, F., Giulio, F., Francesco, G. and Chloé, P. (2020) 'Nonlinear Dynamics of Human Aortas for Material Characterization', *Physical review. X,* 10(1), pp. 011015.

Andersen, T., Auk-Emblem, P. and Dornish, M. (2015) '3D Cell Culture in Alginate Hydrogels', *Microarrays (Basel, Switzerland),* 4(2), pp. 133-161.

Annabi, N., Tamayol, A., Uquillas, J. A., Akbari, M., Bertassoni, L. E., Cha, C., Camci-Unal, G., Dokmeci, M. R., Peppas, N. A. and Khademhosseini, A. (2014) '25th Anniversary Article: Rational Design and Applications of Hydrogels in Regenerative Medicine', *Advanced Materials,* 26(1), pp. 85-124.

Antunes, M., Bonani, W., Reis, R. L., Migliaresi, C., Ferreira, H., Motta, A. and Neves, N. M. (2021) 'Development of alginate-based hydrogels for blood vessel engineering', *Materials Science and Engineering: C*, pp. 112588.

Aortic, T. (2023) *Vascular Graft Division Terumo Aortic*. Available at: https://www.terumo.com/business/aortic (Accessed: 25/06/2023 2023).

Arroyave, G. A. I., Lima, R. G., Martins, P. A. L. S., Ramião, N. and Jorge, R. M. N. (2015) 'Methodology for Mechanical Characterization of Soft Biological Tissues: Arteries', *Procedia Engineering,* 110, pp. 74-81.

Asawa, R. R., Belkowski, J. C., Schmitt, D. A., Hernandez, E. M., Babcock, A. E., Lochner, C. K., Baca, H. N., Rylatt, C. M., Steffes, I. S., VanSteenburg, J. J., Diaz, K. E. and Doroski, D. M. (2018) 'Transient cellular adhesion on poly(ethylene-glycol)-dimethacrylate hydrogels facilitates a novel stem cell bandage approach', *PLOS ONE,* 13(8), pp. e0202825.

Asciak, L., Gilmour, L., Williams, J. A., Foster, E., Díaz-García, L., McCormick, C., Windmill, J. F. C., Mulvana, H. E., Jackson-Camargo, J. C. and Domingo-Roca, R. (2023) 'Investigating multi-material hydrogel three-dimensional printing for in vitro representation of the neo-vasculature of solid tumours: a comprehensive mechanical analysis and assessment of nitric oxide release from human umbilical vein endothelial cells', *Royal Society Open Science,* 10(8), pp. 230929.

Asohan, A. W., Hashim, R., Ku Ishak, K. M., Abdul Hamid, Z. A., Jasme, N. and Bustami, Y. (2022) 'Preparation and Characterisation of Cellulose Nanocrystal/Alginate/Polyethylene Glycol Diacrylate (CNC/Alg/PEGDA) Hydrogel Using Double Network Crosslinking Technique for Bioprinting Application', *Applied Sciences,* 12(2), pp. 771.

ASTM (2011)*: Standard Guide for Characterization of Hydrogels used in Regenerative Medicine*. West Conshohocken, PA: ASTM International.

Aussel, A., Montembault, A., Malaise, S., Foulc, M. P., Faure, W., Cornet, S., Aid, R., Chaouat, M., Delair, T., Letourneur, D., David, L. and Bordenave, L. (2017) 'In Vitro Mechanical Property Evaluation of Chitosan-Based Hydrogels Intended for Vascular Graft Development.(Report)', *Journal of Cardiovascular Translational Research,* 10(5-6), pp. 480.

Azevedo, E. P., Retarekar, R., Raghavan, M. L. and Kumar, V. (2013) 'Mechanical properties of cellulose: chitosan blends for potential use as a coronary artery bypass graft', *Journal of Biomaterials Science, Polymer Edition,* 24(3), pp. 239-252.

Baby, D. K. (2020) 'Chapter 9 - Rheology of hydrogels', in Thomas, S., Sarathchandran, C. and Chandran, N. (eds.) *Rheology of Polymer Blends and Nanocomposites*: Elsevier, pp. 193-204.

Bajpai, S. K. and Sharma, S. (2004) 'Investigation of swelling/ degradation behaviour of alginate beads crosslinked with Ca 2+ and Ba 2+ ions', *Reactive and Functional Polymers,* 59(2), pp. 129-140.

Bakarich, S. E., Panhuis, M. i. h., Beirne, S., Wallace, G. G. and Spinks, G. M. (2013) 'Extrusion printing of ionic–covalent entanglement hydrogels with high toughness', *Journal of Materials Chemistry B,* 1(38), pp. 4939-4946.

Baniasadi, M. and Minary-Jolandan, M. (2015) 'Alginate-Collagen Fibril Composite Hydrogel', *Materials,* 8(2), pp. 799-814.

Bellis, S. L. (2011) 'Advantages of RGD peptides for directing cell association with biomaterials', *Biomaterials,* 32(18), pp. 4205-4210.

Benjamin, A. D., Abbasi, R., Owens, M., Olsen, R. J., Walsh, D. J., LeFevre, T. B. and Wilking, J. N. (2019) 'Light-based 3D printing of hydrogels with high-resolution channels', *Biomedical Physics & Engineering Express,* 5(2), pp. 025035.

Berglund, J. D., Nerem, R. M. and Sambanis, A. (2005) 'Viscoelastic testing methodologies for tissue engineered blood vessels.(Author Abstract)', *Journal of Biomechanical Engineering,* 127(7), pp. 1176.

Berman, S. S., Hunter, G. C., Smyth, S. H., Erdoes, L. S., McIntyre, K. E. and Bernhard, V. M. (1995) 'Application of computed tomography for surveillance of aortic grafts', *Surgery,* 118(1), pp. 8-15.

Bertram, U., Steiner, D., Poppitz, B., Dippold, D., Kohn, K., Beier, J. P., Detsch, R., Boccaccini, A. R., Horch, D. W. S. R. E. and Arkudas, A. (2017) 'Vascular Tissue

Engineering: Effects of Integrating Collagen into a PCL Based Nanofiber Material.(Research Article)', *BioMed Research International,* 2017.

Best, C. A., Pepper, V. K., Ohst, D., Bodnyk, K., Heuer, E., Onwuka, E. A., King, N., Strouse, R., Grischkan, J., Breuer, C. K., Johnson, J. and Chiang, T. (2018) 'Designing a tissue-engineered tracheal scaffold for preclinical evaluation', *International Journal of Pediatric Otorhinolaryngology,* 104, pp. 155-160.

Bianchi, P., Nano, G., Cusmai, F., Ramponi, F., Stegher, S., Dell'Aglio, D., Malacrida, G. and Tealdi, D. G. (2009) 'Uninfected para-anastomotic aneurysms after infrarenal aortic grafting', *Yonsei medical journal,* 50(2), pp. 227-238.

Bidarra, S. J., Barrias, C. C., Fonseca, K. B., Barbosa, M. A., Soares, R. A. and Granja, P. L. (2011) 'Injectable in situ crosslinkable RGD-modified alginate matrix for endothelial cells delivery', *Biomaterials,* 32(31), pp. 7897-7904.

*The Biomedical 3D printing community, Embodi3D* (2023). Available at: https://www.embodi3d.com/files/file/55739-abdominal-aorta/ (Accessed: 09/08/2022.

Birmpili, P., Waton, S., Johal, A., Li, Q., Atkins, E., Boyle, J. R., Cromwell, D. A., Pherwani, A. D. and Williams, R. (2022) *Use of implantable medical devices in aortic aneurysm repair*, London: The Royal College of Surgeons of England.

Bishop, E. S., Mostafa, S., Pakvasa, M., Luu, H. H., Lee, M. J., Wolf, J. M., Ameer, G. A., He, T.-C. and Reid, R. R. (2017) '3-D bioprinting technologies in tissue engineering and regenerative medicine: Current and future trends', *Genes & Diseases,* 4(4), pp. 185-195.

Blaeser, A., Duarte Campos, D. F., Weber, M., Neuss, S., Theek, B., Fischer, H. and Jahnen-Dechent, W. (2013) 'Biofabrication under fluorocarbon: a novel freeform fabrication technique to generate high aspect ratio tissue-engineered constructs', *BioResearch open access,* 2(5), pp. 374-384.

Blase, C., Kadiev, D., Benderoth, G. and Wittek, A. (2012) 'COMBINED TORSION AND INFLATION EXTENSION TESTING OF VASCULAR SPECIMENS', *Journal of Biomechanics,* 45, pp. S20-S20.

Bossone, E. and Eagle, K. A. (2021) 'Epidemiology and management of aortic disease: aortic aneurysms and acute aortic syndromes', *Nature Reviews Cardiology,* 18(5), pp. 331-348.

Burke, G., Devine, D. M. and Major, I. (2020) 'Effect of stereolithography 3D printing on the properties of PEGDMA hydrogels', *Polymers,* 12(9), pp. 2015.

Busby, G. A., Grant, M. H., MacKay, S. P. and Riches, P. E. (2013) 'Confined compression of collagen hydrogels', *Journal of Biomechanics,* 46(4), pp. 837-840.

Bustos, C. A., García-Herrera, C. M. and Celentano, D. J. (2016) 'Mechanical characterisation of Dacron graft: Experiments and numerical simulation', *Journal of Biomechanics,* 49(1), pp. 13-18.

Callaghan, F. M. and Grieve, S. M. (2018) 'Normal patterns of thoracic aortic wall shear stress measured using four-dimensional flow MRI in a large population', *American Journal of Physiology-Heart and Circulatory Physiology,* 315(5), pp. H1174-H1181.

Camasão, D. B. and Mantovani, D. (2021) 'The mechanical characterization of blood vessels and their substitutes in the continuous quest for physiological-relevant performances. A critical review', *Materials Today Bio,* 10, pp. 100106.

Cattelan, G., Guerrero Gerbolés, A., Foresti, R., Pramstaller, P. P., Rossini, A., Miragoli, M. and Caffarra Malvezzi, C. (2020) 'Alginate Formulations: Current Developments in the Race for Hydrogel-Based Cardiac Regeneration', *Frontiers in Bioengineering and Biotechnology,* 8.

Chakfé, N., Bizonne, S. C., Beaufigeau, M., Urban, E., Cardon, A., Doillon, C., Le Magnen, J.-F., Durand, B. and Kretz, J.-G. (1999) 'Impregnated polyester arterial prostheses: performance and prospects', *Annals of vascular surgery,* 13(5), pp. 509-523.

Charbonier, F., Indana, D. and Chaudhuri, O. (2021) 'Tuning Viscoelasticity in Alginate Hydrogels for 3D Cell Culture Studies', *Current Protocols,* 1(5), pp. e124.

Chaudhuri, O. (2017) 'Viscoelastic hydrogels for 3D cell culture', *Biomaterials Science,* 5(8), pp. 1480-1490.

Chen, E. Y., Liu, W. F., Megido, L., Díez, P., Fuentes, M., Fager, C., Olsson, E., Gessner, I. and Mathur, S. (2018) 'Chapter 3 - Understanding and utilizing the biomolecule/nanosystems interface', in Uskoković, V. and Uskoković, D.P. (eds.) *Nanotechnologies in Preventive and Regenerative Medicine*: Elsevier, pp. 207-297.

Chen, P., Pollet, A. M. A. O., Panfilova, A., Zhou, M., Turco, S., den Toonder, J. M. J. and Mischi, M. (2022) 'Acoustic characterization of tissue-mimicking materials for ultrasound perfusion imaging research', *Ultrasound in Medicine & Biology,* 48(1), pp. 124-142.

Chen, X., Yao, Y., Liu, S. and Hu, Q. (2021) 'An integrated strategy for designing and fabricating triple-layer vascular graft with oriented microgrooves to promote endothelialization', *Journal of Biomaterials Applications,* 36(2), pp. 297-310.

Chimene, D., Kaunas, R. and Gaharwar, A. K. (2020) 'Hydrogel Bioink Reinforcement for Additive Manufacturing: A Focused Review of Emerging Strategies', *Advanced Materials,* 32(1), pp. 1902026.

Chlupác, J., Filová, E. and Bacáková, L. (2009) 'Blood vessel replacement: 50 years of development and tissue engineering paradigms in vascular surgery', *Physiological research,* 58 suppl 2, pp. S119-S139.

Christensen, K., Xu, C., Chai, W., Zhang, Z., Fu, J. and Huang, Y. (2015) 'Freeform inkjet printing of cellular structures with bifurcations', *Biotechnology and Bioengineering,* 112(5), pp. 1047-1055.

Chung, J. H. Y., Naficy, S., Yue, Z., Kapsa, R., Quigley, A., Moulton, S. E. and Wallace, G. G. (2013) 'Bio-ink properties and printability for extrusion printing living cells', *Biomaterials Science,* 1(7), pp. 763-773.

Cocciolone, A. J., Hawes, J. Z., Staiculescu, M. C., Johnson, E. O., Murshed, M. and Wagenseil, J. E. (2018) 'Elastin, arterial mechanics, and cardiovascular disease', *American journal of physiology. Heart and circulatory physiology,* 315(2), pp. H189-H205.

Collier, J. H. and Segura, T. (2011) 'Evolving the use of peptides as components of biomaterials', *Biomaterials,* 32(18), pp. 4198-4204.

Costa, A. M. S. and Mano, J. F. (2015) 'Extremely strong and tough hydrogels as prospective candidates for tissue repair – A review', *European Polymer Journal,* 72, pp. 344-364.

Cristovão, A. F., Sousa, D., Silvestre, F., Ropio, I., Gaspar, A., Henriques, C., Velhinho, A., Baptista, A. C., Faustino, M. and Ferreira, I. (2019) 'Customized tracheal design using

3D printing of a polymer hydrogel: influence of UV laser cross-linking on mechanical properties', *3D Printing in Medicine,* 5(1), pp. 12.

ASTM (2014)*: Standard test method for tensile properties of plastics*: ASTM International.

Darnell, M. C., Sun, J.-Y., Mehta, M., Johnson, C., Arany, P. R., Suo, Z. and Mooney, D. J. (2013) 'Performance and biocompatibility of extremely tough alginate/polyacrylamide hydrogels', *Biomaterials,* 34(33), pp. 8042-8048.

Datta, P., Ayan, B. and Ozbolat, I. T. (2017) 'Bioprinting for vascular and vascularized tissue biofabrication', *Acta Biomaterialia,* 51, pp. 1-20.

de Beaufort, H. W. L., Ferrara, A., Conti, M., Moll, F. L., van Herwaarden, J. A., Figueroa, C. A., Bismuth, J., Auricchio, F. and Trimarchi, S. (2018) 'Comparative Analysis of Porcine and Human Thoracic Aortic Stiffness', *European Journal of Vascular and Endovascular Surgery,* 55(4), pp. 560-566.

de Melo, B. A. G., Jodat, Y. A., Mehrotra, S., Calabrese, M. A., Kamperman, T., Mandal, B. B., Santana, M. H. A., Alsberg, E., Leijten, J. and Shin, S. R. (2019) '3D Printed Cartilage-Like Tissue Constructs with Spatially Controlled Mechanical Properties', *Advanced Functional Materials,* 29(51), pp. 1906330.

de Oliveira, M. F., da Silva, L. C. E. and de Oliveira, M. G. (2021) '3D printed bioresorbable nitric oxide-releasing vascular stents', *Bioprinting,* 22, pp. e00137.

Della Sala, F., Biondi, M., Guarnieri, D., Borzacchiello, A., Ambrosio, L. and Mayol, L. (2020) 'Mechanical behavior of bioactive poly(ethylene glycol) diacrylate matrices for biomedical application', *Journal of the Mechanical Behavior of Biomedical Materials,* 110, pp. 103885.

Deng, J., Cheng, C., Teng, Y., Nie, C. and Zhao, C. (2017) 'Mussel-inspired post-heparinization of a stretchable hollow hydrogel tube and its potential application as an artificial blood vessel', *Polymer Chemistry,* 8(14), pp. 2266-2275.

Deng, S., Tomioka, J., Debes, J. and Fung, Y. (1994) 'New experiments on shear modulus of elasticity of arteries', *American Journal of Physiology,* 35(1), pp. H1.

Ding, H. and Chang, R. (2018) 'Printability Study of Bioprinted Tubular Structures Using Liquid Hydrogel Precursors in a Support Bath', *Applied Sciences,* 8(3).

Dobrin, P. B. (1978) 'Mechanical properties of arteries', *Physiological reviews,* 58(2), pp. 397-460.

Domingo-Roca, R., Asciak, L., Windmill, J. F. C., Mulvana, H. and Jackson-Camargo, J. C. (2022a) 'Non-destructive Analysis of the Mechanical Properties of 3D-Printed Materials', *Journal of Nondestructive Evaluation,* 41(1), pp. 22.

Domingo-Roca, R., Gilmour, L., Dobre, O., Sarrigianidis, S., Sandison, M. E., O'Leary, R., Jackson-Camargo, J. C. and Mulvana, H. E. (2022b) '3D printing of noncytotoxic high-resolution microchannels in Bisphenol-a ethoxylate dimethacrylate tissue-mimicking materials', *3D Printing and Additive Manufacturing* *10*(5), pp.1101-1109.

Drury, J. L., Dennis, R. G. and Mooney, D. J. (2004) 'The tensile properties of alginate hydrogels', *Biomaterials,* 25(16), pp. 3187-3199.

Duarte Campos, D. F., Blaeser, A., Weber, M., Jäkel, J., Neuss, S., Jahnen-Dechent, W. and Fischer, H. (2013) 'Three-dimensional printing of stem cell-laden hydrogels submerged in a hydrophobic high-density fluid', *Three-dimensional printing of stem cell-laden hydrogels submerged in a hydrophobic high-density fluid,* 5(1), pp. 015003.

Duprey, A., Khanafer, K., Schlicht, M., Avril, S., Williams, D. and Berguer, R. (2010) 'In Vitro Characterisation of Physiological and Maximum Elastic Modulus of Ascending Thoracic Aortic Aneurysms Using Uniaxial Tensile Testing', *European Journal of Vascular and Endovascular Surgery,* 39(6), pp. 700-707.

Elliott, M. B., Ginn, B., Fukunishi, T., Bedja, D., Suresh, A., Chen, T., Inoue, T., Dietz, H. C., Santhanam, L., Mao, H.-Q., Hibino, N. and Gerecht, S. (2019) 'Regenerative and durable small-diameter graft as an arterial conduit', *Proceedings of the National Academy of Sciences of the United States of America,* 116(26), pp. 12710-12719.

Emmott, A., Garcia, J., Chung, J., Lachapelle, K., El-Hamamsy, I., Mongrain, R., Cartier, R. and Leask, R. L. (2016) 'Biomechanics of the Ascending Thoracic Aorta: A Clinical Perspective on Engineering Data', *Canadian Journal of Cardiology,* 32(1), pp. 35-47.

Ermis, M., Antmen, E. and Hasirci, V. (2018) 'Micro and Nanofabrication methods to control cell-substrate interactions and cell behavior: A review from the tissue engineering perspective', *Bioactive Materials,* 3(3), pp. 355-369.

Fairbanks, B. D., Schwartz, M. P., Bowman, C. N. and Anseth, K. S. (2009) 'Photoinitiated polymerization of PEG-diacrylate with lithium phenyl-2,4,6-trimethylbenzoylphosphinate: polymerization rate and cytocompatibility', *Biomaterials,* 30(35), pp. 6702-6707.

Farkas, A. Z., Galatanu, S.-V. and Nagib, R. (2023) 'The Influence of Printing Layer Thickness and Orientation on the Mechanical Properties of DLP 3D-Printed Dental Resin', *Polymers,* 15(5), pp. 1113.

Farotto, D., Segers, P., Meuris, B., Vander Sloten, J. and Famaey, N. (2018) 'The role of biomechanics in aortic aneurysm management: requirements, open problems and future prospects.(Report)(Author abstract)', *Journal of the Mechanical Behavior of Biomedical Materials,* 77, pp. 295.

Faturechi, R., Hashemi, A., Abolfathi, N. and Solouk, A. (2019) 'Mechanical guidelines on the properties of human healthy arteries in the design and fabrication of vascular grafts: experimental tests and quasi-linear viscoelastic model', *Acta of bioengineering and biomechanics,* 21(3), pp. 13-21.

Ferrari, G., Balasubramanian, P., Tubaldi, E., Giovanniello, F. and Amabili, M. (2019) 'Experiments on dynamic behaviour of a Dacron aortic graft in a mock circulatory loop', *Journal of Biomechanics,* 86, pp. 132-140.

Fields, G. B. (2001) 'Introduction to Peptide Synthesis', *Current Protocols in Protein Science,* 26(1), pp. 18.1.1-18.1.9.

Fitzgerald, M. M., Bootsma, K., Berberich, J. A. and Sparks, J. L. (2015) 'Tunable Stress Relaxation Behavior of an Alginate-Polyacrylamide Hydrogel: Comparison with Muscle Tissue', *Biomacromolecules,* 16(5), pp. 1497-1505.

Floren, M., Migliaresi, C. and Motta, A. (2016) 'Processing Techniques and Applications of Silk Hydrogels in Bioengineering', *Journal of functional biomaterials,* 7(3).

Foss, B. L., Maxwell, T. W. and Deng, Y. (2014) 'Chondroprotective supplementation promotes the mechanical properties of injectable scaffold for human nucleus pulposus tissue engineering', *Journal of the Mechanical Behavior of Biomedical Materials,* 29, pp. 56-67.

Freeman, F. E. and Kelly, D. J. (2017) 'Tuning Alginate Bioink Stiffness and Composition for Controlled Growth Factor Delivery and to Spatially Direct MSC Fate within Bioprinted Tissues', *Scientific reports,* 7(1), pp. 17042-17042.

Galarraga, J. H., Dhand, A. P., Enzmann, B. P., III and Burdick, J. A. (2023) 'Synthesis, Characterization, and Digital Light Processing of a Hydrolytically Degradable Hyaluronic Acid Hydrogel', *Biomacromolecules,* 24(1), pp. 413-425.

Gao, M., Zhang, H., Dong, W., Bai, J., Gao, B., Xia, D., Feng, B., Chen, M., He, X., Yin, M., Xu, Z., Witman, N., Fu, W. and Zheng, J. (2017a) 'Tissue-engineered trachea from a 3D-printed scaffold enhances whole-segment tracheal repair', *Scientific reports,* 7(1), pp. 5246-5246.

Gao, Q., He, Y., Fu, J.-Z., Liu, A. and Ma, L. (2015) 'Coaxial nozzle-assisted 3D bioprinting with built-in microchannels for nutrients delivery', *Biomaterials,* 61, pp. 203-215.

Gao, Q., Liu, Z., Lin, Z., Qiu, J., Liu, Y., Liu, A., Wang, Y., Xiang, M., Chen, B., Fu, J. and He, Y. (2017b) '3D Bioprinting of Vessel-like Structures with Multilevel Fluidic Channels', *ACS Biomaterials Science & Engineering,* 3(3), pp. 399-408.

Gargava, A., Ahn, S., Bentley, W. E. and Raghavan, S. R. (2019) 'Rapid Electroformation of Biopolymer Gels in Prescribed Shapes and Patterns: A Simpler Alternative to 3-D Printing', *ACS Applied Materials & Interfaces,* 11(40), pp. 37103-37111.

Gasser, T. C. (2017) *Aorta.*

Gasser, T. C., Ogden, R. W. and Holzapfel, G. A. (2006) 'Hyperelastic modelling of arterial layers with distributed collagen fibre orientations', *Journal of the Royal Society, Interface,* 3(6), pp. 15-35.

Ghanizadeh Tabriz, A., Hermida, M. A., Leslie, N. R. and Shu, W. (2015) 'Three-dimensional bioprinting of complex cell laden alginate hydrogel structures'.

Ghanizadeh Tabriz, A., Mills, C. G., Mullins, J. J., Davies, J. A. and Shu, W. (2017) 'Rapid fabrication of cell-laden alginate hydrogel 3D structures by micro dip-coating'.

Giuseppe, M. D., Law, N., Webb, B., A Macrae, R., Liew, L. J., Sercombe, T. B., Dilley, R. J. and Doyle, B. J. (2018) 'Mechanical behaviour of alginate- gelatin hydrogels for 3D bioprinting', *Journal of the mechanical behavior of biomedical materials,* 79, pp. 150-157.

Goins, A., Webb, A. R. and Allen, J. B. (2019) 'Multi-layer approaches to scaffold-based small diameter vessel engineering: A review', *Materials Science & Engineering C,* 97, pp. 896-912.

Gold, K. A., Saha, B., Rajeeva Pandian, N. K., Walther, B. K., Palma, J. A., Jo, J., Cooke, J. P., Jain, A. and Gaharwar, A. K. (2021) '3D Bioprinted Multicellular Vascular Models', *Advanced Healthcare Materials,* 10(21), pp. 2101141.

Golledge, J. (2019) 'Abdominal aortic aneurysm: update on pathogenesis and medical treatments', *Nat. Rev. Cardiol.,* 16(4), pp. 225-242.

González, G., Baruffaldi, D., Martinengo, C., Angelini, A., Chiappone, A., Roppolo, I., Pirri, C. F. and Frascella, F. (2020) 'Materials testing for the development of biocompatible devices through vat-polymerization 3d printing', *Nanomaterials,* 10(9), pp. 1788.

Grigoryan, B., Paulsen, S. J., Corbett, D. C., Sazer, D. W., Fortin, C. L., Zaita, A. J., Greenfield, P. T., Calafat, N. J., Gounley, J. P. and Ta, A. H. (2019) 'Multivascular networks and functional intravascular topologies within biocompatible hydrogels', *Science,* 364(6439), pp. 458-464.

Growney Kalaf, E. A., Flores, R., Bledsoe, J. G. and Sell, S. A. (2016) 'Characterization of slow- gelling alginate hydrogels for intervertebral disc tissue- engineering applications', *Materials Science & Engineering C,* 63, pp. 198-210.

Gu, W. Y., Yao, H., Huang, C. Y. and Cheung, H. S. (2003) 'New insight into deformation-dependent hydraulic permeability of gels and cartilage, and dynamic behavior of agarose gels in confined compression', *Journal of Biomechanics,* 36(4), pp. 593-598.

Guan, G., Yu, C., Xing, M., Wu, Y., Hu, X., Wang, H. and Wang, L. (2019) 'Hydrogel Small-Diameter Vascular Graft Reinforced with a Braided Fiber Strut with Improved Mechanical Properties', *Polymers,* 11(5).

Guarnieri, D., De Capua, A., Ventre, M., Borzacchiello, A., Pedone, C., Marasco, D., Ruvo, M. and Netti, P. A. (2010) 'Covalently immobilized RGD gradient on PEG hydrogel scaffold influences cell migration parameters', *Acta Biomaterialia,* 6(7), pp. 2532-2539.

Gungor-Ozkerim, P. S., Inci, I., Zhang, Y. S., Khademhosseini, A. and Dokmeci, M. R. (2018) 'Bioinks for 3D bioprinting: an overview', *Biomaterials Science,* 6(5), pp. 915-946.

Gupta, P., Lorentz, K. L., Haskett, D. G., Cunnane, E. M., Ramaswamy, A. K., Weinbaum, J. S., Vorp, D. A. and Mandal, B. B. (2020) 'Bioresorbable silk grafts for small diameter vascular tissue engineering applications: In vitro and in vivo functional analysis', *Acta Biomaterialia,* 105, pp. 146-158.

Hakim Khalili, M., Zhang, R., Wilson, S., Goel, S., Impey, S. A. and Aria, A. I. (2023) 'Additive Manufacturing and Physicomechanical Characteristics of PEGDA Hydrogels: Recent Advances and Perspective for Tissue Engineering', *Polymers,* 15(10), pp. 2341.

Han, W. T., Jang, T., Chen, S., Chong, L. S. H., Jung, H.-D. and Song, J. (2020) 'Improved cell viability for large-scale biofabrication with photo-crosslinkable hydrogel systems through a dual-photoinitiator approach', *Biomaterials Science,* 8(1), pp. 450-461.

Harkness, M. L. R., Harkness, R. D., McDonald, D. A. and Franklin, K. J. (1957) 'The collagen and elastin content of the arterial wall in the dog', *Proceedings of the Royal Society of London. Series B - Biological Sciences,* 146(925), pp. 541-551.

Harrison, R. G. and Massaro, T. A. (1976) 'Water flux through porcine aortic tissue due to a hydrostatic pressure gradient', *Atherosclerosis,* 24(3), pp. 363-367.

Hasan, A., Memic, A., Annabi, N., Hossain, M., Paul, A., Dokmeci, M. R., Dehghani, F. and Khademhosseini, A. (2014) 'Electrospun scaffolds for tissue engineering of vascular grafts', *Acta Biomaterialia,* 10(1), pp. 11-25.

Hasany, M., Talebian, S., Sadat, S., Ranjbar, N., Mehrali, M., Wallace, G. G. and Mehrali, M. (2021) 'Synthesis, properties, and biomedical applications of alginate methacrylate (ALMA)-based hydrogels: Current advances and challenges', *Applied Materials Today,* 24, pp. 101150.

Hasegawa, M. and Azuma, T. (1979) 'Mechanical properties of synthetic arterial grafts', *Journal of Biomechanics,* 12(7), pp. 509-517.

Haskett, D., Johnson, G., Zhou, A., Utzinger, U. and Vande Geest, J. (2010) 'Microstructural and biomechanical alterations of the human aorta as a function of age and location.(Report)', *Biomechanics and Modeling in Mechanobiology,* 9(6), pp. 725.

Haug, A., Smidsrød, O., Högdahl, B., Øye, H., Rasmussen, S., Sunde, E. and Sørensen, N. A. (1970) 'Selectivity of some anionic polymers for divalent metal ions', *Acta chem. scand,* 24(3), pp. 843-854.

Hemmasizadeh, A., Autieri, M. and Darvish, K. (2012) 'Multilayer material properties of aorta determined from nanoindentation tests', *Journal of the Mechanical Behavior of Biomedical Materials,* 15, pp. 199-207.

Hemmasizadeh, A., Tsamis, A., Cheheltani, R., Assari, S., D'amore, A., Autieri, M., Kiani, M. F., Pleshko, N., Wagner, W. R., Watkins, S. C., Vorp, D. and Darvish, K. (2015) 'Correlations between transmural mechanical and morphological properties in porcine thoracic descending aorta', *Journal of the Mechanical Behavior of Biomedical Materials,* 47, pp. 12-20.

Hersel, U., Dahmen, C. and Kessler, H. (2003) 'RGD modified polymers: biomaterials for stimulated cell adhesion and beyond', *Biomaterials,* 24(24), pp. 4385-4415.

Hisham, M., Saravana Kumar, G. and Deshpande, A. P. (2022) 'Process optimization and optimal tolerancing to improve dimensional accuracy of vat-photopolymerized functionally graded hydrogels', *Results in Engineering,* 14, pp. 100442.

Hockaday, L. A., Kang, K. H., Colangelo, N. W., Cheung, P. Y. C., Duan, B., Malone, E., Wu, J., Girardi, L. N., Bonassar, L. J., Lipson, H., Chu, C. C. and Butcher, J. T. (2012) 'Rapid 3D printing of anatomically accurate and mechanically heterogeneous aortic valve hydrogel scaffolds', *Biofabrication,* 4(3), pp. 035005.

Holland, I., Logan, J., Shi, J., McCormick, C., Liu, D. and Shu, W. (2018) '3D biofabrication for tubular tissue engineering', *Bio-Design and Manufacturing,* 1(2), pp. 89-100.

Hong, S., Sycks, D., Chan, H. F., Lin, S., Lopez, G. P., Guilak, F., Leong, K. W. and Zhao, X. (2015) '3D Printing of Highly Stretchable and Tough Hydrogels into Complex, Cellularized Structures', *Advanced Materials,* 27(27), pp. 4035-4040.

Hospodiuk, M., Dey, M., Sosnoski, D. and Ozbolat, I. T. 2017. The bioink: A comprehensive review on bioprintable materials. *Biotechnology Advances.*

Huang, Y., Jayathilaka, P. B., Islam, M. S., Tanaka, C. B., Silberstein, M. N., Kilian, K. A. and Kruzic, J. J. (2022) 'Structural aspects controlling the mechanical and biological properties of tough, double network hydrogels', *Acta Biomaterialia,* 138, pp. 301-312.

Huh, J., Moon, Y.-W., Park, J., Atala, A., Yoo, J. J. and Lee, S. J. (2021) 'Combinations of photoinitiator and UV absorber for cell-based digital light processing (DLP) bioprinting', *Biofabrication,* 13(3), pp. 034103.

Humphrey, J. D. and Holzapfel, G. A. (2012) 'Mechanics, mechanobiology, and modeling of human abdominal aorta and aneurysms', *Journal of Biomechanics,* 45(5), pp. 805-814.

Hyland, L. L., Taraban, M. B. and Yu, Y. B. (2013) 'Using small-angle scattering techniques to understand mechanical properties of biopolymer-based biomaterials', *Soft Matter,* 9(43), pp. 10218-10228.

Hynes, N., Acharya, Y. and Sultan, S. (2022) 'The contemporary design of endovascular aneurysm stent-graft materials: PTFE versus polyester', *Frontiers in Surgery,* 9.

Ioannou, C. V., Morel, D. R., Katsamouris, A. N., Katranitsa, S., Startchik, I., Kalangos, A., Westerhof, N. and Stergiopulos, N. (2009) 'Left Ventricular Hypertrophy Induced by Reduced Aortic Compliance', *Journal of Vascular Research,* 46(5), pp. 417-425.

ISO7198 (2016) 'Cardiovascular Implants and Extracorporeal Systems—Vascular Prostheses—Tubular Vascular Grafts and Vascular Patches'.

ISO7198 (2017) 'ISO 37: 2017, Rubber, Vulcanized or Thermoplastic: Determination of Tensile Stress–Strain Properties'.

Jacobs, P. F. 'Fundamentals of stereolithography'. *1992 international solid freeform fabrication symposium*.

Jan, S., Federica De, L., Benjamin, T., Andreas, B., Dirk, R., Alexander, J. C. K., Fabian, K. and Horst, F. (2018) 'Engineering biofunctional in vitro vessel models using a multilayer bioprinting technique', *Scientific reports,* 8(1), pp. 1-13.

Jejurikar, A., Lawrie, G., Martin, D. and Grøndahl, L. (2011) 'Anovel strategy for preparing mechanically robust ionically cross- linked alginate hydrogels', *Biomedical Materials,* 6(2), pp. 12.

Jeon, O., Bouhadir, K. H., Mansour, J. M. and Alsberg, E. (2009) 'Photocrosslinked alginate hydrogels with tunable biodegradation rates and mechanical properties', *Biomaterials,* 30(14), pp. 2724-2734.

Jeon, O., Powell, C., Ahmed, S. M. and Alsberg, E. (2010) 'Biodegradable, photocrosslinked alginate hydrogels with independently tailorable physical properties and cell adhesivity.(Report)', *Tissue Engineering, Part A: Tissue Engineering,* 16(9), pp. 2915.

Jia, J., Coyle, R. C., Richards, D. J., Berry, C. L., Barrs, R. W., Biggs, J., James Chou, C., Trusk, T. C. and Mei, Y. (2016a) 'Development of peptide-functionalized synthetic hydrogel microarrays for stem cell and tissue engineering applications', *Acta Biomaterialia,* 45, pp. 110-120.

Jia, W., Gungor-Ozkerim, P. S., Zhang, Y. S., Yue, K., Zhu, K., Liu, W., Pi, Q., Byambaa, B., Dokmeci, M. R., Shin, S. R. and Khademhosseini, A. (2016b) 'Direct 3D bioprinting of perfusable vascular constructs using a blend bioink', *Biomaterials,* 106, pp. 58-68.

Jirofti, N., Mohebbi-Kalhori, D., Samimi, A., Hadjizadeh, A. and Kazemzadeh, G. H. (2018) 'Small-diameter vascular graft using co-electrospun composite pcl/pu nanofibers', *Small-diameter vascular graft using co-electrospun composite PCL/PU nanofibers,* 13(5), pp. 055014.

Johnson, R., Ding, Y., Nagiah, N., Monnet, E. and Tan, W. (2019) 'Coaxially-structured fibres with tailored material properties for vascular graft implant', *Materials Science & Engineering C,* 97, pp. 1-11.

Johnson, W. C. and Lee, K. K. (2000) 'A comparative evaluation of polytetrafluoroethylene, umbilical vein, and saphenous vein bypass grafts for femoral-popliteal above-knee revascularization: A prospective randomized Department of Veterans Affairs cooperative study', *Journal of Vascular Surgery,* 32(2), pp. 268-277.

Juhyun, C., Matonick, J. P. and Li, J. K. J. 'Synthetic arterial graft design on the influence of pulse wave propagation within the aorta'. *Proceedings of the IEEE 28th Annual Northeast Bioengineering Conference (IEEE Cat. No.02CH37342)*, 21-21 April 2002, 17-18.

Kadry, H., Wadnap, S., Xu, C. and Ahsan, F. (2019) 'Digital light processing (DLP) 3D-printing technology and photoreactive polymers in fabrication of modified-release tablets', *European Journal of Pharmaceutical Sciences,* 135, pp. 60-67.

Kalakkunnath, S., Kalika, D. S., Lin, H. and Freeman, B. D. (2006) 'Viscoelastic characteristics of UV polymerized poly(ethylene glycol) diacrylate networks with varying extents of crosslinking', *Journal of Polymer Science Part B: Polymer Physics,* 44(15), pp. 2058-2070.

Kamenskiy, A. V., Dzenis, Y. A., Kazmi, S. A. J., Pemberton, M. A., Pipinos, I. I., Phillips, N. Y., Herber, K., Woodford, T., Bowen, R. E., Lomneth, C. S. and MacTaggart, J. N. (2014) 'Biaxial mechanical properties of the human thoracic and abdominal aorta, common carotid, subclavian, renal and common iliac arteries.(Report)', *Biomechanics and Modeling in Mechanobiology,* 13(6), pp. 1341.

Kassab, G. S. (2006) 'Biomechanics of the cardiovascular system: the aorta as an illustratory example', *Journal of the Royal Society, Interface,* 3(11), pp. 719-740.

Kermani, G., Hemmasizadeh, A., Assari, S., Autieri, M. and Darvish, K. (2017) 'Investigation of inhomogeneous and anisotropic material behavior of porcine thoracic aorta using nano-indentation tests', *Journal of the Mechanical Behavior of Biomedical Materials,* 69, pp. 50-56.

Khan, S., Fakhouri, F., Majeed, W. and Kolipaka, A. (2018) 'Cardiovascular magnetic resonance elastography: A review', *NMR in Biomedicine,* 31(10), pp. n/a-n/a.

Khanafer, K., Schlicht, M. S. and Berguer, R. (2013) 'How Should We Measure and Report Elasticity in Aortic Tissue?', *European Journal of Vascular & Endovascular Surgery,* 45(4), pp. 332-339.

Kim, J. and Baek, S. (2011) 'Circumferential variations of mechanical behavior of the porcine thoracic aorta during the inflation test', *Journal of Biomechanics,* 44(10), pp. 1941-1947.

Kizhakkedathu, J. N. and Conway, E. M. (2022) 'Biomaterial and cellular implants: foreign surfaces where immunity and coagulation meet', *Blood,* 139(13), pp. 1987-1998.

Koch, M. and Włodarczyk-Biegun, M. K. (2020) 'Faithful scanning electron microscopic (SEM) visualization of 3D printed alginate-based scaffolds', *Bioprinting,* 20, pp. e00098.

Krishnamoorthy, S., Zhang, Z. and Xu, C. (2019) 'Biofabrication of three-dimensional cellular structures based on gelatin methacrylate–alginate interpenetrating network hydrogel', *Journal of Biomaterials Applications,* 33(8), pp. 1105-1117.

Kumar, V. A., Caves, J. M., Haller, C. A., Dai, E., Liu, L., Grainger, S. and Chaikof, E. L. (2013) 'Acellular vascular grafts generated from collagen and elastin analogs', *Acta Biomaterialia,* 9(9), pp. 8067-8074.

Kuo, C. K. and Ma, P. X. (2001) 'Ionically crosslinked alginate hydrogels as scaffolds for tissue engineering: Part 1. Structure, gelation rate and mechanical properties', *Biomaterials,* 22(6), pp. 511-521.

Kuo, C. K. and Ma, P. X. (2008) 'Maintaining dimensions and mechanical properties of ionically crosslinked alginate hydrogel scaffolds in vitro', *Journal of Biomedical Materials Research Part A,* 84(4), pp. 899-907.

Labrosse, M. R., Gerson, E. R., Veinot, J. P. and Beller, C. J. (2013) 'Mechanical characterization of human aortas from pressurization testing and a paradigm shift for circumferential residual stress', *Journal of the Mechanical Behavior of Biomedical Materials,* 17, pp. 44-55.

Ladich, E., Yahagi, K., Romero, M. E. and Virmani, R. (2016) 'Vascular diseases: aortitis, aortic aneurysms, and vascular calcification', *Cardiovascular Pathology,* 25(5), pp. 432-441.

Lake, S. P. and Barocas, V. H. (2011) 'Mechanical and Structural Contribution of Non-Fibrillar Matrix in Uniaxial Tension: A Collagen-Agarose Co-Gel Model', *Annals of Biomedical Engineering,* 39(7), pp. 1891-1903.

Lantelme, P., Dzudie, A., Milon, H., Bricca, G., Legedz, L., Chevalier, J. M. and Feugier, P. (2009) 'Effect of abdominal aortic grafts on aortic stiffness and central hemodynamics', *Journal of Hypertension,* 27(6), pp. 1268-1276.

Lee, J. E., Park, S. J., Yoon, Y., Son, Y. and Park, S.-H. (2019) 'Fabrication of 3D freeform porous tubular constructs with mechanical flexibility mimicking that of soft vascular tissue', *Journal of the Mechanical Behavior of Biomedical Materials,* 91, pp. 193-201.

Lee, J. Y., Park, J. H., Ahn, M. J., Kim, S. W. and Cho, D.-W. (2020) 'Long-term study on off-the-shelf tracheal graft: A conceptual approach for urgent implantation', *Materials & Design,* 185.

Lee, K. Y. and Mooney, D. J. (2012) 'Alginate: Properties and biomedical applications', *Progress in Polymer Science,* 37(1), pp. 106-126.

Lee, S. J., Heo, D. N., Park, J. S., Kwon, S. K., Lee, J. H., Lee, J. H., Kim, W. D., Kwon, I. K. and Park, S. A. (2015) 'Characterization and preparation of bio-tubular scaffolds for fabricating artificial vascular grafts by combining electrospinning and a 3D printing system', *Physical chemistry chemical physics : PCCP,* 17(5), pp. 2996-2999.

Lejay, A., Colvard, B., Magnus, L., Dion, D., Georg, Y., Papillon, J., Thaveau, F., Geny, B., Swanström, L., Heim, F. and Chakfé, N. (2018) 'Explanted Vascular and Endovascular Graft Analysis: Where Do We Stand and What Should We Do?', *European Journal of Vascular and Endovascular Surgery,* 55(4), pp. 567-576.

Lejay, A., Geny, B., Kolh, P. and Chakfé, N. (2019) 'Effects of Aortic Graft Implantation on Heart and Downstream Vessels: An Artery is not a Rigid Pipe', *European Journal of Vascular & Endovascular Surgery,* 58(4), pp. 477-478.

Levato, R., Dudaryeva, O., Garciamendez-Mijares, C. E., Kirkpatrick, B. E., Rizzo, R., Schimelman, J., Anseth, K. S., Chen, S., Zenobi-Wong, M. and Zhang, Y. S. (2023) 'Light-based vat-polymerization bioprinting', *Nature Reviews Methods Primers,* 3(1), pp. 47.

Li, H., Tan, C. and Li, L. (2018) 'Review of 3D printable hydrogels and constructs', *Materials & Design,* 159, pp. 20-38.

Lin, M., Firoozi, N., Tsai, C.-T., Wallace, M. B. and Kang, Y. (2019) '3D-printed flexible polymer stents for potential applications in inoperable esophageal malignancies', *Acta Biomaterialia,* 83, pp. 119-129.

Liu, H., Zhou, H., Lan, H., Liu, T., Liu, X. and Yu, H. (2017) '3D Printing of Artificial Blood Vessel: Study on Multi-Parameter Optimization Design for Vascular Molding Effect in Alginate and Gelatin', *Micromachines,* 8(8), pp. 237.

London, G. M. and Pannier, B. (2010) 'Arterial functions: how to interpret the complex physiology', *Nephrology Dialysis Transplantation,* 25(12), pp. 3815-3823.

Macrae, R. A., Miller, K. and Doyle, B. J. (2016) 'Methods in Mechanical Testing of Arterial Tissue: A Review', *Strain,* 52(5), pp. 380-399.

Marra, S. P., Kennedy, F. E., Kinkaid, J. N. and Fillinger, M. F. (2006) 'Elastic and rupture properties of porcine aortic tissue measured using inflation testing', *Cardiovascular engineering (Dordrecht, Netherlands),* 6(4), pp. 123-131.

Martinez-Garcia, F. D., Fischer, T., Hayn, A., Mierke, C. T., Burgess, J. K. and Harmsen, M. C. (2022) 'A Beginner’s Guide to the Characterization of Hydrogel Microarchitecture for Cellular Applications', *Gels,* 8(9), pp. 535.

Mazzoccoli, J. P., Feke, D. L., Baskaran, H. and Pintauro, P. N. (2010) 'Mechanical and cell viability properties of crosslinked low-and high-molecular weight poly (ethylene glycol) diacrylate blends', *Journal of Biomedical Materials Research Part A: An Official Journal of The Society for Biomaterials, The Japanese Society for Biomaterials, and The Australian Society for Biomaterials and the Korean Society for Biomaterials,* 93(2), pp. 558-566.

Meekel, J. P., Mattei, G., Costache, V. S., Balm, R., Blankensteijn, J. D. and Yeung, K. K. (2019) 'A multilayer micromechanical elastic modulus measuring method in ex vivo human aneurysmal abdominal aortas', *Acta Biomaterialia,* 96, pp. 345-353.

Melchels, F. P. W., Feijen, J. and Grijpma, D. W. (2009) 'A poly(d,l-lactide) resin for the preparation of tissue engineering scaffolds by stereolithography', *Biomaterials,* 30(23), pp. 3801-3809.

Melchiorri, A. J., Hibino, N., Best, C., Yi, T., Lee, Y., Kraynak, C., Kimerer, L. K., Krieger, A., Kim, P. and Breuer, C. K. (2016) '3D-printed biodegradable polymeric vascular grafts', *Advanced healthcare materials,* 5(3), pp. 319-325.

Merceron, T. K. and Murphy, S. V. (2015) 'Chapter 14 - Hydrogels for 3D Bioprinting Applications', in Atala, A. and Yoo, J.J. (eds.) *Essentials of 3D Biofabrication and Translation*. Boston: Academic Press, pp. 249-270.

Mi, H.-Y., Jiang, Y., Jing, X., Enriquez, E., Li, H., Li, Q. and Turng, L.-S. (2019) 'Fabrication of triple-layered vascular grafts composed of silk fibers, polyacrylamide hydrogel, and polyurethane nanofibers with biomimetic mechanical properties', *Materials Science & Engineering C,* 98, pp. 241-249.

Michael Lee, J. and J. Wilson, G. (1986) 'Anisotropic tensile viscoelastic properties of vascular graft materials tested at low strain rates', *Biomaterials,* 7(6), pp. 423-431.

Miller, K. S., Edelstein, L., Connizzo, B. K. and Soslowsky, L. J. (2012) 'Effect of preconditioning and stress relaxation on local collagen fiber re-alignment: inhomogeneous properties of rat supraspinatus tendon.(Author abstract)(Report)', *Journal of Biomechanical Engineering,* 134(3), pp. 31007.

Millik, S. C., Dostie, A. M., Karis, D. G., Smith, P. T., McKenna, M., Chan, N., Curtis, C. D., Nance, E., Theberge, A. B. and Nelson, A. (2019) '3d printed coaxial nozzles for the extrusion of hydrogel tubes toward modeling vascular endothelium', *3D printed coaxial nozzles for the extrusion of hydrogel tubes toward modeling vascular endothelium,* 11(4), pp. 045009.

Miramini, S., Fegan, K. L., Green, N. C., Espino, D. M., Zhang, L. and Thomas-Seale, L. E. J. (2020) 'The status and challenges of replicating the mechanical properties of connective tissues using additive manufacturing', *Journal of the Mechanical Behavior of Biomedical Materials,* 103.

Mistry, P., Aied, A., Alexander, M., Shakesheff, K., Bennett, A. and Yang, J. (2017) 'Bioprinting Using Mechanically Robust Core–Shell Cell-Laden Hydrogel Strands', *Macromolecular Bioscience,* 17(6), pp. 1600472.

Mitsui, T., Maeta, H., Fukuda, I., Ijima, H., Okamura, K., Sakai, A., Sakurai, J. and Hori, M. (1986) 'Left ventricular hypertrophy due to aortic bypass grafting with a long prosthesis', *Journal of Cardiovascular Surgery,* 27(2), pp. 201-206.

Mohan, D. and Melvin, J. W. (1983) 'Failure properties of passive human aortic tissue. II—Biaxial tension tests', *Journal of Biomechanics,* 16(1), pp. 31,39-37,44.

Mondschein, R. J., Kanitkar, A., Williams, C. B., Verbridge, S. S. and Long, T. E. (2017) 'Polymer structure-property requirements for stereolithographic 3D printing of soft tissue engineering scaffolds', *Biomaterials,* 140, pp. 170-188.

Mørch, Y. A., Donati, I., Strand, B. L. and Skjåk-Braek, G. (2006) 'Effect of Ca2+, Ba2+, and Sr2+ on alginate microbeads', *Biomacromolecules,* 7(5), pp. 1471-1480.

Mørch, Y. A., Qi, M., Gundersen, P. O. M., Formo, K., Lacik, I., Skjåk-Braek, G., Oberholzer, J. and Strand, B. L. (2012) 'Binding and leakage of barium in alginate microbeads', *Journal of biomedical materials research. Part A,* 100(11), pp. 2939-2947.

Munoz-Pinto, D. J., Jimenez-Vergara, A. C., Gharat, T. P. and Hahn, M. S. (2015) 'Characterization of sequential collagen-poly(ethylene glycol) diacrylate interpenetrating networks and initial assessment of their potential for vascular tissue engineering', *Biomaterials,* 40, pp. 32-42.

Nguyen, Q. T., Hwang, Y., Chen, A. C., Varghese, S. and Sah, R. L. (2012) 'Cartilage-like mechanical properties of poly (ethylene glycol)-diacrylate hydrogels', *Biomaterials,* 33(28), pp. 6682-6690.

Ni, R., Qian, B., Liu, C., Liu, X. and Qiu, J. (2018) 'A cross-linking strategy with moderated pre-polymerization of resin for stereolithography', *RSC Advances,* 8(52), pp. 29583-29588.

Nikkhah, M., Edalat, F., Manoucheri, S. and Khademhosseini, A. (2012) 'Engineering microscale topographies to control the cell–substrate interface', *Biomaterials,* 33(21), pp. 5230-5246.

Niklason, L., Gao, J., Abbott, W. and Hirschi, K. (1999) 'Functional arteries grown in vitro', *Science,* 284(5413), pp. 489-93.

Norman, P. E. and Powell, J. T. (2007) 'Abdominal Aortic Aneurysm', *Circulation,* 115(22), pp. 2865-2869.

Nunamaker, E. A., Otto, K. J. and Kipke, D. R. (2011) 'Investigation of the material properties of alginate for the development of hydrogel repair of dura mater', *Journal of the Mechanical Behavior of Biomedical Materials,* 4(1), pp. 16-33.

Nunn, D. B., Carter, M. M., Donohue, M. T. and Hudgins, P. C. (1990) 'Postoperative dilation of knitted Dacron aortic bifurcation graft', *Journal of Vascular Surgery,* 12(3), pp. 291-297.

O'Connell, C. D., Zhang, B., Onofrillo, C., Duchi, S., Blanchard, R., Quigley, A., Bourke, J., Gambhir, S., Kapsa, R., Di Bella, C., Choong, P. and Wallace, G. G. (2018) 'Tailoring the mechanical properties of gelatin methacryloyl hydrogels through manipulation of the photocrosslinking conditions', *Soft Matter,* 14(11), pp. 2142-2151.

Obrien, T., Morris, L. and McGloughlin, T. (2008) 'Evidence suggests rigid aortic grafts increase systolic blood pressure: Results of a preliminary study', *Medical Engineering and Physics,* 30(1), pp. 109-115.

Ochbaum, G., Davidovich-Pinhas, M. and Bitton, R. (2018) 'Tuning the mechanical properties of alginate–peptide hydrogels', *Soft Matter,* 14(21), pp. 4364-4373.

Olivas, G. I. and Barbosa-Cánovas, G. V. (2008) 'Alginate–calcium films: Water vapor permeability and mechanical properties as affected by plasticizer and relative humidity', *LWT - Food Science and Technology,* 41(2), pp. 359-366.

Panalytical, M. 2016. A Basic Introduction to Rheology. Whitepaper.

Pande, R. L. and Beckman, J. A. (2013) 'Chapter 37 - Pathophysiology, Epidemiology, and Prognosis of Aortic Aneurysms', in Creager, M.A., Beckman, J.A. and Loscalzo, J. (eds.) *Vascular Medicine: A Companion to Braunwald's Heart Disease (Second Edition)*. Philadelphia: W.B. Saunders, pp. 457-470.

Parak, A., Pradeep, P., du Toit, L. C., Kumar, P., Choonara, Y. E. and Pillay, V. (2019) 'Functionalizing bioinks for 3D bioprinting applications', *Drug Discovery Today,* 24(1), pp. 198-205.

Park, J.-H., Yoon, J.-K., Lee, J. B., Shin, Y. M., Lee, K.-W., Bae, S.-W., Lee, J., Yu, J., Jung, C.-R., Youn, Y.-N., Kim, H.-Y. and Kim, D.-H. (2019) 'Experimental Tracheal Replacement Using 3-dimensional Bioprinted Artificial Trachea with Autologous Epithelial Cells and Chondrocytes', *Scientific reports,* 9(1), pp. 2103-2103.

Pashneh-Tala, S., Macneil, S. and Claeyssens, F. (2016) 'The Tissue- Engineered Vascular Graft- Past, Present, and Future', *Tissue Engineering, Part B: Reviews,* 22(1), pp. 68-100.

Pena, J. A., Corral, V., Martinez, M. A. and Pena, E. (2018) 'Over length quantification of the multiaxial mechanical properties of the ascending, descending and abdominal aorta using Digital Image Correlation.(Report)(Author abstract)', *Journal of the Mechanical Behavior of Biomedical Materials,* 77, pp. 434.

Pennel, T. and Zilla, P. (2019) 'Clinical Applications and Limitations of Vascular Grafts', in Walpoth, B., Bergmeister, H., Bowlin, G., Kong, D., Rotmans, J. and Zilla, P. (eds.) *Tissue-Engineered Vascular Grafts*. Cham: Springer International Publishing, pp. 1-32.

Pereira, R., Carvalho, A., Vaz, D. C., Gil, M. H., Mendes, A. and Bártolo, P. (2013) 'Development of novel alginate based hydrogel films for wound healing applications', *International Journal of Biological Macromolecules,* 52, pp. 221-230.

Pereira, R. F. and Bártolo, P. J. (2015) '3D bioprinting of photocrosslinkable hydrogel constructs', *Journal of Applied Polymer Science,* 132(48).

Perlin, L., MacNeil, S. and Rimmer, S. (2008) 'Production and performance of biomaterials containing RGD peptides', *Soft Matter,* 4(12), pp. 2331-2349.

Piras, C. C. and Smith, D. K. (2020) 'Multicomponent polysaccharide alginate-based bioinks', *Journal of Materials Chemistry B,* 8(36), pp. 8171-8188.

Place, E. S., Rojo, L., Gentleman, E., Sardinha, J. P. and Stevens, M. M. (2011) 'Strontium- and Zinc-Alginate Hydrogels for Bone Tissue Engineering', *Tissue Engineering Part A,* 17(21-22), pp. 2713-2722.

Prager, M., Polterauer, P., Böhmig, H.-J., Wagner, O., Fügl, A., Kretschmer, G., Plohner, M., Nanobashvili, J. and Huk, I. (2001) 'Collagen versus gelatin-coated dacron versus stretch polytetrafluoroethylene in abdominal aortic bifurcation graft surgery: Results of a seven-year prospective, randomized multicenter trial', *Surgery,* 130(3), pp. 408-414.

Puza, F. and Lienkamp, K. (2022) '3D Printing of Polymer Hydrogels—From Basic Techniques to Programmable Actuation', *Advanced Functional Materials,* 32(39), pp. 2205345.

Qian, L. and Zhao, H. (2018) 'Nanoindentation of Soft Biological Materials', *Micromachines,* 9(12).

Raghavan, M. L., Webster, M. W. and Vorp, D. A. (1996) 'Ex vivo biomechanical behavior of abdominal aortic aneurysm: Assessment using a new mathematical model', *Annals of Biomedical Engineering,* 24(5), pp. 573-582.

Rahbari, A., Montazerian, H., Davoodi, E. and Homayoonfar, S. (2017) 'Predicting permeability of regular tissue engineering scaffolds: scaling analysis of pore architecture, scaffold length, and fluid flow rate effects', *Computer methods in biomechanics and biomedical engineering,* 20(3), pp. 231-241.

Rekowska, N., Arbeiter, D., Seitz, H., Mau, R., Riess, A., Eickner, T., Grabow, N. and Teske, M. (2022) 'The influence of PEGDA's molecular weight on its mechanical properties in the context of biomedical applications', *Current Directions in Biomedical Engineering,* 8(2), pp. 181-184.

Ren, X., Feng, Y., Guo, J., Wang, H., Li, Q., Yang, J., Hao, X., Lv, J., Ma, N. and Li, W. (2015) 'Surface modification and endothelialization of biomaterials as potential scaffolds for vascular tissue engineering applications', *Chemical Society Reviews,* 44(15), pp. 5680-5742.

Rezvani-Sharif, A., Tafazzoli-Shadpour, M. and Avolio, A. (2019) 'Mechanical Characterization of the Lamellar Structure of Human Abdominal Aorta in the Development of Atherosclerosis: An Atomic Force Microscopy Study', *Cardiovascular Engineering and Technology,* 10(1), pp. 181.

Roach, M. R. and Burton, A. C. (1957) 'The reason for the shape of the distensibility curves of arteries', *Canadian journal of biochemistry and physiology,* 35(8), pp. 681-690.

Robinson, S. S., Aubin, C. A., Wallin, T. J., Gharaie, S., Xu, P. A., Wang, K., Dunham, S. N., Mosadegh, B. and Shepherd, R. F. (2018) 'Stereolithography for personalized left atrial appendage occluders', *Advanced materials technologies,* 3(12), pp. 1800233.

Rocco, K. A., Maxfield, M. W., Best, C. A., Dean, E. W. and Breuer, C. K. (2014) 'In vivo applications of electrospun tissue-engineered vascular grafts: a review', *Tissue engineering. Part B, Reviews,* 20(6), pp. 628-640.

Rosero, E. B., Peshock, R. M., Khera, A., Clagett, P., Lo, H. and Timaran, C. H. (2011) 'Sex, race, and age distributions of mean aortic wall thickness in a multiethnic population-based sample', *Journal of Vascular Surgery,* 53(4), pp. 950-957.

Rowley, J. A., Madlambayan, G. and Mooney, D. J. (1999) 'Alginate hydrogels as synthetic extracellular matrix materials', *Biomaterials,* 20(1), pp. 45-53.

Rylski, B., Desjardins, B., Moser, W., Bavaria, J. E. and Milewski, R. K. (2014) 'Gender-related changes in aortic geometry throughout life†', *European Journal of Cardio-Thoracic Surgery,* 45(5), pp. 805-811.

Sacks, M. (2000) 'Biaxial Mechanical Evaluation of Planar Biological Materials', *Journal of Elasticity,* 61(1-3), pp. 199-246.

Saini, J., Dowling, L., Kennedy, J. and Trimble, D. (2020) 'Investigations of the mechanical properties on different print orientations in SLA 3D printed resin', *Proceedings of the Institution of Mechanical Engineers, Part C: Journal of Mechanical Engineering Science,* 234(11), pp. 2279-2293.

Sameni, F., Ozkan, B., Zarezadeh, H., Karmel, S., Engstrøm, D. S. and Sabet, E. (2022) 'Hot Lithography Vat Photopolymerisation 3D Printing: Vat Temperature vs. Mixture Design', *Polymers,* 14(15), pp. 2988.

Sandvig, I., Karstensen, K., Rokstad, A. M., Aachmann, F. L., Formo, K., Sandvig, A., Skjåk-Bræk, G. and Strand, B. L. (2015) 'RGD-peptide modified alginate by a chemoenzymatic strategy for tissue engineering applications', *Journal of Biomedical Materials Research Part A,* 103(3), pp. 896-906.

Sarker, M., Izadifar, M., Schreyer, D. and Chen, X. (2018) 'Influence of ionic crosslinkers (Ca 2+ /Ba 2+ /Zn 2+ ) on the mechanical and biological properties of 3D Bioplotted Hydrogel Scaffolds', *Journal of Biomaterials Science, Polymer Edition,* 29(10), pp. 1126-1154.

Schoen, F. J., Fioretta, E. S., Mallone, A., Smits, A. I. P. M., Klouda, L. and Bouten, C. V. C. (2019) 'Vascular Tissue Engineering: Pathological Considerations, Mechanisms, and Translational Implications', in Walpoth, B., Bergmeister, H., Bowlin, G., Kong, D., Rotmans, J. and Zilla, P. (eds.) *Tissue-Engineered Vascular Grafts*. Cham: Springer International Publishing, pp. 1-41.

Schroeder, T. V., Eldrup, N., Just, S., Hansen, M., Nyhuus, B. and Sillesen, H. (2009) 'Dilatation of Aortic Grafts Over Time: What to Expect and When to be Concerned', *Seminars in Vascular Surgery,* 22(2), pp. 119-124.

Schwab, A., Levato, R., D'Este, M., Piluso, S., Eglin, D. and Malda, J. (2020) 'Printability and Shape Fidelity of Bioinks in 3D Bioprinting', *Chemical Reviews,* 120(19), pp. 11028-11055.

Seo, H., Heo, S. G., Lee, H. and Yoon, H. (2017) 'Preparation of PEG materials for constructing complex structures by stereolithographic 3D printing', *RSC Advances,* 7(46), pp. 28684-28688.

Seo, J. W., Kim, G. M., Choi, Y., Cha, J. M. and Bae, H. (2022) 'Improving printability of digital-light-processing 3D bioprinting via photoabsorber pigment adjustment', *International Journal of Molecular Sciences,* 23(10), pp. 5428.

Seok, J. M., Oh, S. H., Lee, S. J., Lee, J. H., Kim, W. D., Park, S.-H., Nam, S. Y., Shin, H. and Park, S. A. (2019) 'Fabrication and characterization of 3D scaffolds made from blends of sodium alginate and poly(vinyl alcohol)', *Materials Today Communications,* 19, pp. 56-61.

Shadwick, R. (1998) 'Elasticity in arteries', *American Scientist,* 86(6), pp. 535-541.

Sherifova, S. and Holzapfel, G. A. (2019) 'Biomechanics of aortic wall failure with a focus on dissection and aneurysm: A review', *Acta Biomaterialia,* 99, pp. 1-17.

Shi, P., Laude, A. and Yeong, W. Y. (2017) 'Investigation of cell viability and morphology in 3D bio-printed alginate constructs with tunable stiffness', *Journal of Biomedical Materials Research Part A,* 105(4), pp. 1009-1018.

Shiraev, T., Barrett, S., Heywood, S., Mirza, W., Hunter-Dickson, M., Bradshaw, C., Hardman, D., Neilson, W. and Bradshaw, S. (2019) 'Incidence, Management, and Outcomes of Aortic Graft Infection', *Annals of Vascular Surgery,* 59, pp. 73-83.

Silva, R., Singh, R., Sarker, B., Papageorgiou, D. G., Juhasz-Bortuzzo, J. A., Roether, J. A., Cicha, I., Kaschta, J., Schubert, D. W., Chrissafis, K., Detsch, R. and Boccaccini, A. R. (2018) 'Hydrogel matrices based on elastin and alginate for tissue engineering applications', *International Journal of Biological Macromolecules,* 114, pp. 614-625.

Silver, F., Snowhill, P. and Foran, D. (2003) 'Mechanical Behavior of Vessel Wall: A Comparative Study of Aorta, Vena Cava, and Carotid Artery', *Annals of Biomedical Engineering,* 31(7), pp. 793-803.

Singh, C., Wong, S. C. and Wang, X. (2015) 'Medical Textiles as Vascular Implants and Their Success to Mimic Natural Arteries', *Journal of Functional Biomaterials,* 6(3).

Skardal, A., Zhang, J., McCoard, L., Xu, X., Oottamasathien, S. and Prestwich, G. D. (2010) 'Photocrosslinkable hyaluronan-gelatin hydrogels for two-step bioprinting.(Report)', *Tissue Engineering, Part A: Tissue Engineering,* 16(8), pp. 2675.

Skardal, A., Zhang, J. and Prestwich, G. D. (2010) 'Bioprinting vessel-like constructs using hyaluronan hydrogels crosslinked with tetrahedral polyethylene glycol tetracrylates', *Biomaterials,* 31(24), pp. 6173-6181.

Skoog, S. A., Goering, P. L. and Narayan, R. J. (2014) 'Stereolithography in tissue engineering', *Journal of Materials Science: Materials in Medicine,* 25(3), pp. 845-856.

Sokolis, D. P. (2007) 'Passive mechanical properties and structure of the aorta: segmental analysis', *Acta Physiologica,* 190(4), pp. 277-289.

Sokolis, D. P., Boudoulas, H. and Karayannacos, P. E. (2002) 'Assessment of the aortic stress–strain relation in uniaxial tension', *Journal of Biomechanics,* 35(9), pp. 1213-1223.

Soliman, S., Laurent, J., Kalenjian, L., Burnette, K., Hedberg, B. and La Francesca, S. (2019) 'A multilayer scaffold design with spatial arrangement of cells to modulate esophageal tissue growth', *Journal of Biomedical Materials Research - Part B Applied Biomaterials,* 107(2), pp. 324-331.

Sommer, G. (2008) 'Mechanical properties of healthy and diseased human arteries', *TU Graz*.

Sommer, G., Gasser, T. C., Regitnig, P., Auer, M. and Holzapfel, G. A. (2008) 'Dissection properties of the human aortic media: an experimental study.(Author abstract)(Report)', *Journal of Biomechanical Engineering,* 130(2), pp. 21007.

Spadaccio, C., Nappi, F., Al-Attar, N., Sutherland, F. W., Acar, C., Nenna, A., Trombetta, M., Chello, M. and Rainer, A. (2016) 'Old Myths, New Concerns: the Long-Term Effects of Ascending Aorta Replacement with Dacron Grafts. Not All That Glitters Is Gold', *Journal of Cardiovascular Translational Research,* 9(4), pp. 334-342.

Spronck, B. and Humphrey, J. (2019) 'Arterial Stiffness: Different Metrics, Different Meanings', *Journal of biomechanical engineering,* 141(9).

Stowell, C. E. T. and Wang, Y. (2018) 'Quickening: Translational design of resorbable synthetic vascular grafts', *Biomaterials,* 173, pp. 71-86.

Sun, J.-Y., Zhao, X., Illeperuma, W. R. K., Chaudhuri, O., Oh, K. H., Mooney, D. J., Vlassak, J. J. and Suo, Z. (2012) 'Highly stretchable and tough hydrogels', *Nature,* 489(7414), pp. 133-136.

Sun, J. and Tan, H. (2013) 'Alginate- Based Biomaterials for Regenerative Medicine Applications', *Materials (Basel, Switzerland),* 6(4), pp. 1285-1309.

Sun, Z., Wong, Y. H. and Yeong, C. H. (2023) 'Patient-Specific 3D-Printed Low-Cost Models in Medical Education and Clinical Practice', *Micromachines,* 14(2), pp. 464.

Suntornnond, R., Tan, E. Y. S., An, J. and Chua, C. K. (2017) 'A highly printable and biocompatible hydrogel composite for direct printing of soft and perfusable vasculature-like structures', *Scientific reports,* 7(1), pp. 16902-16902.

Tai, N. R., Salacinski, H. J., Edwards, A., Hamilton, G. and Seifalian, A. M. (2000) 'Compliance properties of conduits used in vascular reconstruction', *BJS (British Journal of Surgery),* 87(11), pp. 1516-1524.

Takami, Y., Tajima, K., Kato, W., Fujii, K., Hibino, M., Munakata, H., Uchida, K. and Sakai, Y. (2012) 'Long-term size follow-up of knitted Dacron grafts (Gelseal™) used in the ascending aorta', *Interactive CardioVascular and Thoracic Surgery,* 14(5), pp. 529-531.

Tan, E. Y. S. and Yeong, W. Y. (2015) 'Concentric bioprinting of alginate-based tubular constructs using multi-nozzle extrusion-based technique', *International Journal of Bioprinting,* 1(1), pp. 49-56.

Tan, L., Ang, H. and Huang, Y. (2020) 'Bioresorbable Polymeric Scaffold in Cardiovascular Applications', *International Journal of Molecular Sciences,* 21(10), pp. 3444.

Tomal, W. and Ortyl, J. (2020) 'Water-Soluble Photoinitiators in Biomedical Applications', *Polymers,* 12(5), pp. 1073.

Tong, J., Cohnert, T., Regitnig, P., Kohlbacher, J., Birner-Gruenberger, R., Schriefl, A. J., Sommer, G. and Holzapfel, G. A. (2014) 'Variations of dissection properties and mass fractions with thrombus age in human abdominal aortic aneurysms', *Journal of Biomechanics,* 47(1), pp. 14-23.

Torres, I. and Luccia, N. D. (2018) 'Artificial vascular models for endovascular training (3D printing)', *Innovative Surgical Sciences,* 3(3), pp. 225-234.

Townsend, N., Kazakiewicz, D., Lucy Wright, F., Timmis, A., Huculeci, R., Torbica, A., Gale, C. P., Achenbach, S., Weidinger, F. and Vardas, P. (2022) 'Epidemiology of cardiovascular disease in Europe', *Nature Reviews Cardiology,* 19(2), pp. 133-143.

Tremblay, D., Zigras, T., Cartier, R., Leduc, L., Butany, J., Mongrain, R. and Leask, R. L. (2009) 'A Comparison of Mechanical Properties of Materials Used in Aortic Arch Reconstruction', *The Annals of Thoracic Surgery,* 88(5), pp. 1484-1491.

Tsamis, A., Krawiec, J. T. and Vorp, D. A. (2013) 'Elastin and collagen fibre microstructure of the human aorta in ageing and disease: a review', *Journal of the Royal Society, Interface,* 10(83), pp. 20121004-20121004.

Tubaldi, E., Ferrari, G., Balasubramanian, P. and Amabili, M. 'Dynamic Behaviour of a Dacron Aortic Graft'. Volume 3: Biomedical and Biotechnology Engineering.

Unkovskiy, A., Bui, P. H.-B., Schille, C., Geis-Gerstorfer, J., Huettig, F. and Spintzyk, S. (2018) 'Objects build orientation, positioning, and curing influence dimensional accuracy and flexural properties of stereolithographically printed resin', *Dental Materials,* 34(12), pp. e324-e333.

Utech, S. and Boccaccini, A. R. (2016) 'A review of hydrogel- based composites for biomedical applications: enhancement of hydrogel properties by addition of rigid inorganic fillers', *Journal of Materials Science,* 51(1), pp. 271-310.

Uzcategui, A. C., Muralidharan, A., Ferguson, V. L., Bryant, S. J. and McLeod, R. R. (2018) 'Understanding and Improving Mechanical Properties in 3D printed Parts Using a Dual-Cure Acrylate-Based Resin for Stereolithography', *Advanced Engineering Materials,* 20(12), pp. 1800876.

Vahabli, E., Mann, J., Heidari, B. S., Lawrence-Brown, M., Norman, P., Jansen, S., De-Juan-Pardo, E. and Doyle, B. (2022) 'The Technological Advancement to Engineer Next-Generation Stent-Grafts: Design, Material, and Fabrication Techniques', *Advanced healthcare materials,* 11(13), pp. 2200271.

Vallabhaneni, S. R., Gilling-Smith, G. L., How, T. V., Carter, S. D., Brennan, J. A. and Harris, P. L. (2004) 'Heterogeneity of Tensile Strength and Matrix Metalloproteinase Activity in the Wall of Abdominal Aortic Aneurysms', *The Journal of Endovascular Therapy,* 11(4), pp. 494-502.

Vande Geest, J. P., Sacks, M. S. and Vorp, D. A. (2004) 'Age dependency of the biaxial biomechanical behavior of human abdominal aorta.(Author Abstract)', *Journal of Biomechanical Engineering,* 126(6), pp. 815.

Vande Geest, J. P., Sacks, M. S. and Vorp, D. A. (2006) 'The effects of aneurysm on the biaxial mechanical behavior of human abdominal aorta', *Journal of Biomechanics,* 39(7), pp. 1324-1334.

Vardoulis, O., Coppens, E., Martin, B., Reymond, P., Tozzi, P. and Stergiopulos, N. (2011) 'Impact of Aortic Grafts on Arterial Pressure: A Computational Fluid Dynamics Study', *European Journal of Vascular & Endovascular Surgery,* 42(5), pp. 704-710.

Villard, C. and Hultgren, R. (2018) 'Abdominal aortic aneurysm: Sex differences', *Maturitas,* 109, pp. 63-69.

Virani, S. S., Alonso, A., Benjamin, E. J., Bittencourt, M. S.*, et al.* (2020) 'Heart Disease and Stroke Statistics—2020 Update: A Report From the American Heart Association', *Circulation,* 141(9), pp. e139-e596.

Vorp, D. A., Lee, P. C., Wang, D. H. J., Makaroun, M. S., Nemoto, E. M., Ogawa, S. and Webster, M. W. (2001) 'Association of intraluminal thrombus in abdominal aortic aneurysm with local hypoxia and wall weakening', *Journal of Vascular Surgery,* 34(2), pp. 291-299.

Vorp, D. A., Raghavan, M. L., Muluk, S. C., Makaroun, M. S., Steed, D. L., Shapiro, R. and Webster, M. W. 1996. Wall strength and stiffness of aneurysmal and nonaneurysmal abdominal aorta. *Annals of the New York Academy of Sciences.*

Walden, R., L'Italien, G. J., Megerman, J. and Abbott, W. M. (1980) 'Matched Elastic Properties and Successful Arterial Grafting', *Archives of Surgery,* 115(10), pp. 1166-1169.

Walraevens, J., Willaert, B., De Win, G., Ranftl, A., De Schutter, J. and Sloten, J. V. (2008) 'Correlation between compression, tensile and tearing tests on healthy and calcified aortic tissues', *Medical Engineering and Physics,* 30(9), pp. 1098-1104.

Wang, D., Xu, Y., Li, Q. and Turng, L.-S. (2020a) 'Artificial small-diameter blood vessels: materials, fabrication, surface modification, mechanical properties, and bioactive functionalities', *Journal of Materials Chemistry B,* 8(9), pp. 1801-1822.

Wang, R., de Kort, B. J., Smits, A. I. P. M. and Weiss, A. S. (2020b) 'Elastin in Vascular Grafts', in Walpoth, B.H., Bergmeister, H., Bowlin, G.L., Kong, D., Rotmans, J.I. and Zilla, P. (eds.) *Tissue-Engineered Vascular Grafts*. Cham: Springer International Publishing, pp. 379-410.

Wang, W., Guo, L., Yu, Y., Chen, Z., Zhou, R. and Yuan, Z. (2015) 'Peptide REDV-modified polysaccharide hydrogel with endothelial cell selectivity for the promotion of angiogenesis', *Journal of Biomedical Materials Research Part A,* 103(5), pp. 1703-1712.

Waton, S., Johal, A., Li, Q., Atkins, E., Cromwell, D. A., Williams, R., Harkin, D. W. and Pherwani, A. D. (2023) *National Vascular Registry: 2023 State of the Nation Report*, London: The Royal College of Surgeons of England.

Wei, D., Xiao, W., Sun, J., Zhong, M., Guo, L., Fan, H. and Zhang, X. (2015) 'A biocompatible hydrogel with improved stiffness and hydrophilicity for modular tissue engineering assembly', *Journal of Materials Chemistry B,* 3(14), pp. 2753-2763.

Wei, Q., Zhou, J., An, Y., Li, M., Zhang, J. and Yang, S. (2023) 'Modification, 3D printing process and application of sodium alginate based hydrogels in soft tissue engineering: A review', *International Journal of Biological Macromolecules,* 232, pp. 123450.

Weinberg, C. B. and Bell, E. (1986) 'A blood vessel model constructed from collagen and cultured vascular cells', *Science (New York, N.Y.),* 231(4736), pp. 397-400.

Wenger, R. and Giraud, M.-N. (2018) '3D Printing Applied to Tissue Engineered Vascular Grafts', *Applied Sciences,* 8(12).

Whale, M., Grodzinsky, A. and Johnson, M. (1996) 'The effect of aging and pressure on the specific hydraulic conductivity of the aortic wall', *Biorheology,* 33(1), pp. 17-44.

Williams, D., Thayer, P., Martinez, H., Gatenholm, E. and Khademhosseini, A. (2018) 'A perspective on the physical, mechanical and biological specifications of bioinks and the development of functional tissues in 3D bioprinting', *Bioprinting,* 9, pp. 19-36.

Williams, D. F. (2008) 'On the mechanisms of biocompatibility', *Biomaterials,* 29(20), pp. 2941-2953.

Wu, J., Hu, C., Tang, Z., Yu, Q., Liu, X. and Chen, H. (2018) 'Tissue-engineered Vascular Grafts: Balance of the Four Major Requirements', *Colloid and Interface Science Communications,* 23, pp. 34-44.

Wu, W., Allen, R. A. and Wang, Y. (2012) 'Fast-degrading elastomer enables rapid remodeling of a cell-free synthetic graft into a neoartery.(TECHNICAL REPORTS)(Report)', *Nature Medicine,* 18(7), pp. 1148.

Xie, F., Cao, H., Ma, L., Hua, X. and Li, C. (2021) 'Biofabrication of controllable tubular calcium alginate hydrogel for tissue engineering', *Journal of Materials Research,* 36(7), pp. 1487-1495.

Xiong, R., Zhang, Z., Chai, W., Huang, Y. and Chrisey, D. B. (2015) 'Freeform drop-on-demand laser printing of 3D alginate and cellular constructs', *Biofabrication,* 7(4), pp. 045011.

Xu, C., Dai, G. and Hong, Y. (2019) 'Recent advances in high-strength and elastic hydrogels for 3D printing in biomedical applications', *Acta Biomaterialia,* 95, pp. 50-59.

Xu, H., Casillas, J., Krishnamoorthy, S. and Xu, C. (2020) 'Effects of Irgacure 2959 and lithium phenyl-2,4,6-trimethylbenzoylphosphinate on cell viability, physical properties, and microstructure in 3D bioprinting of vascular-like constructs', *Biomedical Materials,* 15(5), pp. 055021.

Xue, L. and Greisler, H. P. 2003. Biomaterials in the development and future of vascular grafts.

Yan, J., Chen, F. and Amsden, B. G. (2016) 'Cell sheets prepared via gel–sol transition of calcium RGD–alginate', *Acta Biomaterialia,* 30, pp. 277-284.

Yan, J., Huang, Y. and Chrisey, D. B. (2013) 'Laser-assisted printing of alginate long tubes and annular constructs', *Laser-assisted printing of alginate long tubes and annular constructs,* 5(1), pp. 015002.

Yan, Q., Dong, H., Su, J., Han, J., Song, B., Wei, Q. and Shi, Y. (2018) 'A Review of 3D Printing Technology for Medical Applications', *Engineering,* 4(5), pp. 729-742.

Yang, F., Williams, C. G., Wang, D.-a., Lee, H., Manson, P. N. and Elisseeff, J. (2005) 'The effect of incorporating RGD adhesive peptide in polyethylene glycol diacrylate hydrogel on osteogenesis of bone marrow stromal cells', *Biomaterials,* 26(30), pp. 5991-5998.

Yang, Y., Zhou, Y., Lin, X., Yang, Q. and Yang, G. (2020) 'Printability of external and internal structures based on digital light processing 3D printing technique', *Pharmaceutics,* 12(3), pp. 207.

Yeh, M.-Y., Zhao, J.-Y., Hsieh, Y.-R., Lin, J.-H., Chen, F.-Y., Chakravarthy, R. D., Chung, P.-C., Lin, H.-C. and Hung, S.-C. (2017) 'Reverse thermo-responsive hydrogels prepared from Pluronic F127 and gelatin composite materials', *RSC Advances,* 7(34), pp. 21252-21257.

Yu, C., Schimelman, J., Wang, P., Miller, K. L., Ma, X., You, S., Guan, J., Sun, B., Zhu, W. and Chen, S. (2020) 'Photopolymerizable Biomaterials and Light-Based 3D Printing Strategies for Biomedical Applications', *Chemical Reviews,* 120(19), pp. 10695-10743.

Yu, F., Han, X., Zhang, K., Dai, B., Shen, S., Gao, X., Teng, H., Wang, X., Li, L., Ju, H., Wang, W., Zhang, J. and Jiang, Q. (2018) 'Evaluation of a polyvinyl alcohol-alginate based hydrogel for precise 3D bioprinting', *Journal of Biomedical Materials Research Part A,* 106(11), pp. 2944-2954.

Yu, J., Gu, Y., Du, K. T., Mihardja, S., Sievers, R. E. and Lee, R. J. (2009) 'The effect of injected RGD modified alginate on angiogenesis and left ventricular function in a chronic rat infarct model', *Biomaterials,* 30(5), pp. 751-756.

Yuan, H., Chen, C., Liu, Y., Lu, T. and Wu, Z. (2020) 'Strategies in cell-free tissue-engineered vascular grafts', *Journal of Biomedical Materials Research Part A,* 108(3), pp. 426-445.

Yue, K., Trujillo-de Santiago, G., Alvarez, M. M., Tamayol, A., Annabi, N. and Khademhosseini, A. (2015) 'Synthesis, properties, and biomedical applications of gelatin methacryloyl (GelMA) hydrogels', *Biomaterials,* 73, pp. 254-271.

Zhang, M., Qian, T., Deng, Z. and Hang, F. (2021) '3D printed double-network alginate hydrogels containing polyphosphate for bioenergetics and bone regeneration', *International Journal of Biological Macromolecules,* 188, pp. 639-648.

Zhao, X., Huebsch, N., Mooney, D. J. and Suo, Z. (2010) 'Stress-relaxation behavior in gels with ionic and covalent crosslinks', *Journal of applied physics,* 107(6), pp. 63509-63509.

Zhen, L., Xinda, L., Tao, X. and Lei, Z. (2019) 'Acellular Small-Diameter Tissue-Engineered Vascular Grafts', *Applied sciences,* 9(14), pp. 2864.

Zhijie, W., Mark, J. G. and Naomi, C. C. (2016) 'Viscoelastic Properties of Cardiovascular Tissues', in Mohamed Fathy, E.-A. (ed.) *Viscoelastic and Viscoplastic Materials*. Rijeka: IntechOpen, pp. Ch. 7.

Zhou, Y., Gui, Q., Yu, W., Liao, S., He, Y., Tao, X., Yu, Y. and Wang, Y. (2019) 'Interfacial Diffusion Printing: An Efficient Manufacturing Technique for Artificial Tubular Grafts', *ACS Biomaterials Science & Engineering,* 5(11), pp. 6311-6318.

Zhu, J. (2010) 'Bioactive modification of poly(ethylene glycol) hydrogels for tissue engineering', *Biomaterials,* 31(17), pp. 4639-4656.

Zhu, J., He, P., Lin, L., Jones, D. R. and Marchant, R. E. (2012) 'Biomimetic Poly(ethylene glycol)-Based Hydrogels as Scaffolds for Inducing Endothelial Adhesion and Capillary-Like Network Formation', *Biomacromolecules,* 13(3), pp. 706-713.

Zia, A. W., Liu, R. and Wu, X. (2022) 'Structural design and mechanical performance of composite vascular grafts', *Bio-Design and Manufacturing,* 5(4), pp. 757-785.

Appendix 1: 3D designs used for 3D-printing.

**AutoCAD Inventor tensile test grips and moulds3D models**

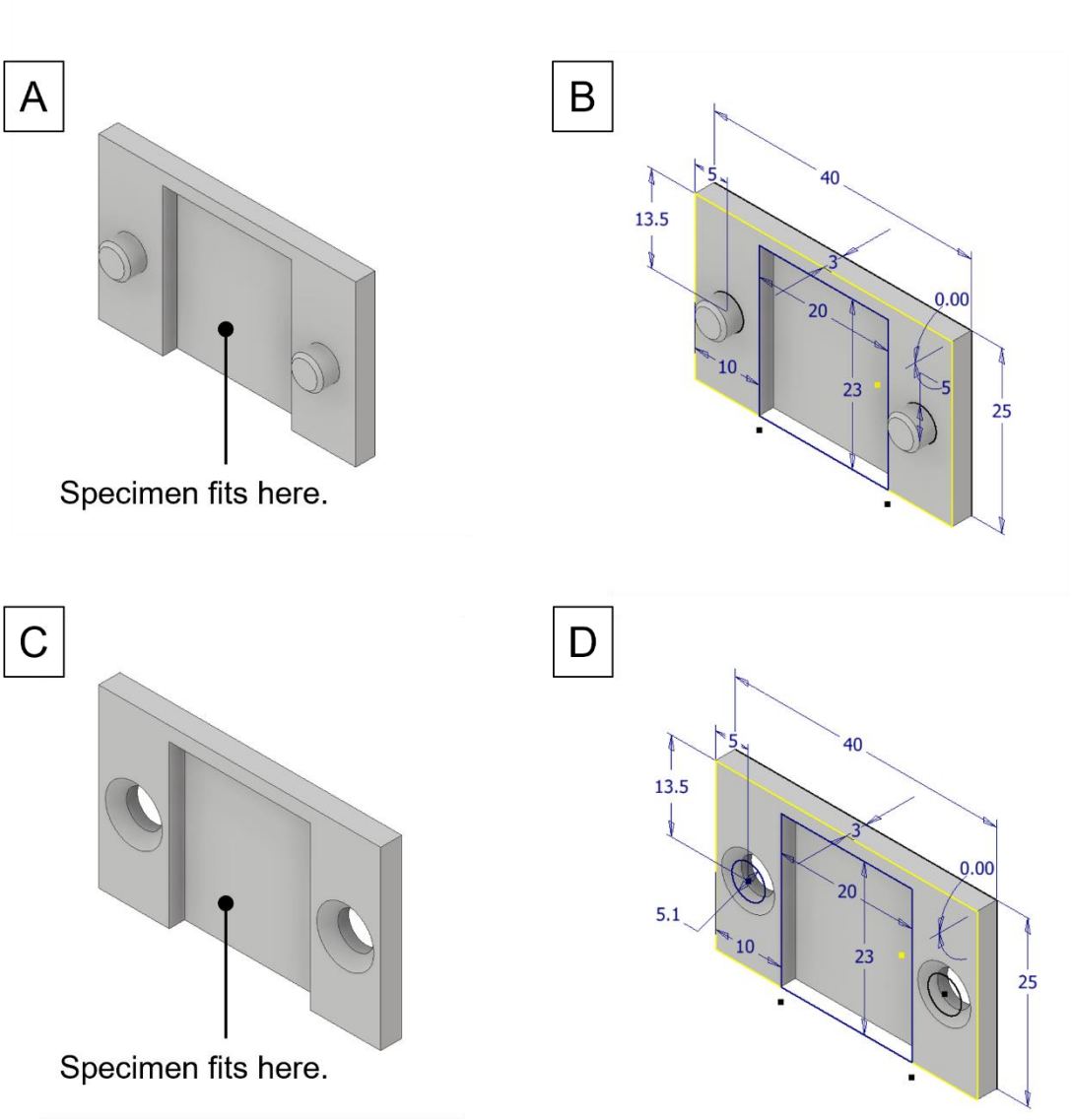


*Autodesk Inventor model of the tensile specimen grip adapter. (A) Pin and (C) Hole parts that fit together sandwiching the specimen in between. (B) and (D) show the dimensions in mm of the respective pin-hole grip parts.*

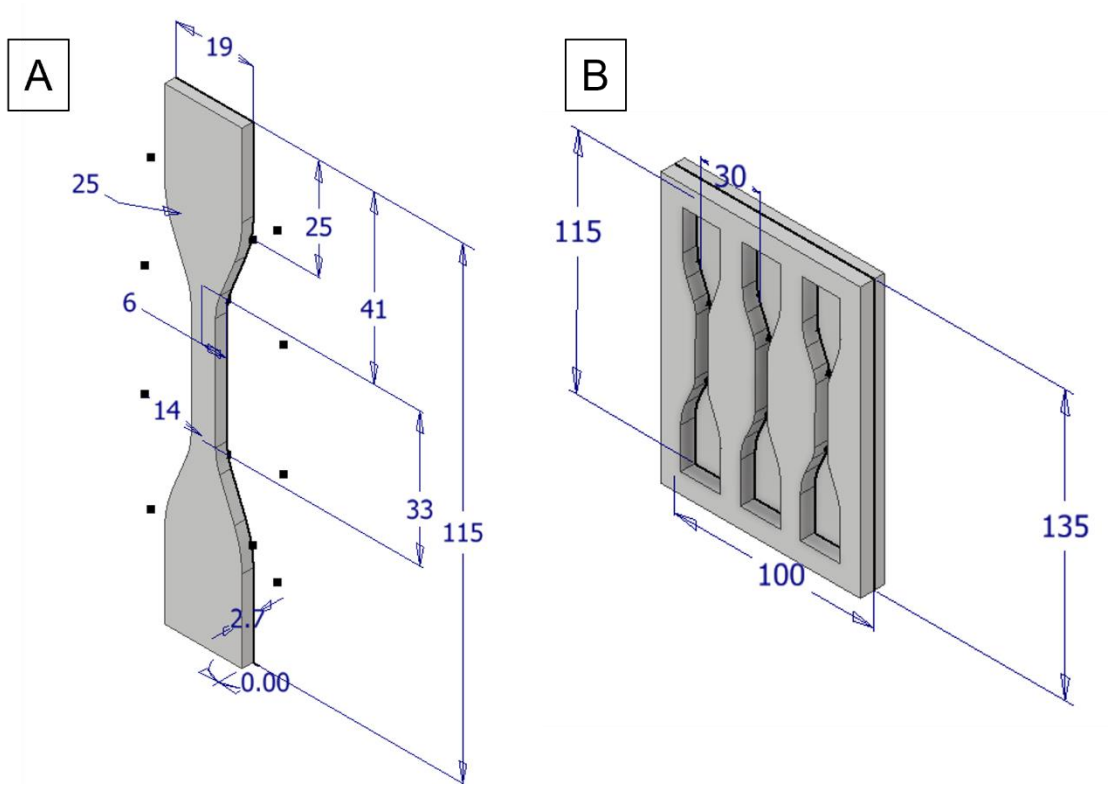


*Autodesk inventor model of (A) the tensile specimen designed according to Type V of the ASTM D638 Standard test method for the tensile properties of plastics, and (B) the corresponding tensile specimen mould based on the same dimensions shown in (A). Dimensions are in mm.*

**AutoCAD Inventor aortic-like tubular conduits 3D models**

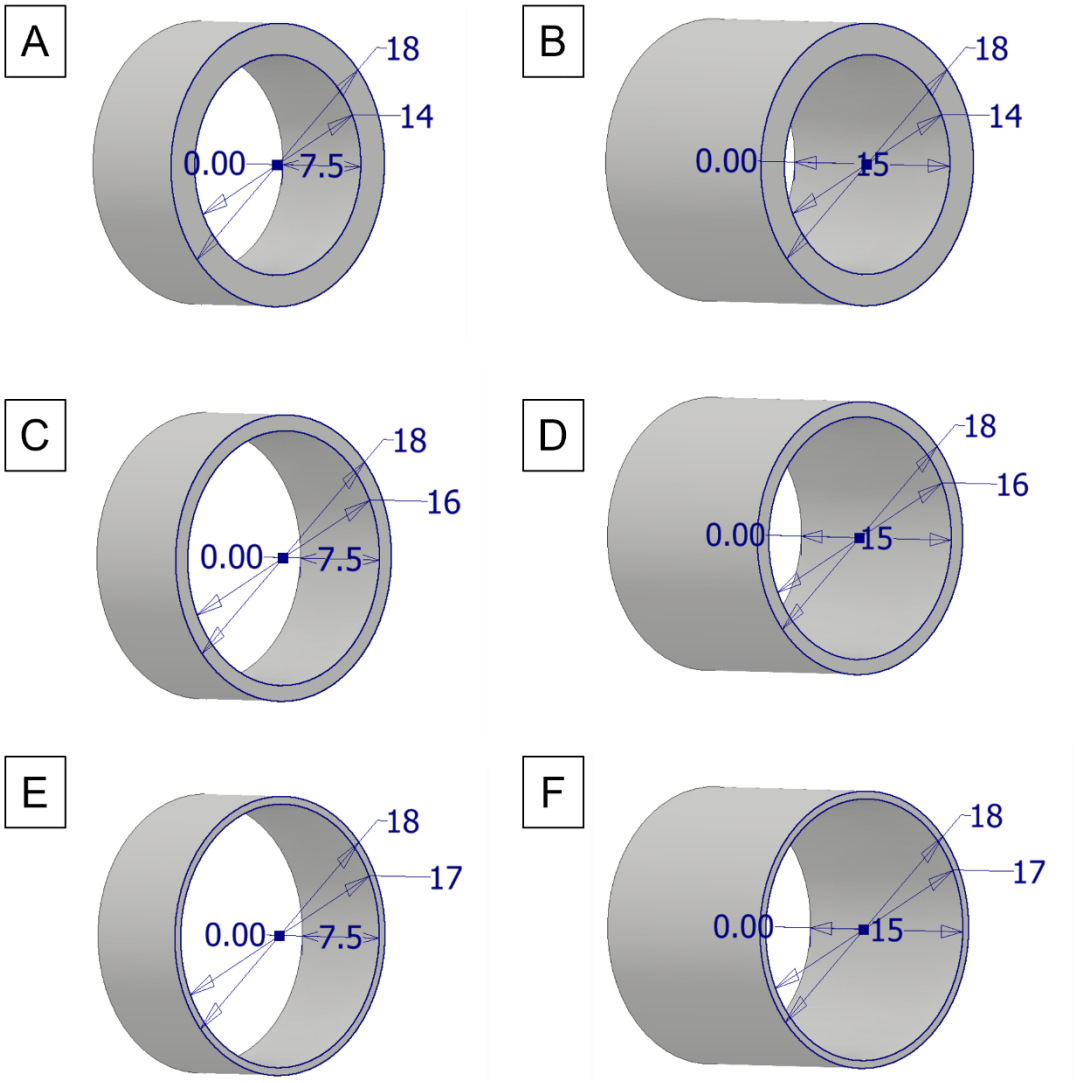


*Autodesk inventor models of tubular conduits with a fixed outer diameter of 18 mm with different lengths and wall thicknesses: (A) wall thickness (WT) 2 mm, and length 7.5 mm, (B) WT of 2 mm and length of 15 mm, (C) WT of 1 mm, and length of 7.5 mm, (D) WT of 1 mm, and length of 15 mm, (E) WT of 0.5 mm, and length of 7.5 mm, and (F) WT of 0.5 mm, and length of 15 mm. The corresponding 3D-printed tubular structures are presented in Figure 7.8, Figure 7.9, and Figure 7.10. Dimensions in figure are in mm.*

# Appendix 2: NMR and MS spectra

## $^{1}$H NMR spectra relevant to Chapter 8

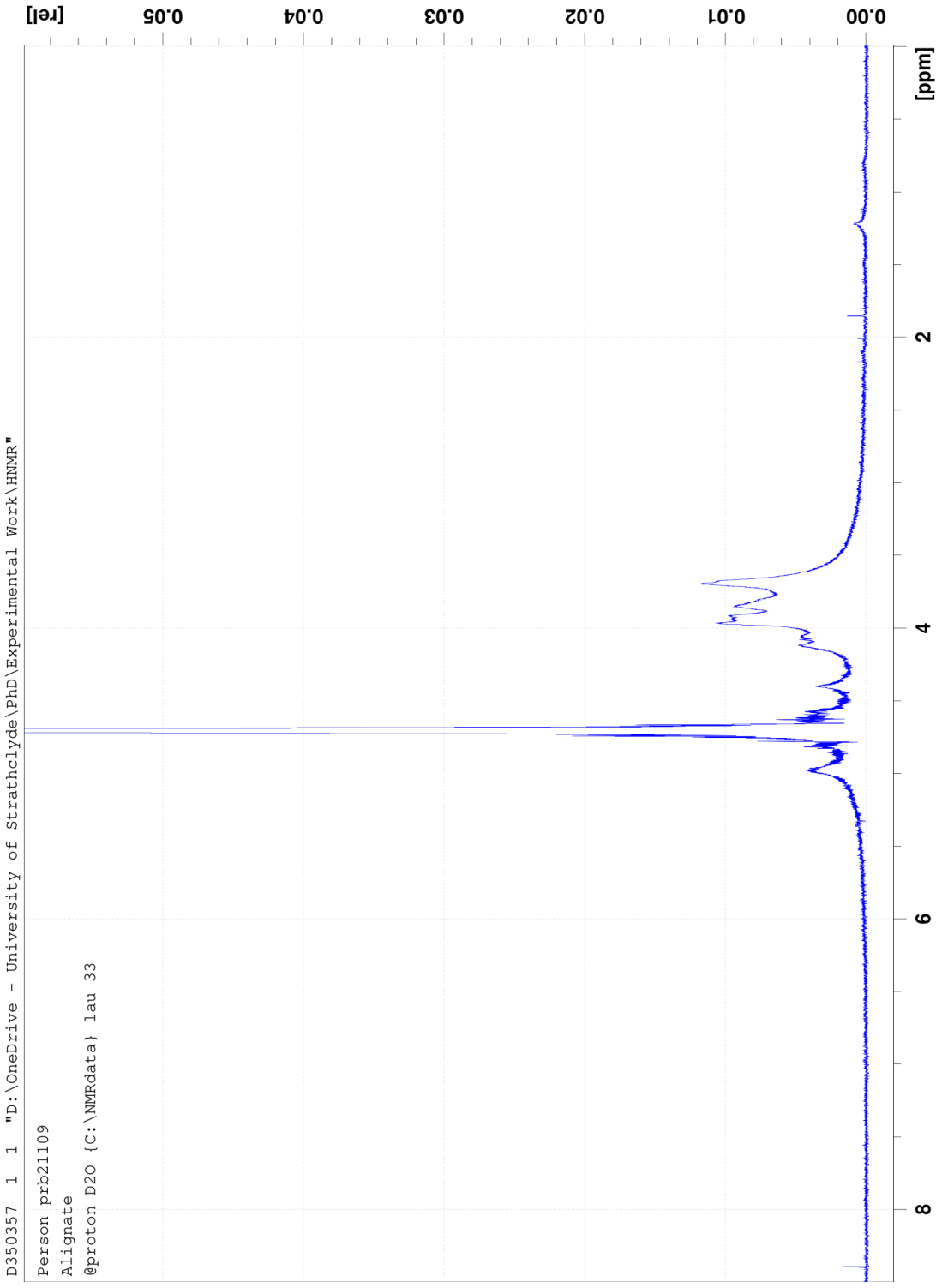


*Full $^{1}$H NMR spectra of sodium alginate corresponding to Figure 8.16.*

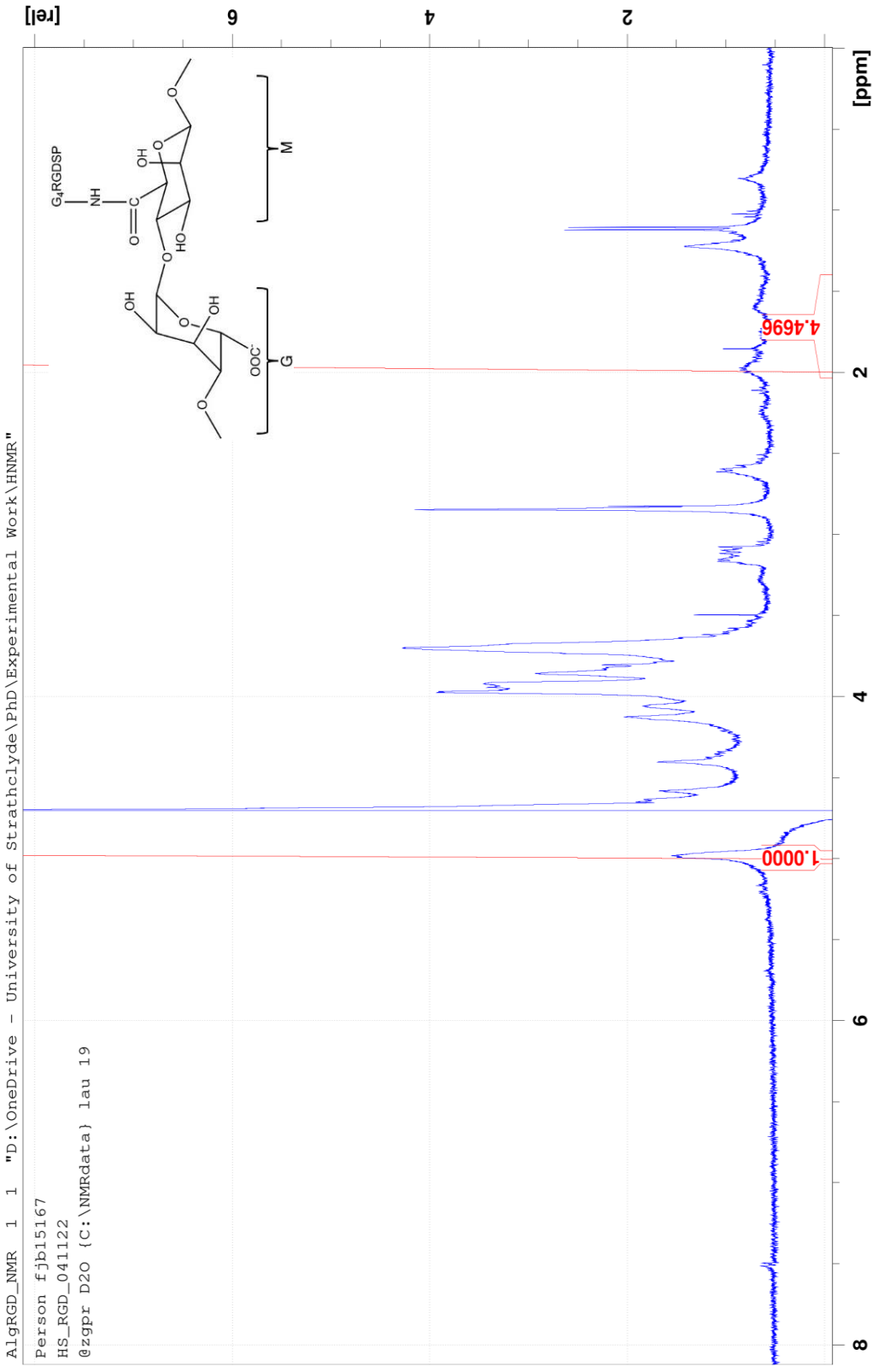


*Full $^{1}H$ NMR spectra of RGD-conjugated alginate corresponding to Figure 8.16.*

## LCMS spectra relevant to Chapter 8

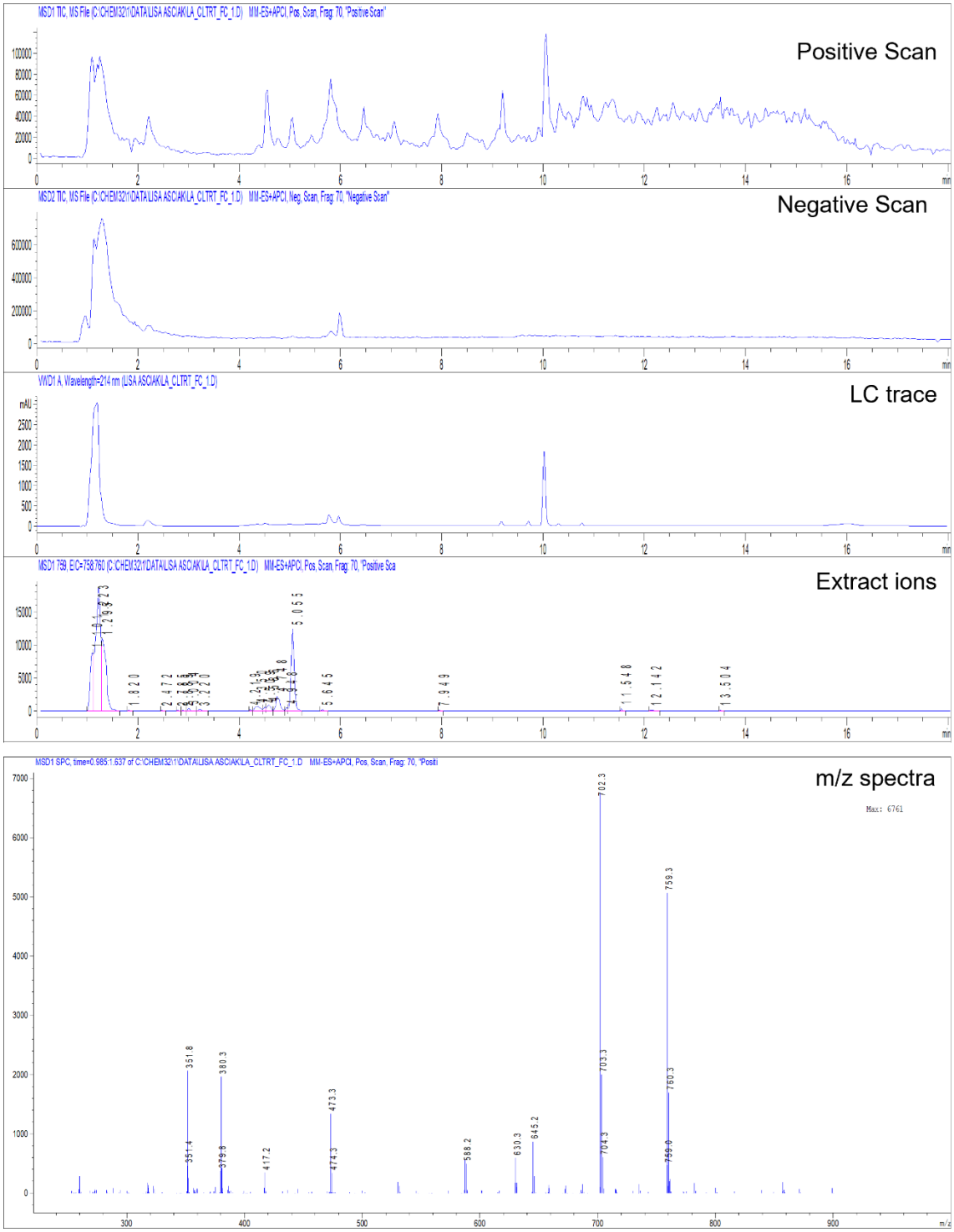


*Full LCMS spectra following full cleave of peptide 1 (Batch 1) corresponding to Figure 8.7 (A, C, E).*

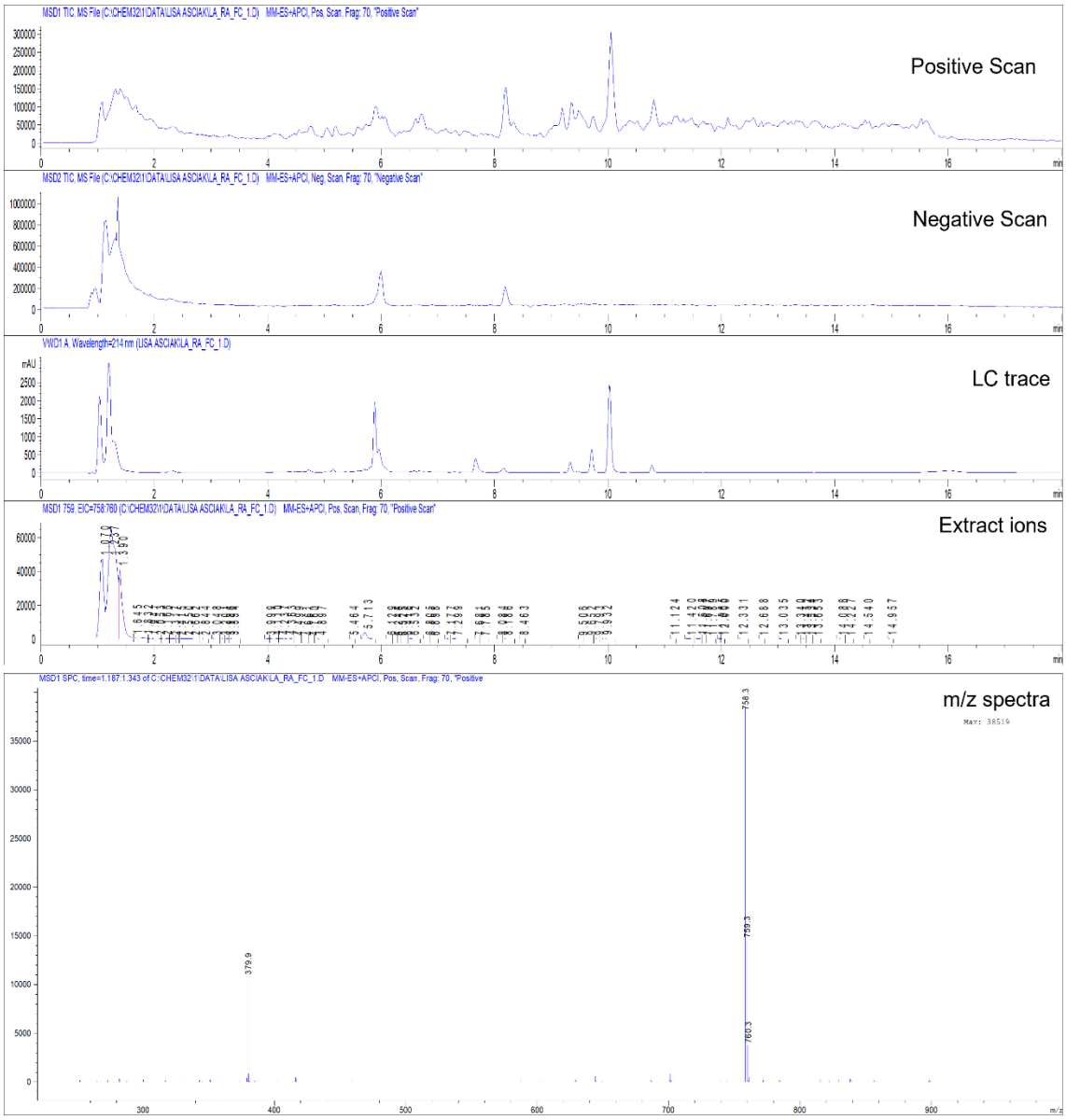


*Full LCMS spectra following full cleave of peptide 2 (Batch 1) corresponding to Figure 8.7 (B, D, F).*

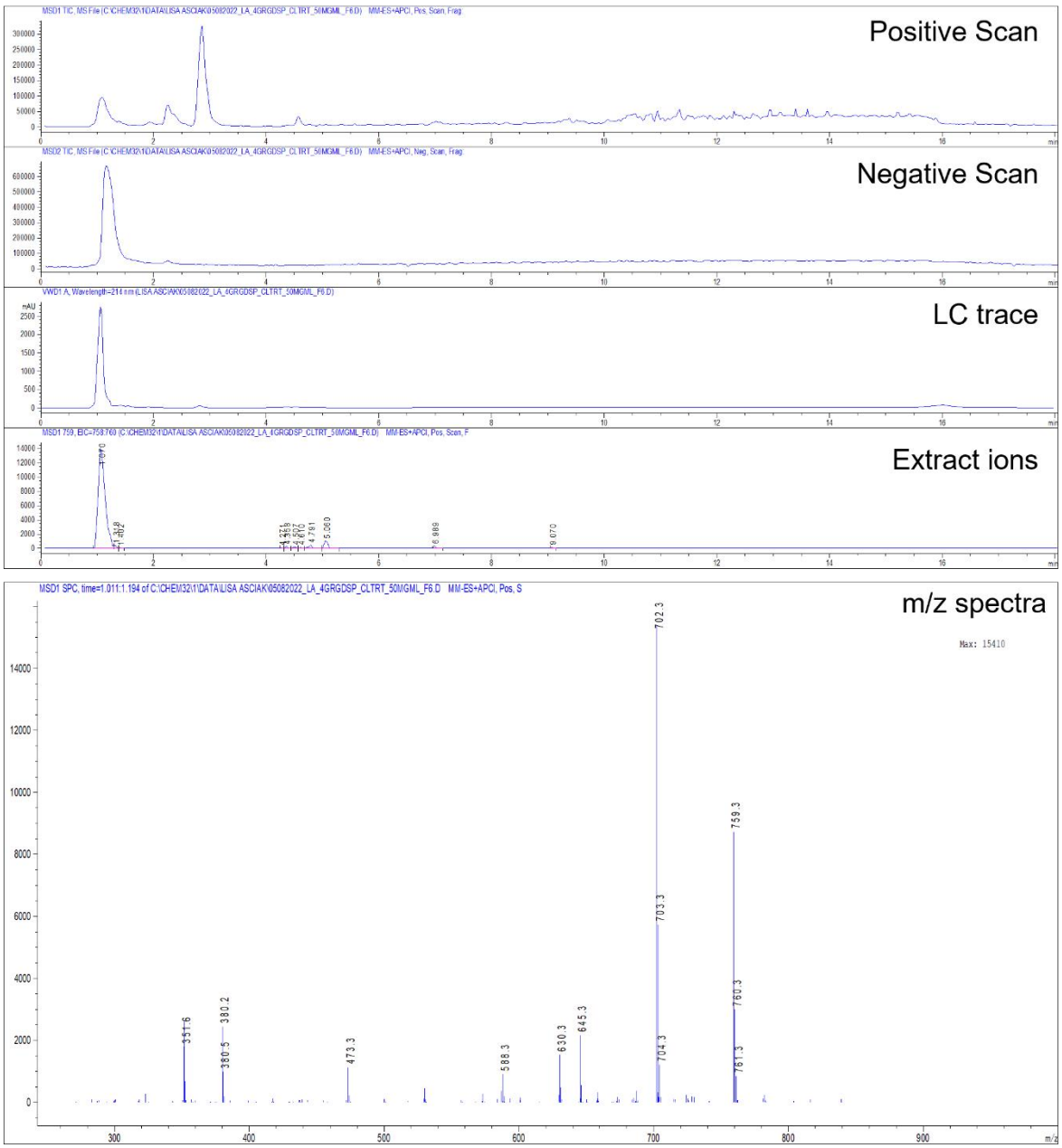


*Full LCMS spectra of peptide 1 fraction 06 corresponding to Figure 8.8 (C, D, E).*

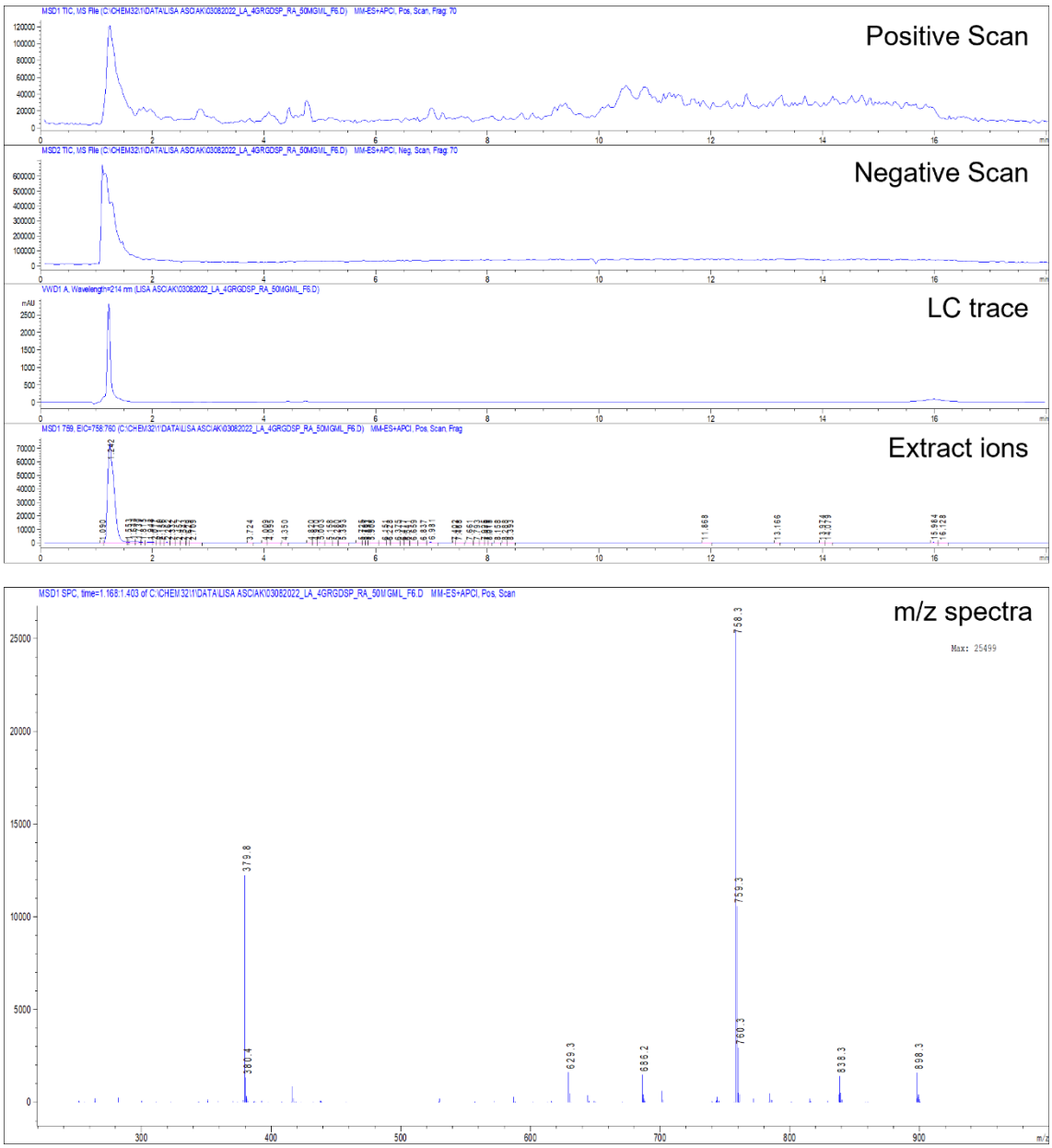


*Full LCMS spectra of peptide 2 fraction 06 corresponding to Figure 8.9 (C, D, E).*

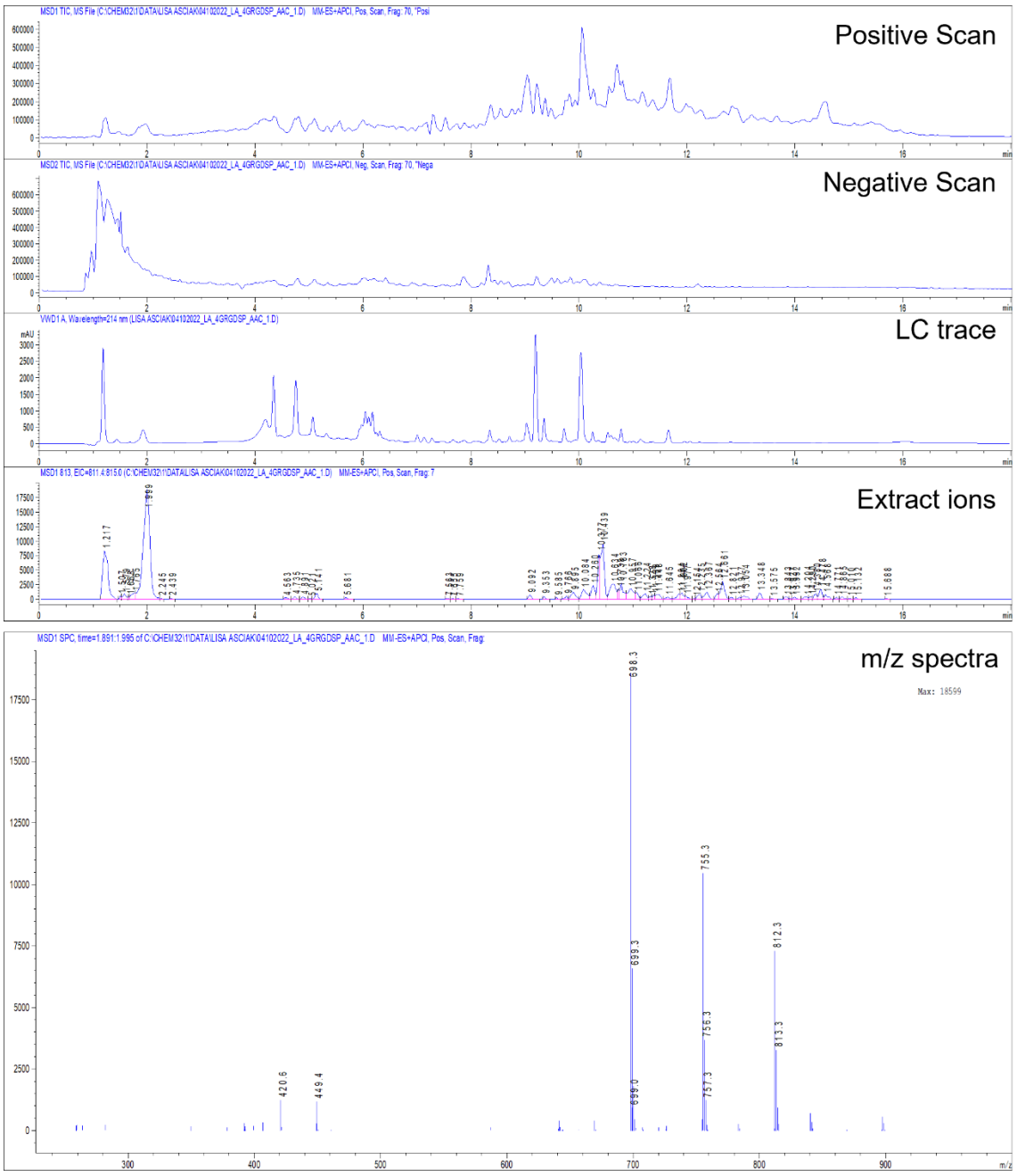


*Full LCMS spectra following a full cleave of peptide 3 (Batch 1) corresponding to Figure 8.13.*

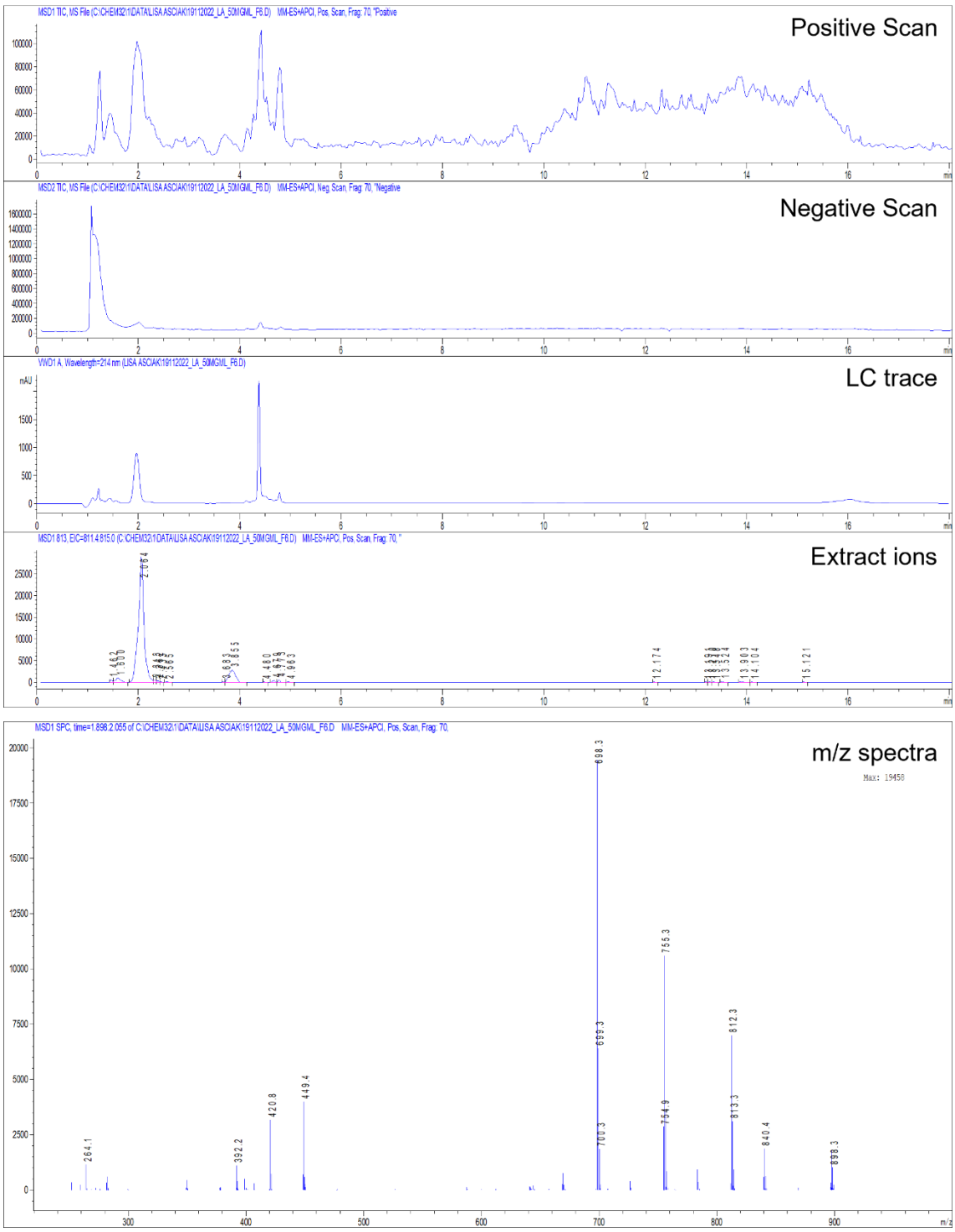


*Full LCMS spectra of peptide 3 fraction 06 corresponding to Figure 8.14 (C, D, E).*

# Appendix 3: Absorption spectra of the photoinitiators and photoblocker used to fabricate the alginate:PEGDA hydrogels.

To obtain absorption spectra of the photoinitiators and photoblocker used for the fabrication of the alginate:PEGDA hydrogels, solutions were prepared according to the concentrations present in the hydrogel formulations investigated in the thesis, i.e., 0.5% (w/v) LAP, 0.5% (w/v) Irgacure 2959, and 0.01% (w/v), 0.025% (w/v), and 0.03% (w/v) tartrazine. A small volume (100 µl) for each photoinitiatior and photoblocker concentration was pipetted in a 96-well plate. All solutions were dissolved in DI water. A Multiskan™ Go microplate spectrophotometer (Thermo Scientific™, UK) was used to measure the absorption spectra for each sample over a wavelength range between 200 nm and 500 nm. Measurements were taken at 1 nm increments.

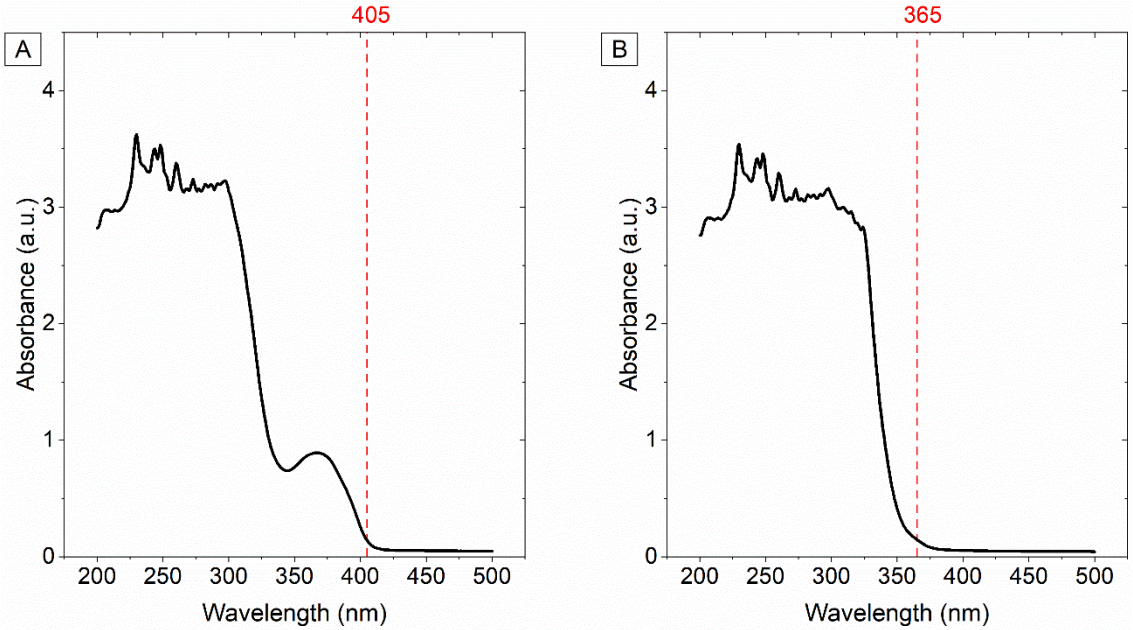


*Absorption spectra of the photoinitiators: (A) LAP (0.5% w/v in DI water) and (B) Irgacure 2959 (0.5% w/v in DI water) from 200 nm to 500 nm. The 405 nm and 365 nm wavelengths corresponding to the light emitted by the 3D printer and UV lamp respectively are represented on each respective spectrum by a red dashed line.*

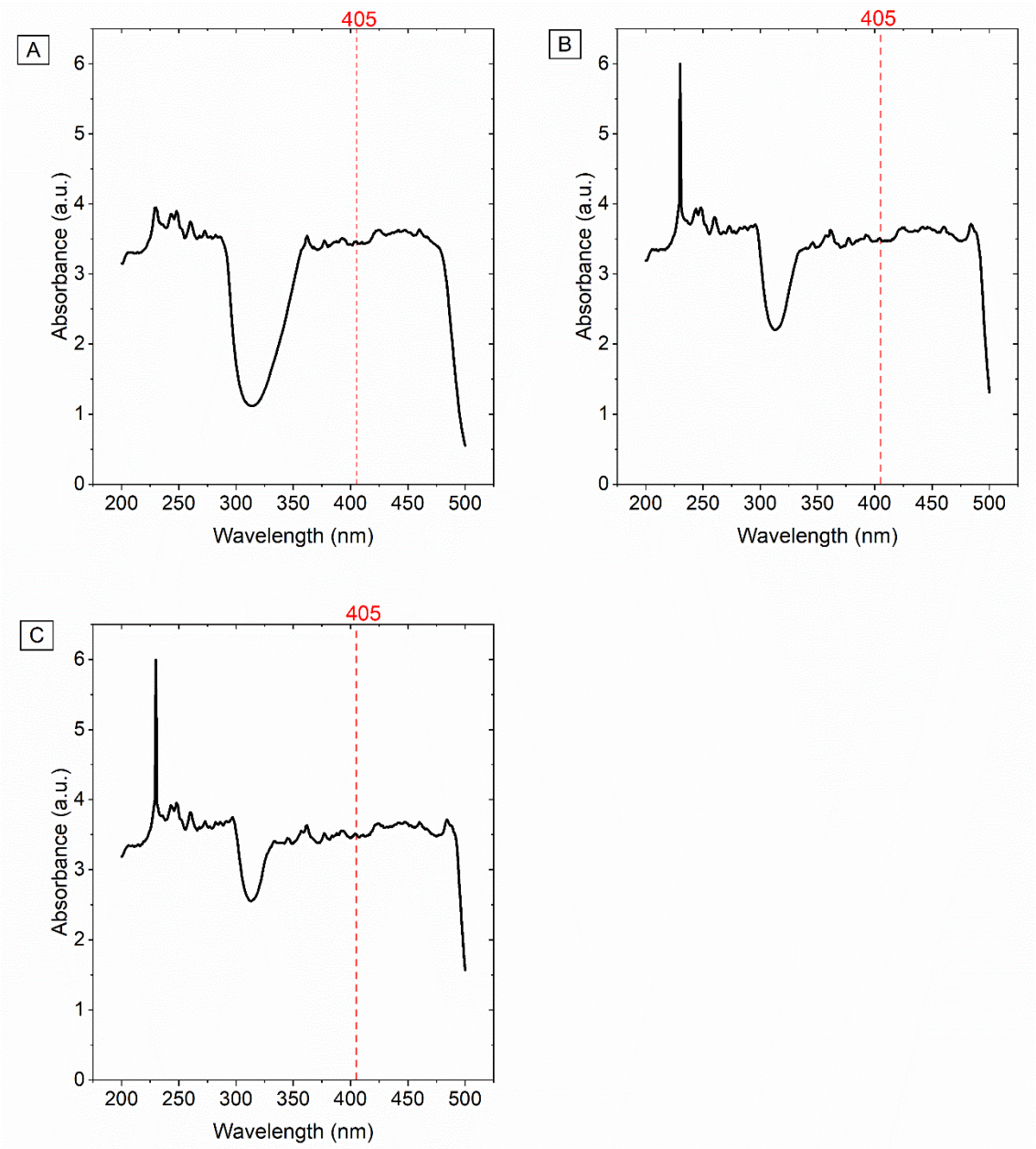


*Absorption spectra for the tartrazine dye photoblocker at different concentrations (A) 0.01% (w/v), (B) 0.025% (w/v), and (C) 0.03% (w/v) from 200 nm to 500 nm. The 405 nm corresponding to the light emitted by the 3D printer is represented on each spectrum by a red dashed line.*